3.2 First-Principles Calculation of Material Properties

Construction of anharmonic phonon property database using first-principles calculations

Masato OHNISHI

Institute of Statistical Mathematics,

Research Organization of Information and Systems, Tachikawa, Tokyo 190-8562

Introduction

Phonons, arising from collective atomic vibrations, play a key role in thermal transport and influence electronic, optical, and magnetic properties. While materials informatics (MI) has accelerated materials discovery, existing databases mainly focus on electronic properties, and datasets for anharmonic phonon properties remain limited.

First-principles calculations of these properties are computationally demanding due to large supercells and extensive force evaluations, making supercomputing resources essential. In this study, we construct a first-principles database of anharmonic phonon properties and develop machine learning models for thermal property prediction (Fig. 1) [1].

Methods

We developed an automated workflow (auto-kappa: https://github.com/phonix-db/auto-kappa) integrating first-principles calculations with VASP and phonon analysis with ALAMODE. It includes structural optimization, evaluation of harmonic and anharmonic force constants, and calculation of lattice thermal conductivity by solving the phonon Boltzmann transport equation.

The workflow enables high-throughput calculations and automatically handles unstable structures through additional optimization or larger supercells. Graph neural network (GNN)-based models were also developed for thermal property prediction.

High-throughput calculations were performed using the bulk job scheme on system B (Ohtaka), enabling massively parallel execution across many materials and improving efficiency. System C (Kugui) was used for machine learning tasks, including model training and large-scale screening.

Results and Discussion

Using supercomputing resources, we calculated anharmonic phonon properties for over 6,800 materials and constructed the Phonix database (https://phonix-db.org). The dataset provides comprehensive phonon transport information, including thermal conductivity and lifetimes.

Machine learning models trained on this dataset achieved high accuracy and revealed a scaling law, where prediction improves with increasing training data size. The models were further applied to screen approximately 380,000

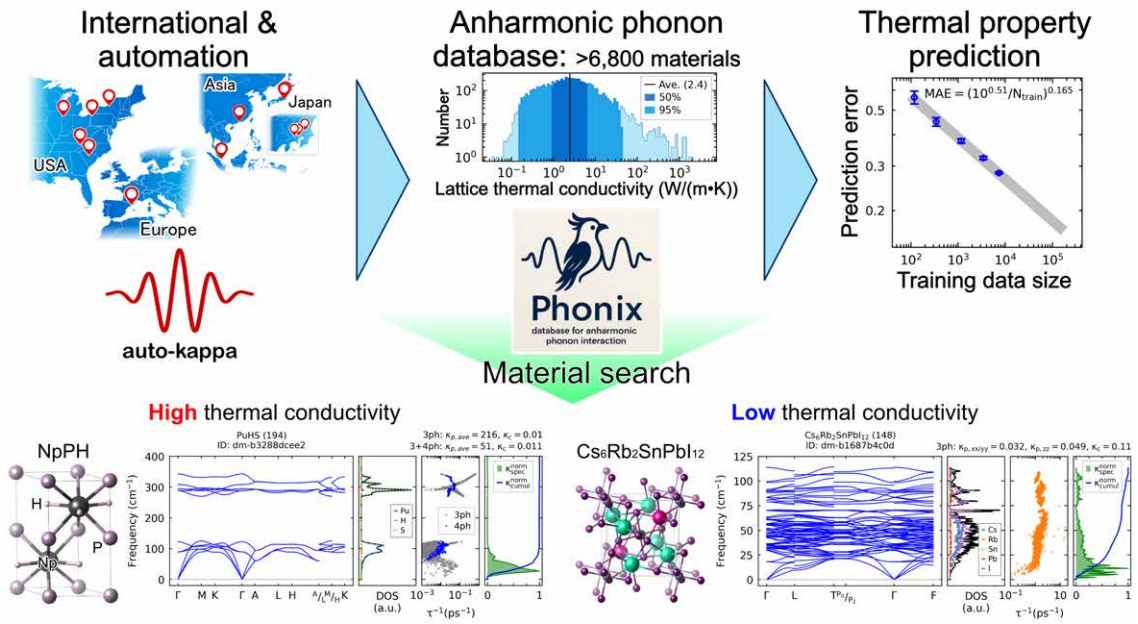

Fig. 1: Project overview. High-throughput calculations were conducted using automation software for anharmonic phonon properties (auto-kappa) through international collaboration. Anharmonic phonon properties, including lattice thermal conductivity, were calculated for over 6,800 crystal compounds and released as the Phonix database. Using the developed database and graph neural networks (GNNs), machine learning models for thermal property prediction were constructed, and a deep-learning scaling law—showing improved prediction accuracy with increasing training data size—was demonstrated. Finally, the prediction model was applied to screen high- and low-thermal-conductivity materials from approximately 380,000 candidates.

materials, identifying candidates with high and low thermal conductivity. These results demonstrate the effectiveness of combining first-principles calculations and machine learning.

Conclusion

We developed an automated high-throughput framework for anharmonic phonon calculations (auto-kappa) and constructed a large-scale database (Phonix) using supercomputing resources. The integration of first-principles calculations and machine learning enables efficient prediction and screening of thermal properties, providing a foundation for data-driven materials design.

References

[1] M. Ohnishi, npj Comp. Mater. (2026) accepted.

Theoretical study on chemical reaction processes at surfaces and interfaces using density functional theory and machine learning methods

Meliton R. Chiong III, Muhammad Fadhlan ANSHOR, Beatriz A. C. TAN, Samuel E. M. P. PUTRA, Harry Handoko HALIM, and Yoshitada MORIKAWA
Department of Precision Engineering, The University of Osaka
Yamada-oka 2-1, Suita, Osaka 565-0871

First-principles electronic structure methods offer high predictive accuracy and have been widely employed to elucidate a variety of reaction processes. However, their application has traditionally been constrained to spatial scales of a few nanometers and time scales on the order of hundreds of picoseconds due to their substantial computational cost. Recently, the integration of machine learning techniques has made it possible to overcome these limitations.

By combining first-principles electronic structure calculations with machine learning, kinetic Monte Carlo methods, and microkinetic modeling within a multiscale simulation framework, we aim to elucidate heterogeneous catalytic reaction processes. In particular, this approach enables long-timescale simulations at surfaces and interfaces that were previously inaccessible.

By comparing our simulation results with the latest experimental data, we seek to identify the key factors governing catalytic reactivity and to establish guiding principles for the rational design of more efficient catalysts.

In this fiscal year, using Supercomputer Systems at the SCC-ISSP, we have investigated 1) photodetachment in Al_{13}^- anions and photoionization in Al_{13} neutrals[1], 2) reactive graphene edge-adsorbed Pt single-atom catalyst structures for oxygen reduction reactions[2], 3) the effect of hydrogen gas pressure in hydrogenation of CO_2 to Formate on Cu(100)[3] and 4) improvement of global structural optimization method, "The Scaled-LCB"[4]. In this report, we focus on the first topic.

The Al_{13} anion has attracted particular attention due to its remarkable stability arising from its high symmetry and closed-shell electronic structure. Consequently, Al_{13} neutral behaves as a "superhalogen", characterized by a notably high electron affinity. Experimentally, the Al_{13}^- anion exhibits an adiabatic detachment energy (ADE) of 3.62 $\pm$0.06 eV and a vertical detachment energy (VDE) of 3.75 $\pm$0.1 eV. Within the jellium model, its 40 valence electrons complete the superatomic orbitals $(1S)^2(1P)^6(1D)^{10}(2S)^2(2P)^6(1F)^{14}$ into a closed shell. The ground-state structure of Al_{13}^- is icosahedral, where symmetry splits the closely spaced 2P and 1F superatomic states into overlapping hybrid PF states. In contrast, the ground state Al_{13}^+ cation adopts a low-symmetry cap-like structure consisting of $1-5-1-6$ layers of Al atoms.

In this study, we employ diffusion Monte Carlo (DMC) to compute the vertical and adiabatic detachment energies (VDE, ADE) of Al_{13}^- anion and the corresponding ionization energies (VIE, AIE) of Al_{13} neutral. We assess the effects of basis set choice and multideterminant expansions on the trial wave function, and simulate the vibronic transitions to enable direct comparison with experimental photoelectron spectra. Finally, we use these results to clarify

the photodetachment of Al_{13}^- anions and the photoionization of Al_{13} neutrals and to provide benchmark-quality values for future theoretical and experimental work.

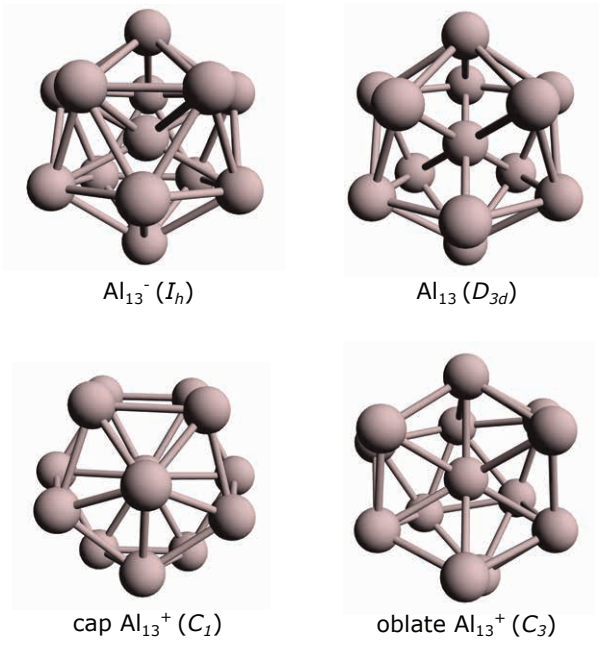

Figure 1: Isomers of Al_{13}^-, Al_{13}, and Al_{13}^+ optimized at the PBE0/6−311+G(d,p) level. The anionic Al_{13}^- has an icosahedral geometry (Ih), the neutral Al_{13} undergoes a Jahn-Teller distortion to a distorted icosahedron (D3d), and the cationic Al_{13}^+ has two low-symmetry isomers: a cap-like structure (C1) and an oblate structure (C3). The cap isomer is 0.51 eV lower in energy than the oblate.

We have employed diffusion Monte Carlo to clarify the photodetachment and photoionization processes of the prototypical superatom Al_{13}. For the anion, DMC combined with vibronic analysis accurately reproduces both adiabatic and vertical detachment energies, highlighting the need to account for finite-temperature effects when comparing with experiment. For the Al_{13} neutral cluster, we resolve a long-standing controversy by revealing that the experimental ionization energy corresponds to the adiabatic ionization into a metastable oblate cation, not into the cap-like ground state. This structural assignment is supported by laser photoionization mass spectra and reconciles prior theoretical inconsistencies.

References

[1] M. R. Chiong III, A. Nakajima, and Y. Morikawa: J. Phys. Chem. A **130**, 1851-1860 (2026).

[2] B. A. C. Tan, N. A. Sofi, P. N. Thanh, K. I. M. Rojas, S. E. P. P. Masan, Y. Hamamoto, I. Hamada, and Y. Morikawa: Phil. Trans. R. Soc. A, **384**, 20240555 (2026).

[3] W. O. N. F. Rajaelo †, H. H. Halim †, M. F. Anshor, Y. Yamada, S. Ramadhani, F. A. Mubarok, S. E. M. Putra, A. L. Ivansyah, T. D. K. Wungu, Suprijadi, Y. Morikawa*, and F. Muttaqien*, † These authors contributed equally: ACS Catal., **16**, 5068-5079 (2026).

[4] S. E. P. P. Masan, T. N. Pham, K. I. M. Rojas, B. A. C. Tan, F. Rusydi, Y. Hamamoto, and Y. Morikawa: J. Ceram. Soc. Jpn., **133**, 602-609 (2025).

Identification of Semiconductor Donor Structures Using First-Principles Calculations and Development of Quantum Algorithms

Yu-ichiro MATSUSHITA

Department of Physics,

The University of Tokyo, Hongo, Bunkyo-ku, Tokyo 113-8654

This research project leveraged the high-performance computing (HPC) resources of the Institute for Solid State Physics and other centers to address two of the most significant frontiers in computational materials science: the advancement of quantum algorithms for spectroscopy and the microscopic elucidation of semiconductor defect physics. Throughout this fiscal year, the utilization of large-scale parallel processing has enabled us to achieve major scientific milestones that provide a new blueprint for both future material simulations and next-generation device optimization.

The first major achievement is the advancement of quantum computing methodologies for materials science, specifically the implementation of a logical Quantum Phase Estimation (QPE) framework for spectroscopic analysis[1]. Calculating the X-ray absorption spectra (XAS) of strongly correlated systems, such as transition metal oxides, is notoriously difficult for classical computers. We focused on the iron $L_{2,3}$-edge of $FePO_4$, initially utilizing HPC resources to define a chemically relevant active space through the Automated Valence Active Space (AVAS) method. To address the inherent noise of current quantum hardware, we integrated the [k+2, k, 2] Iceberg code for quantum error detection (QED). Validation on a trapped-ion quantum computer demonstrated that the application of QED effectively reduced the spectral ℓ^2 error, marking a critical step toward high-fidelity material diagnostics in the era of fault-tolerant quantum computing. This achievement establishes a robust framework for integrating classical supercomputing with quantum processors to solve complex multi-body problems in materials science.

The second major achievement is the definitive identification of the microscopic origin of "hydrogen-related donors" (HDs) in silicon, a phenomenon that has remained an enigma in semiconductor physics for over fifty years[2]. By performing large-scale first-principles calculations based on the HSE06 hybrid functional, we identified the core of the HD defect as a cluster of four silicon self-interstitials (I_4). Our analysis revealed a unique synergistic mechanism where the I_4 cluster generates empty defect levels just below the

conduction band edge, which then capture an electron from an incorporated hydrogen atom to function as a shallow donor. This discovery represents a paradigm shift from traditional substitutional doping, where an impurity atom is expected to take the place of a host atom. Furthermore, our results suggest that this HD mechanism is transferable to other covalently bonded wide-bandgap semiconductors like diamond, offering a novel strategy for achieving efficient n-type doping in power electronics and potentially overcoming long-standing material constraints in high-performance device fabrication. In summary, the computational achievements of this year have yielded significant dividends in both fundamental quantum research and practical semiconductor applications. These results, published in prestigious journals such as Physical Review Applied and Communications Materials, underscore the vital role of supercomputing in driving the future of material science and industrial technology.

References

[1] H. Nishi, T. Kosugi, S. Hirose, T. Okayama, and Y. Matsushita, Phys. Rev. Applied **25**, 034026 (2026).

[2] A. Kiyoi, Y. Nishiya, Y. Matsushita, and T. Umeda, Comm. Materials **7**, 8 (2026).

First-principles study on functionality of electronic devices

Tomoya ONO
Graduate School of Engineering, Kobe University
Rokkodai-cho, Nada, Kobe 657-8501

Tunneling magnetoresistance plays an important role in spintronics in magnetic tunnel junctions (MTJs), which consist of two ferromagnetic electrodes divided by an extremely thin tunnel barrier with controllable magnetization directions. Tunnel barrier is the key element of an MTJ, which is traditionally composed of MgO or Al_2O_3. Recently, two-dimensional (2D) materials with atomic-layer thickness have gained significant interest as useful nonmagnetic materials for tunnel barriers in MTJs.

We performed the density functional theory calculations to investigate the atomic and electronic structures of the graphene/NiFe alloy interface[1] using the DFT-based code Vienna Ab initio Simulation Package.[2] FM metal is deposited on the graphene in some experiments while the graphene is transferred to the FM metal substrate in many cases. We assume that Ni is adsorbed with (111) face because (111) face is the most stable face for a fcc crystal and the lattice constant mismatch between Ni(111) and graphene is less than 1%. In our computational model, the bare metal substrate consists of nine atomic layers, in which the topmost and bottommost layers are referred to as the surface layers and the remaining layer is defined as the bulk layer. The surface layers consist of a binary alloy $Ni_\alpha Fe_{1-\alpha}$ (α=0.00, 0.25, 0.50, 0.75, and 1.00), whereas the bulk layer is composed of $Ni_\beta Fe_{1-\beta}$ with β=0.50, 0.75, and 1.00. In the bulk layer of Ni_3Fe, Fe atoms lie on a $(\bar{1}10)$ plane, while the atomic configuration is $L1_0$ in the bulk layer for NiFe. The atomic configurations of Ni and Fe atoms in the surface layers are defined so as to keep the stacking sequence of $Ni_\beta Fe_{1-\beta}$ when $\alpha = \beta$. Monolayer graphenes are adsorbed on both the edges of the substrate. Four possible adsorption geometries are examined, with C atoms located at the hcp-fcc, top-fcc, top-hcp, and bridge-top sites. The Perdew–Burke–Ernzerhof generalized gradient approximation are used for electronic exchange and correlation interactions and The projector-augmented wave method is employed for the electron–ion interactions. The supercell size is $\sqrt{2}a_b \times \sqrt{6}a_b/2 \times 36.34$ Å^3 with a_b (=3.524 Å) being the experimental lattice constant of the Ni fcc bulk. A 19 × 19 × 1 Monkhorst–Pack mesh of k points is used for the Brillouin-zone integration. Structural optimization for the atoms in the surface layers and graphenes is performed until all the force components decrease to below 0.02 eV/Å.

The formation energy of surface layer $E_{\rm form}^{\rm surf}$ is defined as follows:

$$E_{\rm form}^{\rm surf} = \frac{-E_{\rm NiFe}^{(9)} + E_{\rm NiFe}^{(7)}}{N} + \alpha\mu_{\rm Ni} + (1-\alpha)\mu_{\rm Fe}, \quad (1)$$

where $E_{\rm NiFe}^{(n)}$ is the total energy of n layers of $Ni_\beta Fe_{1-\beta}$, $N(=8)$ is the number of metal atoms in the surface layers, and $\mu_{\rm Ni}$ ($\mu_{\rm Fe}$) is the chemical potential of the Ni (Fe) atom, which is taken from an fcc (bcc) bulk. Equation (1) implies that the surface with higher formation energies are preferred. The formation energy of the bare NiFe alloy substrate is shown in Fig. 1. The surface layer with $\alpha = 0.75$ ex-

hibits the largest formation energies. In addition, the substrates with the Fe-rich surface layer ($\alpha < 0.50$) are less preferable than those with the Ni-rich surface layer for all the binary compounds of the bulk layer, which can be explained by the formation energy of the bulk.

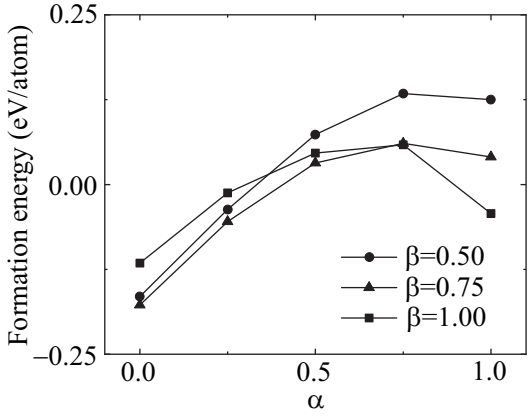

Figure 1: Formation energy of surface layer. Reprinted from Ref. 1.

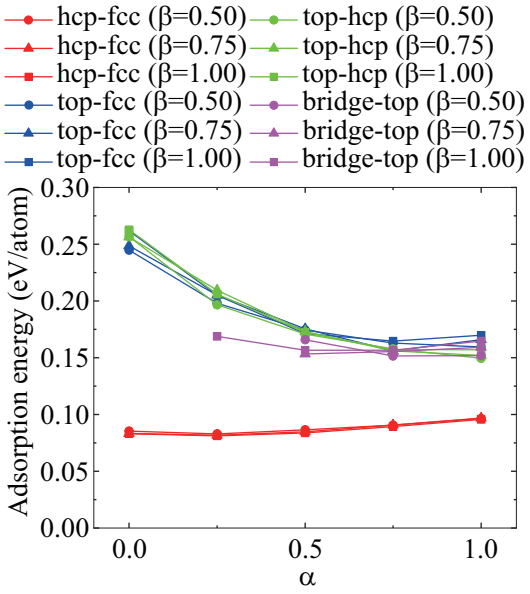

Figure 2: Adsorption energy of graphene on NiFe alloy substrate. Reprinted from Ref. 1.

The adsorption energy of graphene on the NiFe alloy substrate E_{ads} is defined as follows:

$$E_{\mathrm{ads}} = \frac{-E_{\mathrm{Gr/NiFe}} + E_{\mathrm{NiFe}} + 2E_{\mathrm{Gr}}}{N_C}, \qquad (2)$$

where E_{NiFe} is the total energy of nine layers of the NiFe alloy substrate, E_{Gr} is the total energy of the graphene monolayer, $E_{\mathrm{Gr/NiFe}}$ is the total energy of the NiFe alloy substrate with the graphene monolayer at both ends, and $N_C(= 16)$ is the number of C atoms in the supercell. Equation (2) indicates that the interface with large adsorption energy is preferable. Figure 2 shows the adsorption energy. In the case of the Fe-rich surface, the graphene adsorbed at the bridge-top site shifts to the top-fcc or top-hcp site after the structural optimization. When graphene is adsorbed on the Fe-rich surface at the top-hcp site, the adsorption energy is the largest. In contrast, for Ni-rich surfaces, the graphene adsorption at the top-fcc or bridge-top site is favorable, and the difference in the adsorption energy among top-hcp, top-fcc and bridge-top sites is small. It is found that the distance d between the atoms in the surface layer and graphene is *ca* 2.1 Å. The interfaces with the surface layer of α=0.00 are the most stable regardless of the adsorption sites and binary compounds of the bulk layer. These results do not agree with the stability of the bare NiFe alloy substrate with respect to the composition ratio of the surface layer. Our results imply that the composition ratio of the interface of graphene/NiFe alloy substrate is affected by the fabrication process.

References

[1] N. Matsumoto, R. Endo, M. Uemoto, and T. Ono, J. Appl. Phys. **138** 104305 (2025).

[2] G. Kresse and J. Hafner, Phys. Rev. B **47**, 558 (1993).

Density functional theory study of adsorption, reaction, and manipulation of molecules on solid surfaces

Ikutaro Hamada

Department of Precision Engineering, Graduate School of Engineering,

The University of Osaka, 2-1 Yamadaoka, Suita, Osaka 565-0871

Understanding molecular adsorption and reactions at solid surfaces is crucial for a wide range of phenomena, from everyday processes such as wetting and corrosion to technologically important applications including heterogeneous and electrochemical catalysis. Despite their importance, the atomic-scale mechanisms governing surface adsorption and reactions remain incompletely understood, hindering the rational design of efficient materials and energy conversion devices.

In this project, we performed density functional theory (DFT)-based simulations to investigate adsorption states and reaction mechanisms of molecules relevant to heterogeneous catalysis and energy conversion. In addition, extending beyond static descriptions of surface adsorption, we aim to elucidate the microscopic mechanisms of adsorbate manipulation induced by scanning probe microscopy (SPM) tips.

Our DFT simulations cover a wide range of systems, including:

- organic molecules on semiconductor surfaces [1],
- molecular adsorption on terraces and edges of hexagonal boron (HB) sheets [2,3],
- H_2 formation from bilayers of HB sheets [4],
- intermolecular complexes such as C_6H_6–H_2 and H_2–H_2 [5], and
- oxygen reduction reactions on OH-functionalized Fe- and Co-based single-atom catalysts [6].

These simulations were carried out using several DFT codes, including STATE [7], Quantum ESPRESSO [8], VASP [9], and MOLGW [10]. Below, we describe selected results obtained mainly using System B of the ISSP supercomputer facility.

We investigated the adsorption states of PTCDA and its derivatives on Si(111)-(7×7) surfaces [1], successfully determining their adsorption sites and adsorption energies, as well as characterizing their vibrational modes.

For HB sheets, we predicted that H_2 adsorption can be enhanced by introducing boron vacancies, and clarified the origin of this enhancement [2]. We also investigated water adsorption and the reaction of H_2O at the edges of HB sheets. We found that H_2O is adsorbed

near the edges, rather than directly at edge sites. Furthermore, the activation energy for H_2O dissociation to form OH near the edge is lower than that on the terrace. This result indicates that H_2O dissociation—considered the onset of the hydrolysis reaction observed experimentally—preferentially occurs in the near-edge region of HB sheets [3].

Finally, we investigated H_2 formation from bilayers composed of HB sheets. We found that the H–H distance is a key factor governing H_2 formation on HB sheets [4].

References

[1] Y. Park, I. Hamada, M. Wolf, and A. Shiotari, Angew. Chem. Int. Ed. e202514215 (2025).

[2] S. Naka, K. I. M. Rojas, and I. Hamada, e-J. Surf. Sci. Nanotechnol **23**, 339-345 (2025).

[3] K. I. M. Rojas,L. T. Ta, S. Naka, Y. Morikawa, and Ikutaro Hamada, J. Chem. Phys. **163**, 124702-1-11 (2025).

[4] Y. Yasuda, O. Ok, K. Goto, N. Noguchi, S. Ito, M. Hikichi, R. Tsuji, Y. Nakahira, R. Utsumi, H. Saitoh, S. Nakano, S. Naka, I. Hamada, S. Orimo, and T. Kondo, ACS Nano **20**, 9951-9960 (2026).

[5] Y. Kataoka and I. Hamada, Phys. Rev. B **113**, 085143 (2026).

[6] A. F. Z. Abidin and I. Hamada, Phil. Trans. R. Soc. A **384**, 2318 (2026).

[7] STATE documentation, https://state-doc.readthedocs.io/

[8] P. Giannozzi et al., J. Phys. Condens. Matter **21**, 395502 (2009).

[9] G. Kresse and J. Furthmüller, Comput. Mat. Sci. **6**, 15 (1996); G. Kresse and J. Furthmüller, Phys. Rev. B **54**, 11 169 (1996).

[10] F. Bruneval, et al., Comput. Phys. Commun. **208**, 149 (2016)

Theoretical Studies on the Electron Traps in a-SiN for Flash Memory Application

Kenji SHIRAISHI

Center for Innovative Integrated Electronic Systems, Tohoku University,

468-1 Aramaki Aza Aoba, Aoba-ku, Sendai, Miyagi 980-8572

The a-SiN known as a useful hard material is now indispensable in current semiconductor technology: It is placed near the interface of Si-based metal-oxide-semiconductor structures and utilized as a nonvolatile flash memory which sustains our current data-driven society [1]. We focused on the charge-trap properties of amorphous silicon nitride (a-SiN) acting as charge-trap layer in 3D NAND flash memories. The scope is to improve the device performance by tuning the relevant microscopic properties. The electron trapping mechanism in silicon-rich a-SiN is primarily facilitated by the presence of the peculiar LFS, associated with tetracoordinated Si atoms. As the amount of Si increases, the a-SiN displays deeper trap levels, a higher density of electron traps, and improved programming/erase (P/E) endurance, which can all be ascribed to the characteristics of LFS as shown in Fig.1. By considering the influence of shallow trap levels, we identified an optimal nitrogen-to-silicon (N/Si) ratio is approximately 1.13. Furthermore, by accurate tuning of the H concentration, mainly passivating undercoordinated N, we have shown how the device performance can improve, since H atoms affect indirectly (i.e. upon N–H bond formation) the percentage of Si–Si bonds in the material, where LFS can form. By carefully adjusting both the N/Si ratio and the H content, the performance of charge-trap silicon nitride (CT-SiN) can be maximized.

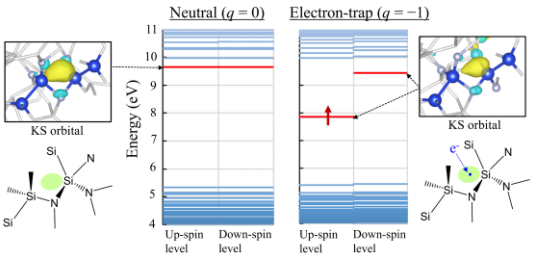

Fig.1. Kohn–Sham (KS) energy levels (central panels) and their corresponding orbitals along with the local schematic structures (side panels), in the neutral (q = 0) and charged electron-trap state (q = −1) for the $Si_{48}N_{63}H_3$ model. KS orbitals are shown by yellow (+) and blue (−) isosurfaces at a value of 50 % of the maximum. In the schematic structures, the light green areas indicate the LFS where electrons are trapped.

References

[1] M Boero, K Shiraishi, T Nagahashi, F Nanataki, and A Oshiyama, Physical Review Materials **9**, 084601 (2025).

Clarification of Atomic Level Operation Mechanism of New Vibration-Powered Generator Using Si/SiO_2 Interfaces

Kenji SHIRAISHI

Center for Innovative Integrated Electronic Systems, Tohoku University,

468-1 Aramaki Aza Aoba, Aoba-ku, Sendai, Miyagi 980-8572

A potassium-ion electret, which is a key element of vibration-powered micro-electromechanical generators, can store negative charge almost permanently. However, the mechanism by which this negative charge is stored is still unclear. We theoretically study the atomic and electronic structures of amorphous silica (a-SiO_2) with and without potassium atoms using first-principles molecular-dynamics calculations. Our calculations show that a fivefold-coordinated Si atom with five Si–O bonds (an SiO_5 structure) is the characteristic local structure of a-SiO_2 with potassium atoms, which becomes negatively charged and remains so even after removal of the potassium atoms. These results indicate that this SiO5 structure is the physical origin of the robust negative charge observed in potassium-ion electrets. Here we identify pentacoordinate silicon in potassium-ion-processed amorphous silica by XPS and first-principles calculations. The XPS spectra is consistent with the predicted electronic fingerprint of SiO_5. These results establish pentacoordinate silicon as the microscopic origin of long-lived negative charge retention in silica electrets.

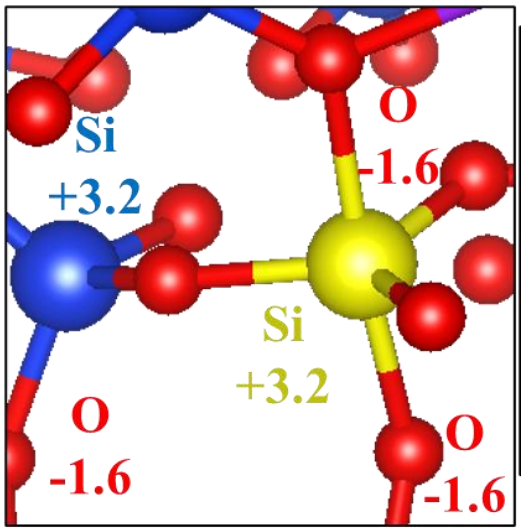

Fig.1. Structure around a fivefold-coordinated Si atom in a-SiO2.

References

[1] T. Nakanishi, T. Miyajima, K. Chokawa, M. Araidai, H. Toshiyoshi, T. Sugiyama, G. Hashiguchi, and K. Shiraishi, Appl. Phys. Lett., 117, 193902 (2020).

[2] Y. Ohata, T. Nakanishi, K. Chokawa, M. Araidai, T. Ishiguro, H. Mitsuya, H. Toshiyoshi, Y. Shibata, G. Hashiguchi, and K. Shiraishi, Appl. Phys. Lett., 121, 243903 (2022).

First-Principles Methods for Spin Conversion and Real-Space Transport Analysis

Fumiyuki ISHII, Naoya YAMAGUCHI, Hana Pratiwi KADARISMAN, Shohei MIURA, Rifky SYARIATI, Yaotang ZHANG, Yedija Yusua Sibuea TEWENG, Jin INOUE, Sota YAMATE, Shota SASAJIMA, Jingwen YANG, Zohan Syah FATOMI, Ahmad SOHIB, Syifa Fauzia Hariyanti PUTRI, Ahmad Al GHIFFARI, Salsabila Amanda PUTRI, Nadia Maharani CHADIZA, Shigetomo YANASE

Nanomaterials Research Institute, Kanazawa University

Kanazawa, 920-1192, Japan

This report summarizes the results obtained in the ISSP projects 2025-Ca-0091 and 2025-Cb-0054. The common objective was to extend first-principles methods for spin conversion phenomena and to analyze transport coefficients in layer- and real-space-resolved forms. We used OpenMX-based density-functional calculations, local Berry phase methods, hybrid Wannier functions, effective-screening-medium calculations, and Green's-function transport calculations on the ISSP supercomputer systems.

1. *First-principles method for spin Hall conductivity*

We developed a first-principles method for spin Hall conductivity (SHC), a key quantity for spin-current generation in spin-orbit-coupled materials. Conventional SHC calculations often rely on maximally localized Wannier functions and a spin-current operator. In contrast, our approach uses Bloch wave functions and the Fukui–Hatsugai–Suzuki Berry-phase formalism, enabling SHC calculations without Wannierization and without explicitly introducing a spin-current operator. Benchmark calculations for Pt showed qualitative agreement with conventional Kubo-formula results.

The method was further extended to slab geometries by constructing spin-resolved hybrid Wannier functions localized along the surface normal. This allowed the spin Hall conductivity to be decomposed into layer contributions. Applications to $MnBi_2Te_4$ and Bi_2Se_3 thin films showed surface-localized contributions associated with topological surface states and surface spin responses. This extension uses the same uniaxial-Wannier framework as layer anomalous Hall conductivity [1]. Dense Brillouin-zone sampling on the ISSP systems was essential for checking convergence of surface and bulk contributions in topological thin films.

2. *Real-space topological indices in skyrmion systems*[2]

We investigated how topological transport responses can be visualized in real space for finite magnetic textures. As a first step toward first-principles real-space Chern-marker calculations, we studied a tight-binding model of finite skyrmion lattices under open boundary conditions. The local Chern marker $C(\mathbf{r})$ was evaluated from the projector onto occupied states and was used to map the spatial distribution of the Chern-number contribution. The resulting maps showed a clear correlation between the skyrmion spin texture and the local topological response, while edge regions carried compensating contributions as expected for finite samples.

We also calculated the Bott index as a real-space topological invariant. By varying the number of occupied states and the skyrmion supercell size, we confirmed that the Bott index converges to the Chern number obtained

under periodic boundary conditions in the large-system limit. This benchmark clarifies the numerical requirements for applying real-space topological markers to more realistic systems, including skyrmion crystals, magnetic thin films, and disordered or inhomogeneous topological materials.

3. *Thermoelectric transport in atomically thin materials*[3]
We applied first-principles Green's-function transport calculations to few-layer SnSe in order to clarify the thickness dependence of its thermoelectric performance. The transport coefficients were evaluated within the Landauer formalism using density-functional Hamiltonians. The monolayer showed the largest thermoelectric figure of merit along the zigzag direction, with calculated values reaching $ZT = 4.08$ for n-type doping and $ZT = 3.41$ for p-type doping at 723 K. The enhancement is attributed to the suppression of interlayer electronic coupling, an enlarged band gap, and reduced lattice thermal conductivity caused by phonon-boundary scattering.

These results demonstrate that atomic-scale thickness engineering is an effective strategy for controlling thermoelectric properties in layered materials and provide useful test cases for real-space decomposition of longitudinal conductivity based on closest Wannier functions.

4. *Spin conversion and polarization-driven functional materials*
Several applications were carried out to connect the method development with materials design. For Janus WSSe, first-principles calculations showed that the broken mirror symmetry produces an out-of-plane electric dipole moment. Born effective charge analysis clarified the microscopic origin of the dipole, and the internal electric field was found to induce Rashba-type spin splitting near the Γ point. This result shows that Janus transition-metal dichalcogenides can realize spin-split electronic states without an external electric field, making them promising spin-conversion materials[4].

We also investigated the capacitance profile of graphene electrodes using the effective-screening-medium method[5]. This calculation provided a reference model for separating electrode and dielectric contributions in nanoscale capacitors. Together with multilayer h-BN polarization and strain-induced shift-current responses in $CsPbI_3$[6], these applications show the usefulness of ISSP supercomputers for designing spin, charge, thermal, and optical energy-conversion materials.

References

[1] Y. Morishima, F. Ishii, and N. Yamaguchi, arXiv:2506.01160 (2025).

[2] J. Yang, N. Yamaguchi, and F. Ishii, submitted.

[3] Z. S. Fatomi, R. Syariati, N. Yamaguchi, and F. Ishii, submitted.

[4] S. A. Putri, M. A. U. Absor, N. Yamaguchi, and F. Ishii, Jpn. J. Appl. Phys. **64**, 10SP21 (2025).

[5] A. Sohib, N. Yamaguchi, and F. Ishii, Jpn. J. Appl. Phys. **64**, 11SP11 (2025).

[6] Y. Y. S. Teweng, N. Yamaguchi, and F. Ishii, Appl. Phys. Express **18**, 121001 (2025).

Analyses on correlation between material properties and atomic structures in complex structures via ab-initio-based methods

Satoshi WATANABE
Department of Materials Engineering, the University of Tokyo
7-3-1 Hongo, Bunkyo-ku, Tokyo, 113-8656

Understanding the relationship between atomic structure and physical properties in complex materials systems–such as surfaces, interfaces, defects, and amorphous phases–has become increasingly important for the development of next-generation information devices and energy-related technologies. In particular, phenomena involving dynamics, including ion transport, phonons, and thermal conduction, are often governed by structural features that extend beyond nearest-neighbor atomic configurations. Elucidating such structure–property correlations, especially those involving medium-range order in structurally disordered systems, remains a major scientific challenge. At the same time, these problems are computationally demanding and constitute important targets for large-scale simulations utilizing modern supercomputing resources.

To address these challenges, our research aims to achieve a microscopic and quantitative understanding of such phenomena through first-principles calculations based on density functional theory (DFT), as well as large-scale atomistic simulations employing machine-learning interatomic potentials (MLIPs) constructed from first-principles datasets. In fiscal year 2025, building upon our previous efforts, we have carried out computational and methodological studies on a variety of systems, including defects in layered materials, metal–solid electrolyte interfaces, ceramics, metallic and oxide glasses, and alloy nanoparticle catalysts. In the following, we highlight our recent results on grain boundaries in ceramic materials as a representative example.

Grain boundaries (GBs) in ceramics play a crucial role in ionic transport and are central to processes such as sintering, flash sintering, and electrochemical functionality. However, the microscopic mechanisms governing ion behavior at GBs, particularly under applied electric fields, remain insufficiently understood. To address this issue, we performed DFT and density functional perturbation theory (DFPT) calculations for the $\Sigma5(310)/[001]$ grain boundary in cubic ZrO_2 [1].

The calculations were carried out using VASP, employing a GGA with the PBE functional and the grain boundary supercell containing 120 atoms. The DFPT calculations were conducted to evaluate Born effective charges (BECs), which quantify the response of atomic forces to external electric fields.

The calculated electronic structure reveals the emergence of acceptor-like states just above the valence band maximum localized near the grain boundary region, indicating a distinct electronic environment compared to the bulk. Furthermore, we found significant deviations in the BECs of both Zr and O ions near the GB as seen in Fig. 1. Especially, some of the off-diagonal components of BECs took finite values.

These anomalous BEC characteristics imply that, under applied electric fields, ions near

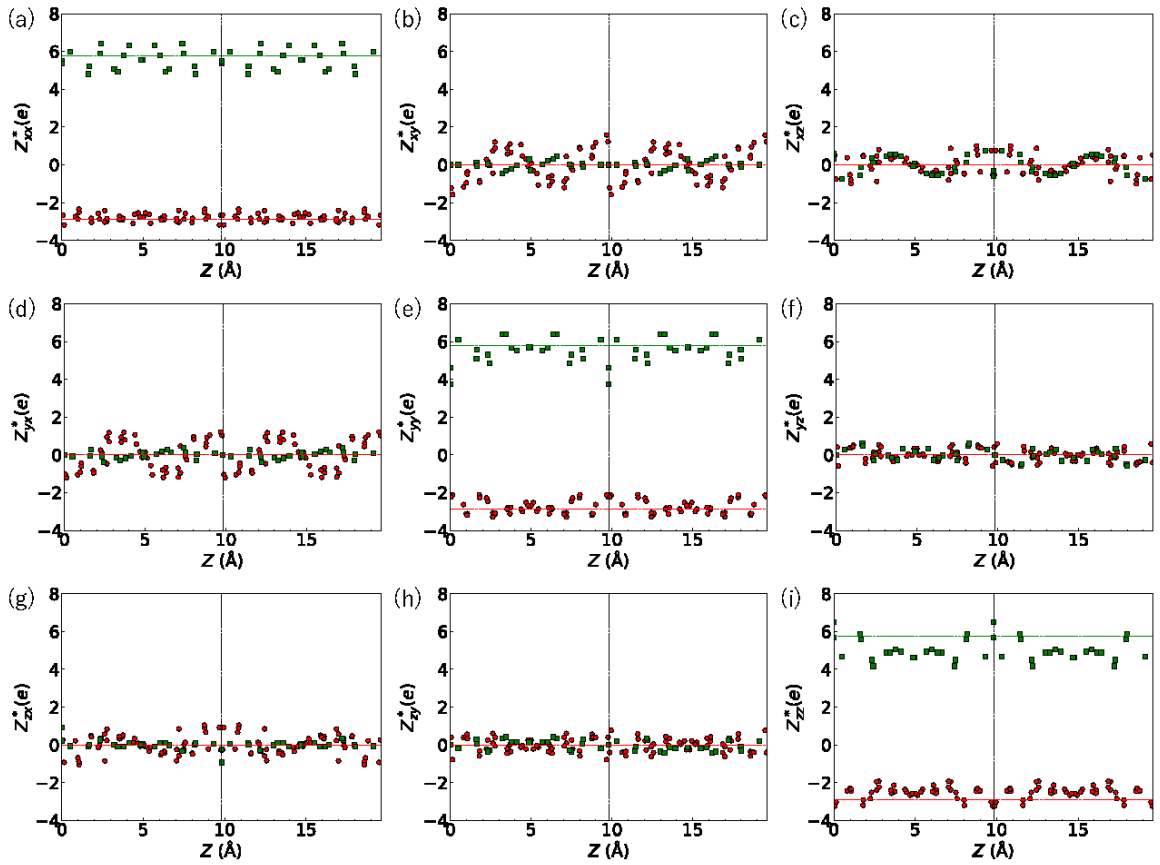

Figure 1: Calculated BECs Z^* for each ion. Each tensor component is depicted along the Z-direction (perpendicular to the GB plain). Green and red circles denote values of Zr and O, respectively. The vertical dotted lines indicate the boundary between two grains, while the horizontal dotted lines represent the Z^* values of bulk cubic-ZrO_2. Reprinted from Ref. [1].

the grain boundary experience enhanced and anisotropic forces, including components perpendicular to the field direction. Such effects are expected to play a crucial role in enhancing ionic mobility and may provide a microscopic basis for phenomena such as flash sintering, where rapid densification occurs under strong electric fields at relatively low temperatures. Importantly, these findings highlight that polarization effects and environment-dependent charge responses must be explicitly considered in modeling ion transport in structurally complex systems.

References

[1] S. Arai, K. Shimizu, A. K. A. Lu, H. Masuda, H. Yoshida, and S. Watanabe: e-J. Surf. Sci. Nanotechnol. **23** (2025) 323.

Analysis of atomic and ionic behavior in complex structures using first-principles calculations and machine learning

Koji SHIMIZU

Materials DX Research Center, National Institute of Advanced Industrial Science and Technology, Umezono, Tsukuba, Ibaraki 305-8568

Understanding physical properties emerging from complex atomic environments, such as amorphous phases, defects, and interfaces, is increasingly important for advanced electronic and ionic devices. Although recent advances in computational techniques have enabled the study of more complex structural models, first-principles calculations based on density functional theory (DFT) remain restricted in system size and time scale due to their high computational cost.

Machine-learning interatomic potentials (MLPs) trained on first-principles datasets offer an effective solution by achieving near-DFT accuracy with substantially reduced computational cost, enabling large-scale and long-time simulations beyond the limits of conventional first-principles approaches.

The author has studied lithium-ion conduction mechanisms in solid electrolytes using MLP-based simulations, focusing on property changes induced by additive incorporation. Applications to metal/solid-electrolyte interfacial systems were also explored using an equivariant neural network potential based on graph representations, trained on extensive DFT datasets and applied to molecular dynamics simulations.

High-entropy alloys (HEAs), solid-solution materials composed of five or more elements, were examined with a focus on catalytic applications. CO adsorption, a key elementary step in the CO_2 conversion, was investigated on CoCuFeMnNi HEA surfaces. A machine-learning approach based on local surface descriptors enabled accurate prediction of adsorption energies and revealed the influence of local surface structures on adsorption strength and the electronic states of surface atoms [1].

Furthermore, reaction-energy analyses provided theoretical support for experimentally identified synthesis pathways of solid electrolytes [2]. Additional studies included analyses of Born effective charges at zirconia grain boundaries [3].

References

[1] E.R. Beronio et al., Surf. Interfaces 82, 108457 (2026).

[2] K. Onoue et al., submitted.

[3] S. Arai et al., e-J. Surf. Sci. Nanotechnol. 23, 323 (2025).

Development of First-Principles Self-Interaction-Corrected GWΓ Method

Yoshifumi NOGUCHI

Department of Applied Chemistry and Biochemical Engineering, Graduate School of Engineering, Shizuoka University, Johoku 3-5-1, Hamamatsu, Shizuoka 432-8561, Japan

We have developed a first-principles self-interaction-corrected GWΓ method and implemented it into our original all-electron mixed basis program. To completely remove self-interaction contributions from the GWΓ one-electron self-energy operator, we have also developed a self-screening-corrected GW (SSC-GW) method [1]. Figure 1 shows the Γ terms for (a) self-interaction-included and (b) self-interaction-corrected cases. It should be noted that the $\nu = \mu$ matrix elements in the Γ terms correspond to the self-interaction contributions. We applied our methods to simulate the first ionization potentials of 97 atoms and molecules.

For all systems, the self-interaction contributions in the GW one-electron self-energy operator range within ± 0.5 eV. Consequently, there is no significant difference in computational accuracy between the conventional GW and SSC-GW methods, with both yielding a mean absolute error (MAE) of approximately 0.4 eV. In contrast to the GW methods, significant self-interaction contributions were observed in the GWΓ method. The MAE of the self-interaction-included GWΓ method is approximately twice as large as that of the GW method. However, by applying self-interaction corrections to the Γ term, this error is reduced by approximately half [2]. Indeed, the self-interaction contributions in the GWΓ one-electron self-energy operator correlate clearly with the errors found in uncorrected method; that is, systems with more pronounced self-interaction contributions exhibit larger errors. These results demonstrate that the self-interaction corrections are essential for the GWΓ method.

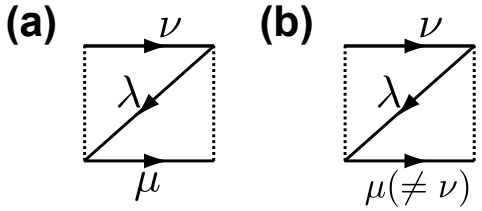

Fig. 1 Feynman diagrams of (a) self-interaction-included and (b) self-interaction-corrected Γ terms.

References

[1] F. Aryasetiawan, R. Sakuma, and K. Karlsson, Phys. Rev. B, **85**, 035106 (2012).

[2] T. Isago, Y. Noguchi, and K. Ohno, Phys. Rev. B, **111**, 195146 (2025).

Study of unconventional multi-orbital and multi-layer superconductors in first-principles

Hirofumi Sakakibara

Faculty of Engineering, Tottori University, Tottori, Tottori 680-8552

Cuprate superconductor is one of the hottest scientific topic throughout this decade. One of the standard models of cuprates is single orbital square lattice Hubbard model, which incorporates only one degrees of orbital/site freedom. Lately this single orbital physics, some theorists proposed bilayer Hubbard model in which the interlayer coupling is crusial to superconductivity. Cooper pair is formed in such models between faced layers and relatively high Tc compared to single orbital square lattice model is realized. However, no material in which such "ideal" bilayer model manifest was discovered until 2023.

The recent discovery of the Ruddlesden-popper type bilayer nickelate superconductor $La_3Ni_2O_7$ in 2023 [1] have stimulated a ton of works, where one reason is it have high T_c as cuprates. Only pressurized sample exhibits superconductivity in bulk system, on the contrary, thin-film samples with compressive strain from substrates exhibits superconductivity even in ambient pressure [2]. In our previous report [3], the essence of high- T_c superconductivity is the bilayer Hubbard model originated from the Ni-$d_{3z^2-r^2}$ orbitals coupled between layers. In this project, we have investigated the possibility of new superconductors in which bilayer Hubbard model manifests.

First, here we report our investigation of thin-film sample in Ref. [4]. In bulk samples, it is believed, although another possible symmetries are under debate, that the space group changes from *Amam* (*Cmcm*) to *I*4/*mmm* and this transition can be a trigger to the superconducting transition. In Ref. [4], we have shown that $La_3Ni_2O_7$ on the substrate of $SrLaAlO_4$(SLAO), is close to the critical point between Amam and I4/mmm. This may be consistent with experimental report that I4/mmm phase probably realizes even in ambient pressure [5]. Another remarkable point is that the γ Fermi surface, which is regarded to be important for pairing especially along the traditional low energy theories, is about to be vanished. By adopting fluctuation-exchange approximation (FLEX), we have found that the (nearly) vanished γ Fermi surface is still effective, especially for finite energy spin-fluctuation and superconductivity mediated by it. This implies that the robustness of superconductivity.

Second, we report our advanced studies of

effective bilayer models. As described in Refs. [6,7], two-band Hubbard model is identical to the bilayer Hubbard model in a special condition that $U=U'=J=J'$, where these denote intra-orbital repulsion, inter-orbital repulsion, Hund's coupling, and pair hopping parameters, respectively. Even there may be some quantitative ambiguity, Kitamine *et al*. have demonstrated that $s\pm$wave superconductivity similar to that of bilayer Hubbard model can be realized through some numerical calculations [6]. Recently we have named this effective model as an orbital space bilayer model (OSBM). As described in Ref. [6], band insulator can be a parent compound of OSBM, this aspect is very contrasting to cuprates superconductors, a doped Mott insulator. In Ref. [8], we have investigated an infinite layer nickelate as a candidate of OSBM. We have performed first-principles calculation to obtain parameters of an effective Hubbard model not only the hopping integrals but also interaction parameter using RESPACK code [9] in which constrained random phase approximation method is implemented. By adopting FLEX approximation to the derived model, we have found that $s\pm$wave can be realized in heavily hole doped region [8].

This design concept can be adopted to several candidates. In Ref. [9], we have investigated T'- and T- structure of $La_3Ni_2O_6$, in which oxygen bonding the faced Ni-O layer does not exist unlike $La_3Ni_2O_7$. Based on an analysis using FLEX and rigid band approximation, we have found that $s\pm$wave can be realized in hole fewer doped region compared to that of infinite layer nickelate. This material design is very promising strategy because stochiometric $La_3Ni_2O_6$ has already synthesized, although it is an insulator. We will show the further studies, where the calculations are partially done but paper is now under preparation, related to OSBM in the next forum of activity report.

References

[1] H. Sun *et al*., Nature (London) **621**, 493 (2023).

[2] E. K. Ko *et al*., Nature (London) **638**, 935 (2025).

[3] H. Sakakibara, N. Kitamine, M. Ohi, and K. Kuroki, Phys. Rev. Lett. **132**, 106002 (2024).

[4] K. Ushio *et al*., arXiv: 2506.20497.

[5] C. Yue *et al*., Natl. Sci. Rev. **12**, nwaf253 (2025).

[6] N. Kitamine *et al*.., Phys. Rev. Res. 2, 042032 (2020).

[7] H. Shinaoka *et al*., Phys. Rev. B 92, 1951256 (2015).

[8] H. Sakakibara *et al*., Phys. Rev. B **111**, 224511 (2025)

[9] K. Nakamura *et al*., Comput. Phys. Commun 261, 107781 (2021).

[10] S. Kamiyama, H. Sakakibara *et al*., arXiv: 2603.11771 (2026).

Analyses on electronic structure and magnetic anisotropy in high-performance spintronics magnetic materials and development/application in quasi-particle self-consistent GW code

Tatsuki ODA, Takumi KATSUTA, Haruya NIWA, Hikaru YAMAGUCHI, Itsuki NAKANISHI, Puke Lajaladita Litle MECCI, Masao OBATA,

Graduate School of Natural Science and Technology, Kanazawa University, Kakuma, Kanazawa, Ishikawa 920-1192

We have studied several systems in high-performance spintronics and magnetic materials on electronic structure and magnetic anisotropy. In these investigations, we have checked physical accuracy in the materials of spintronics application. We have also studied electronic structures in some systems using a quasi-particle self-consistent GW code. Here, we report (A) developments of a refined version of grand canonical force theorem approach (reGCFT) on the estimation of magnetic anisotropy energy (MAE) and (B) applications of the computational code for the quasi-particle self-consistent GW method (QSGW).

(A) The method of reGCFT

This method, based on the total energy associated with density functional theory including the magnetic dipole contribution, improves the numerical accuracy of MAEs. The original approaches of conventional GCFT or simple FT frequently fail to reproduce the resulting value obtained from the method of total energy difference (TET), in which the heavy element is included, such as Pt element, expecting a large spin-orbit coupling (SOC). We have demonstrated the properties mentioned above in the interface PtCoO/ZnO and some systems [1]. Its demonstration indicated the agreement between reGCFT and TET within only a few percents.

(B) The method of QSGW

The computational code of QSGW has been optimized to obtain efficient computation. The computational demonstrations, such as magnetic shape memory alloy Ni_2MnGa [2], some transition mental oxides, etc., were performed. QSGW provides narrowing of band manifolds to the electronic structure of *d*-orbitals, indicating the property of electron correlation .

References

[1] T. Katsuta, M. Obata, et al., submitted.

[2] J. Luštinec, M. Obata, et al., J. Phys.: Condens. Matter **38**, 015502 (2026).

Development/application in quasi-particle self-consistent GW and analyses on magnetic anisotropy in spintronics magnetic materials

Tatsuki ODA, Haruya NIWA, Hikaru YAMAGUCHI, Takumi KATSUTA, Itsuki NAKANISHI, Puke Lajaladita Litle MECCI, Masao OBATA,

Graduate School of Natural Science and Technology, Kanazawa University, Kakuma, Kanazawa, Ishikawa 920-1192

We have studied first-principles electronic structures in several materials using a quasi-particle self-consistent GW code (QSGW). QSGW provides narrowing of band manifolds to the electronic structure of *d*-orbitals and reasonable crystal field splitting on the transition metal atoms induced by the anion atoms. The former indicates the property of large electron correlation, compared with the results obtained with the conventional first-principles approach based on the density functional theory (DFT).

Here, we briefly report achievements on the transparent transition metal oxides $LiTi_2O_4$ [1], which has a normal spinel-type crystal structure. This structure belongs to a cubic space-group symmetry as same as diamond and, but has 14 atoms in the unit cell, requiring a large amount of computational resources. The current supercomputer in ISSP fortunately allows us to investigate electronic structures within GW approximation, and optical properties through the microscopically calculated dielectric function with independent particle approximation. This approach demonstrates the transparent property in the visible range to the light. Such transparency cannot be explained in the electronic structure obtained with the DFT approach. This is because the DFT does not provide narrow band manifolds to Ti 3d t_{2g}- and e_g-bands and the small separation between the oxygen band manifolds and t_{2g}-band manifolds. In QSGW, the self-energies of single particle are evaluated, and thus one-particle electronic spectra also evaluated. In this work, the cumulant approach (CA) was applied to investigate their improved spectra (QSGW+CA), so that the plasmon satellites are included in the resulting spectra. These spectra were compared with those observed in experimental photoemission measurement. In QSGW, renormalization factors can be calculated at each state in the Brillouin zone. In the current calculation, these are around 0.5 at the Fermi level.

References

[1] H. Niwa, M. Obata, et al., Phys. Rev. B **113**, 155114 (2026).

Reduction of Rare Metals in Fuel Cell and Formic Acid Decomposition Catalysts

Norihito Sakaguchi

Center for Advanced Research of Energy and Materials, Faculty of Engineering, Hokkaido University, Sapporo, Hokkaido 060-8628

We investigated the effects of light irradiation on the stability of single Pt atoms on light-element-doped graphene using first-principles calculations based on density functional theory (DFT) and time-dependent DFT (TDDFT).[1] Furthermore, we evaluated the catalytic selectivity of single Pt and Cu atoms supported on light-element-doped graphene for formic acid decomposition reactions. Additionally, we examined the adsorption and magnetic states of an O_2 monolayer on Ag(111) surfaces.[2]

Regarding the effects of light irradiation, we focused on the diffusion barriers of single Pt atoms on light-element-doped graphene. Total energy and electronic structure calculations were performed using the Vienna Ab initio Simulation Package (VASP) and the Scalable Ab-initio Light-Matter simulator for Optics and Nanoscience (SALMON). The VASP code was parallelized using the Intel® MPI and Math Kernel Libraries. The influence of electron temperature on the diffusion barriers was approximated via Fermi-Dirac smearing. The results demonstrated that while the diffusion barrier decreased with increasing electron temperature, the change remained within a few percent, indicating that the overall impact was not significant.

In the analysis of catalytic selectivity for formic acid decomposition, we compared single Pt and Cu atoms on light-element-doped graphene. It was found that single Cu atoms, when supported on suitable supports, exhibit higher catalytic activity and selectivity than single Pt atoms.

Finally, we also investigated the adsorption of an O_2 monolayer on Ag(111) surfaces.[2] The calculated adsorption structures and magnetic states revealed that the lattice distortion observed via atomic force microscopy (AFM) is attributable to a reduction in the O_2 magnetic moment. This finding suggests that measuring lattice distortion can serve as a means of determining local magnetic structures.

References

[1] Y. Kunisada, K. Sato, N. Sakaguchi, Vacuum and Surface Science 69 (2026) 135.

[2] M. Kimura, Y. Kunisada, Y. Sugimoto, ACS Nano 20 (2026) 263.

Hydrogen Ion Doping and Property Modulation Focused on Acid–Base Sites in Solids

Soshi IIMURA

National Institute for Materials Science (NIMS), Tsukuba, Ibaraki 305-0044

Hydrogen in materials plays a crucial role as an active site that determines functionality in energy and environmental materials such as amorphous silicon, zeolites, and next-generation fuel cell electrolytes. In these materials, hydrogen typically loses an electron and is incorporated as a proton. On the other hand, hydrogen is also known to accept an electron from the host material and form a hydride anion [1,2]. In molecular systems, hydrides exhibit strong hydrogenation and reduction ability toward positively polarized carbon atoms, such as those in carbonyl groups.

Recently, we have found that oxides capable of incorporating protons and intermetallic compounds capable of incorporating both protons and hydrides can act as active sites in photocatalysts and electrocatalysts, enabling the activation of carbon dioxide. In this study, we investigated the electronic states of hydrogen and the conditions under which hydrogen can be incorporated into materials, using first-principles calculation software such as VASP and pydefect, which is used to calculate defect formation energies in semiconductors.

First, structural models of materials were obtained from the Materials Project database. Next, interstitial sites capable of accommodating hydrogen were systematically searched, and hydrogen atoms were introduced into these sites. By evaluating the total energy differences before and after hydrogen incorporation, we successfully identified a large number of intermetallic compounds capable of incorporating hydrogen.

Subsequently, we analyzed the electronic structures prior to hydrogen incorporation, as well as the charge densities and wave functions at hydrogen incorporation sites. The results revealed that empty s and p orbitals of transition metals—whose d orbitals are fully occupied due to electron donation from electropositive metals—act as Lewis acid sites, thereby stabilizing hydrogen within the material. In future work, we will establish computational methods to quantify the acidity and basicity of metals and apply them to the discovery of new catalysts.

References

[1] S. Iimura et al., Nat. Commun., **3**, 943-1-6, (2012).

[7] K. Fukui, S. Iimura et al., J. Am. Chem. Soc., **144**, 1523-1527, (2022).

First-principles study on the control of valley transport properties in two-dimensional honeycomb structured materials

Yoshiyuki EGAMI
Division of Applied Physics, Faculty of Engineering, Hokkaido University
Kita 13, Nishi 8, Kita-ku, Sapporo, Hokkaido 060-8628

Recently, the valley degree of freedom has attracted considerable attention as a unique electronic property of graphene, promoting intensive research on valleytronics. One of the major challenges in realizing valleytronic devices is the establishment of a valley filter function that enables the selective generation and detection of electrons from a specific valley. Recent studies have revealed a strong correlation between the geometric symmetry of defect structures with respect to the electron-transport axis and valley-dependent transport properties. For instance, in graphene systems incorporating Stone–Wales defects or blister defects, it has been reported that mirror symmetry of defect with respect to the transport axis facilitates both the generation of valley polarization and the suppression of its relaxation. Beyond graphene, other 2D materials known as Xenes also possess similar valley degrees of freedom, suggesting that analogous transport properties may emerge in these systems.

In this study, we focused on arsenene, a 2D material composed of arsenic atoms. Although pristine arsenene typically exhibits a buckled honeycomb structure with a band gap, the adsorption of atoms such as hydrogen or fluorine induces a transition to a planar honeycomb structure. This transition results in a band structure with linear dispersion near the Fermi level, similar to graphene. However, unlike graphene, where electronic states are dominated by π orbitals, the bands in this system are derived from σ orbitals. To clarify how this difference in orbital character influences valley-dependent transport properties, we theoretically evaluated fluorinated arsenene using first-principles electron-transport calculations[1, 2].

Our results for arsenene systems incorporating 5-8-5 type defects confirm that electron transport occurs without hybridization between the two valley states. Furthermore, a valley filtering function was observed, in which electrons from a specific valley exhibit nearly unity transmission. We also evaluated the hybridization of valley states caused by the structural symmetry breaking, which acts as "noise" in valley information. While this noise increases exponentially with atomic displacements from the ideal symmetric structure, we found that the hybridization remains sufficiently suppressed under lattice vibrations at room temperature.

This work has been performed on System B of the Supercomputer Center, the Institute for Solid State Physics, the University of Tokyo.

References

[1] K. Hirose *et al.*: First-principles calculations in real-space formalism (Imperial College Press, 2005).

[2] Y. Egami, S. Tsukamoto and T. Ono: Phys. Rev. Res. **3**, 013038 (2021).

First-principles calculations of electronic structures in molecular spintronic devices

Hideo KAIJU, Mizuki MATSUZAKA, Chika HASHIMOTO, and Koki TERAI

Faculty of Science and Technology, Keio University

Yokohama, Kanagawa 223-8522, Japan

Molecular spintronics has been attracted attention because of the unique possibilities. Molecular spintronic devices exhibit magnetoresistance (MR) effect, in which the resistance changes with magnetic field [1, 2]. A large MR effect was observed in molecular spintronic devices at low temperature because of the high spin polarization, which is attributed to the effective orbital hybridization between molecules and magnetic materials. Recently, we have observed MR effect in $Ni_{78}Fe_{22}$/tris-(8-hydroxyquinoline) erbium (Erq_3)/FeCo organic spin valves [3]. In this study, we calculate the density of states (DOS) at each atom in FeCo/Erq_3/FeCo and Ni_3Fe/Erq_3/Ni_3Fe systems, and estimate the spin polarization of the magnetic atoms.

We used Quantum ESPRESSO for first-principles calculations. The calculations were performed using density functional theory, plane wave approximation, and pseudopotential model. We prepared the supercells of FeCo/Erq_3/FeCo and Ni_3Fe/Erq_3/Ni_3Fe, as shown in Fig. 1. The size of the supercells is 14.305 × 14.305 × 25.489 Å^3 in Fig. 1(a) and 14.156 × 14.156 × 28.201 Å^3 in Fig. 1(b), respectively. The energy

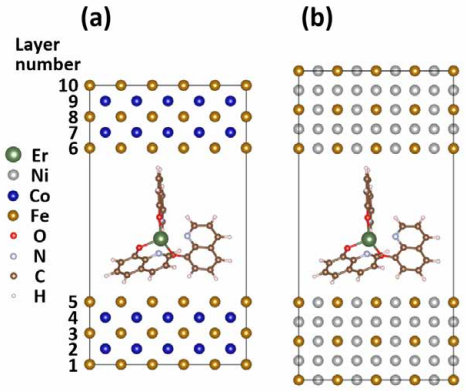

Figure 1: Supercells of (a) FeCo/Erq_3/FeCo and (b) Ni_3Fe/Erq_3/Ni_3Fe.

cutoff for the plane wave basis were 60 Ry for wave function and 480 Ry for charge density and the convergence criterion for energy estimation was set to 1×10^{-6} Ry in all calculations. The *k*-point mesh was set to 3 × 3 × 1 for the self-consistent field calculations and 5 × 5 × 1 for calculating the DOS.

Figure 2 shows the calculated DOS of Fe atom at the 1st and 5th layers in the FeCo/Erq_3/FeCo, and Ni atom at the 1st and 5th layers and Fe atom at the 1st and 5th layers in Ni_3Fe/Erq_3/Ni_3Fe. The Fermi level is at 0 eV in each DOS. The DOS of Fe and Ni atoms at the 5th layer is different from that at the 1st layer. We have confirmed that the DOS of Fe and Ni

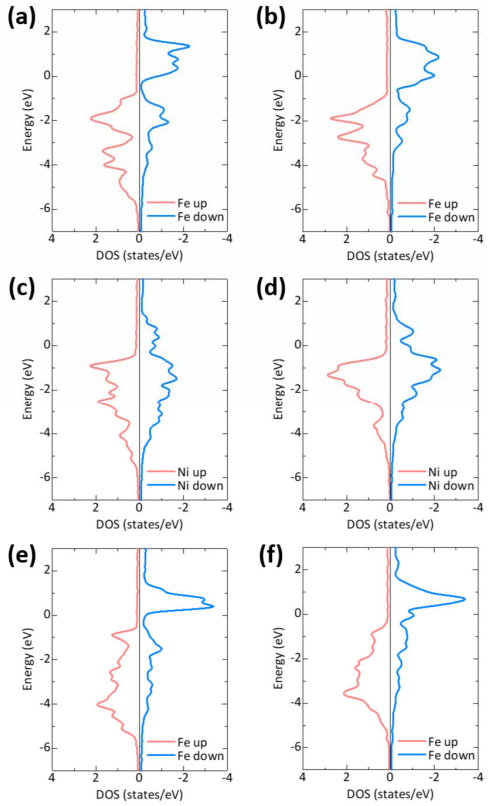

Figure 2: Calculated DOS of Fe atom at (a) 1st and (b) 5th layers in FeCo/Erq$_3$/FeCo, and Ni atom at (c) 1st and (d) 5th layers and Fe atom at (e) 1st and (f) 5th layers in Ni$_3$Fe/Erq$_3$/Ni$_3$Fe.

atoms in bulk FeCo and Ni$_3$Fe is almost the same as that at the 1st layers in the FeCo/Erq$_3$/FeCo and Ni$_3$Fe/Erq$_3$/Ni$_3$Fe. This result suggests that our calculations are reasonably reliable. Then, the DOS at the Fermi energy for each atom was summed up at each layer. Figure 3 shows the spin polarization at each layer number in the FeCo/Erq$_3$/FeCo and Ni$_3$Fe/Erq$_3$/Ni$_3$Fe supercells. The spin polarization of Fe atom at the interface of FeCo/Erq$_3$ is higher than that in

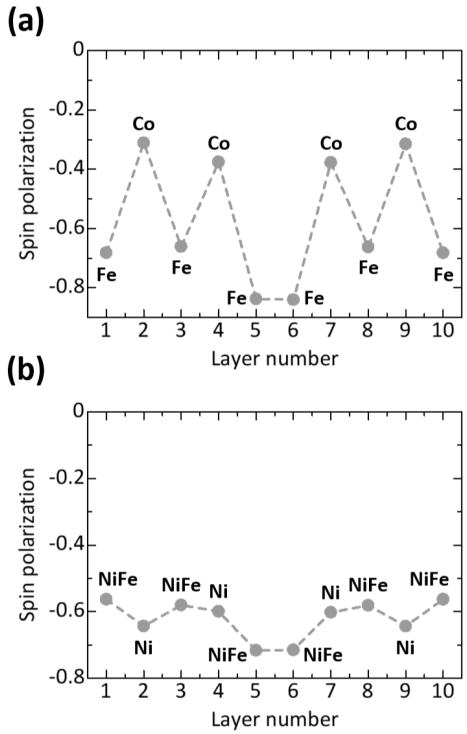

Figure 3: Spin polarization at each layer number in (a) FeCo/Erq$_3$/FeCo and (b) Ni$_3$Fe/Erq$_3$/Ni$_3$Fe supercells.

Fe and Co atoms in the inner site of FeCo. The same tendency is also found in Ni$_3$Fe/Erq$_3$/Ni$_3$Fe. Additionally, the spin polarization of the Fe atom at the FeCo/Erq$_3$ interface is slightly higher than that of Ni and Fe atoms at the Ni$_3$Fe/Erq$_3$. The findings of this study may contribute to the development of molecular spintronics.

References

[1] Z. H. Xiong et al., *Nature* **427**, 821 (2004).

[2] C. Barraud et al., *Nat. Phys.* **6**, 615 (2010).

[3] M. Matsuzaka et al., *J. Magn. Magn. Mater.* **630**, 173465 (2025).

Simulation of Metal Nitriding by Ammonia Flame

Peijie FENG, Minhyeok LEE, and Yuji SUZUKI
Department of Mechanical Engineering, School of Engineering,
The University of Tokyo, 7-3-1 Hongo, Bunkyo-ku, Tokyo 113-8656

As the energy sector transitions from fossil fuel to green ammonia, the "unwanted" nitriding of iron-based materials in ammonia-fueled combustion systems [1] has become a major concern. Our previous work [1,2] revealed a mutual interaction between ammonia and iron-based materials: ammonia molecules are thermally decomposed on an iron-based material, and the nitrogen atoms diffuse into the material forming iron nitrides. To understand the dynamics of ammonia decomposition when the iron-based material is nitrided, we incorporated density functional theory (DFT) calculations using VASP. The primary objective is to elucidate the reaction mechanisms governing "unwanted nitriding" in high-temperature environments and to derive reliable kinetic data for the iron nitrides (γ'-Fe_4N and ε'-Fe_2N).

To investigate the reaction energetics and microkinetics on iron nitrides, two representative phases are selected: γ'-Fe_4N and ε'-Fe_3N. These phases correspond to experimentally observed layers in the bilayer structures formed during typical gas nitriding processes [3].

First, we used the method proposed by Tian et al [4] and Yalcin et al. [5] to identify the stable surface. The stable surface corresponds to the energetically most favorable configuration; hence, when polycrystalline metals form, surfaces with low surface energy tend to be exposed, contributing to the macroscopic surface morphology. Therefore, macroscopic surface reactions are most likely to occur on facets with low surface energy. The results shows that the γ'-Fe_4N (001) and ε'-Fe_3N (101) termination exhibit low surface energies, indicating that these facets are likely to dominate the macroscopic surface

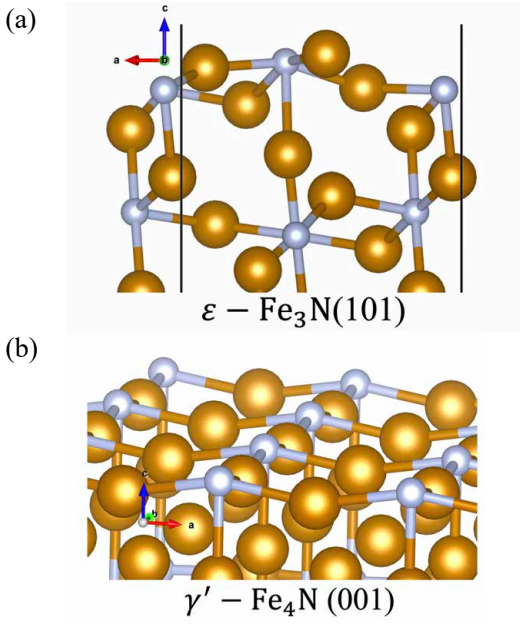

Fig 1: (a) ε'-Fe_3N (101) termination, (b) γ'-Fe_4N (001) termination.

morphology, the atomic model is shown in Fig. 1.

Then it is necessary to identify the adsorption sites for reactional species, e.g. NH_3, NH_2, NH, N, and H. Therefore, a Python code using Delaunay triangulation is developed to exhaustively identify the symmetry-reduced set of possible adsorption sites. The results are shown in Fig. 2.

Finally, we investigated the barrier of the key N–N recombination step to quantify how strongly the surface binds nitrogen atoms derived from ammonia decomposition. This step is the rate-limiting reaction on pure iron surfaces [5].

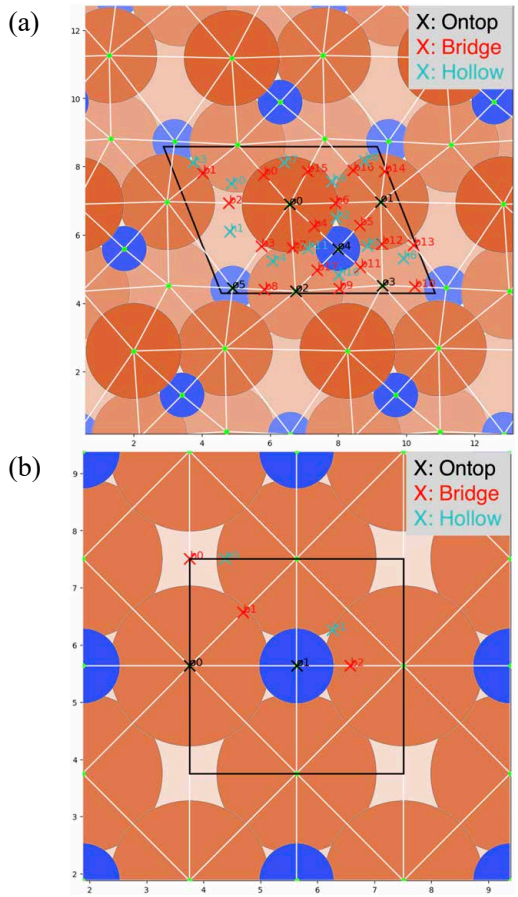

Fig. 2: Possible adsorption sites identified on (a) ε'-Fe_3N (101), and (b) γ'-Fe_4N (001).

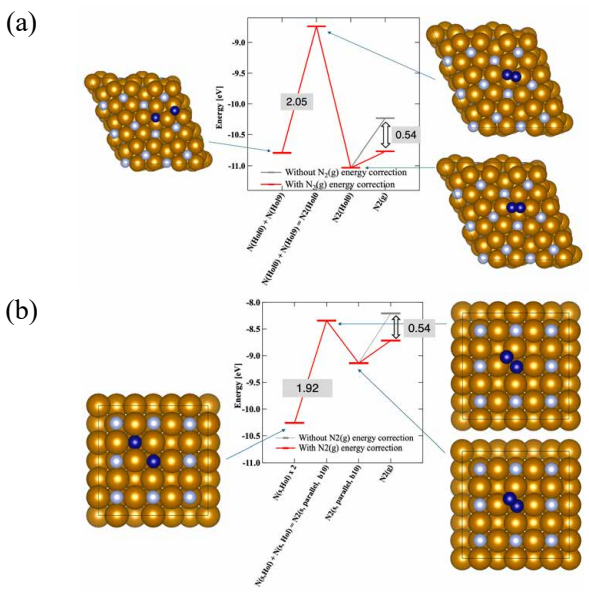

Fig. 3: DFT computed reactional energetics of N-N recombination reaction on (a)ε'-Fe_3N (101), and (b) γ'-Fe_4N (001).

We used the dimer method to locate the transition states. As shown in Fig. 3, iron nitride has a lower barrier than pure iron (2.38 eV [5]) for the same step, indicating higher reactivity, consistent with our experimental observation [2]. In total, approximately 1,000 node-days of CPU computation is used on ISSP System B.

References

[1] Wang, D., Lee, M., and Suzuki, Y., Proc. Combust. Inst., 40, 105562 (2024).

[2] Feng, P., Lee, M., Wang, D., and Suzuki, Y., Int. J. Hydrog. Energy 48, 75 (2023).

[3] Middendorf, C., and Mader, W., Int. J. Mater. Res. 94, 3 (2003).

[4] Tian, X., et al., Appl. Surf. Sci. 427,357 (2018).

[5] Yalcin, F. and Wolloch, M., Comput. Mater. Sci. 234 (2024)

[6] Weiss, M. et al., Appl. Surf. Sci. 2, 4 (1979).

Development of Ceramic Protective Coating to Suppress Corrosion and Hydrogen Embrittlement of Metallic Materials

Yuji Kunisada

Center for Advanced Research of Energy and Materials, Faculty of Engineering, Hokkaido University, Sapporo, Hokkaido 060-8628

To develop efficient hydrogen-permeation barriers, we investigated the formation energies of hydrogen impurities at the interface between ceramic and metallic materials using first-principles calculations based on density functional theory (DFT). We also investigated the behaviors of hydrogen impurities at the grain boundaries of FeCrAl alloys.

In addition to our previous investigations into the behavior of hydrogen impurities at interfaces between different ceramics,[1] we also investigated the behaviors of hydrogen impurities at the interface between ceramic and metallic materials using the Vienna Ab initio Simulation Package (VASP). We installed a parallelized version of VASP using the Intel® MPI Library and the Intel® Math Kernel Library. We considered α-Al_2O_3/Fe interfaces. Previously, it was clarified that the stability of hydrogen impurities varies significantly across impurity sites due to the incoherent nature of the α-Al_2O_3/Fe interface. Therefore, in the current fiscal year, we have performed systematic analyses by calculating the formation energies of hydrogen impurities at all interfacial sites within the supercell. As a result, the interfacial sites were found to be classified into four categories. Furthermore, the results revealed that the stability of hydrogen impurities strongly depends on the size of the interstitial voids at the interfacial sites. It was also clarified that an increase in the concentration of hydrogen impurities significantly promotes the delamination of the α-Al_2O_3 film.

We also investigated the formation energies of hydrogen impurities at the grain boundaries of FeCrAl alloys. The results indicated that hydrogen impurities are more stable at the grain boundaries than in the bulk regions of the FeCrAl alloy. Furthermore, it was found that the presence of alloying elements, such as Al and Cr, reduces the stability of hydrogen impurities. This observed tendency is consistent with previously reported behavior on FeCrAl alloy surfaces.[2]

References

[1] Y. Kunisada, R. Sano, N. Sakaguchi, Int. J. Hydrog. Energy 97 (2025) 1327.

[2] X. Li, Y. Ma, W. Zhou, Z. Liu, Appl. Surf. Sci. 581 (2022) 152273.

Advancement and application of methods for predicting dielectric properties and structure exploration of materials

Shinji TSUNEYUKI

Department of Physics, The University of Tokyo

Hongo, Bunkyo-ku, Tokyo 113-0033

The dielectric properties of polymer materials in the sub-terahertz to terahertz range—which are critical for the development of electronic and communication devices in the 6G and beyond-5G eras—are difficult to understand because they are influenced by various physical phenomena, including anharmonic lattice vibrations, molecular rotation, intra- and inter-molecular polarization, and structural relaxation. Furthermore, due to strong anharmonic effects and slow relaxation, computational simulations are extremely challenging to date. We have been developing dielectric property calculation methods and data-assimilation-based crystal structure search methods for the development of these dielectric materials.

By FY2024, we proposed a versatile machine learning model for organic molecular dipoles and demonstrated that it can calculate the complex dielectric constants of alcohols in the terahertz and lower frequency ranges at relatively low cost. We also developed a method for crystal structure exploration using low-quality powder X-ray diffraction experimental data and succeeded in distinguishing and reproducing multiple crystal structures mixed in the diffraction data; furthermore, we have demonstrated that highly reliable structural models can be obtained using experimental data from amorphous materials. In fiscal year 2025, we further developed these methods.

Calculation of the THz dielectric properties

The dielectric constant of liquids and polymers is calculated from the autocorrelation function of the system's dipole moment. Therefore, to quantitatively predict the molecular dipole moment, we proposed a machine learning model that predicts the position of the Wannier centers of electrons for each chemical bond based on atomic configurations. This fiscal year, using this chemical-bond-based machine learning model for dipole moments, we performed first-principles calculations on the dielectric properties of liquid propylene glycol (PG) and liquid polypropylene glycol (PPG), demonstrating that the frequency and temperature dependencies of the dielectric properties can be accurately calculated even at

frequencies below the terahertz range. We also identified the rebranding peak at 600 cm^{-1} and the intermolecular mode at 100 cm^{-1}, which had been experimentally reported. A key finding was that the model trained using data from propylene glycol dimers can also be applied to PPG with longer chains not included in the training data [1]. This research demonstrates the potential to predict the dielectric properties of polymer materials with various chain lengths and compositions using models trained with inexpensive first-principles calculations of low-molecular-weight oligomers.

On the other hand, it was also found that attempting to calculate the dielectric constants of π-conjugated systems with a Kekulé structure using this method is difficult because the representation of the double bond is ambiguous, making it hard to improve the model's accuracy. Therefore, we developed a new type of machine learning model that accurately predicts the dipole moment of π-conjugated systems by distributing the dipole moment calculated from the Wannier center to each atom [2].

Structure Search Using Experimental Data

We performed a structure search for yttrium under ultra-high pressure using a data-assimilation structure search method.

It is known that yttrium exhibits a phase transition characterized by a change in the stacking order of atomic layers upon compression. However, details regarding the high-pressure phase remain unclear, and no widely accepted consensus has yet been reached regarding the distorted face-centered cubic (dfcc) structure that appears at 45 GPa. Therefore, in this study, we combined machine learning potentials with data assimilation crystal structure search methods to expand the search range to structures containing up to 128 atoms per unit cell and conducted a search for the dfcc structure. As a result, we discovered the *Ibam* and *R*-3 structures, which differ from the previously known *R*-3*m* and $I4_1/a$ structures. First-principles calculations revealed that, among these structures, the *R*-3*m* structure—which had previously been the most widely accepted—is the least stable, and that the enthalpy differences between the other structures are very small. Furthermore, Rietveld analysis showed that, among these, the $I4_1/a$ and *Ibam* structures agree well with experimental diffraction data [3].

References

[1] T. Amano, T. Yamazaki, N. Matsumura, Y. Yoshimoto and S. Tsuneyuki, Phys. Rev. B 111, 165148 (2025).

[2] Y. Zhao, T. Yamazaki, R. Hosoya, Y. Matsushita and S. Tsuneyuki, to be submitted.

[3] Y. Kubo, T. Ishikawa, Y. Tanaka, Y. Nakamoto, M. Sakata and S. Tsuneyuki, submitted.

Polaronic Nature of Impurity Doping in Two-Dimensional Transition-Metal Dichalcogenides from First-Principles Calculations

Soungmin Bae

Institute for Materials Research, Tohoku University, 2-1-1 Katahira, Aoba-ku, Sendai, 980-8577, Japan

Introduction

Two-dimensional transition-metal dichalcogenides (TMDs), such as MoS_2, WS_2, and $MoSe_2$, have attracted considerable attention as promising channel materials for next-generation electronic devices. Owing to their atomically thin layered structures and semiconducting electronic properties, TMDs offer a potential route toward device architectures beyond the scaling limit of conventional silicon-based technology. However, reliable control of carrier concentration and contact properties remains a major challenge for practical device applications. Impurity doping is therefore a key strategy for tuning the electronic properties of TMDs.

In conventional bulk semiconductors, dopants are often understood within the shallow donor/acceptor picture, where introduced carriers are spatially extended and contribute to band-like conduction. In contrast, our previous first-principles study on monolayer MoS_2 revealed that doped carriers can be strongly localized around impurity atoms, forming dopant-bound polaron states.[1] This finding indicates that impurity doping in two-dimensional TMDs cannot be fully described by the conventional shallow-dopant model.

In this project, we extend this perspective from monolayer MoS_2 to representative two-dimensional TMD materials, including MoS_2, WS_2, and $MoSe_2$. We focus on Re and Nb as representative n-type and p-type dopants, respectively, and investigate their electronic structures using PBE0 hybrid-functional calculations. By comparing the impurity-induced carrier distributions across different TMD hosts, we aim to clarify whether dopant-bound polaron formation is a general feature of impurity doping in two-dimensional TMD materials.

Computational Methods

First-principles calculations were performed within the framework of density functional theory using the projector-augmented-wave method as implemented in the Vienna Ab initio Simulation Package (VASP). Representative monolayer transition-metal dichalcogenides, MoS_2, WS_2, and $MoSe_2$, were considered as host materials. Re and Nb atoms were introduced as substitutional dopants at the transition-metal

sites, corresponding to representative n-type and p-type dopants, respectively.

To properly describe impurity-induced carrier localization, electronic-structure calculations were carried out using the PBE0 hybrid functional. For each doped system, atomic structures were relaxed, and the resulting charge-density distributions were analyzed to examine the spatial localization of doped electrons and holes around the impurity sites. These calculations allow us to distinguish localized dopant-bound polaron states from spatially extended shallow donor or acceptor states.

Defect-related quantities, including formation energies and charge-state stability, were analyzed using our pydefect-based workflow where appropriate. The use of the ISSP supercomputer enabled systematic PBE0 calculations for multiple doped TMD supercells, which are computationally demanding due to the large supercell sizes and the high cost of hybrid-functional calculations.

Discussion

The PBE0 hybrid-functional calculations reveal a clear tendency toward carrier localization in Re- and Nb-doped monolayer TMDs. Re and Nb are widely regarded as representative n-type and p-type dopants in TMD materials, respectively. In a conventional shallow donor/acceptor picture, Re doping is expected to donate an electron to the conduction band, while Nb doping is expected to introduce a hole near the valence-band maximum. In such a case, the doped carriers would be spatially extended over the host lattice and could contribute to band-like electrical conduction. However, the present calculations show a qualitatively different behavior.

For Re-doped MoS_2, WS_2, and $MoSe_2$, the additional electron introduced by Re substitution does not spread uniformly over the TMD layer. Instead, the electron density is strongly concentrated around the Re dopant and its neighboring transition-metal and chalcogen atoms. This indicates that the donor electron is trapped near the impurity site rather than forming a shallow, delocalized conduction-band state. Similarly, in Nb-doped MoS_2, WS_2, and $MoSe_2$, the hole introduced by Nb substitution is localized around the Nb dopant. The localized hole state is accompanied by a modification of the electronic structure near the valence-band edge, suggesting that Nb does not simply act as a conventional shallow acceptor.

Importantly, this localization behavior is consistently observed in all three host materials considered in this study: MoS_2, WS_2, and $MoSe_2$. The result indicates that dopant-induced carrier localization is not an exceptional feature of a particular material, such as MoS_2, but rather a

general characteristic of impurity doping in monolayer TMD systems. The common behavior found for both Re-donor and Nb-acceptor cases suggests that the reduced dimensionality of TMDs, together with local lattice relaxation and electron-lattice coupling, plays an essential role in stabilizing dopant-bound carrier states.

These localized impurity-induced states can be interpreted as dopant-bound polaron states. In this picture, the carrier introduced by the dopant becomes trapped near the impurity and is stabilized by local lattice relaxation. This is fundamentally different from the standard shallow donor/acceptor model used for conventional three-dimensional semiconductors, where doped carriers are often assumed to be weakly bound and spatially extended. The present results therefore suggest that electrical doping in two-dimensional TMDs should be understood in terms of carrier localization and polaron formation, rather than only in terms of simple carrier donation or acceptance.

The present study also highlights the importance of using hybrid-functional calculations for describing impurity doping in TMDs. Conventional semi-local exchange-correlation functionals tend to over-delocalize impurity-induced carriers because of self-interaction errors, and they may therefore fail to capture the polaronic nature of doped states. In contrast, the PBE0 hybrid functional stabilizes localized carrier states and provides a more appropriate description of the electronic structure around dopants. This difference is particularly important for evaluating whether a dopant can generate mobile carriers or instead forms localized impurity states.

Overall, these results extend our previous MoS_2-based study to a broader class of two-dimensional TMD materials. The consistent localization of doped electrons and holes in MoS_2, WS_2, and $MoSe_2$ demonstrates that dopant-bound polaron formation is a general feature that must be considered when designing impurity doping strategies for TMD-based electronic devices.

References

[1] Universal Polaronic Behavior in Elemental Doping of MoS_2 from First-Principles,
Soungmin Bae, Ibuki Miyamoto, Shin Kiyohara, Yu Kumagai, ***ACS Nano*** 8, 33988–33997(2024).

[2] Koopmans-compliant density functional framework for polaron self-trapping in titanate oxides Soungmin Bae*, Yu Kumagai
npj Computational Materials (accepted, date: 2026.03.19)

Hydrogen–Vacancy Interactions in bcc Iron: Effects of Mo, C, and N

Naoki UEMURA

Department of Physics, Kansai Medical University,

2-5-1 Shin-machi, Hirakata, Osaka 573-1010

This study investigates the interactions among hydrogen (H), vacancies, and alloying elements (Mo, C, and N) in body-centered cubic (bcc) iron using density functional theory calculations performed with the VASP code [1]. Both bulk lattice and grain boundary (GB) models (Σ3 and Σ5) were considered to evaluate trapping behavior and interaction energies.

In the bulk lattice, hydrogen is strongly trapped at vacancies, indicating that vacancies act as dominant trapping sites. In contrast, solute atoms repel hydrogen, with stronger repulsion observed for C and N than for Mo. Although Mo exhibits weaker interaction with hydrogen, its higher solubility suggests that it may reduce hydrogen diffusivity by limiting available diffusion pathways.

The interaction between vacancies and solute atoms shows differences among elements. C and N exhibit relatively strong interactions with vacancies and stabilize H–vacancy complexes, which may influence vacancy behavior and reduce vacancy diffusion. In contrast, Mo shows weaker interaction with vacancies and has limited influence on vacancy formation.

At grain boundaries, solute atoms segregate to the GB plane, while vacancies are stabilized in adjacent layers. Hydrogen is also trapped at GBs. C and N exhibit stronger repulsion with hydrogen at the GB compared to Mo, which may reduce hydrogen segregation at these sites in the absence of vacancies, although this effect is diminished in the presence of vacancies. Mo shows weaker repulsion and has a smaller direct effect on hydrogen distribution at GBs. When a vacancy is present near the GB, hydrogen trapping becomes dominant regardless of the solute species.

These results suggest that C and N suppress hydrogen locally while influencing vacancy-related behavior, whereas Mo has limited influence on vacancy formation and may reduce hydrogen mobility, although hydrogen trapping is primarily governed by vacancies.

References

[1] S. Kato, N. Uemura, M. Vijendran, and R. Matsumoto, ISIJ Int. **66**, 702 (2026).

Development of the optimization method for the long-range correlation factor in the first-principles wave-function theory

Masayuki OCHI
Department of Physics, The University of Osaka
1-1 Machikaneyama-cho, Toyonaka, Osaka 560-0043

We have developed a first-principles electronic structure calculation software using the transcorrelated (TC) method [1, 2]. The TC method is a many-body wave function theory, where Hamiltonian is similarity-transformed with the Jastrow correlation factor. By this transformation, electron correlation effects are efficiently considered. In particular, one-electron orbitals in the Jastrow-Slater-type wave function can be optimized in the same manner as the Hartree–Fock (HF) method, to say, by solving a one-body self-consistent-field (SCF) equation. It is advantageous that the computational cost for this process is the same order as that for the HF method [3].

We have developed our computational code TC++, which was published on github [4, 5]. One can perform TC calculations using TC++ by reading some output files dumped by DFT calculation using the Quantum-Espresso package [6]. TC++ supports the following functionalities: HF, TC, and biorthogonal TC (BITC) calculations, SCF and band calculations, solids and homogeneous electron gas, a plane-wave-basis set, and norm-conserving pseudopotentials. MPI+OpenMP parallelization is supported.

In this year, we have developed the optimization method of the Jastrow factor with the variational quantum Monte Carlo (VMC) method using the CASINO [7] code. In particular, we have tried to construct the long-range correlation factor as required in TC++ calculation from the short-range polynomial Jastrow factor obtained by VMC calculations. An RPA long-range asymptotic form, which is often used in metallic calculations, was fixed through optimization. We have performed test calculations for Na metal. We achieved stable optimization of the short-range part of the Jastrow factor using VMC. On the other hand, an efficient convergence with respect to the number of k points is one of the ongoing problems.

We have also calculated the total energy and the band gap of narrow-gap semiconductors using the TC+VMC method. The accuracy of the lattice constants seem to be improved while the Jastrow factor is at present short-ranged as is usually adopted in quantum Monte Carlo calculations.

References

[1] S. F. Boys and N. C. Handy, Proc. R. Soc. London Ser. A **309**, 209 (1969); *ibid.* **310**, 43 (1969); *ibid.* **310**, 63 (1969); *ibid.* **311**, 309 (1969).

[2] N. C. Handy, Mol. Phys. **21**, 817 (1971).

[3] M. Ochi, K. Sodeyama, R. Sakuma, and S. Tsuneyuki, J. Chem. Phys. **136**, 094108 (2012).

[4] https://github.com/masaochi/TC

[5] M. Ochi, Comput. Phys. Commun. **287**, 108687 (2023).

[6] https://www.quantum-espresso.org/

[7] https://vallico.net/casinoqmc/

Implementation of Self-Consistent *GWΓ* in TOMBO

Kaoru OHNO

Yokohama National University, Tokiwadai, Hodogaya-ku, Yokohama 240-8501

So far, we have applied a self-consistent *GWΓ* method, which incorporates a vertex correction to the first order in the bare Coulomb interaction or the screened Coulomb interaction, to small molecules using a different version of TOMBO [1,2]. TOMBO is the all-electron mixed basis code, in which both plane waves and numerical atomic orbitals are used as a basis set [3]. The code is highly parallelized using MPI and OpenMP. Recently, we have ported the self-consistent *GWΓ* routine from the different version to the latest version of TOMBO. We modified the routine to save the memory usage by extensively using a distributed memory for each process. We also modified the code to be able to handle all applications including Hartree-Fock, one-shot *GW*, and Bethe-Salpeter equation approaches just by changing a flag in an input file. The self-consistent *GWΓ* method can use three different plasmon-pole models by von der Linden and Horsch [4], Engel and Farid [5], and Hybertsen and Louie [6], as well as the full ω integration [7]. To treat the ω dependence of the self-energy, we introduced the linearized *GW* technique [8], in which the self-energy is expanded linearly around a reference energy, which is usually set at the middle point between the HOMO and LUMO levels of the target molecule. We have checked that all the results in our test calculations fully coincide with the ones that calculated by the old, separate version of TOMBO. Independ to these studies, we have also performed extensive one-shot *GWΓ* calculations for variety of molecules [9,10].

References

[1] R. Kuwahara, Y. Noguchi, and K. Ohno, Phys. Rev. B **94**, 121116(R) (2016).

[2] T. Isobe, R. Kuwahara, and K. Ohno, Phys. Rev. A **97**, 060502(R) (2018).

[3] S. Ono, Y. Noguchi, R. Sahara, Y. Kawazoe, and K. Ohno, Comp. Phys. Comm. **189**, 20-30 (2015).

[4] W. von der Linden and P. Horsch, Phys. Rev. B **37**, 8351-8362 (1988).

[5] E. Engel and Behnam Farid, Phys. Rev. B **47**, 15931-15934 (1993).

[6] M. S. Hybertsen and S. G. Louie, Phys. Rev. B **34**, 5390-5413 (1986).

[7] Z. Ming, S. Ono, N. Nagatsuka, and K. Ohno, Phys. Rev. B **93**, 155116 (2016).

[8] R. Kuwahara and K. Ohno, Phys. Rev. A **90**, 032506 (2014).

[9] T. Isago, Y. Noguchi, and K. Ohno, Phys. Rev. B **111**, 195146 (2025).

[10] T. Isago, Y. Noguchi, and K. Ohno, J. Chem. Phys. **164**, 144110 (2026).

Ab Initio Study of Finite-Temperature Magnetic Properties in Transition Metal Systems

Ryoya HIRAMATSU, Takashi MIYAKE, and Tetsuya FUKUSHIMA
Materials DX Research Center
National Institute of Advanced Industrial Science and Technology
1-1-1 Umezono, Tsukuba, Ibaraki 305-8568

Recent advances in magnetic devices have rapidly accelerated their role as a key enabling technology in modern information society. Achieving further performance improvements requires not only understanding the intrinsic properties of magnetic materials but also accurately predicting their behavior under realistic device operating conditions. Traditional device-design workflows typically combine microscopic electronic-structure analysis with macroscopic device-level simulations in a sequential manner. However, this multistage approach often loses detailed information about the underlying electronic states, which has become a bottleneck in exploring and designing next-generation magnetic materials.

To address this challenge, the present project has developed and applied a first-principles evaluation framework capable of incorporating operational environment effects—specifically temperature and external magnetic fields—into electronic-structure calculations. In this fiscal year, our primary goal was to validate the effectiveness of the proposed scheme through quantitative evaluation of a representative magnetic material, $L1_0$-FePt.

Electronic structures are calculated using the tight-binding linear muffin-tin orbital method based on density functional theory within the local spin-density approximation. Finite-temperature magnetic behavior is modeled using the disordered local moment (DLM) picture, while external magnetic-field effects are incorporated via a spin-Zeeman Hamiltonian. The effective medium required in the DLM framework is computed using the coherent potential approximation. Because the evaluation requires electronic-structure calculations for each temperature and magnetic-field condition, the simulations involve large-scale computations. To this end, OpenMP parallelization is employed to improve computational efficiency.

Figure 1 shows the calculated magnetization curves along the hard-magnetization axis. The magnetization initially increases linearly with increasing field and then gradually saturates. As temperature increases, the linear regime systematically decreases and eventually disappears near the Curie temperature (820 K). These behaviors are characteristic of experimentally observed magnetization curves, and our results demonstrate—for the first time—quantitative reproduction of magnetization-curve profiles of real materials using a fully first-principles approach. This accomplishment not only confirms the validity of our evaluation framework but also establishes a computational technique capable of directly providing magnetization-curve data suitable for practical materials design.

In summary, the project has successfully developed and validated a first-principles methodology capable of predicting finite-temperature magnetic properties under external magnetic fields. The quantitative repro-

duction of the magnetization curve of $L1_0$-FePt confirms the potential of the method as a powerful tool for magnetic-material design. Future work will extend this framework to a broader range of materials.

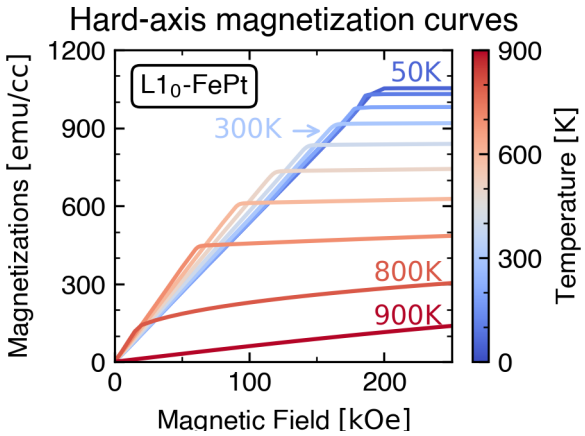

Figure 1: Magnetization curves of $L1_0$-FePt along the hard axis obtained from first-principles calculations.

Weak electronic interaction at the pentacene/graphene interface

Susumu Yanagisawa
University of the Ryukyus
Senbaru 1, Nishihara, Okinawa 903-0213

Understanding the molecule−substrate interactions and formation mechanism of interfacial level alignment at organic molecular semiconductor/metal interface is a critical issue. It may contribute to the advancement of organic electronic materials, while it addresses fundamental academic interests. In this study, to gain insight into the electronic properties of the system, the electronic states of pentacene molecular films adsorbed on graphene were investigated using first-principles calculations.

Electronic states at the pentacene/graphene interface were theoretically examined using the Vienna Ab-initio Simulation Package (VASP). A periodic slab model was constructed based on the experimentally determined adsorption configuration (Structure A), with lattice parameters $a = b = 16.16$ Å and $\beta = 60°$ [1]. The unit cell contained two pentacene molecules. Electron wave functions were expanded in a plane-wave basis set, and the projector augmented wave (PAW) potential was employed to describe the ionic cores. A 2×2 **k**–point mesh was used for sampling the two-dimensional Brillouin zone. A vacuum layer of 2 nm was inserted normal to the substrate to eliminate artificial interactions between slabs. Lattice constants and adsorption geometries were optimized using the van der Waals density functional (vdW-DF) [2]. Numerical calculations were performed using up to 1,024 cores on System B.

It was found that the molecular plane of pentacene is slightly tilted relative to the graphene substrate. The result suggests that the physisorption structure is determined by subtle interplay between intermolecular and molecule-substrate interactions. In the calculated band structure, the HOMO- and LUMO-derived bands of pentacene exhibit almost no dispersion, indicating that they retain the characteristics of the single molecule. Furthermore, energy levels above the conduction band show non-negligible dispersion, and it was found that those bands involve contributions from the wave functions of both the graphene and the pentacene molecules. In contrast, for an adsorption configuration with larger intermolecular distances (Structure D) compared to Structure A, the dispersion of the energy bands near the conduction band was weaker than that of Structure A. This reveals that the band dispersion in the high-energy region originates from the intermolecular interactions. The nature of the intermolecular and molecule-substrate interactions contributing to high-energy band dispersion was found to be consistent with experimental measurements of Fano resonance [1].

References

[1] Y. Hasegawa, T. Yamaguchi, M. Meissner, T. Ueba, F. Bussolotti, S. Ideta, K. Tanaka, S. Yanagisawa and S. Kera: Phys. Rev. B **112**, 085301 (2025).

[2] I. Hamada: Phys. Rev. B **89**, 121103(R) (2014).

Materials Design Through Defect Analysis and First-Principles Calculations

Tomoki YAMASHITA
Department of Electrical, Electronics and Information Engineering,
Nagaoka University of Technology
Kamitomioka-machi, Nagaoka, Niigata, 940-2188

$Li_{2(1-x)}Mg_{1+x}Cl_4$ is attracting attention as a solid electrolyte material in which vacancies are introduced depending on x [1]. Prior to performing large-scale molecular dynamics (MD) simulations using a universal machine learning potential (UMLP), we validated the agreement between density functional theory (DFT) and the UMLP for small-cell calculations. Specifically, DFT-MD was carried out for 56-atom Li_2MgCl_4, as shown in Fig. 1, under NVT conditions at 700 K for 10 ps using the VASP code within the PAW framework and the PBE exchange-correlation functional on System B of the ISSP supercomputer. To evaluate the force accuracy of the UMLP, 50 structures were extracted from the trajectory at 0.2 ps intervals. Force evaluations using MatterSim [2] for these structures showed a mean absolute error of 30 meV/Å relative to DFT, indicating that the UMLP is sufficiently accurate for MD simulations of this system.

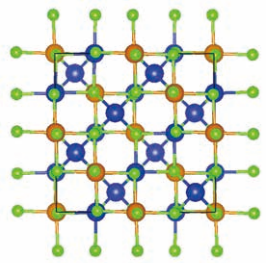

Figure 1: Computational model used for the DFT-MD simulation. Blue, orange, and green spheres represent Li, Mg, and Cl, respectively.

Another research topic addressed in this study was the investigation of defect formation in the semiconductor materials Cu_2SnS_3 (CTS) and Cu_2GeS_3 (CGS). Formation energies of native and Cd-related defects in CTS and CGS were calculated using VASP on System B of the ISSP supercomputer. The HSE06 hybrid functional, which provides a good reproduction of the band gap, was employed for the exchange-correlation treatment. The eFNV correction scheme by Kumagai and Oba [3] was applied to account for defect formation energy corrections, as implemented in the pydefect code [4]. Although calculations for all defect species have not yet been completed, the results obtained so far indicate that Cd substitutional defects at cation sites are likely to form preferentially. In particular, Cd substituting for Cu was found to have the potential to act as a shallow donor.

References

[1] J. Pan et al., Inorg. Chem. **63**, 3418 (2024).

[2] H. Yan et al., arXiv:2405.04967 (2024).

[3] Y. Kumagai and F. Oba, Phys. Rev. B **89**, 195205 (2014).

[4] Y. Kumagai, N. Tsunoda, A. Takahashi, and F. Oba, Phys. Rev. Mater. **5**, 123803 (2021).

Material design of perovskite photocatalysts using first-principle calculations

Seiichiro L. TEN-NO
Graduate School of System Informatics, Kobe University
Rokkodai-Cho, Nada-Ku, Kobe 657-8501

Photocatalytic water splitting under solar irradiation is a promising route to sustainable hydrogen production. Semiconductor photocatalysts are attractive because in principle they can drive the reaction without external bias. [1]

First-principles analysis of layered perovskite $\mathbf{Sr}_{n+1}\mathbf{Ti}_n\mathbf{O}_{3n+1}$ ($n = 1, 2, 3$)

Ruddlesden–Popper (RP) compounds have attracted considerable attention as photocatalysts. In particular, $Sr_{n+1}Ti_nO_{3n+1}$ ($n = 1, 2, 3$) has been regarded as a model system for water-splitting because of its chemical stability and tunable band structure. [2] The electronic properties of the layered RP titanate series Sr_2TiO_4 (**214**), $Sr_3Ti_2O_7$ (**327**), and $Sr_4Ti_3O_{10}$ (**4310**) were systematically investigated using first-principles calculations based on density functional theory (DFT).

From the band calculations, we have identified the conduction band minimum (CBM) and valence band maximum (VBM) of the RP titanates and STO and estimated their effective masses (Figure 1). The anisotropy of the effective masses at the CBM and VBM indicates that RP titanates exhibit a higher degree of two-dimensionality than STO, particularly in **214**. Moreover, the pronounced difference between the in-plane and out-of-plane effective masses leads to anisotropic carrier transport: electron carriers preferentially move in the in-plane direction, whereas hole carriers move out of plane. In addition, the chemical-potential phase diagram indicates that **214** has the widest stability region among the RP titanates (Figure 2). Finally, the analysis of the formation energies suggests that **214** is the least likely to form oxygen defects among the RP titanates and STO, and is therefore less susceptible to photocatalytic degradation associated with defect states.

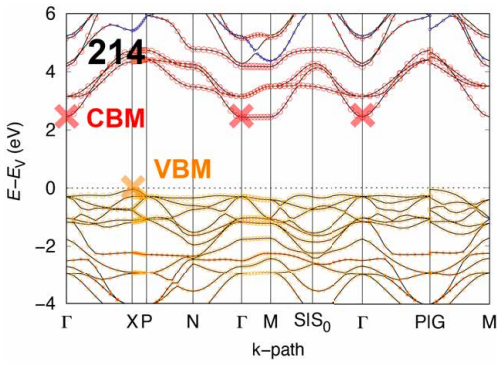

Figure 1: Band structure and CBM/VBM position of **214**. The orbital components are represented by colored circles: Sr 4*d* in blue, Ti 3*d* in red, and O 2*p* in yellow.

Band edge positions for preovskeite oxynitrides $A\mathbf{TaO_2N}$ (*A* = Ba, Sr, Ca)

The design of photocatalysts for visible-light-driven water splitting requires both appropriate band-edge alignment and a sufficiently narrow band gap. Oxynitrides are promising candidates because partial substitution of oxygen by nitrogen raises the valence band maximum (VBM) via N-2*p* states while retaining the chemical stability of oxide frameworks. [3] Here, we examine the band edge positions of $ATaO_2N$ (A=BaSrCa) by DFT calculations and compare them with experimental data.

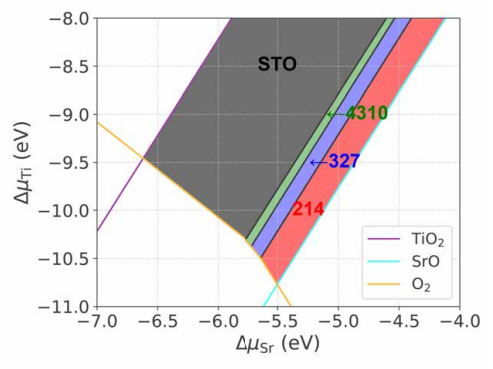

Figure 2: Ternary phase diagram of the chemical potentials. The stable regions for STO and the **214**, **327**, and **4310** phases are highlighted in gray, red, blue, and green, respectively. The purple, cyan, and yellow lines represent the phase boundaries of TiO_2, SrO, and O_2 molecule, respectively.

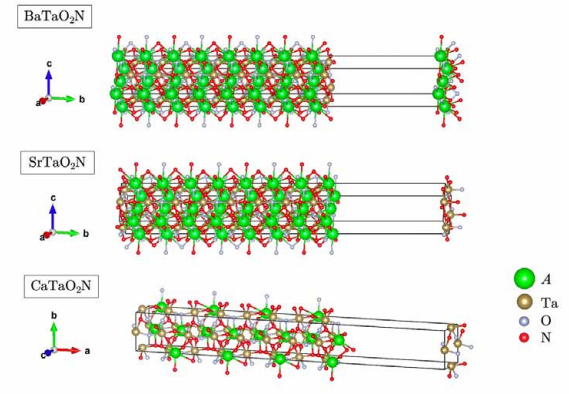

Figure 3: Slab models of *A*TaO2N (*A* = Ba, Sr, Ca).

For the bulk electronic structures of $ATaO_2N$, PBE systematically underestimates the band gaps, whereas HSE06 reproduces both the experimental values and their trend with the A-site cation. The CBM is mainly composed of Ta 5*d* states, while the VBM arises from hybridized O/N 2*p* states, explaining the band-gap narrowing upon nitrogen incorporation. Slab calculations (Figure 3) further show that the VBM and CBM positions depend on the A-site cation through changes in lattice parameters and local bonding. After uniform energy shift correction based on HSE06 by potential alignment, all $ATaO_2N$ compounds satisfy the energetic requirements for visible-light-driven water splitting, although their CBM positions and thus reduction abilities differ appreciably. A direct empirical correction was also tested by aligning the calculated VBM of $BaTaO_2N$ to the experimental value of −6.03 eV reported in Ref. [3], confirming the validity of the relative band-edge trends obtained under identical computational conditions (Figure 4).

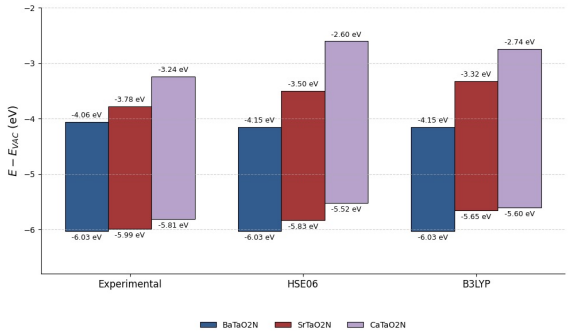

Figure 4: CBM and VBM values for $ATaO_2N$ using uniform energy shift in comparison with experiments.

Calculation conditions

We have performed hybrid (MPI+OpenMP) parallel computing using, where the parallelization over bands and k-points is used by VASP version 6.4.2. [4]

References

[1] K. Nishiguchi, T. Takayama, S. Takasuka, Y. Harashima, M. Fujii, and S. L. Ten-no: J. Phys. Chem. Lett. 2025, 16, 11, 2823–2830.

[2] P. Wang *et. al.*: Nanomaterials **2013**, 15, 20.

[3] S. Balaz *et. al.*: Chem. Mater. 2013, 25, 16, 3337–3343.

[4] G. Kresse *et. al.*: Phys. Rev. B **47**, 558 (1993); Phys. Rev. B **49**, 14251 (1994); Computational Materials Science **6** (1996) 15–50; Phys. Rev. B **54**, 11169 (1996).

Materials discovery for quantum materials: MAX phase and haeckelite systems

Hannes RAEBIGER[1], Mitsuaki KAWAMURA[1], Soungmin BAE[2], Mohammad KHAZAEI[3]

[1)]*Department of Physics,*

Yokohama National University, Hodogaya-ku, Yokohama, Kanagawa 250-8501

[2)] *Institute of Materials Research,*

Tohoku University, Aoba-ku, Sendai, Miyagi 980-0812

[3)] *Department of Physics,*

University of Tehran, North Kargar Avenue, Tehran 14395547, Iran

The discovery of novel quantum materials, including superconductors and systems with emergent electronic properties, is a central objective in condensed matter physics and materials science. A widely adopted computational approach is high-throughput screening, in which large numbers of candidate compounds are generated or collected, and their energetic and mechanical stability is evaluated. Only those systems that are both energetically favorable and mechanically stable are retained for further investigation of their electronic and quantum properties.

This conventional framework has proven highly successful and forms the basis of part of our work. Using first-principles calculations within this approach, we identify new superconducting materials in both MAX phase–derived systems and haeckelite-based compounds. In particular, superconductivity is predicted in o-MAX phase systems and in three-dimensional metallic haeckelite structures, demonstrating that both classes of materials provide fertile ground for quantum materials discovery within the space of energetically and mechanically stable compounds [1,2].

At the same time, conventional screening inherently excludes a large class of materials—those that are mechanically unstable—from consideration. To overcome this limitation, we develop a complementary materials design paradigm, first introduced in Ref. [3], that instead utilizes these unstable systems as starting points. The key idea is to exploit imaginary phonon modes as directional guides in the energy landscape. By following these unstable vibrational modes and relaxing the resulting distorted structures, we obtain new configurations corresponding to local or global energy minima. This instability-driven framework enables access to a previously unexplored region of the materials space and

represents a conceptual shift in materials discovery [3,4].

Applying this approach to MAX phase systems, we discover a series of reconstructed structures that significantly expand their structural landscape. In particular, we identify MAX phase variants with expanded A-layer periodicity, leading to enlarged unit cells and new stacking sequences. These reconstructed phases demonstrate that MAX phases possess a much richer structural diversity than previously recognized, providing additional degrees of freedom for tuning electronic and quantum properties [3,4].

In addition to bulk reconstructions, we identify a wide range of surface reconstructions in MAX phase systems. The predicted surface structures exhibit significant complexity, comparable to that observed in semiconductor surfaces, and arise from the interplay between bulk instability and surface energetics. This is especially relevant for MXene-related materials, where surface structure plays a central role in determining functional properties [4].

Taken together, these results demonstrate that the conventional high-throughput approach and the instability-driven design paradigm are highly complementary. While conventional screening identifies superconducting materials within the stable region of the materials space, the instability-driven approach expands this space by uncovering new reconstructed phases that may serve as future platforms for quantum materials.

References

[1] K. Hamidi et al., Prediction of superconductivity in haeckelite compounds using first-principles calculations, iScience **28**, 113219 (2025).

[2] M. Keivanloo et al., Superconductivity in o-MAX phases, Nanoscale **17**, 5341 (2025).

[3] M. Khazaei et al., Superlattice MAX phases with A-layers reconstructed into 0D-clusters, 1D-chains, and 2D-lattices, J. Phys. Chem. C **127**, 14906 (2023).

[4] M. Khazaei et al., Diverse surface reconstructions in MAX phases, Nanoscale **17**, 24184 (2025).

Hydrogen Atoms Diffusion on Ru(001) Surface

Yiping Chen[1], Kotaro Matsuda[1], Takehiko Sasaki[1],
Bo Thomsen[2], Motoyuki Shiga[2]

1 Department of Complexity Science and Engineering, Graduate School of Frontier Sciences, The University of Tokyo, Kashiwa-no-ha, Kashiwa, Chiba 277-8561

2 Center for Computational Science and e-Systems, Japan Atomic Energy Agency, 178-4-4, Wakashiba, Kashiwa, Chiba , 277-0871

The hydrogen adsorption state on Ru(001) has been extensively studied from the perspectives of surface physics and chemistry. Detailed studies on the diffusion of adsorbed hydrogen atoms by laser-induced thermal desorption (LITD) have been reported by S.M. George et al.[1]. Ru nanoparticles are known to be active in ammonia synthesis, and the behavior of adsorbed hydrogen is important in the ammonia production process. In addition, LITD measurement results have been shown for Ru step surfaces Ru(S)-[15(001)x2(100)], and the diffusion coefficient is smaller than that on Ru(001) surfaces [2]. It is expected that surface diffusion is anisotropic on such step surfaces. Hydrogen diffusion on Ru(001) is a benchmark problem for nuclear quantum effects in surface kinetics. DFT was used to identify stable adsorption sites and representative migration paths, and a neural-network potential (NNP) was trained to reproduce the DFT potential-energy surface (Fig. 1) . Using the NNP, diffusion coefficients were evaluated over a wide temperature range by (i) classical molecular dynamics with mean-squared-displacement analysis and (ii) path-integral approaches combining quantum transition state theory (QTST) and ring-polymer dynamics. The resulting D(T) was compared with laser-induced thermal desorption measurements on Ru(001) and stepped Ru surfaces. Ongoing H/D/T calculations will quantify isotope effects and the sensitivity to the underlying exchange–correlation functional.

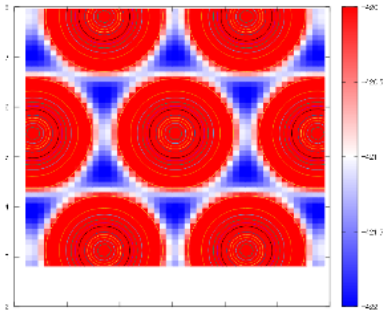

Fig. 1 Contour map of DFT total energy for H/Ru(001).

References

[1] C. H. Mak *et al.*, J. Chem. Phys. **1986**, 85, 1676.

[2] M. V. Arena *et al.*, Surf. Sci. **1995**, 325, 151.

Structures and Stability of Adsorbed Oxygen Species on Pt Nanoparticles

Takehiko SASAKI

Department of Complexity Science and Engineering, Graduate School of Frontier Sciences, The University of Tokyo, Kashiwa-no-ha, Kashiwa, Chiba 277-8561

For the purpose of high-energy resolution fluorescence detected Xray absorption near-edge structure (HERFD-XANES) simulations, structural models for oxygen atoms and hydroxyl groups adsorbed on a platinum truncated octahedron NP, which consists of 586 Pt atoms (corresponding to 2.62 nm diameter close to 2.70 nm particle size (averaged) estimated by TEM) with (111) facets and (100) facets, were obtained by DFT calculations. We used a Pt_{586} truncated octahedron NP as a model structure closest to spheric Pt NPs in MEA Pt/C. In the truncated octahedron model structure the fraction of (111) facets involving edges and corners at the boundary of (111) facets is 91.2 % as shown in Figure 1. The stabilized energies of adsorbed oxygen species on the (100) facets were smaller than those on the (111) facets of Pt truncated octahedron NPs. Hence, in this study we have discussed on the behavior of oxygen species on the (111) facets, edges, and corners.

In order to reduce computational costs for calculating the system consisted of adsorbed oxygen species

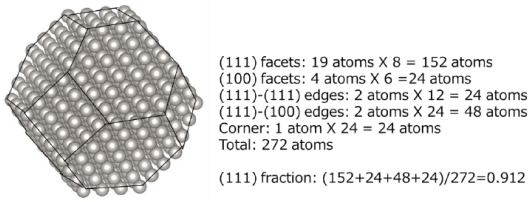

Fig. 1: Pt_{586} truncated octahedron model structure and the numbers of surface atoms at various surface sites.

and Pt_{586} cluster, small Pt clusters consisted of 3-layers, 6-layers and 8-layers, which can reproduce Pt_{586} truncated octahedron NP by applying symmetry operations, were prepared. The adsorption models on the corners, edges and facets of the small Pt clusters were built. Nearest neighbor and second nearest neighbor Pt atoms around adsorbed species were allowed to relax and other Pt atoms were fixed as the bulk Pt crystal. After the structural optimization, symmetry operations were achieved to obtain the 586 Pt truncated octahedron NP with adsorbed oxygen species, namely adsorbed oxygen adatoms and adsorbed hydroxyl groups on edge, corner and terrace sites on Pt NP surfaces as shown in Fig. 2.

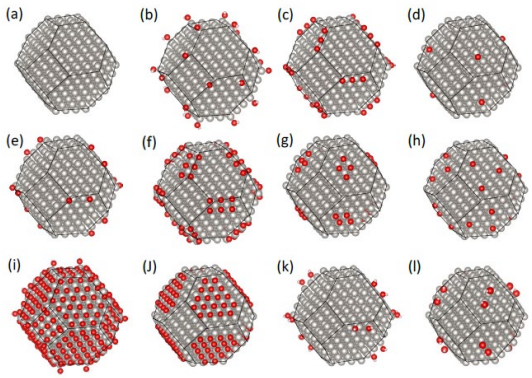

Fig. 2: Model truncated octahedron structures with oxygen-species employed for DFT calculations.

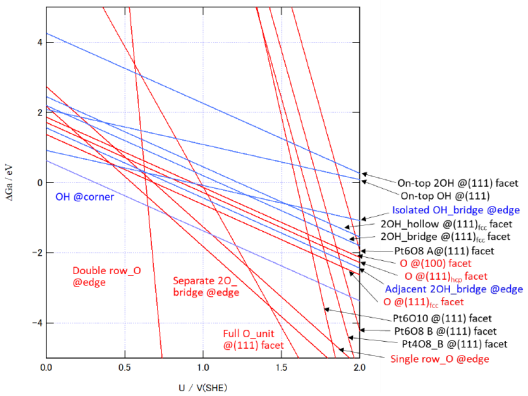

Fig. 3: Potential-dependent stability of adsorbed oxygen species at the corners, edges and facets on Pt NPs calculated by DFT.

DFT calculations were performed using the Vienna ab initio Simulation Package (VASP version 5.4.4). The generalized gradient approximation (GGA) with the exchange correlation functional of Perdew-Burke-Ernzerhof (PBE) was adopted. The projector-augmented wave pseudopotentials (PAW) were used to describe interaction between cores and valence electrons. Cut-off energy for the plane wave basis sets was taken as 400 eV. The unit cells containing Pt cluster and adsorbed species were prepared as mentioned above. The Monkhorst-Pack k-mesh of 3x2x2 was used for the structural optimization calculation. Vibrational frequency calculations were achieved for the Gibbs free energy calculations assuming that all Pt atoms are fixed. Reaction Gibbs free energies of electrochemical processes at 353 K were calculated in the similar way to the previous reports [1,2] to obtain the potential dependence of adsorbed species as shown in Fig. 3. Structural models were used to compute FDMNES simulation for XANES analysis. The potential dependent Pt L_{III} edge XANES data could be successfully reproduced by the linear curve fit on the basis of the potential-dependent stability data (Fig. 3). The whole results were published in 2025 [3].

References

[1] J.K. Norskov et al. , J. Phys. Chem. B **108**, 17886 (2004).

[2] R. Jinnouchi et al., Catal. Today **262**, 100 (2016).

[3] H. Ariga-Miwa et al., ACS Catal. 15, 9856 (2025).

Dopant segregation behavior at grain boundaries in oxide material

Kazutoshi INOUE
Advanced Institute for Materials Research, Tohoku University
Katahira 2-1-1, Aoba, Sendai, Miyagi 980-8577

Wide-bandgap oxides are important materials for insulating and electronic applications. However, their local electronic properties can be significantly affected by lattice defects such as grain boundaries (GBs). MgO, a representative wide-bandgap oxide with a simple rock-salt structure, provides a suitable model system for clarifying how GB atomic structures and dopant segregation modify local electronic states. In particular, rare-earth dopants are expected to interact strongly with MgO GBs because of their large ionic size and different valence states compared to Mg.

In this study, we investigate the atomic and electronic structures of high-angle tilt and twist GBs in MgO using atomistic simulations and first-principles calculations. Possible pristine GB core structures were first explored by molecular dynamics (MD) simulations with a Buckingham-type force field. Simulated annealing was repeatedly performed to identify stable and metastable GB configurations corresponding to local energy minima. For the high-angle tilt GB, two representative low-energy core structures were identified, whereas further analysis is required for the twist GB. First-principles calculations were then carried out for the high-angle tilt GB structures obtained from the MD simulations. We applied the the plane-wave basis projector-augmented wave method included in VASP to screen and determine the stable atomic structure by using the CPU nodes in System B. The generalized gradient approximation was used for the exchange-correlation potentials in the Perdew-Burke-Ernzerhof form, employing an ultrasoft pseudopotential. The GB energy is the interfacial excess free energy calculated by

$$\Delta E = \frac{1}{2A}\left(E_{\mathrm{total}} - N\sigma_i\right),$$

where E_{total} is the total energy of the system including GBs, σ_i is the energy of the unit cell of the bulk crystal, N is the number of unit cells contained in the supercell, and A is the area of the GB. The substitution energies of rare-earth dopants at different GB sites were then evaluated to determine their preferred segregation sites. In addition, the density of states near the GB was calculated to assess the effects of GB structure and dopant incorporation on the electronic properties.

The results indicate that dopant atoms preferentially segregate at specific GB core sites. Dopant substitution can also induce a structural transformation between the two representative GB configurations, suggesting that dopant segregation not only decorates the GB but actively modifies its local structural units. Furthermore, the calculated density of states shows that both the presence of the GB and dopant incorporation reduce the bandgap of MgO [1].

References

[1] Q. Chen, M. Saito, K. Kawahara, A. Nakamura, K. Inoue, Y. Ikuhara, to be submitted (2026).

First-principles study of surface and defect systems for power electronics materials II

Kaori SEINO
Department of Materials Science and Engineering, Kyushu Institute of Technology
1-1 Sensui-cho, Tobata, Kitakyushu, Fukuoka 804-8550

In the field of power electronics, SiC and GaN are considered promising materials of the future beyond silicon, while diamond is expected to surpass both. To date, experiments and computational approaches have been employed to elucidate the mechanisms of surface reconstructions and defect control in crystals, with a view to deepening the fundamental understanding of Si-based semiconductors. However, since SiC, GaN, and diamond exhibit surface reconstructions and crystal structures that differ from those of silicon, research findings and experience obtained from silicon cannot be directly transferred to these materials. In this project, therefore, we investigated (i) defect complexes of Mg impurities in GaN, and (ii) surface structure and properties of wide-bandgap power semiconductor materials. This report is dedicated to an investigation of the former.

Selective doping in GaN by ion implantation is a key technique for GaN power devices, particularly those with a vertical structure. Understanding the atomic diffusion of Mg acceptors as a thermally activated process governed by an energy barrier provides important insights into the device performance. We performed spin-polarized density functional theory (DFT) calculations using the Vienna *Ab initio* Simulation Package (VASP) to investigate Mg diffusion in GaN [1]. Energy barriers were obtained using the climbing-image nudged elastic band (CINEB) method. Our calculations clarify microscopic atomic processes of Mg migration in GaN via the vacancy-mediated mechanism. We identified the microscopic processes involving not only the Mg hopping into a Ga vacancy (V_{Ga}) site but also the subsequent Ga hopping process to the nearby vacant site.

In the CINEB method, the intermediate points along the reaction pathways are treated as a series of *images*, and the atomic structure corresponding to each image must be optimised. In the system B (ohtaka), each of the seven images, based on using a 360-atom supercell, can be assigned to a separate node, enabling parallel CINEB calculations.

We also focused on the fundamental properties of the pair of a substitutional Mg and a Ga vacancy ($\mathrm{Mg_{Ga}}$-V_{Ga}) in GaN, which are the key structures for the vacancy-mediated mechanism of Mg diffusion in GaN. The structural and electronic properties were studied using the Heyd-Scuseria-Ernzerhof (HSE) hybrid functional for $\mathrm{Mg_{Ga}}$-V_{Ga} defect pair as well as an isolated $\mathrm{Mg_{Ga}}$ and an isolated V_{Ga} [2]. A competition between the spin polarization due to localized nitrogen orbitals and the crystal-field splitting of tetrahedral semiconductors is revealed by the present calculations.

References

[1] K. Seino, K. Shiraishi, and A. Oshiyama, Phys. Rev. B **113**, 045201 (2026).

[2] K. Seino, K. Shiraishi, and A. Oshiyama, Jpn. J. Appl. Phys. **64**, 121004 (2025).

First-principles electron theory of strain-induced magnetic switching

Yoshihiro GOHDA

Department of Materials Science and Engineering, Institute of Science Tokyo
J2-22, Nagatsuta-cho 4259, Midori-ku, Yokohama 226-8501, Japan

Switching of magnetic states, in the sense of both the magnetic coupling and the magnetization direction, is of importance in the operation of magnetic devices. One of the promising route for such control is the application of strain [1]. The strain can be imposed by, for example, ferroelectric substrates under applied electric fields [2].

In this project, we demonstrated that the chromium diiodide (CrI_2) monolayer exhibits a strong coupling between lattice geometry and magnetism, allowing for tunable magnetic order as shown in Fig. 1. The in-plane tensile strain drives the phase transition from antiferromagnetic (AFM)-stripe to ferromagnetic (FM) states. In this magnetic phase transition, tensile strain increases the FM $d-p-d$ superexchange mediated by Iodine p-orbitals relative to direct AFM Cr-Cr $d-d$ interaction [3]. In addition, we investigated Janus CrICl and CrIBr monolayers as multiferroic platforms, where broken structural inversion symmetry activates the Dzyaloshinskii-Moriya Interaction (DMI). We found that the DMI in these Janus structures can be tuned by an external electric field.

Similar to CrI_2, an switching of FM-AFM couplings has also been demonstrated for Co/Ru/Co synthetic antiferromagnets, where the experimental behavior of the interlayer exchange coupling was consistent with the first-principles one [4].

Furthermore, magnetocrystalline-anisotropy (MCA) energy dependent on strain has been investigated from first principles: The behavior of the MCA energy of Co_2FeSi depends significantly on the Miller indices of the plane of applied strains [5]. The origin of the MCA modulation can be attributed to energy-band shifts [1].

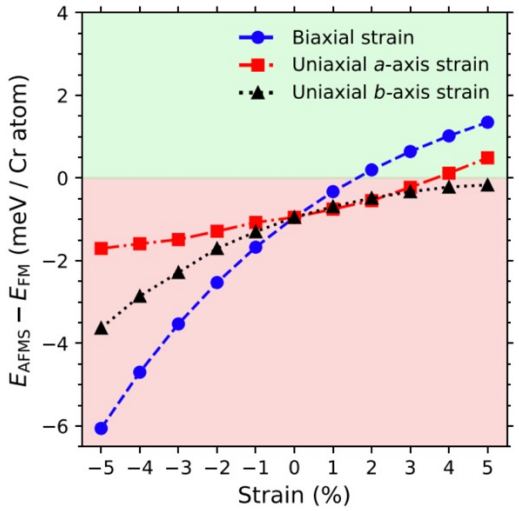

Figure 1: Energy difference between collinear antiferromagnetic-stripe (AFMS) and ferromagnetic (FM) CrI_2 under strain. Reproduced from Ref. [3] ©The Authors.

[1] A.M. Yatmeidhy and Y. Gohda, Sci. Technol. Adv. Mater. **25**, 2391268 (2024).

[2] T. Taniyama, Y. Gohda, K. Hamaya, and T. Kimura, Sci. Technol. Adv. Mater. **25**, 2412970 (2024).

[3] H. Y. Widyandaru and Y. Gohda, npj Spintronics **3**, 34 (2025).

[4] Y. Hisada, S. Komori, K. Imura, C. Shen, Y. Gohda, C.C.I. Ang, W.S. Lew, and T. Taniyama, Adv. Sci. **13**, e17798 (2026).

[5] R. Watarai and Y. Gohda, npj Spintronics **3**, 50 (2025).

Electrochemical reaction analysis using density functional calculation + implicit solvation model 7

Jun Haruyama

Pioneering Research Institute,

RIKEN, 2-1 Hirosawa, Wako, Saitama 351-0198

The Li-ion battery (LIB) has been attracted attention for use in mobile batteries and electric vehicles due to its high energy density. Currently, Li-excess positive electrodes and high-capacity negative electrodes are necessary to overcome the conventional LIB performance. However, the conventional organic electrolytes easily decompose and cannot be used with such electrodes. Recently reported high-concentration electrolytes are promising due to their high durability at both high and low potentials. [1, 2]

In this study, we aim to determine the theoretical electrochemical windows (ECWs) and candidate redox species of the high-concentration electrolytes using FPMD (first principles: FP, molecular dynamics: MD) simulations. A previous study by Ong et al. suggested that the electronic (HOMO and LUMO) levels during FPMD simulations can be used as the approximated values of ECW. [3] The vacuum level outside the solution was used as the reference to align the electronic levels, however, a solution surface cannot be formed for a volatile solvent unlike ionic liquids. Instead of the vacuum level, we introduce a ferrocene molecule (Fc, $FeC_{10}H_{10}$) into the solution and used its time-averaged molecular level as the reference, see Fig. 1 (a). Then, we calculated various kind of electrolyte solutions: 1 M $LiPF_6$ ethylene carbonate (EC): dimethyl carbonate (DMC), LiTFSI and LiFSI salts with acetonitrile (AN) and DMC solvents at low and high concentrations, and some ionic liquids. The calculation cell size was set to adjust the solution density equal to experimental values, and typical cell included about 40–50 molecules as shown in Fig. 1 (a). VASP was used for FPMD simulations. [4]

We obtained the ECWs of ionic liquids referenced by Fc level and compared them with those obtained by the previous study. The results suggest that the Fc reference level works well in these electrolytes.

We obtained the radial pair distribution functions of the mixed solution of 1 M $LiPF_6$ EC/DMC as shown in Fig. 1 (c). The coordination numbers of Li^+ ions were good agreement with previous MD results based on quantum-chemical calculation. [5] Then, we found that the LUMOs during FPMD simulation can be attributed to EC molecules,

which suggests the main component of solid electrolyte interphase (SEI) at a negative electrode comes from the EC decomposition.

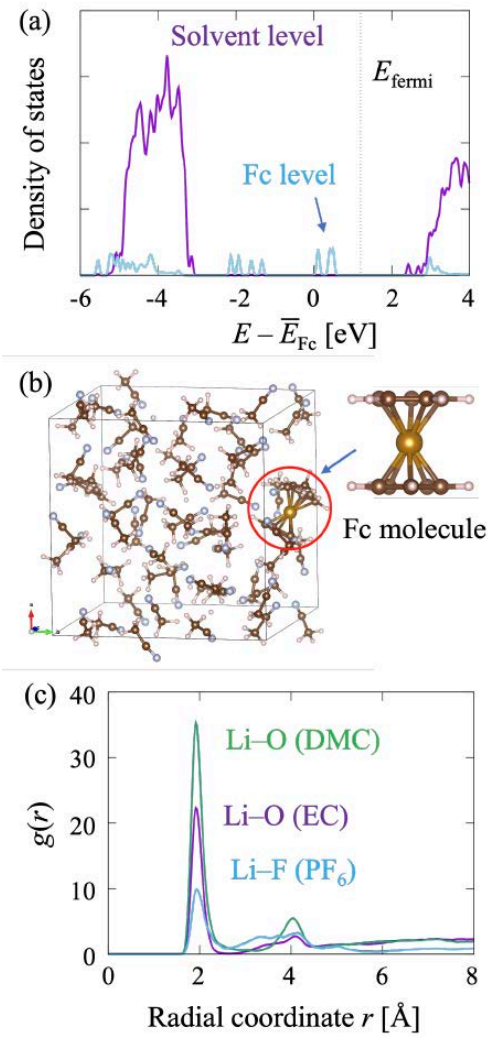

Fig. 1: (a) The density of states of Fc included AN solution. (b) FPMD simulation cell. (c) Radial distribution function $g(r)$.

For the LiFSI DMC solutions, the low-concentrate solution showed a similar ECW compared with that of 1 M $LiPF_6$ EC/DMC. However, the ECW of high-concentrate solution showed an approximately 0.3 V shift to the higher potential side, and the possible oxidation (HOMO) state can be attributed to anion species.

For the AN solution, the pure solvent showed a wide ECW, but the introduction of electrolyte ions shifted the oxidation potential to the lower potential side. The reduction potential of high-concentrate solution was slightly shifted to the higher potential side, which suggests that the high reduction durability for the high-concentrate AN solution [1] cannot be explained by the ECW. In that case, we need to discuss kinetic reasons such as the sacrificial decomposition of anion species. [6] Finally, we need to discuss that the reference Fc level can be used for many kind of solutions in future.

References

[1] Y. Yamada, K. Furukawa, K. Sodeyama, K. Kikuchi, M. Yaegashi, Y. Tateyama, A. Yamada, J. Am. Chem. Soc. **136**, 5039 (2014).

[2] J. Wang, Y. Yamada, K. Sodeyama, C. H. Chiang, Y. Tateyama, and A. Yamada, Nat. Commun. **7**, 12032 (2016).

[3] S. P. Ong, O. Andreussi, Y. Wu, N. Marzari, and G. Ceder, Chem. Mater. **23**, 2979 (2011).

[4] G. Kresse and J. Furthmüller, Phys. Rev. B **54**, 11169 (1996).

[5] O. Borodin and G. D. Smith, J. Phys. Chem. B **113**, 1763 (2009).

[6] K. Sodeyama, Y. Yamada, K. Aikawa, A. Yamada, and Y. Tateyama, J. Phys. Chem. C **118**, 14091 (2014).

Development of an electrolyte database based on automated molecular dynamics simulations

Atsuo YAMADA

Department of Chemical System Engineering,

The University of Tokyo, Bunkyo-ku, Hongo, Tokyo 113-8656

With the expanding application of rechargeable batteries, electrolytes must simultaneously achieve high ionic conductivity, wide electrochemical stability windows, and chemical/thermal stability. As these properties often conflict, efficient exploration of the vast compositional space requires a data-driven approach. However, existing databases provide physicochemical properties of isolated molecules and lack structural/thermodynamic information for electrolyte solutions.

To address this challenge, we systematically generated large-scale structural and physicochemical data for electrolyte solutions using automated high-throughput molecular dynamics simulations (Fig. 1). Specifically, a total of 5,616 compositions were investigated, consisting of combinations of three cations (Li^+, Na^+, K^+), nine anions, twenty-six solvents, and concentrations ranging from 0.5 to 4.0 mol kg^{-1}. For each system, structural and transport properties, including coordination numbers, ionic conductivity, diffusion coefficients, viscosity, and density, were evaluated.

The resulting dataset was organized into the Open Electrolyte Database for Batteries (OEDB, https://oedb.jp). Furthermore, integration with a large language model enables natural language queries to suggest candidate electrolyte compositions and summarize property trends based on user-defined requirements.

References

[1] K. Nakamura, et al., A. Yamada, *npj Comp. Mater.* Accepted, DOI: 10.1038/s41524-026-02093-y (2026).

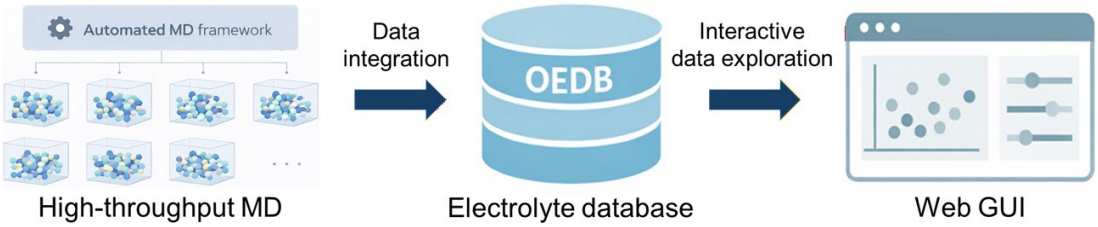

Figure 1 Overview of the workflow employed in this study, including high-throughput molecular dynamics (MD) simulations, construction of the Open Electrolyte Database for Batteries (OEDB), interactive data exploration using a web-based graphical user interface, and use of the database by LLM-based agents.

First-Principles Study of the OER Catalytic Performance of a High-Entropy Oxide with a Stable Atomic Configuration

Haolun LI, Yuta TSUJI

Department of Advanced Analytical Science for Materials and Devices, Faculty of Engineering Sciences,

Kyushu University, Kasuga-koen 6-1, Kasuga, Fukuoka 816-8580

High-entropy oxides (HEOs) have attracted considerable attention because of their promising catalytic activity. In our previous work [1], a stable atomic configuration of a rock-salt type HEO structure, (NiMgCuCoZn)O, was obtained through Bayesian optimization. In this study, the oxygen evolution reaction (OER) catalytic performance of this stable HEO structure was investigated by density functional theory (DFT) calculations using the Vienna Ab initio Simulation Package (VASP).

For many rock-salt transition-metal oxides, the AFM-II configuration is generally considered to be the energetically preferred magnetic ordering. However, because of the complex atomic configurations in HEOs, the most stable spin configuration of the rock-salt type HEOs at room temperature remains unclear. Thus, in this study, two representative spin configurations, ferromagnetic (FM) and type-II antiferromagnetic (AFM-II), were considered for comparison. To investigate the catalytic performance, after optimization of the initial bulk structure, a series of slab models were constructed to identify the most stable surfaces. Then, the most active sites on these surfaces were determined, and the Gibbs free energies of the OER intermediates were calculated.

The most active sites were found to be either Co or Cu atoms in both spin configurations. In all cases, the potential-determining step in the OER was the *OH → *O step, with the largest ΔG among all reaction steps. The average ΔG_{max} of the Co sites was lower than that of the Cu sites, indicating that the Co sites are more favorable for OER catalysis. In addition, the ΔG_{max} values of the Co sites in the FM configuration were lower than those in the AFM-II configuration, suggesting that the FM-ordered HEO structure exhibits better catalytic activity.

References

[1] T. Ueno, and Y. Tsuji, J. Chem. Theory Comput. **21**, 11697 (2025).

Quantum transport theory based on large-scale first-principles electron transport calculations

NOBUHIKO KOBAYASHI
Department of Applied Physics, University of Tsukuba
1-1-1 Tennodai Tsukuba Ibaraki 305-8573

Quantum transport theory based on large-scale first-principles electron transport calculations is important from the viewpoint of materials science and technology. We have developed the nonequilibrium Green's function (NEGF) method and the O(N) time dependent wave-packet diffusion (TD-WPD) method on the basis of the density functional theory (DFT) as techniques for analyzing electronic structure and transport properties. We have also developed methods to predict the crystal structures of organic materials, and have applied the methods to the design of organic semiconductors.

Organic semiconductors have attracted much attention for their applications to flexible, printable, lightweight, and low-cost electronic devices. The organic crystals are assemblies of π-conjugated molecules weakly bonded by van der Waals interactions, and it is difficult to predict the crystal structures. We have developed an efficient method based on DFT to predict the crystal structures of organic semiconductors from molecular structural formulas without using experimental data. We successfully obtained organic crystal structures from the molecular structural formulas. The predicted stable structures agree well with the experimentally observed structures,[1] Furthermore, we developed a method to rapidly predict structures by combining with machine learning.

We investigated charge or spin ordering instabilities in organic semiconductors induced by hole doping via EDLT in low temperature. We calculated phase diagrams against the off-site Coulomb repulsion energy and hole concentration. We elucidated a sufficiently large off-site Coulomb repulsion energy could induce charge ordering instability in the system, which aligns with the experimentally observed unusual temperature dependence of the Hall coefficient as the hole concentration increases.[2]

We calculated the field emission from vertically aligned graphene edges at the apex of the pencil lead. The pencil lead emitter exhibits characteristic emission patterns of the graphene edge, suggesting the presence of the sparsely distributed, vertically aligned graphene edges at the apex of the pencil lead. We showed that the energy spectrum of the emitted electrons exhibits the characteristic lineshape due to the characteristic electronic states of π-bands of graphene [3]

References

[1] S. Hakata, H. Ishii, H. Takaki, T. Okamoto, J. Takeya, N. Kobayashi,
Appl. Phys. Express 17 101001 (2024)

[2] N. Kasuya, T. Furukawa, H. Ishii, N. Kobayashi, K. Hirose, H. Takayanagi, T. Okamoto, S. Watanabe, J. Takeya,
*Nat. Commun.*16, 3214 (2025)

[3] T. Igari, R. Tsuruta, Y. Nishiyama, M. Adachi, T. Myojin, K. Asanagi, M. Sasaki, N. Kobayashi, Y. Yamada
Sci. Rep. 15, 27456 (2025)

Ab initio molecular-dynamics study on self-healing in cement-based hydrated minerals

Ikumi KANEMASU and Satoshi OHMURA

Graduate School of Science and Engineering,

Division of Informatics and Computation, Premier Institute for Advanced Studies,

Ehime University, Matsuyama, Ehime 790-8577, JAPAN

Concrete is one of the most widely used construction materials and plays a central role in sustainable development and carbon neutrality. To improve the mechanical properties of concrete, it is essential to understand the properties of cement hydration products. In particular, the mechanical response of calcium silicate hydrates (C–S–H) is a key factor governing the stability of cementitious materials. Tobermorite, a crystalline analog of the C–S–H phase, serves as an ideal model system for investigating pressure-dependent mechanical properties at the atomic and molecular scales. In this study, we investigated the deformation behavior of tobermorite under tensile and compressive loading using molecular dynamics simulations based on density functional theory and a machine-learning interatomic potential.

The results of the tensile simulations indicate that stretching tobermorite along the stacking direction causes the CaO layers to break, resulting in delamination of layers. On the other hand, the stress-strain curve obtained from the compression simulation indicates that the stress initially increased linearly, followed by a sudden decrease and subsequent increase with the application of further strain. This behavior indicates the occurrence of a stress recovery phenomenon.

To understand the atomic origin of the stress recovery under compression, we investigated the time evolution of the atomic configuration during the compression. Before compression, the interlayer oxygen atoms aligned parallel to the direction of compression. Consequently, compressive deformation induced resistance owing to repulsive interactions between the oxygen atoms in the upper and lower layers. Under the influence of this repulsive force, the Si–O chains slipped, leading to the rearrangement of the silicon and oxygen atoms. Under further compression, new Si–O bonds that penetrated and bridged the Ca–O layers were formed. This is the origin of stress recovery of tobermorite.

References

[1] I Kanemasu and S. Ohmura, *High Pressure Research*, 1–9 (2026)

Ab Initio Molecular Dynamics Study of the Structural Instability of Ettringite under Dehydration and Rehydration Conditions

Tomohiro SASAOKA, Ikumi KANEMASU and Satoshi OHMURA

1) Department of Civil and Environmental Engineering Hiroshima Institute of Technology, Hiroshima, Hiroshima 731-5193

2) Graduate School of Science and Engineering, Ehime University, Matsuyama, 790-8577,

3) Division of Informatics and Computation, Premier Institute for Advanced Studies, Ehime University, Matsuyama, Ehime 790-8577,

Ettringite, a hydration product of Portland cement, is known to play an important role in the development of early strength in cement paste. It has a hexagonal structure and forms needle-like crystals. Ettringite undergoes dehydration upon heating and rehydrates upon cooling in the presence of water. This dehydration–rehydration reaction is reversible and enables the material to absorb and release thermal energy. For this reason, ettringite has attracted attention as a thermochemical energy storage material. To evaluate its instability at high temperatures, we performed *ab initio* molecular dynamics simulations.

The simulation results indicate that sulfate ions are linked through hydrogen bonds mediated by water molecules, and that the S–S correlation becomes weaker with increasing temperature. We also investigated dehydrated ettringite by means of machine-learning molecular dynamics simulations. The simulations show that the S–O distance in the dehydrated system is shorter than that in the hydrated system. This result is consistent with experimental observations.

.

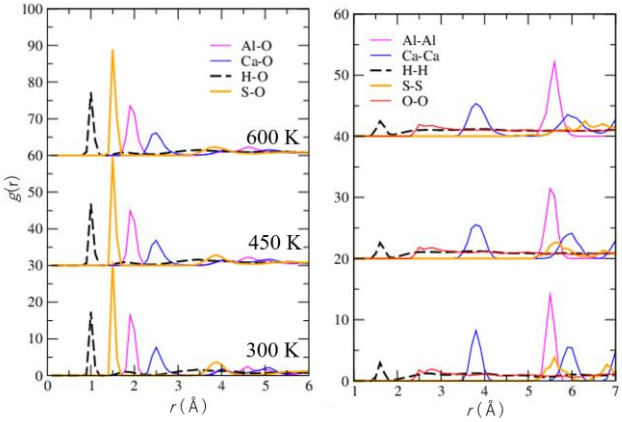

Fig. 1. Temperature dependence of $g(r)$ of ettringite.

References

[1] K. Nomura, *et al.*, The Journal of Physical Chemistry Letters **16**, 6637-6644 (2025).

Thermodynamics of disordered crystalline systems considering charge and spin ordering

Shusuke KASAMATSU

Academic Assembly (Faculty of Science),

Yamagata University, Kojirakawa, Yamagata-shi, Yamagata 990-8560

When first-principles calculations based on the DFT+U method are applied to transition-metal oxides, the electronic state is often trapped in local minima corresponding to various charge and spin configurations, preventing convergence to the true ground-state solution. This can often lead to qualitatively wrong energies, which, in turn, would lead to completely wrong understanding of the thermodynamics of the material. To address this issue, we implemented in the abICS framework [1] a *local perturbation* + *relaxation* scheme, in which transition-metal ions in the structure are randomly selected, locally distorted, and the electronic structure is subsequently re-optimized in an iterative manner. VASP code was used for the DFT+U calculation part. We validated the effectiveness of this approach using benchmark tests with known "correct" solutions: (i) the antiferromagnetic ordering in NiO, (ii) the Mn^{3+}/Mn^{4+} charge ordering in $LiMn_2O_4$, and (iii) the optimization of polaron configurations in oxygen-deficient TiO_2, obtaining physically reasonable results in all cases (the $LiMn_2O_4$ example is given in Fig. 1). Furthermore, applying the present method to the lithium-ion battery cathode material $LiNi_{1/3}Mn_{1/3}Co_{1/3}O_2$, we obtained an electronic configuration whose energy is lower by as much as 1 eV compared to that obtained via conventional structural optimization based on standard first-principles calculations.

These results clearly demonstrate that, for transition-metal complex oxides with disordered elemental distributions or defects, conventional structural optimization alone is insufficient for accurate thermodynamic calculations, and explicit optimization of electronic configurations, as performed in this study, is essential.

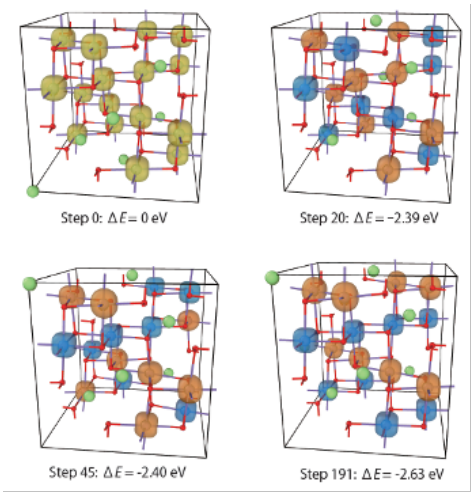

Fig. 1: Optimization of charge ordering in $LiMn_2O_4$.

References

[1] https://www.pasums.issp.u-tokyo.ac.jp/abics

First-Principles Molecular-Dynamics Study of Structural and Electronic Properties of Disordered Materials under Extreme Conditions

Fuyuki SHIMOJO

Institute for Solid State Physics,

Department of Physics, Kumamoto University, Kumamoto 860-8555

Computer simulations are essential for studying the structural and dynamic properties of disordered materials, which lack the long-range order found in crystals. Using first-principles molecular dynamics (FPMD) simulations, we have investigated pressure-induced structural transformation in glassy covalent materials [1], and the intermolecular correlations in molecular liquids [2].

While FPMD simulations are sufficiently accurate to reproduce a wide range of material properties, they are computationally expensive. In contrast, machine-learning interatomic potentials (MLIPs) based on artificial neural networks offer much higher efficiency with FPMD accuracy. In this study, we have applied robust MLIPs developed for highly covalent materials [3] to silica glass and liquid lactic acid.

To elucidate the microscopic mechanism of permanent densification in silica glass, we have investigated the decompression process from 60 to 0 GPa at room temperature using MLIPs for a system containing about 250,000 atoms. We confirmed that the transformation from sixfold- to fourfold-coordinated structures occurs most significantly at 14 GPa, consistent with the result obtained for the 30,000-atom system. A remarkable finding is that a peak in the static structure factor appears at a small wave number of about k = 0.1 Å^{-1}, which has never been reported in either experimental or theoretical studies. This result indicates the existence of density fluctuations on length scales exceeding 60 Å.

To clarify the intermediate-range intermolecular correlations in liquid lactic acid, we have employed MLIPs for systems containing about 24,000 atoms. We found that the number of molecular dimers differs between liquid racemic lactic acid and liquid L-lactic acid, which may be related to the difference in their melting temperatures.

References

[1] E. Ryuo, D. Wakabayashi, A. Koura, and F. Shimojo, Phys. Rev. B **96**, 054206 (2017).

[2] K. Ito, H. Shimakura, S. Tahara, K. Ohara *et al*., J. Phys. Soc. Jpn. **94**, 044604 (2025).

[3] D. Wakabayashi, K. Shimamura, A. Koura, F. Shimojo, J. Phys. Soc. Jpn. **92**, 074002 (2023).

HPC-based fusion of simulation, experiment analysis and data driven science

Takeo Hoshi[1,2]

[1] *National Institute for Fusion Science,*

322-6 Oroshi-cho, Toki city, Gifu Prefecture, 509-5292, Japan.

[2]*Interfaculty Initiative in Information Studies, The University of Tokyo, 7-3-1 Hongo, Bunkyo-ku, Tokyo 113-8654, Japan*

The HPC-based integration of simulation, experiment analysis and data driven science was performed among material science and fusion science. The research was carried out mainly using our open-source software Open Data Analysis Tool for Science and Engineering (ODAT-SE), which was developed by the PASUMS project in FY2024 as a major upgrade of 2DMAT [1]. ODAT-SE (2DMAT) was developed for the data analysis of advanced experimental measurements and offers five analysis methods: (i) grid search, (ii) Nelder-Mead optimization, (iii) Bayesian optimization, (iv) replica exchange Monte Carlo method, and (v) population-annealing Monte Carlo method. The parallel computation with ODAT-SE was carried out on the ISSP supercomputers and other supercomputers such as Fugaku.

At this year, we have improved the ODAT-SE for general applicability to measurement informatics by separating codes of forward models (emulation or simulation of experimental measurement) from the ODAT-SE code.

As an application study, we used the improved ODAT-SE code to calculate incoherent Thomson scattering spectra in high temperature plasmas. [3] The basic idea is to treat the entire scattering process as the superposition of individual photon-electron interactions. We introduce macro-particles, referred from particle-in-cell simulations, to reduce the computational cost, and obtain scattered spectra within a reasonable computational time. The simulated spectra show good agreement with both analytical and numerical results, demonstrating that the present analysis method can reliably reproduce incoherent Thomson scattering spectra.

[1] Y. Motoyama *et al*., Comput. Phys. Commun. 280, 108465 (2022).

[2] https://www.pasums.issp.u-tokyo.ac.jp/odat-se/

[3] K. Sakai *et al.*, JINST 21, C01002 (2026).

Electron excitation induced phase transformation of quantum materials

Koichi KUSAKABE
Graduate School of Science, University of Hyogo
Kouto, Kamigori-cho, Ako-gun, Hyogo 678-1297

We analyzed the photo-induced phase transition phenomenon in quantum materials using density functional theory calculations based on the variational principle for excited states. Wannier orbital analysis was performed on the stable crystal structure of (EDO-TTF)$_2$PF$_6$, revealing that the electron occupation of antibonding orbitals appearing in the molecular pair forming the CDW ground state is the origin of local strain generation.[1] We derived a picture in which reducing the number of electrons occupying this antibonding orbital through photoexcitation leads to strain relaxation in the insulating CDW structure, ultimately resulting in metallization.

Based on phenalenyl tesselation molecules (PTMs) designed by our group, we have developed a design method for poly-PTMs, which form a super-honeycomb structure of the zero modes. By controlling the connection order between adjacent PTMs, it became possible to design Dirac electron systems with systematically altered Fermi velocities.[2] We then expanded our research to the design of electronic devices based on this material structure.

The deaggregation mechanism of amyloid-β may involve the formation of a reaction pathway that stabilizes degradation reaction intermediates due to a unique steric hindrance effect. We set up a parallel stacking model of two molecules and estimated the activation barrier of the molecular dissociation pathway triggered by structural deformation to a twisted molecular structure.[3] Based on this reaction pathway, we discussed the deaggregation from the quasi-one-dimensional microcrystal end faces.

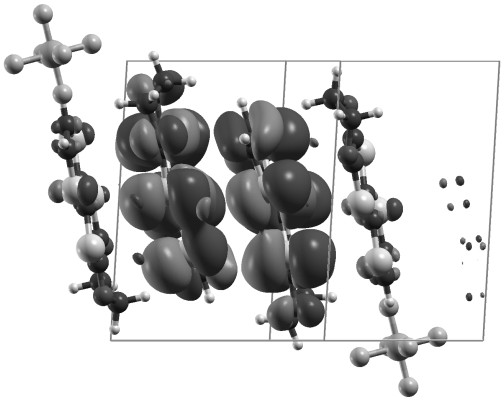

Figure 1: The intermolecular anti-bonding Wannier orbital appearing in the valence band of (EDO-TTF)$_2$PF$_6$.

References

[1] K. Fukumoto, K. Onda, T. Tanaka, K. Kusakabe, E. Pyatenko, H. Yamochi, S. Adachi, S. Koshihara, preprint, submitted to Phys. Rev. Res.

[2] N. Morishita, K. Komatsu, M. Kitatani, and K. Kusakabe, Physical Review B **111**, 235117 (2025).

[3] Y. Oishi, M. Kitatani, K. Nakajima, H. Ogi, and K. Kusakabe, RSC Advances, **15**, 42395 (2025).

Study on physical properties of structural elementary excitations at solid surfaces and interfaces

Hiroyuki KAGESHIMA
Graduate School of Natural Science and Technology, Shimane University
1060 Nishi-Kawatsucho, Matsue, Shimane 690-8504

In this project, we have been focused on physical properties of structural elementary excitations, such as point defects and precursors, of semiconductor surfaces and interfaces. In this year, we have focused on the physical properties of excess Si transport in Si oxide growing on Si(100) [1, 2, 3, 4]. The calculations were performed based on the first-principles calculation. Program package PHASE/0 was employed [5].

In the Si thermal oxidation process, structural elementary excitations, namely 'excess Si's', released from the interface toward the Si oxide film play a significant role. Although the generation of this released Si's originates from compressive stress at the interface, it is essential for providing a consistent explanation of phenomena such as the initial enhanced oxidation and PADOX.

We have used a quartz interface model up to now because quartz can be formed by oxidizing Si and then releasing the Si appropriately to relieve strain. Roughly speaking, oxidizing Si simply involves inserting O into the Si-Si bonds; however, this results in the formation of an extremely dense cristobalite-like structure that requires a 2.25-times volume expansion to relieve strain. The quartz interface model was developed to account for the Si release required to alleviate this high density.

We have also shown that we must use the quartz interfacial model to reproduce the barrier heights of interfacial reactions observed in experiments. Since quartz is expected to maintain a stable structure even at high temperatures and under pressure, it is reasonable to assume that such layers exist at the interface during the process of structural relaxation.

On the other hand, we have shown that we must use the cristobalite model to reproduce the experimental values for the barrier height of O_2 diffusion in the oxide film. This differs from the quartz-like interfacial layer. Although β-cristobalite has a lower density of 2.21 g/cm^3 compared to β-quartz's 2.54 g/cm^3, this is consistent with the idea that cristobalite forms in regions slightly removed from the interface due to further structural relaxation from quartz. In fact, the Deal-Grove theory cannot be reproduced unless the quartz layer at the interface has a constant thickness, regardless of the thickness of the oxide film. In other words, it can be assumed that the Si thermal oxide film consists of at least two layers: a quartz-like high-density interface layer and a cristobalite-like upper oxide layer.

Just as removing excess Si from cristobalite produces quartz, removing excess Si from quartz causes it to transform into cristobalite. Based on various experiments, the density of the upper oxide layer is estimated to be 2.2 g/cm^3, which indeed matches the density of cristobalite. Therefore, it is consistent to assume that further Si is released from the quartz-like high-density interfacial layer, resulting in strain relaxation and the formation of a cristobalite-like upper oxide layer. Incidentally, the thickness of the high-density in-

terfacial layer is reported to be approximately 1 nm, and the Si oxide layer is reported to exhibit cristobalite-like order on average.

Based on these observations, we have successfully developed a model of the Si thermal oxide film interface consisting of two layers: a quartz-like interfacial high-density layer and a cristobalite-like upper relaxed oxide layer (Fig. 1). Since there are no dangling bonds anywhere and the structure consists of a seamless network of only Si-Si and Si-O-Si bonds, there are no interface defects. This contrasts with the situation where Si dangling bonds invariably appear at the interface when structurally relaxed cristobalite is directly bonded to Si.

Next, using this two-layer oxide film model, we investigated the transport pathways of excess Si within the oxide film and the associated energy changes via first-principles calculations. In the upper cristobalite layer, as in quartz, both the tetrahedral and dihedral Si structures become metastable. Furthermore, unlike in quartz, the kick-out mechanism – where Si atoms are transported via a domino effect – does not operate in cristobalite; instead, the deformation step of the dihedral Si plays a crucial role, resulting in the characteristic continuous transport of the same Si atom.

The barrier height in the upper cristobalite layer was 5.38 eV, which agreed well with the experimental value of 5.13 eV. The barrier height in the quartz layer was 5.61 eV, which is higher than that in the cristobalite layer. This difference is thought to be due to the fact that the kick-out mechanism does not operate in cristobalite. Furthermore, the cristobalite surface is approximately 1.92 eV more stable than the initial structure, indicating that Si emission toward the oxide film is indeed energetically favorable. Furthermore, the boundary between cristobalite and quartz is also stable by about 1.44 eV; this implies that Si released at the interface precipitates at the boundary, suggesting that the $L_1 \sim 1$ nm reported by Massoud et al. for the initial enhanced oxidation phenomenon is closely related to the thickness of the high-density layer at the interface within the thermally oxidized film.

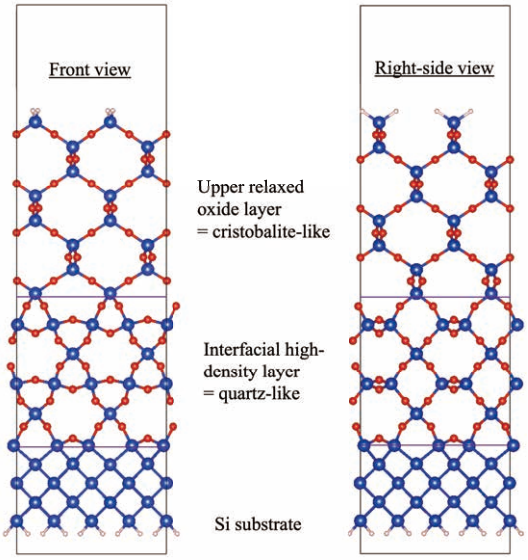

Figure 1: Schematic picture of the atomic model of the Si thermal oxide film interface consisting of two layers with a quartz-like interfacial high-density layer and a cristobalite-like upper relaxed oxide layer.

References

[1] H. Kageshima, T. Akiyama, and K. Shiraishi, J. Phys. Soc. Jpn. 94 (2025) 074707 (4 pages).

[2] H. Kageshima, T. Akiyama, and K. Shiraishi, e-J. Surf. Sci. Nanotechnol. 23 (2025) 306 (8 pages).

[3] H. Kageshima, I. Seo, T. Akiyama, and K. Shiraishi, Jpn. J. Appl. Phys. 65 (2026) 03SP18 (10 pages).

[4] H. Kageshima, I. Seo, T. Akiyama, K. Shiraishi, Mater. Sci. Semicond. Process. 209 (2026) 110582 (8 pages).

[5] https://azuma.nims.go.jp

Effects of anomalous chemical bonding and local structures on thermal transport and thermoelectric properties

Naoki SATO

Research Center for Materials Nanoarchitectonics (MANA),

National Institute for Materials Science (NIMS), 1-1 Namiki, Tsukuba, Ibaraki 305-0044

For the development of high-performance thermoelectric power generation and cooling materials, it is essential to explore classes of materials with low lattice thermal conductivity and to elucidate their microscopic heat transport mechanisms. The factors governing lattice thermal conductivity can be broadly classified into two categories: intrinsic factors, such as chemical composition and crystal structure, and extrinsic factors, such as lattice defects and grain boundaries. Establishing methods to control both types of factors is highly beneficial for the systematic discovery and design of low lattice thermal conductivity materials. In this study, we focused on chemical bonding and local structural motifs in materials, which are closely related to both intrinsic and extrinsic factors. By clarifying specific forms of bonding and local structure that can strongly influence thermal transport and thermoelectric properties, we aimed to establish useful design principles for realizing high-performance thermoelectric materials.

We developed a script to define cation-centered coordination polyhedra in crystal structures and to automatically calculate the distortion index (DI) proposed by Baur [1]. Using this script, we ranked materials in the Materials Project database according to their DI values. For the top 30 compounds in this ranking, we performed phonon calculations and calculations of thermal transport properties based on density functional theory (DFT). The DFT calculations were carried out using VASP [2], while the calculations of harmonic and anharmonic interatomic force constants, as well as lattice thermal conductivity, were performed using ALAMODE [3]. Chemical bonding analyses were conducted using LOBSTER [4].

Most of the materials containing markedly distorted coordination polyhedra with DI > 0.20 exhibited anisotropic crystal structures, and pronounced anisotropy was also observed in their lattice thermal conductivity. Among them, several mixed-anion compounds with complex layered structures, such as Sillén–Aurivillius-type layered perovskites, were predicted to exhibit extremely low lattice thermal conductivities below 0.10 W m^{-1} K^{-1}. The microscopic origins of these ultralow lattice thermal conductivities were identified as rattling-like anharmonic vibrations of off-

centered cations at the centers of highly distorted coordination polyhedra, highly localized phonon modes, and a large scattering phase space arising from bonding heterogeneity. These results demonstrate that focusing on the distortion index enables efficient screening of materials with low lattice thermal conductivity and provides useful guidelines for the discovery of novel thermoelectric and thermal-insulation materials.

References

[1] W.H. Baur, Acta Crystallogr. B **30**, 1195–1215 (1974).

[2] G. Kresse and J. Hafner, Phys. Rev. B **48**, 13115 (1993).

[3] T. Tadano et al., J. Phys.: Condens. Matter **26**, 225402 (2014).

[4] S. Maintz et al., J. Comput. Chem. **37**, 1030–1035 (2016).

Structure and properties of Fe-Pd-In and Pt-based nanoalloys from Ab-initio research

Yasutomi TATETSU

Meio University, Biimata, Nago, Okinawa 905-8585

The development of novel ordered alloy nanoparticles relies on controlling atomic arrangements at the nanoscale. In this project, we investigated the formation mechanisms and structural properties of ternary alloy systems, specifically focusing on $Z3$-type Fe–Pd–In and $L1_0$-type Pt-based alloys. We explored how inter-element miscibility and chemical ordering can be manipulated to stabilize unexplored crystal phases. All first-principles calculations were performed using the OpenMX code [1].

We first explored the kinetic aspects of $Z3$-type phase formation in the Fe–Pd–In system by calculating atomic diffusion barriers [2]. Experimental results indicated that the formation temperature of the $Z3$ structure depends significantly on the initial precursor (e.g., $FePd_3$:In vs. $PdIn_x$:Fe). Our calculation results using Matlantis [3] and DFT clarified that this difference originates from the varying activation energy barriers of atomic diffusion, which are governed by the inter-element miscibility between Fe, Pd, and In. Specifically, the repulsion between Fe and In atoms creates high energy barriers along certain diffusion paths, dictating the non-equilibrium process of phase transition. These findings suggest that diffusion pathway design is essential for the synthesis of complex intermetallic nanoparticles.

Next, we investigated the effect of Zinc (Zn) addition on the ordering and catalytic performance of $L1_0$-type Pt-based alloys for the oxygen reduction reaction (ORR) [4]. The calculations demonstrated that Zn effectively lowers the disorder-to-order transition temperature, allowing for the formation of highly ordered $L1_0$ phases at lower temperatures. This mechanism is crucial for maintaining a small particle size while achieving a high degree of chemical order. Furthermore, we showed that the surface strain induced by Zn–Pt coordination optimizes the adsorption energy of oxygen-containing species, thereby enhancing the ORR activity and durability.

References

[1] T. Ozaki, *Phys. Rev. B*, **67**, 155108 (2003); http://www.openmx-square.org

[2] K. Matsumoto, *et. al.*, *Chem. Sci.*, **16**, 18705-18712 (2025).

[3] S. Takamoto, *et al*., Nat Commun 13, 2991 (2022); https://matlantis.com/

[4] W. Tian, *et. al.*, *J. Mater. Chem. A*, **14**, 7552-7562 (2026).

Materials design for interfacial spin-orbitronics

Kohji NAKAMURA

Graduate School of Engineering, Mie University, Tsu Mie 5148507

Search of materials with desired magnetic properties is an important issue in the field of spintronics. Two examples are presented related this proposal by using full-potential linearized augmented plane-wave (FLAPW) method.[1]

Rashba effect at magnetic tunnel junction interface Fe/MgO: At the Fe/MgO interface in magnetic tunnel junctions (MTJs), a sharp electrostatic potential gradient results in the breaking of inversion symmetry of the system and gives rise to the Rashba-type spin–orbit coupling. Based on FLAPW method, this coupling is found to govern voltage-controlled magnetic anisotropy (VCMA) of MgO-based MTJs. The Rashba splitting, arising from the asymmetric character of wavefunction along the out-of-plane direction, is driven by orbital admixture between the intra-atomic *d* and *p* orbitals at the interfacial Fe near the Fermi energy, together with hybridization with O *p* orbitals. The study further predicts that interfacial modification by AlN/MgO and LiF/MgO, enhancing the VCMA coefficient by 60% for the former, while reducing 15% for the latter than that of the pristine Fe/MgO model.

Magnon in antiferromagnetic insulator NiO: Magnetic interactions in an antiferromagnet govern the spin moment carried by magnons and the strength of multimagnon interactions that lead to magnetization relaxation. A numerical method to generate a four-magnon interactions Hamiltonian by fourth-rank tensor was here developed, and applied to an antiferromagnetic insulator NiO where magnetic dipolar interactions (MDIs) have non-negligible effects on the magnon states. First, we confirmed the suppressed magnon spin moment of two magnon modes, α and β modes, owing to non-spin-conserving interactions of the MDIs. Second, by expressing the four-magnon scattering probability in the fourth-rank tensor form, we found that the low magnon decay rates of both magnon modes are mainly caused by the suppressed magnon spin moment.

References

[1] K. Nakamura et.al., Phys. Rev. B **67**, 014420 (2003).

Theoretical Study Aiming at Novel Renewable Energy Materials Using First-Principles Calculations

Azusa MURAOKA

Department of Mathematics, Physics and Computer Science,

Japan Women's University, 2-8-1, Mejirodai, Bunkyo-ku, Tokyo 112-8681

Perovskite solar cells are promising next-generation photovoltaic materials because of their high-power conversion efficiency and low-cost fabrication [1]. However, Pb-based perovskites raise toxicity concerns [2]. Sn-based perovskites are attractive Pb-free alternatives, but their performance and stability are limited by Sn(II) oxidation to Sn(IV), self-p-doping, and defects such as Sn vacancies [3]. In this study, DFT calculations were used to investigate Sn single perovskites, $FASnI_3$ and $MASnI_3$, and Sn/Ge double perovskites, FA_2SnGeI_6 and MA_2SnGeI_6.

The ISSP Supercomputer System was used mainly for parallel first-principles calculations with VASP at the PBE-D3 level [4,5]. The computational resources were used to perform structural optimizations, electronic-structure calculations, and a large number of defect calculations using 2×2×2 supercells for the four target perovskite systems.

The calculated band gaps of $FASnI_3$, $MASnI_3$, FA_2SnGeI_6, and MA_2SnGeI_6 were 0.60, 0.70, 0.57, and 0.89 eV, respectively, and all were direct-gap semiconductors. The valence-band edge was mainly composed of iodine p orbitals, while Ge contributions became important at the conduction-band edge in the double perovskites, especially in FA_2SnGeI_6. The effective-mass analysis showed that FA-based systems have more favorable carrier transport than MA-based systems. In addition, partial substitution of Sn with Ge balanced the electron and hole effective masses while maintaining strong optical absorption, suggesting improved carrier transport without loss of light-harvesting ability. Chemical-potential analysis showed that iodine-rich conditions promote formation of SnI_4, corresponding to oxidation from Sn(II) to Sn(IV). This explains the intrinsic instability of Sn-based perovskites under iodine-rich or oxidative environments. $FASnI_3$ showed a narrower stability region than $MASnI_3$, indicating that FA-based tin perovskites require careful control of growth conditions. For the Sn/Ge double perovskites, the chemical-potential ranges were estimated from overlapping Sn and Ge single-perovskite stability regions.

As shown in Figure 1, defect formation strongly depends on growth conditions. Under Sn-poor/I-rich conditions, acceptor-type defects

such as I_{Sn} and V_{Sn} show low formation energies. These defects are related to tin loss and Sn oxidation and can promote self-p-doping and carrier trapping. In contrast, Sn-rich/I-poor conditions increase their formation energies, reducing stable in-gap trap levels. Thus, chemical-environment control is essential for improving defect tolerance.

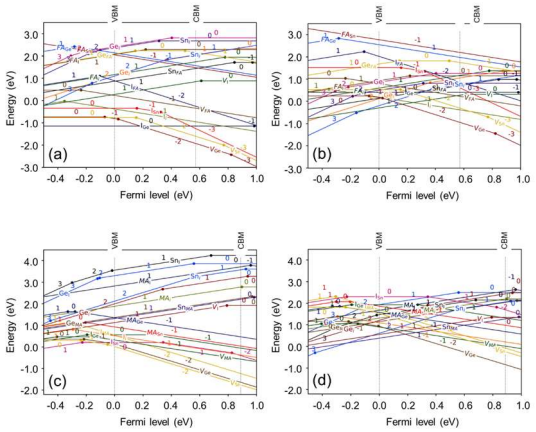

Fig 1: Defect formation energies of Sn/Ge double perovskites calculated using the PBE-D3 level: FA_2SnGeI_6 under (a) Sn-poor/I-rich and (b) Sn-rich/I-poor conditions, and MA_2SnGeI_6 under (c) Sn-poor/I-rich and (d) Sn-rich/I-poor conditions.

Across all four compositions, I_{Sn} and V_{Sn} were the dominant low-energy defects. In $FASnI_3$, stable in-gap defect levels appeared under Sn-poor/I-rich conditions, whereas $MASnI_3$ showed no thermodynamically stable in-gap levels within the examined limits. The Sn/Ge double perovskites also showed Sn-related defect levels under Sn-poor/I-rich conditions. HSE06 calculations confirmed the same qualitative trend as PBE-D3: I_{Sn} remained the lowest-energy defect, followed by V_{Sn}.

Overall, by using the ISSP Supercomputer System to complete many independent supercell defect calculations and selected hybrid-functional calculations, this study showed that low-energy tin-loss defects, especially I_{Sn} and V_{Sn}, are the microscopic origin of poor stability in Sn-based perovskites. Ge alloying improves carrier-transport balance while maintaining strong absorption, but Sn-related defects remain important. Therefore, combining Sn/Ge alloying with Sn-rich and I-poor growth conditions is a promising strategy to suppress deep traps, mitigate Sn oxidation, and improve the defect tolerance of Pb-free perovskite solar-cell absorbers.

References

[1] A. K. Jena, A. Kulkarni and T. Miyasaka, Chem. Rev. **119**, 3036 (2019).

[2] J. Li, H. L. Cao, H. L, W. B. Jiao, Q. Wang, M. Wei, I. Cantone, J. Lü and A. Abate, Nat. Commun. **11**, 310 (2020)

[3] D. Meggiolaro, D. Ricciarelli, and A. A. Alasmari, J. Phys. Chem. Lett. **11**, 3546 (2020).

[4] Kresse, G.; Furthmüller, J. Phys. Rev. B. **54**, 11169 (1996).

[5] J. P. Perdew, K. Burke, M. Ernzerhof, Phys. Rev. Lett. **77**, 3865 (1996).

Microscopic Structure and Proton Dynamics at Methanol/CeO_2 Interfaces

Akira NAKAYAMA
Department of Chemical System Engineering,
The University of Tokyo, Tokyo 113-8656, JAPAN

1. Introduction

Interfaces between metal oxides and alcohols are central to heterogeneous catalysis, including CO_2 conversion reactions over CeO_2. At such interfaces, alcohol molecules can undergo molecular and dissociative adsorption, and the resulting methoxy and hydroxyl species participate in proton-transfer processes. Because these reactions involve bond breaking and formation in a fluctuating liquid environment, conventional force fields are not sufficient. In this study, we constructed neural network potentials (NNPs) trained on density functional theory (DFT) data and performed nanosecond-scale molecular dynamics (NNP-MD) simulations of liquid methanol on CeO_2(111) and CeO_2(110) surfaces.

2. Results and Discussion

The NNPs were trained using DFT-MD data generated with CP2K and DeePMD-kit, and production NNP-MD simulations were carried out with LAMMPS at 300 K for 5 ns using large *p*(8×8) surface models. The simulations revealed clear facet-dependent adsorption equilibria. On CeO_2(111), methanol formed a well-ordered interfacial monolayer. Approximately 79% of the surface Ce sites were coordinated by methanol-derived species, while only 24% were coordinated by dissociated methoxy species, even though single-molecule DFT adsorption energies favor dissociation. This indicates that collective hydrogen-bonding interactions in the dense adlayer stabilize molecular adsorption. In contrast, CeO_2(110) showed weaker interfacial ordering and a larger degree of dissociation, with about 60% of surface Ce sites coordinated by methoxy species and 47% by molecular methanol.

Frequent proton hopping events were observed at both interfaces. The dominant pathway was direct adlayer proton transfer between adsorbed methanol and methoxy species, whereas solvent-assisted pathways involving additional methanol molecules were much less frequent. On CeO_2(110), proton hopping exhibited strong directional anisotropy reflecting the surface geometry. These results demonstrate that the surface facet and the collective structure of the adsorbed methanol layer jointly control dissociation equilibria and proton mobility at alcohol/CeO_2 interfaces. This work provides microscopic insight relevant to CeO_2-catalyzed alcohol activation and CO_2 conversion reactions.

Software used

CP2K was used for DFT and DFT-MD calculations, DeePMD-kit was used to construct neural network potentials, PLUMED was used to apply wall potentials during training-data generation, and LAMMPS was used for production NNP-MD simulations.

References

[1] Sakaguchi, C.; Ikeda, T.; Nakayama, (in revision).

Challenge of *in-silico* design for negative-thermal-expansion materials: $KNbSi_2O_7$

Yasuhide MOCHIZUKI

Department of Materials Science and Engineering,

Institute of Science Tokyo, Ookayama, Meguro-ku, Tokyo 152-8550

Negative thermal expansion (NTE) materials, whose lattice constant or volume shrinks upon heating, are essential for applications such as heat-resistant fillers, microdevices in light-emitting diodes (LEDs), large-scale integration (LSI), power semiconductors, and micropositioners in telescopes [1]. Despite over a century of intensive study, the rational design of NTE materials remains a challenging research topic. How can we design an NTE material?

In the previous reports, it has been empirically shown that larger average atomic volume (AAV) tends to yield NTE behavior, indicating that the framework structure with large AAV is expected to possess an NTE behavior. Alkali-metal ions have a large ionic radius compared to other cations. Particularly, inserting K and Rb into the framework structure is expected to increase the AAV (Figure 1a), consisting of corner-sharing octahedral and tetrahedral coordination structures. A material that has these characteristics is NASICON (Na Super Ionic CONductor) family: $AZr_2(PO_4)_3$ (*A* = Li, Na, K, and Rb), in which ZrO_6 octahedra and PO_4 tetrahedra are corner-sharing, and as the *A*-site atoms become larger, the volumetric thermal expansion switches from positive to negative. Note that $KZr_2(PO_4)_3$ has negative volumetric coefficient of thermal expansion (CTE), whereas $NaZr_2(PO_4)_3$ has the positive volumetric CTE. Based on the aforementioned perspective, we have selected Nb, generally forming octahedral coordination, and Si, usually forming tetrahedral coordination. Given that inserting K into the crystal structure (Figure 1b),

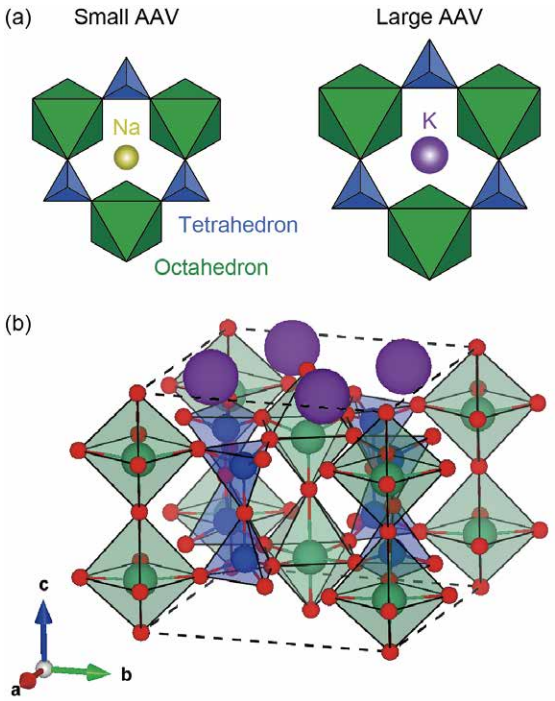

FIG. 1. (a) Perspective to design an NTE material. (b) Crystal structure of $KNbSi_2O_7$.

we have extracted $KNbSi_2O_7$ (KNSO), which we expect to show NTE, from Materials Project by searching for K-Nb-Si-O composition.

We have calculated the equilibrium lattice constants of KNSO from the molecular-dynamics (MD) calculations using the machine-learning force field (MLFF) in the range 100–800 K, indicating its biaxial NTE behavior. Then, we have prepared polycrystalline KNSO by a solid-state reaction method, and experimentally observed the temperature-dependent XRD patterns, which indicate the biaxial NTE behavior of KNSO.

As a result of the MD calculations, KNSO has been predicted to exhibit the NTE behavior in the *a*- and *b*-axes (Figure 2a), whereas the PTE behaviors are predicted in the *c*-axis (Figure 2b) and volume (Figure 2c). The calculated CTE from the MD calculations were found to be –2.3 ppm/K in the *a*-axis, 20.0 ppm/K in the *c*-axis, and 11.4 ppm/K in the volume at room temperature (300 K). Then, we also prepared a polycrystalline sample of KNSO by the solid-state reaction method using Nb_2O_5, KNO_3, and SiO_2 powders as starting materials. From the temperature-dependent XRD patterns, we have also derived the lattice constants of KNSO over the temperature range 303 K to 673 K, as shown in Figure 2d–2f [2]. The experimentally observed linear CTEs of *a*- and *c*-axis at 300 K are –2.3 ppm/K and 20.0 ppm/K, respectively. The experimentally observed

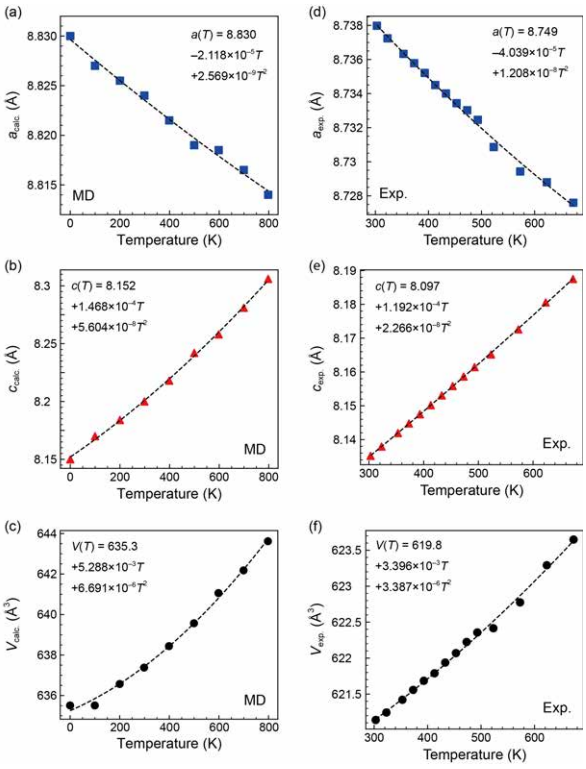

FIG. 1. (a–c) Calculated temperature dependences of (a) *a*- and (b) *c*-lattice constants, and that of (c) unit cell volume of $KNbSi_2O_7$ at equilibrium states in the relevant temperature using the MD calculations. (d–f) Experimentally observed temperature dependences of (a) *a*- and (b) *c*-lattice constants, and that of (c) unit cell volume. in the relevant temperature for KNSO.

volumetric CTE at 300 K is 11.4 ppm/K. We can see that the computationally predicted CTEs are well compatible with the experimental values.

References

[1] Y. Mochizuki et al., J. Phys. Chem. C **128**, 525 (2024).

[2] H. Koiso and Y. Mochizuki et al., J. Phys. Chem. C **129**, 9509 (2025).

Design and Understanding of the Activity and Stability of Promising CO_2 Reduction Electrocatalysts via Precise Catalysis Theory and AI
Precise Catalysis Theory and AI

HAO LI

Advanced Institute for Materials Research (WPI-AIMR),

Tohoku University, Sendai, 980-8577

We have studied the development of new catalytic theories and AI-assisted models, as well as the design of effective catalysts for CO_2 reduction reactions, by integrating precise theoretical models, high-level computations, machine learning (ML), and experimental validation.

This year, we utilized supercomputing resources to perform high-throughput density functional theory (DFT) calculations and ab initio molecular dynamics (AIMD) simulations to provide predictive insights into the activity, selectivity, and stability of CO2 reduction electrocatalysts. This integrated computational framework enables us to understand how magnetic properties affect catalytic behavior in two-dimensional transition-metal-based catalysts, making it possible to identify promising materials with improved CO2RR performance efficiently. Beyond this, high-throughput screening and data-driven analysis were employed to establish quantitative correlations between magnetic features and catalytic activity, thereby accelerating the discovery of advanced catalysts. Leveraging the synergy between physics-based insights and data-driven methods, we aim to develop catalysts that are not only highly active and selective but also robust for long-term operation. Through this integrated approach, the work presented here outlines a path toward optimizing CO_2 electro-reduction catalysts and demonstrates the broader potential of combining fundamental theory with cutting-edge computational strategies.

During the project period, **76 papers** were published in leading journals, including JACS, Angew. Chem., Nature Commun., etc., under this ISSP supercomputer support. Some notable works will be discussed in the following:

1. Closed-Loop Framework for Discovering Stable and Low-Cost Bifunctional Metal Oxide Catalysts for Efficient Electrocatalytic Water Splitting in Acid (JACS; Hao Li as the Last and Corresponding Author)

In this work, we developed a closed-loop framework integrating catalyst exploration, synthesis and electrochemical testing, and advanced characterization to identify stable and

low-cost metal oxide catalysts for acidic water splitting. By combining data mining, surface state analysis, microkinetic modeling, and proof-of-concept experiments, we identified RbSbWO6 as a promising bifunctional catalyst for acidic OER and HER. Experimental results confirmed its excellent stability and performance, surpassing many reported non-noble stoichiometric metal oxides without major modification. This study highlights the effectiveness of our DigCat-based data-driven workflow as a powerful strategy for accelerating electrocatalyst discovery.

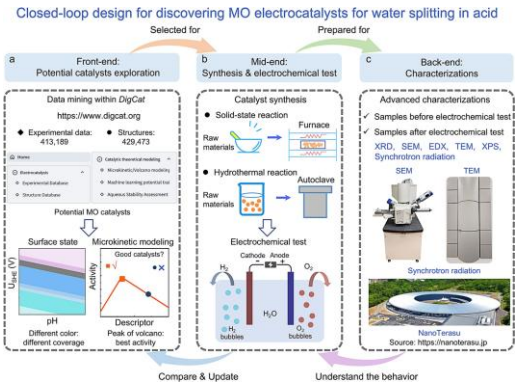

Fig. 1. Closed-loop design for discovering non-noble MO electrocatalysts for water splitting.

2. C60 Fullerene as the Active Site for CO2 Electroreduction (Angewandte Chemie; Hao Li as the Last and Corresponding Author)

we integrate large-scale data mining (with >2,300 CO2RR catalysts from available experimental literature during the past decade), ab initio computations, ML force field accelerated molecular dynamic simulations, and pH-field coupled modelling to unravel their pH dependence. We reveal a fascinating contrast: the electric field response of the binding strength of *OCHO on Sn−N4−C and polyatomic Sn exhibits opposite behaviors due to their differing dipole moment changes upon *OCHO formation. Such response leads to an intriguing opposite pH-dependent volcano evolution for Sn−N4−C and polyatomic Sn.

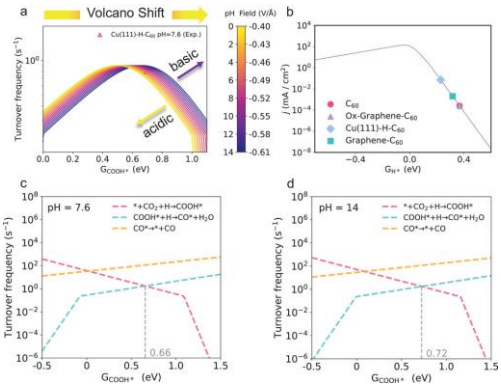

Figure 2. pH-dependent microkinetic CO2RR volcano models at the RHE scale and rate-determining analysis of C60-based catalysts

References

[1] X. Jia, Z. Zhou, F. Liu, T. Wang, Y. Wang, D. Zhang, H. Liu, Y. Wang, S. Ye, K. Amezawa*, L. Wei*, and H. Li*, Journal of the American Chemical Society, 2025, 147, 22642–22654.

[2] S.-W. Ying, Y. Wang, P. Du, Q. Wang*, C. Yue, D. Zhang, Z.-C. Chen, J.-W. Zheng*, S.-Y. Xie*, and H. Li*, Angewandte Chemie International Edition, 2025, 64, e202511924.

Investigation of polarization switching in Li_2GeO_3

Sou YASUHARA

School of Materials and Chemical Technology,

Institute of Science Tokyo, Ookayama, Meguroku, Tokyo 152-8550

Since the discovery of ferroelectricity in Sc-doped AlN in 2019,[1] wurtzite-type materials have attracted significant attention. Exploring new wurtzite-type structures is essential for understanding the mechanisms of polarization switching. In the previous fiscal year, we focused on $LiGaO_2$[2, 3] and evaluated the energy changes associated with single-ion motions.

In this year, we extended our research to Li_2GeO_3, which possesses a similar crystal structure. Our objective was to investigate the polarization switching pathways and energy barriers more accurately using the Nudged Elastic Band (NEB) method and to examine the effects of various element substitutions on the switching characteristics.

First-principles calculations were performed using the projector augmented wave (PAW) method as implemented in the VASP. The PBEsol-type generalized gradient approximation (GGA) was utilized as the exchange-correlation functional. The k-point mesh was 8×8×8. The cutoff energy and convergence energy were 550 eV and 1.0×10^{-7} eV, respectively. The NEB method was employed to identify the minimum energy path and calculate the activation energy for polarization switching in Li_2GeO_3.

Calculations result of the NEB method for Li_2GeO_3 polarization switching was shown in Fig. 1. The activation energy of Li_2GeO_3 is lower than that of $LiGaO_2$, suggesting that Li_2GeO_3 is more favorable for polarization switching. Additionally, the effects of elemental substitution about 20 patterns were investigated, revealing that and (Mn, Y) co-substitution is the most effective for achieving the switching.

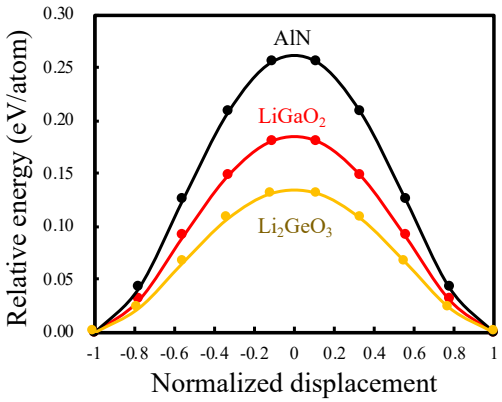

Fig. 1 Relative energy during polarization switching of AlN (black), $LiGaO_2$ (red) and Li_2GeO_3 (yellow).

References

[1] S. Fichtner *et al.*, J. Appl. Phys. **125**, 114103 (2019). [2] S. Yasuhara *et al.*, RSC adv. **14**, 13900 (2024). [3] S. Yasuhara *et al.*, J. J. Appl. Phys. **64**, 08SO02 (2026).

Topological surface state in RuO_2

Kunihiko YAMAUCHI

Center for Spintronics Research Network, Osaka University, Toyonaka, Osaka 560-8531, Japan

We have studied the electronic structure of RuO_2, a candidate altermagnetic material, by means of first-principles calculations, focusing on the origin of surface-dependent states observed in recent ARPES measurements. The calculations were performed within density functional theory as implemented in VASP, adopting the generalized gradient approximation.

The calculated bulk band structure is dominated by Ru-*4d* states near the Fermi level and shows good agreement with ARPES results, supporting a nonmagnetic description without clear spin splitting. In particular, the absence of sizable band splitting is consistent with a spin-degenerate picture of the bulk states.

To investigate the surface electronic structure, we constructed Wannier-based tight-binding models using Wannier90 and computed surface spectral functions for different crystallographic terminations. The calculations reveal surface-dependent states whose dispersion and intensity vary depending on the surface orientation.

These surface states are found to originate from bulk Dirac nodal lines inherent to the rutile crystal structure of RuO_2. The nodal-line topology leads to spin-polarized nontrivial surface states appearing near the Fermi level, providing a natural explanation for the surface-dependent features observed in ARPES as shown in Figure.[1]

We are also pursuing several research directions aimed at potential spintronics applications.[2, 3]

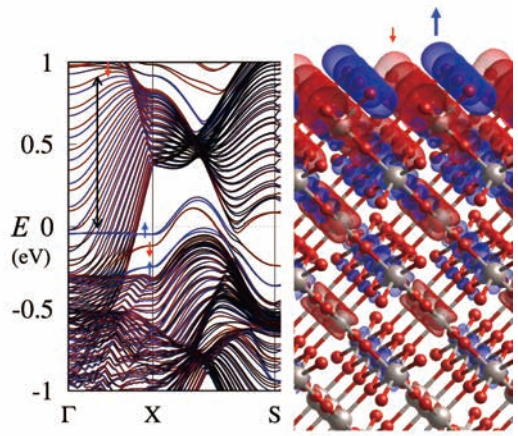

Figure: Topological surface bands (left) and the spin density (right) in nonmagnetic RuO_2.

References

[1] T. Osumi, K. Yamauchi, S. Souma, *et al.*, Phys. Rev. B **113**, 085116/1-18 (2026).

[2] T. P. T. Nguyen and K. Yamauchi, arXiv: 2603.29202 (2026).

[3] K. Yamauchi and T. Oguchi, arXiv: 2604.04557 (2026).

Mechanism of fast ion conductivity

Osamu SUGINO

Institute for Solid State Physics,

The University of Tokyo, Kashiwa-no-ha, Kashiwa, Chiba 277-8581

We have studied the hydride-ion (H^-) conduction mechanism in a K_2NiF_4-type Ba–Li oxyhydride, $Ba_{1.75}LiH_{2.7}O_{0.9}$ (BLHO), using the System B of the ISSP supercomputer. Density functional calculations and first-principles molecular dynamics (FPMD) simulations were conducted using Quantum ESPRESSO and VASP, respectively. BLHO had been synthesized by some of the collaborators as the first H^--based conducting material whose conduction mechanism had not been elucidated.

We modeled the disordered phases of BLHO using supercells $Ba_{56}Li_{32}H_{88}O_{28}$, $Ba_{57}Li_{32}H_{90}O_{28}$, and $Ba_{58}Li_{32}H_{90}O_{29}$, which successfully reproduced experimental data on electronic structures and diffusion coefficients. The Lindemann index of H atoms exceeds the threshold (0.1) for a solid–liquid transition at temperatures above 700 K, which provides theoretical evidence for sublattice melting of the H^- equatorial sites.

Fast conducting behavior of H^- was analyzed using the descriptor called rearrangement indicator (RI), which allows us to distinguish slow atomic motion from fast vibrational motions. The analysis revealed a highly cooperative diffusion mechanism, typical of supercooled liquids.

H^- ions transiently form a string-like cluster consisting of several ions. The tendency to form clusters is suggested to reduce the activation energy of ion diffusion, as was found for superionic conductors like PbF_2, but the tendency looks stronger for BLHO presumably due to densely populated Ba and H vacancies contained in this material.

Fast diffusion is known generally related to glass property of materials. The elucidation of diffusion from the perspective of glassy properties is a key target for our future studies, which we plan to pursue using machine learning potentials.

O. Sugino, "Statistical Mechanics of Atomic Diffusion via Machine Learning Potentials," Project Proposal 2025-Ca-0064 (2025).

References

[1] J. Haruyama, F. Takeiri, G. Kobayashi, and O. Sugino, "Elucidation of superionic conduction in K_2NiF_4-type Ba–Li oxyhydride from a first-principles molecular dynamics study," J. Mater. Chem. A, 14, 8332 (2026).

First principles study of germanene superstructures on Ag(111)

Yuji Hamamoto

Department of Communication Engineering,

Okayama Prefectural University, Kuboki, Soja, Okayama 719-1197

Germanene, a germanium analog of graphene, is important not only as a potential two-dimensional topological insulator but also for applications due to its higher compatibility with existing semiconductor technology. Recently, Ge atoms segregated through an Ag(111) thin film on Ge(111) were shown to form a two-dimensional Ge sheet [1]. Unlike freestanding germanene with an alternating buckled structure, this sheet exhibits a nontrivial $7\sqrt{7} \times 7\sqrt{7}$ superstructure on Ag(111), making structure determination by first-principles calculations computationally demanding.

To investigate the geometrical and electronic structures of germanene on Ag(111), we here performed first-principles calculations of the $7\sqrt{7} \times 7\sqrt{7}$ superstructure based on the recently proposed structural model [2], which consists of 332 Ge atoms and 1029 Ag atoms. Large-scale parallel computing enabled us to obtain the relaxed structure of the system, as shown in Fig. 1, which includes five- and seven-membered rings in the Ge sheet, unlike the naïve honeycomb model suggested in Ref. [1]. We also analyzed the electronic structure, especially derived from the Ge layer, by performing band structure unfolding [3] and projection onto the region where the Ge layer exists.

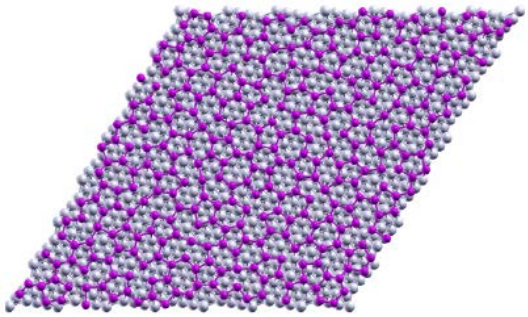

Fig. 1: Relaxed structure of the $7\sqrt{7} \times 7\sqrt{7}$ superstructure of germanene on Ag(111). Pink and gray balls represent Ge and Ag atoms, respectively.

References

[1] J. Yuhara et al., ACS Nano **12**, 11632 (2018).

[2] K. Zhang et al., ACS Nano **17**, 15687 (2023).

[3] V. Popescu and A. Zunger, Phys. Rev. B **85**, 085201 (2012).

Structure search for planar silicene on Au(111) thin films based on Gaussian process regression

Yuji Hamamoto

Department of Communication Engineering,

Okayama Prefectural University, Kuboki, Soja, Okayama 719-1197

Silicene, a silicon analog of graphene, is important not only as a potential two-dimensional topological insulator but also for applications due to its higher compatibility with existing semiconductor technology. Recently, Si atoms segregated through an Au(111) thin film on Si(111) were shown to form a two-dimensional Si sheet [1]. Intriguingly, scanning tunneling microscopy revealed a planar honeycomb pattern, unlike the theoretically predicted buckled structure of freestanding silicene. Although angle-resolved photoemission spectroscopy suggested a Dirac-cone-like linear dispersion at the Γ point, its origin remains unclear due to the unresolved structure of the Si sheet.

Expanding the machine-learned structure search for silicene on the Ag(111) surface [2], we here searched for stable structures of Si sheets formed on Au thin films using GOFEE [3], which accelerates structure search by leveraging the energy landscape predicted by a Gaussian process trained on the fly during the search. Our results revealed that silicene formed on a pristine Au thin film is not rotated with respect to Si(111), whereas that on an Au thin film doped with an Si atom is rotated by 21.8 degrees, in good agreement with low-energy electron diffraction measurements. This suggests that the Au thin film underlying silicene is slightly silicified by segregation of Si atoms, consistent with the fact that Au forms a silicide more easily than Ag. Although silicene formed on such a doped Au thin film is significantly buckled, it has also been found that a more planar structure can be obtained by introducing lattice vacancies into the honeycomb lattice, as shown in Fig. 1.

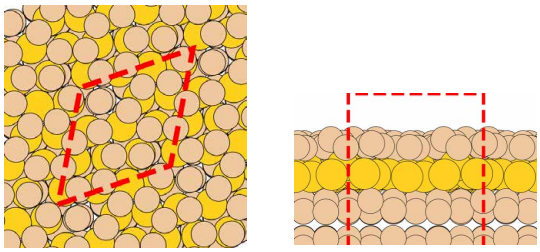

Fig 1: Stable structure of Si sheet on a Au thin film obtained by the structure search.

References

[1] A. Stępniak-Dybal et al., Adv. Funct. Mater. **29**, 1906053 (2019).

[2] Y. Hamamoto et al., Phys. Rev. Materials 7, 124002 (2023).

[3] M. Bisbo and B. Hammer, Phys. Rev. Lett. **124**, 086102 (2020).

Investigating the Role of Oxidation in Amorphous TeO_2 Properties from First Principles

Rafael COSTA-AMARAL

Institute for Materials Research, Tohoku University, 2-1-1 Katahira, Aoba-ku, Sendai, 980-8577, Japan

Introduction

Amorphous oxide semiconductors are attractive for large-area and low-temperature electronics, but high-mobility p-type counterparts remain rare because O-2p-derived valence states are usually deep and localized. Motivated by recent experimental reports of unusually high hole mobilities in oxygen-deficient amorphous tellurium oxides (*a*-TeO_x), this study [1] aimed to clarify how oxygen deficiency reorganizes the amorphous network, which defects supply holes, and how network connectivity controls transport. These questions require atomistic modeling of disordered structures across multiple compositions together with accurate defect and electronic-structure calculations, making large-scale use of the ISSP supercomputer essential.

Computational Methods

First-principles calculations were performed with the Vienna Ab initio Simulation Package (VASP) within density functional theory using the projector augmented-wave method. Models of *a*-TeO_x spanning x = 0.0-2.0, including the experimentally relevant x = 1.2 composition, were generated by melt-quench molecular dynamics. To make large-cell sampling tractable, the quench simulations were accelerated by an on-the-fly machine-learning force-field workflow in VASP. The resulting structures were relaxed and Hybrid-functional calculations were then used to evaluate electronic structure. Bader charge analysis was used to distinguish tellurium atoms between oxidized Te^{4+} and reduced Te^{0}.

Results and Discussion

The calculations show that oxygen deficiency in *a*-TeO_x drives spontaneous nanoscale segregation into interpenetrating Te-rich and oxide-rich amorphous domains, which play distinct and complementary roles in transport. Te vacancies located in oxide-like or interfacial environments act as the dominant source of holes, whereas hole transport itself is mediated by connected Te-5p states within the Te-rich subnetwork. Thus, carrier generation and carrier transport originate from different structural motifs.

Further lowering the oxygen content expands

the Te-rich network and improves the connectivity of transport-supporting pathways. This compositional trend strengthens the link between oxygen deficiency, nanoscale phase segregation, and hole transport, and shows that control of oxygen content provides a practical route to tuning the electronic functionality of *a*-TeO_x.

Our results demonstrate the value of combining machine-learning-accelerated molecular dynamics with hybrid-functional electronic-structure calculations for disordered materials. In addition, we provide a physically consistent explanation for the high hole mobility reported experimentally in oxygen-deficient *a*-TeO_x films, establishing a basis for the rational design of defect-engineered amorphous semiconductors.

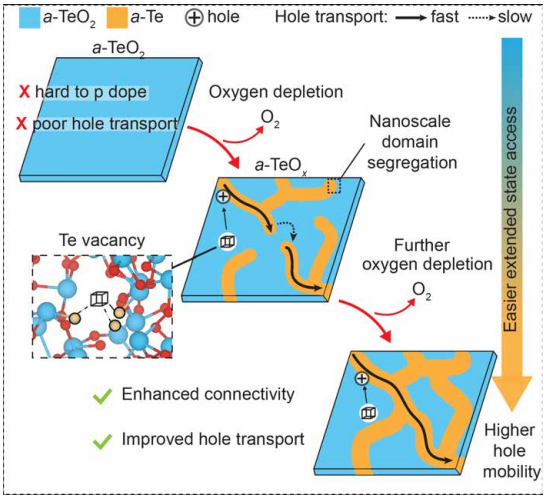

Figure 1. Oxygen deficiency modify nanoscale connectivity and transport pathways for holes in amorphous tellurium oxide.

References

[1] R. Costa-Amaral and Y. Kumagai, "Oxygen-deficiency-driven phase segregation enables enhanced hole transport in amorphous tellurium oxides," submitted to ***Chemistry of Materials***; preprint available as arXiv:2510.00473.

Understanding the Super High-Pressure Synthesis of Superhydride by Machine-Learning Potential MD Simulations

Ryuhei Sato

Department of Materials Engineering,

The University of Tokyo, 7-3-1 Hongo, Bunkyo-ku, Tokyo 113-8656, Japan

The realization of room-temperature superconductivity is considered one of the holy grails in physics. Polyhydrides with high hydrogen-to-metal (H/M) ratios are among the most promising candidates in terms of superconducting transition temperature (Tc). For instance, CaH_6 exhibits an exceptionally high Tc of 210 K at 160 GPa [1], suggesting that room-temperature superconductivity may be achievable through the exploration of ternary or quaternary compounds within this material class. However, the synthesis of such materials remains a significant challenge. As an example, although CaH_6 was theoretically predicted in 2010 [2], its experimental synthesis was not realized until nearly a decade later [1]. Thus, in addition to predicting stable structures and T_c values, it is crucial to identify feasible synthetic pathways and gain a fundamental understanding of the underlying reaction mechanisms.

In previous our study, machine learning potential molecular dynamics (MLP-MD) simulations successfully reproduced the synthesis of CaH_4 polyhydride [3]. Based on the observation, we constructed the thermodynamic model to explain how the superhydride synthesis is promoted under high pressure [3]. However, this thermodynamic model only shows the synthesis guideline of stable superhydride and there is no clear guideline to synthesize metastable superhydride phase. In this study, we conducted MLP-MD simulations of the $CaHx/H_2$ interface to seek for the synthesis route of metastable CaH_6 [4]. Note that the DFT training dataset (with over 0.15 million structures) calculations and all the MLP-MD simulations were performed in system B in ISSP supercomputer center.

MLP–MD simulations of the CaH_x/H_2 interface revealed two competing hydrogenation pathways [4]. One is the formation of the $CaH_{5.75}$ observed at high temperature (~1500 K; Fig. 1). Above ~100 GPa, hydrogen-rich phases such as CaH_{12}, in which Ca is incorporated into molecular hydrogen, become stable. Accordingly, Ca first dissolves into the H_2 phase. Upon supersaturation, heterogeneous nucleation occurs near the CaH_4/H_2 interface, leading to the formation of $CaH_{5.75}$. This phase grows

with time and becomes dominant after ~1 ns.

The second pathway is the formation of CaH_6 at the CaH_2/H_2 interface under 1000 K and 150 GPa (Fig. 2). Here, the less stable CaH_2 is used as a precursor under high pressure. Here, due to the relatively low temperature, significant Ca rearrangement is suppressed. As a result, a diffusionless, martensitic-like transformation occurs, resulting in the formation of CaH_6.

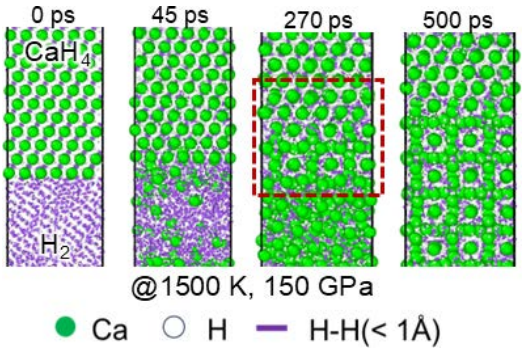

Fig. 1 $CaH_{5.75}$ synthesis at 1500K and 150GPa during MLP-MD for CaH_4/H_2 interface.

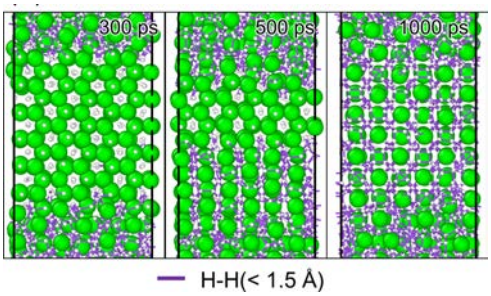

Fig. 2 CaH_6 synthesis at 1000 K and 150 GPa during MLP-MD for CaH_2/H_2 interface.

The competition between these pathways can be understood in terms of hydrogenation enthalpy and lattice similarity between precursors and products. Figure 3 shows the hydrogenation enthalpies of the superhydrides. $CaH_{5.75}$ is thermodynamically stable above 100 GPa, whereas CaH_6 is metastable over the entire pressure range. However, $CaH_{5.75}$ has a complex crystal structure, requiring substantial Ca diffusion and rearrangement from precursors such as Ca, CaH_2, and CaH_4 with hcp/fcc-like Ca lattices. Therefore, its formation is only observed at high temperature. In contrast, although CaH_6 is metastable, it possesses a bcc-like Ca lattice similar to these precursors, enabling formation via diffusionless transformation at lower temperatures.

These results demonstrate that MLP–MD simulations can capture competing hydrogenation pathways of superhydrides under extreme conditions, and that metastable phases can be selectively synthesized by controlling temperature and lattice compatibility between precursors and target structures.

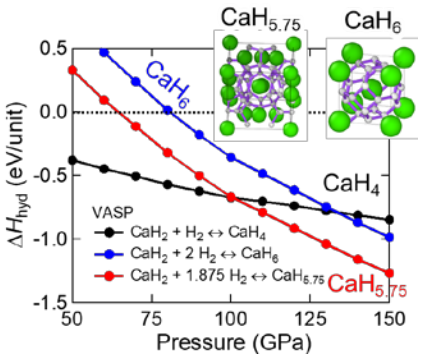

Fig. 3 Hydrogenation enthalpy of CaH_4, $CaH_{5.75}$, and CaH_6 obtained from DFT calculation as a function of pressure.

References

[1] H. Wang et. al. PNAS 109 (2012) 6463.
[2] L. Ma et. al. PRL 128 (2022) 167001.
[3] R. Sato et. al. PNAS 122 (2025) e2413480122.
[4] R. Sato et. al. arXiv (2026). DOI: 10.48550/arXiv.2603.08950

Improving Stability of Molecular Dynamics Simulation using Machine-Learning Interatomic Potentials II

Kohei Shimamura

Department of Physics,

Kumamoto University, 2-39-1 Kurokami, Chuo-ku, Kumamoto 860-8555

The development of machine-learning interatomic potentials (MLIPs) has enabled molecular dynamics (MD) simulations that retain the accuracy of first-principles molecular dynamics (FPMD) while significantly extending accessible time and length scales. In our previous work, we proposed the Potential Averaging (PA) method [1], an ensemble-learning-based approach in which multiple MLIPs are combined by averaging the predicted atomic forces. This approach improves robustness and provides a natural framework for uncertainty estimation through the variance of predicted forces. However, the stability of MD simulations using MLIPs, particularly for systems outside the training domain, remains an important challenge. In the present study, we continued our efforts to improve the stability of MD simulations by extending the PA method to a graph neural network (GNN)-based MLIP, namely the Allegro model [2].

A major focus of this year's work was the implementation of the PA method within the Allegro framework. Since Allegro is implemented in Python using PyTorch, whereas MD codes typically interface through C++ (e.g., via libtorch), careful modification of the interface layer was required. We successfully implemented the use of multiple Allegro models within the MD framework and confirmed that the PA method can be applied without altering the core structure of the Allegro model. This achievement ensures the portability of the approach across different MD codes.

The developed framework was tested using silver chalcogenide systems. We evaluated the stability of MD simulations as well as the accuracy of thermal conductivity calculated via the Green–Kubo method. The results demonstrate that the PA method improves the stability of simulations.

Overall, the project in FY2025 progressed steadily. The successful implementation of the PA method for the Allegro model and the initial development of computational optimization strategies represent important steps toward practical large-scale MD simulations using MLIPs.

References

[1] D. Wakabayashi, *et al.*: J. Phys. Soc. Jpn., **92**, 074002 (2023).

[2] A. Musaelian, *et al.*: Nat. Commun. **14**, 579 (2023).

Active Sites Evolution in Cu Catalysts: Insights from Machine Learning Molecular Dynamics

Harry H. Halim, M. Fadhlan Anshor, Syahrul Ramadhani, Asahi Morita, and Yoshitada Morikawa
Graduate School of Engineering, The University of Osaka

Results Report

We performed large-scale atomistic simulations to investigate Cu-based catalysts for CO_2 hydrogenation and the water–gas shift reaction (WGSR), using a combination of density functional theory (DFT), machine learning interatomic potentials (MLIPs), and multi-scale modeling techniques. The main objective was to elucidate dynamic catalytic behavior under realistic reaction conditions and to resolve the inconsistency between theory and experiment by bridging the pressure and materials gap.

Use of Supercomputer Resources

The supercomputer (ISSP system B and system C) was utilized for (i) first-principles DFT calculations, (ii) training of MLIPs via active learning, and (iii) large-scale molecular dynamics (MD) simulations.

DFT calculations were carried out to generate high-quality training datasets covering diverse surface configurations, adsorbate states, and reaction intermediates. These calculations were computationally demanding due to the need to sample high-coverage adsorbate configurations and reconstructed surface structures.

To overcome the limitations of DFT in terms of system size and simulation time, we employed MLIPs trained on the DFT dataset. The training process involved iterative active learning cycles, where new configurations were generated from MD simulations and selectively added to the dataset.

The MLIPs were trained using two machine learning frameworks: Gaussian Process regression within the Gaussian Approximation Potential (GAP) formalism (for the Water Gas Shift Reaction project), and Graph Neural Network (GNN) architectures (for H-induced surface reconstruction project) as implemented in Allegro. The training workflows were executed on high-performance computing systems, where DFT-generated datasets were iteratively refined via active learning, and model optimization was parallelized to handle diverse configurational spaces. Molecular dynamics simulations were performed using LAMMPS, while post-processing and analysis of atomic structures and trajectories were conducted using the Atomic Simulation Environment (ASE). This integrated workflow enables both high accuracy and computational efficiency in modeling complex catalytic systems.

Algorithmic Improvements and Efficiency

We neither developed nor improved the algorithms of the methods in this project. However, we implemented active learning strategy to build the MLIPs with more compact database while keeping the high accuracy. In particular, we applied committee method and further point sampling to select the most unique and relevant atomic structures to be included in the database.

Scientific Results

Figure 1 shows the time evolution of the lateral coordination number (LCN) of Cu atoms in Cu(100) at $T = 300$ K under different hydrogen coverages. As the coverage increases, the average coordination number shifts toward higher values, approaching LCN ~ 6. This indicates that hydrogen induces significant restructuring of the Cu surface, leading to the formation of three-fold hollow sites [1]. Such structural evolution is not accessible within static surface models and highlights the importance of capturing dynamic surface states under realistic conditions.

In the second project, we evaluated the impact of the formation of Cu clusters on the catalytic performance of the water gas shift reaction [2]. The turnover frequency (TOF) of the water–gas shift reaction (WGSR) is significantly enhanced for the surface with Cu clusters (Cu_n) compared to the flat Cu(111) surface. The calculated temperature dependence of TOF shows good agreement with experimental trends, confirming that dynamically formed clusters act as highly active catalytic sites.

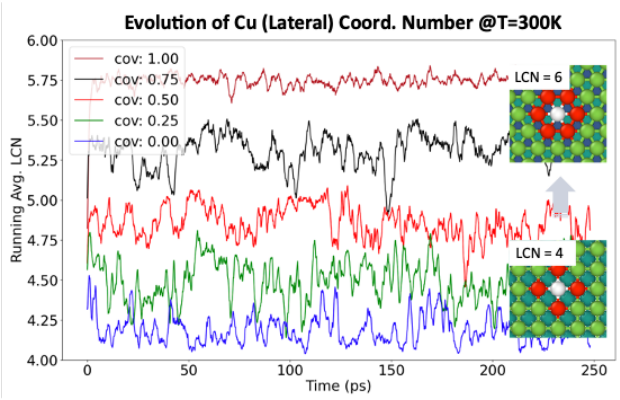

Figure 1: Time evolution of the lateral coordination number (LCN) of Cu atoms at $T = 300$ K under different adsorbate coverages. Increasing coverage leads to higher average coordination (LCN ~ 6), indicating adsorbate-induced surface restructuring and the formation of three-fold hollow sites.

Summary and Future Work

This project shows that MLIP-based simulations, combined with HPC resources, provide a framework for investigating complex catalytic systems beyond the limitations of conventional approaches. We will continue expanding the training dataset, incorporating kinetic Monte Carlo simulations for higher-scale modeling, and developing the inverse catalyst design.

List of Publications and Related Outputs

International Journal Publications:

- W. O. N. F. Rajaelo, H. H. Halim, M. F. Anshor, Y. Yamada, S. Ramadhani, F. A. Mubarok, S. E. M. Putra, A. L. Ivansyah, T. D. K. Wungu, Suprijadi, Y. Morikawa, and F. Muttaqien, "Bridging the Pressure Gap in Hydrogenation of CO_2 to Formate on Cu(100) by Machine Learning Molecular Dynamics and First-Principles Microkinetic Modeling," *ACS Catalysis* **16**, 5068–5079 (2026).
- M. F. Anshor, H. H. Halim, and Y. Morikawa, "CO Coadsorption Effects on Water–Gas Shift Reaction over Cu Clusters on Cu(111): Insights from Machine Learning Force Field and Microkinetic Modeling," *Phys. Chem. Chem. Phys.* (2026). In press.

Software Used:

- **First-principles calculations:** STATE, Quantum ESPRESSO
- **Machine learning potentials:** GAP, Allegro
- **MD simulations:** LAMMPS
- **Data analysis:** ASE (Atomic Simulation Environment)

Machine-Learning Molecular Dynamics for High-Pressure Hydride Synthesis and Superionic Transport

Kartik Sau

Advanced Institute for Materials Research (WPI- AIMR), Tohoku University, Sendai 980-8577, Japan

Two recent papers I worked on, both powered by AI-assisted atomic-scale simulations, ask very different questions but share the same trick: let a machine learn the rules of how atoms talk to each other, then watch what happens. One paper [1] catches hydrogen sneaking into a crystal at crushing pressures — a clue for the long hunt for room-temperature superconductors. The other [2] draws a kind of subway map of how ions go through next-generation battery materials.

Squeeze hydrogen hard enough and it slips inside metals to form "superhydrides" — exotic compounds that may one day carry electricity without losing a watt. The trouble is, even when theorists predict a winner, the lab can take a decade to actually make it. Why is the hydrogen so slow to get in? Our simulations caught the surface of a calcium hydride crystal doing something unexpected: instead of slowly soaking up hydrogen like a sponge, it briefly melts, swallows the gas as a liquid, then snaps back into a new crystal. Pressure doesn't just make the reaction possible — it greases the slide by stabilizing that fleeting liquid step. The takeaway is a simple rulebook for picking which materials are worth the effort: look for ones with a low melting point and a thermodynamic appetite for hydrogen under pressure.

The best solid battery materials don't move one ion at a time — their ions travel in packs, like commuters pushing through a crowded train. Spotting those coordinated dashes in a flood of simulation data has always been part science, part guesswork. We turned the problem into a network: every ion hop is an arrow, and arrows that land close together in space and time get linked, sketching a map of who pushed whom. The cutoffs aren't fudged — they fall out of the physics of the material itself. Tested on three very different battery candidates — a lithium sulfide, a sodium oxide, and an old silver iodide — the same map reveals the same kind of crowd dynamics, giving battery designers a clean way to ask: does this material's traffic actually flow?

References

[1] R. Sato, L. J. Conway, D. Zhang, C. J. Pickard, K. Akagi, K. Sau, H. Li, S. Orimo, Proc. Natl. Acad. Sci. U.S.A. 122 (22), e2413480122 (2025).

[2] R. Sato, Y. Ando, K. Sau, Y. Shibuta, Chem. Mater. 38 (1), 287–295 (2026).

Exploration of hydride superconductors

Takahiro ISHIKAWA
Department of Physics, The University of Tokyo
7-3-1 Hongo, Bunkyo-ku, Tokyo 113-0033

Lanthanum hydride (La-H) shows superconductivity at 260 K under 170 GPa [1, 2]. Recently, it has been suggested that the superconducting critical temperature (T_c) may further increase through repeated cooling and heating of the sample [3]. This enhancement has been speculated to originate from reactions between La-H and other materials present in the diamond anvil cell, such as nitrogen (N) and boron (B) from the hydrogen source (NH_3BH_3), and platinum (Pt), gold (Au), and gallium (Ga) from electrodes.

Assuming a reaction between La-H and Pt, we searched for thermodynamically stable phases in the La-Pt-H system at 20 GPa using a structure-search framework combining evolutionary algorithms (EA), density functional theory (DFT), and neural network potentials (NNPs) [4]. At each generation, a few thousand EA-generated structures were rapidly optimized using pre-trained NNPs calculations implemented in Matlantis [5], and several dozen low-enthalpy structures near the convex hull (CH) were further refined using DFT calculations with the Quantum ESPRESSO (QE) code [6] on the ISSP supercomputer. For the stable compounds, we estimated T_c using the Allen–Dynes formula [7]. Our results show that thermodynamically stable $LaPtH_6$ exhibits the highest T_c of 18.7 K at 20 GPa [8].

We also explored superconducting phases in another candidate system, La–N–B–H, at 20 GPa using a similar approach, and predicted ternary $LaBH_5$ (T_c = 29.0 K) and quaternary La_2NBH (T_c = 6.3 K). In addition, because the accuracy of pre-trained NNPs implemented in Matlantis may be limited in hydrogen-containing systems at pressures above 100 GPa, we are developing machine-learning potentials specifically for this quaternary system using an active learning scheme implemented in the GeNNIP4MD code [9] on the ISSP supercomputer.

References

[1] M. Somayazulu *et al.*: Phys. Rev. Lett. **122**, 027001 (2019).

[2] A. P. Drozdov *et al.*: Nature **569**, 528 (2019).

[3] A. D. Grockowiak *et al.*: Front. Electron. Mater. **2**, 837651 (2022).

[4] T. Ishikawa *et al.*: Phys. Rev. B **109**, 094106 (2024).

[5] Matlantis (https://matlantis.com/), software as a service style material discovery tool.

[6] P. Giannozzi *et al.*: J. Phys.: Condens. Matter **21**, 395502 (2009).

[7] P. B. Allen and R. C. Dynes: Phys. Rev. B **12**, 905 (1975).

[8] T. Ishikawa *et al.*: Phys. Scr. **101**, 105903 (2026).

[9] N. Matsumura *et al.*: J. Chem. Theory Comput. **21**, 3832 (2025).

Prediction of properties of organic ferroelectrics and piezoelectrics by first-principles calculation

Shoji ISHIBASHI
National Institute of Advanced Industrial Science and Technology (AIST)
Tsukuba, Ibaraki 305-8565

We have been searching for dielectric crystals composed of relatively small organic molecules that can be expected to exhibit multiple dipole moment arrangements due to proton displacement [1]. Here, two of the most recent examples 1,2-phenylenedipropiolic acid (PDPLA) and α,α'-dihydroxy-1,3-diisopyopylbenzene (DHIB), which have been discovered by data mining the Cambridge Structural Database, are shown.

The previously reported crystal structure of PDPLA assumed hydrogen disorder on the carboxyl group, but our re-examination reveals that PDPLA has a ferroelectric (FE) crystal structure where the hydrogen atoms are ordered (Fig. 1) [1]. To confirm the validity of the assignment, its relative stability against a few hypothetical antiferroelectric (AFM) forms is investigated by means of DFT calculations. As shown in Fig. 1, the FE form is the most stable. The calculated polarization value of 8.8 μC/cm^2 closely matches the measured value of 9 μC/cm^2.

As for DHIB, our reassessment reveals that the hydrogen atoms in the intermolecular hydrogen bonding are disordered (Fig. 2) [1]. We calculate and compare relative energies of one FE and two AFE forms (Fig. 2) and find that they are almost degenerate within 0.12 meV/molecule. The calculated polarization for the FE form (4.6 μC/cm^2) agrees well with the saturated polarization observed in the polarization-electric field (P-E) curve. Thus, the experimental and computational findings are consistent with each other.

All the calculations have been performed using the QMAS code.

References

[1] S. Horiuchi, H. Minemawari, J. Tsutsumi, and S. Ishibashi, Crystals **15**, 736 (2025).

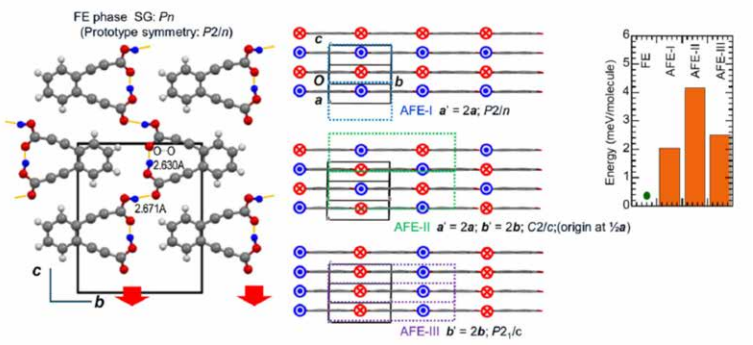

Figure 1: Crystal structure of PDPLA (left), arrangements of dipole moments in hypothetical AFE forms (middle), and relative energy comparison (right) (S. Horiuchi, H. Minemawari, J. Tsutsumi, and S. Ishibashi, Crystals **15**, 736 (2025), DOI: 10.3390/cryst15080736).

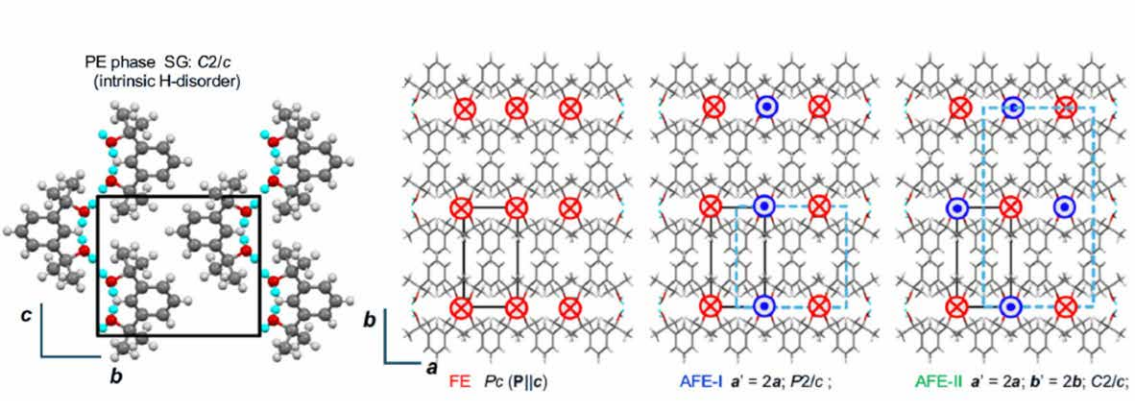

Figure 2: Crystal structure of DHIB (left) and arrangements of dipole moments in candidate FE and AFE forms (right) (S. Horiuchi, H. Minemawari, J. Tsutsumi, and S. Ishibashi, Crystals **15**, 736 (2025), DOI: 10.3390/cryst15080736).

First-principles study of surface atomic structure and chemical properties of intermetallic compounds

Kazuki Nozawa

Department of Physics and Astronomy, Kagoshima University,

1-21-35, Korimoto, Kagoshima 890-0065

In this fiscal year, we performed first-principles density functional theory (DFT) calculations to study the atomic-scale origin of the catalytic activity in the quasicrystal-related intermetallic compound $Al_{13}Fe_4$ and the applicability of cluster-based methods for molecular adsorption calculations on quasicrystal surfaces.

For $Al_{13}Fe_4$, we focused on the site-selective occupation behavior of trace transition metal additives [1]. Using the VASP code, we examined the substitution behavior of Rh and Ru atoms introduced into the monoclinic and orthorhombic phases of $Al_{13}Fe_4$. Calculations were performed for systems in which Rh or Ru was added at concentrations of approximately 1 at. % and 4 at. %, and the formation energies were evaluated by systematically substituting the additive elements into the crystallographically non-equivalent atomic sites. For the monoclinic phase, periodic bulk models consisting of 102 atoms were employed and calculated mainly on System B using flat MPI parallelization with 6 nodes (768 cores), while for the orthorhombic phase, 204 atom bulk models were used and calculated on System C with 2 nodes (256 cores). All calculations were performed using the VASP code within the generalized gradient approximation, and structural optimizations were performed to evaluate the relative stability of the substituted structures.

In addition, we studied the applicability of cluster-based DFT calculations for molecular adsorption on a quasicrystalline surface by comparing the slab model calculations [2]. Although the slab model is a well-established method for periodic crystal surfaces, it cannot be applied to quasicrystal surfaces that lack translational periodicity, even in the surface-parallel directions. Therefore, using both slab and disk-shaped cluster models, we investigated the adsorption of pentacene molecule on a periodic Cu(111) surface. By comparing the potential energy surfaces obtained using these two approaches, we examined the accuracy and limitations of the cluster approximation. Although small clusters produce artificial corrugation in the potential energy surface near unstable regions, we confirmed that the most stable adsorption positions were correctly reproduced even with moderately sized clusters, and that the potential energy surface smoothly converged toward the slab-model results with

increasing cluster radius. In these calculations, large cluster models containing approximately 700–1100 atoms were employed, and flat MPI-parallelized calculations were mainly performed on System B using 1 to 4 nodes (128–512 cores) with the VASP code.

References

[1] M. Hanaoka, S. Iwado, K. Nozawa, M. Aoyama, S. Ohhashi, N. Fujita, S. Kameoka, Appl. Mater. Today, 46, 102878 (2025).

[2] M. Sato and K. Nozawa, Mat. Trans. (in press).

Adsorption Reactions at the Solid Electrode/Aqueous Solution Interfaces

Satoshi Hagiwara
Center for Computational Sciences, University of Tsukuba
1-1-1 Tennodai, Tsukuba, Ibaraki 305-8577

An interface between the electrode and aqueous solution (electrochemical interface) is known as one of the important reaction fields in electrochemistry. To compute electrochemical interface problems, the effective screening medium (ESM) method [1] combined with the three-dimensional reference interaction site model (3D-RISM) method [2], termed ESM-RISM, has been developed by Nishihara and Otani [3]. Since the ESM-RISM method treats the electronic structure of the target electrode with reactant and solvation environment by density functional theory and the classical solution theory, respectively, we can simulate the electrochemical interface with relatively lower computational costs. However, the original implementation of ESM-RISM includes an unphysical approximation, which serves to broaden the molecular structure in the solution and deviated results from the original 3D-RISM ones and requires the higher computational costs for solving Laue-represented RISM equation (order $N^{4/3}$) compared to the 3D-RISM method (order $N \log N$).

For a sufficient simulation of the electrochemical interface, we have reconsidered the formulation of ESM-RISM and implemented it into the QMAS (Quantum MAterials Simulator) code [4]. Our reformulation successfully removes the unphysical approximation. We numerically confirmed that the calculated hydration free energy by ESM-RISM converges to that by 3D-RISM. In addition, the reformulation enables us to reduce the computational complexity, which scales on the order $N \log N$. Subsequently, we have applied the current version of the ESM-RISM method to the Pt(111)/HCl aqueous solution interface. The results of the potential of zero charges (PZC) of the Pt electrode, interfacial capacitance, and standard hydrogen electrode (SHE) potential reasonably reproduced the original ESM-RISM ones. Then, we have computed the hydrogen adsorption energy at the electrified interface. The results of the adsorption energy demonstrated that the stable hydrogen adsorption site depends on the applied bias voltage measured from the SHE potential [5]. We will apply the reformulated ESM-RISM method to understand the details of adsorption phenomena at the electrochemical interfaces in near future.

References

[1] M. Otani, and O. Sugino, Phys. Rev. B **73**, 115407 (2006).

[2] A. Kovalenko, and F. Hirata, J. Chem. Phys. **110**, 10095 (1999).

[3] S. Nishihara and M. Otani, Phys. Rev. B **96**, 115429 (2017).

[4] QMAS website: https://www.qmas.jp

[5] S. Hagiwara, and M. Otani, J. Chem. Theory Comput. **22**, 3633 (2026).

First-Principles and Data-Driven Design of Electrocatalysts for CO_2 Reduction, Water Splitting, and H_2O_2 Synthesis

Di ZHANG

Frontier Research Institute for Interdisciplinary Sciences (FRIS),

Tohoku University, Sendai 980-8577, Japan

We have studied electrocatalytic materials for sustainable energy conversion using massive parallel first-principles simulations on the Supercomputer System at ISSP. This year, we focused on the computational design and mechanistic understanding of advanced catalysts for several important electrochemical reactions, including CO2 electroreduction, oxygen evolution reaction, alkaline hydrogen evolution reaction, and electrochemical hydrogen peroxide synthesis [1–6]. Large-scale density functional theory calculations were performed to construct realistic catalyst surface models, evaluate adsorption free energies of key reaction intermediates, analyze electronic structures, and identify activity descriptors under electrochemical conditions.

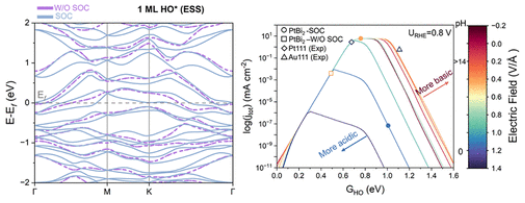

Fig. 1 2D Topological Electrocatalysts with Spin–Orbit Coupling

For CO2 electroreduction, we investigated both extended solid surfaces and molecular carbon-based active sites. In two-dimensional topological electrocatalysts, monolayer PtBi2 was used as a representative platform to clarify how electrochemical surface states induced by adsorbates can interact with spin-orbit-coupling-enabled topological surface states (Fig. 1). The calculations showed that reconstructed surface electronic states under reaction conditions can strongly influence the adsorption energetics of oxygen intermediates and thereby regulate oxygen reduction activity [1]. In another study, C60 fullerene was examined as a molecular active site for CO2-to-CO conversion. By combining first-principles calculations with pH- and electric-field-dependent microkinetic analysis, we revealed that the curved molecular surface of C60 can stabilize COOH* intermediates through large dipole moment changes, providing a mechanism beyond its conventional role as an electronic promoter [2] (Fig. 2).

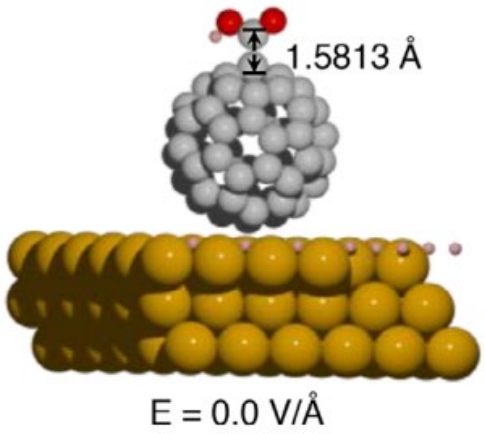

Fig. 2 Electric field effects on the adsorption energies of CO2RR adsorbates

We also studied pyridinic-N incorporated cobalt phthalocyanine catalysts, where

electronic-structure calculations demonstrated that molecular backbone modification optimizes the adsorption of key CO2 reduction intermediates such as *COOH and *CO, explaining the enhanced intrinsic activity and high CO selectivity [3].

For oxygen evolution catalysis, we investigated high-density tungsten single atoms anchored in two-dimensional spinel oxide matrices. The first-principles simulations clarified how W single atoms modify the local coordination environment of Co sites, strengthen OH adsorption, promote surface reconstruction into active oxyhydroxide species, and optimize the adsorption energetics of OER intermediates [4]. For alkaline hydrogen evolution, we studied Ru/VO2-based catalysts and identified a stepwise acceleration mechanism involving both water dissociation and hydrogen spillover. The simulations showed that interfacial V–O–Ru bonding dynamically modulates the electronic structure around Ru active sites, facilitates Volmer-step water dissociation, and optimizes hydrogen adsorption through reversible spillover, thereby improving the overall alkaline HER kinetics [5]. In addition, for electrochemical hydrogen peroxide synthesis through the two-electron water oxidation reaction, we developed a data-driven catalyst design framework by integrating density functional theory, weighted atom-centered symmetry function descriptors, machine learning, and microkinetic modeling. This framework enabled efficient prediction of adsorption free energies and high-throughput screening of catalyst candidates across different material families [6].

Overall, these studies demonstrate how atomic-scale simulations can connect catalyst structure, electronic properties, adsorbate-induced surface reconstruction, and reaction kinetics. The obtained insights provide theoretical guidance for the rational design of efficient electrocatalysts for sustainable energy conversion. The density functional calculations and microkinetic/data-driven simulations were conducted using VASP and in-house Python scripts, respectively.

References

[1] H. Liu et al., J. Phys. Chem. Lett. 16, 12892 (2025).

[2] T. Liu et al., Small 21, e202507824 (2025).

[3] S.-W. Ying et al., Angew. Chem. Int. Ed. 64, e202511924 (2025).

[4] Y. Wang et al., J. Am. Chem. Soc. 147, 32249 (2025).

[5] T. Lu et al., ACS Catal. 16, 2827 (2026).

[6] Z. Liu et al., Angew. Chem. Int. Ed. 65, e202518027 (2026).

Molecular Dynamics Analysis for Water Molecule Dynamics Under Local-Electric-Field Exited by Microstructures

Ayumu TAKAHASHI[1], Kiyoto KAWAI[1], Hiroki GONOME[1]

[1]*Graduate School of Science and Engineering,*

Yamagata University, Jonan, Yonezawa, Yamagata 992-8510

Mitigating global warming requires the development of highly efficient, low-energy energy conversion processes. Controlling water-mediated processes is essential for many energy technologies. While these processes traditionally rely on thermal processes, the photomolecular effect, which is the non-thermal excitation of water molecules by light, offers a promising alternative [1]. Because light is an electromagnetic wave, we hypothesize that electric fields can similarly activate polar water molecules.

In this study, we evaluated the dynamics of water molecules under exited electric field when light was irradiated into microstructures. The electric fields exited by microstructures were pre-calculated by COMSOL Multiphysics and applied to the MD analysis. Figure 1 shows that temperature distribution at no electric field and with electric field. It shows that the thermal diffusivity during transient response varies depending on presence or absence of an exited electric field. Table 1 shows that thermal reach distance over the same elapsed time. It shows that thermal propagation proceeded more rapidly under conditions where an electric field was applied. In these results, it has been suggested that applying an electric field may improve the thermal diffusivity of water.

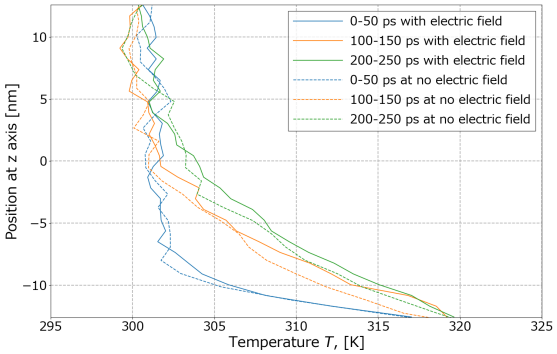

Fig.1: Temperature distribution at no electric field and with electric field.

Table 1: Thermal reach position over the same elapsed time

	With EF [nm]	Without EF [nm]
0-50 ps	-9.4	-9.6
100-150 ps	-2.7	-3.8
200-250 ps	0.2	-1.3

References

[1] Yaodong Tu, Jiawel Zhou, Shaoting Lin, and Gang Chen, Proceedings of the National Academy of Science, 120, e2312751120 (2023).

Electronic state calculations under photoinduced reactions

Kaori Niki

Graduate school of science

Chiba University, Yayoi-cho, Inage-ku, Chiba 263-8522

Introduction

In recent years, understanding the dynamics of hot carriers generated by photoexcitation and their spin-dependent electronic states has become a crucial issue in photocatalytic reactions and spintronic material design. However, a unified understanding of electronic transitions and relaxation processes after photoirradiation, as well as interactions with the substrate and coupling with phonons, is still insufficient. This research performed hot carrier relaxation process in CuPc/$TiSe_2$ systems by combining electronic states obtained by Vienna *Ab initio* Simulation Package (VASP) with non-adiabatic molecular dynamics (NAMD) calculations.

Method

We performed density functional theory (DFT) calculations using VASP version 6.4.3 [1,2]. Exchange–correlation effects were treated within the spin-polarized generalized gradient approximation (GGA) using the Perdew–Burke–Ernzerhof (PBE) functional [3]. The $TiSe_2$ slab model (8×8×1) was constructed with lattice constants. The projector augmented wave (PAW) method was employed with a plane-wave cutoff energy of 380 eV.

NAMDk simulations were carried out [4], which operates directly in momentum space. In this framework, the time-dependent carrier wave function is expanded in the basis of Kohn–Sham eigenstates. Nonadiabatic transitions between electronic states are described using the fewest switches surface hopping (FSSH) algorithm [5], hopping probabilities are determined from the time evolution of the density matrix. Electron–phonon coupling matrix elements were computed using the Perturbo code [6] The Ti 3d and Se 4p orbitals were used as initial projections for constructing Wannier functions [7]. Phonon properties were calculated using density functional perturbation theory (DFPT) [8] on q-point grids of 4×4×4 for the bulk and 16×16×1 for the single-layer system.

Results

This study tracked the hot carrier relaxation process in the CuPc/$TiSe_2$ system. By using a model with an increased number of substrate layers, relaxation times consistent with experimental results, suggesting the important contribution of substrate phonons to electron relaxation. Filtering the calculation results by specific momentum (M point) and energy to correspond to the tr-ARPES experimental conditions revealed that intra-band relaxation

proceeds as an energy-dependent multi-step (cascade) process.

Conclusion

In summary, NAMDk demonstrates that it is a powerful theoretical analysis method that complements tr-ARPES experiments for a wide range of systems, including charge density wave materials.

References

[1] G. Kresse and J. Hafner, Phys. Rev. B **47**, 558 (1993).

[2] G. Kresse and D. Joubert, Phys. Rev. B **59**, 1758 (1999).

[3] J. P. Perdew, K. Burke, and M. Ernzerhof, Phys. Rev. Lett. **77**, 3865 (1996).

[4] Z. Zheng, Y. Shi, J.-J. Zhou, O.V. Prezhdo, Q. Zheng, and J. Zhao, Sci. **3**, 532 (2023).

[5] J.C. Tully, J. Chem. Phys. **93**, 1061 (1990).

[6] J.-J. Zhou, J. Park, I.-T. Lu, I. Maliyov, X. Tong, and M. Bernardi, Comput. Phys. Commun. **264**, 107970 (2021).

[7] G. Pizzi, V. Vitale, R. Arita, S. Bl¨ugel, F. Freimuth, G. G´eranton, M. Gibertini, D. Gresch, C. Johnson et al., Condens. Matter **32**, 165902 (2020).

[8] S. Baroni, S. de Gironcoli, A. Dal Corso, and P. Giannozzi, Rev. Mod. Phys. **73**, 515 (2001).

Prediction of materials properties and exploration of materials with materials informatics

Yosuke HARASHIMA
Graduate School of Science and Technology, Nara Institute of Science and Technology
Takayama-cho, Ikoma, Nara 630-0192

1 Background

Machine learning for materials discovery requires large datasets, yet experimental data on materials properties are scarce. First-principles simulations supply more data but carry systematic errors (e.g. GGA-PBE underestimates band gaps). We developed **CLAUDE** (**C**ovariance **L**inkage **A**ssimilation method for **U**nobserved **D**ata **E**xploration), which integrates experimental and simulation data via data assimilation and couples the resulting model with Bayesian optimization for efficient materials search. As a practical application, the band gap of the perovskite solid solution $(\mathrm{Sr}_{1-x_1-x_2}\mathrm{La}_{x_1}\mathrm{Na}_{x_2})(\mathrm{Ti}_{1-x_1-x_2}\mathrm{Ga}_{x_1}\mathrm{Ta}_{x_2})\mathrm{O}_3$ was modeled for photocatalytic water splitting.

2 Data Assimilation Methodology

Descriptors x and $y = (y_{\mathrm{sim}}, y_{\mathrm{exp}})^\top$ are concatenated into $z = (x^\top, y^\top)^\top$, assumed to follow a multivariate Gaussian distribution with precision matrix Λ: $p(z \mid \Lambda) \propto \exp(-\frac{1}{2} z^\top \Lambda z)$. The off-diagonal block Λ_{yx} encodes the simulation–experiment correlation. The conditional mean $\mu = -(\Lambda_{yy})^{-1}\Lambda_{yx}x$ gives the assimilated prediction of y_{exp}. Λ is estimated via MAP estimation using the sufficient statistic $C^N_{\gamma_1\gamma_2} = \sum_i z_{i\gamma_1} z_{i\gamma_2}$, enabling sequential updates without retaining raw data.

Mismatched composition grids between datasets produce missing values. These are treated via the *direct likelihood*: missing variables are integrated out analytically, and the integration result in the Schur complement $\bar{\Lambda} = \Lambda_{\alpha\alpha} - \Lambda_{\alpha\bar{\alpha}}\Lambda^{-1}_{\bar{\alpha}\bar{\alpha}}\Lambda_{\bar{\alpha}\alpha}$. Each data point thereby contributes to Λ regardless of whether its counterpart in the other dataset exists.

3 Bayesian Optimization with Assimilation

M=500 models are sampled from the posterior of Λ to capture uncertainty without a Gaussian process. Each iteration:

- Retrain the assimilation model with added data.
- Propose one experimental candidate maximising $\alpha_{\mathrm{EI}} = \langle \max(\mu_k - y^*, 0) \rangle_k$.
- Propose ξ simulation candidates maximising the variance $\alpha_{\mathrm{Var}} = \langle (\mu_k - \mu)^2 \rangle_k$.

Because the two models share components of Λ, simulation data (Step 3) narrows the posterior of the experimental model (Step 2) even before new experiments are performed.

4 Computations at ISSP Supercomputer Center

The KKR-CPA band gap calculations using AkaiKKR were conducted primarily

on the ISSP supercomputer. AkaiKKR (`http://kkr.issp.u-tokyo.ac.jp/`) is a first-principles code based on the Korringa–Kohn–Rostoker (KKR) Green's function method. Coupled with the Coherent Potential Approximation (CPA), the code treats chemical substitutional disorder self-consistently without explicit supercells, enabling band gap evaluation across a continuous (x_1, x_2) composition space. A uniform mesh of 54 compositions of $(Sr_{1-x_1-x_2}La_{x_1}Na_{x_2})(Ti_{1-x_1-x_2}Ga_{x_1}Ta_{x_2})O_3$ was computed with GGA-PBE ($l_{\max}$=4 for cations, 3 for O; `bzqlty` = 8). These 54 simulation points, combined with 24 experimental values from master's theses of the Kudo group (Tokyo Univ. of Science), form the complete training set for CLAUDE (simulation RMSE: 0.13 eV; experimental RMSE: 0.17 eV).

5 First-Principles Calculations

Four types of first-principles calculations were performed. First, band gap training data for the assimilation model were generated using AkaiKKR with the KKR-CPA method and the GGA-PBE functional, covering 54 compositions on a uniform grid. Second, the lattice constants of the end-member compounds $SrTiO_3$, $LaGaO_3$, and $NaTaO_3$ were optimised with VASP using the projector augmented-wave (PAW) method and GGA-PBE (energy cutoff: 400 eV; k-mesh: 8^3); these values served as the basis for Vegard's law interpolation across the solid-solution composition space. Third, total energies of all 867 symmetry-inequivalent substitutional configurations in a 2×2×2 supercell were evaluated with VASP at the GGA-PBE level to identify the most stable atomic arrangement. Finally, the band gap of the most stable configuration was calculated at a higher level of theory using the hybrid functional HSE06 in VASP, providing an accurate verification of the convex-downward E_g trend predicted by the assimilation model.

The HSE06 calculations confirmed the convex-downward E_g at $(0.375, 0.375)$: 2.87 eV vs. $SrTiO_3$ (3.02), $LaGaO_3$ (4.67), $NaTaO_3$ (3.73 eV). The assimilation model predicted test compositions in data-sparse regions with errors of -0.05, -0.22, -0.13 eV at (x_1, x_2)=$(0.25, 0.50)$, $(0.50, 0.25)$, $(1/3, 1/3)$, respectively, reproducing the atomic cocktail effect (enhanced visible-light absorption) consistent with both experiment and HSE06 calculations.

References

[1] Y. Harashima, *et al.*: Phys. Rev. Materials **9**, 093803 (2025); `https://github.com/yy-harashima/CLAUDE`.

Closed-Loop Framework for Discovering Stable and Low-Cost Bifunctional Metal Oxide Catalysts for Efficient Electrocatalytic Water Splitting in Acid

XUE JIA

Advanced Institute for Materials Research (WPI-AIMR),

Tohoku University, Sendai, 980-8577

We develop a loop-based design framework comprising front-end exploration of potential catalysts, mid-end synthesis and electrochemical testing, and back-end characterizations to identify promising non-noble MO catalysts for acidic water splitting.

This year, we utilized supercomputing resources to perform density functional theory (DFT) calculations to accurately evaluate the theoretical activity for a promising MO electrocatalyst, $RbSbWO_6$, which was determined by data mining. First, we calculated the surface energy (γ) among various surface structures, and two surface structures with a Miller index of (011) were identified as the most thermodynamically favorable surfaces. Therefore, these two $RbSbWO_6$ surfaces were selected as potential exposed surfaces for subsequent surface state analysis. Based on adsorption energy calculations across the adsorption sites, 2D surface Pourbaix diagrams are displayed. Based on these altered surface structures, theoretical activities were analyzed using microkinetic modeling. For the OER, structure A, with 1/6 ML of O* coverage and adsorption of O* or OH* on the W site, is positioned near the peak of the volcano model, indicating a promising OER activity at this site. For HER, Structure B, with 11 Ov, which is almost at the top of the volcano model, indicating a promising HER activity. Therefore, both sides of the $RbSbWO_6$(011) surface can provide active sites for catalyzing the OER and HER, suggesting that this could be a bifunctional catalyst for water splitting.

Experimental validations successfully synthesized $RbSbWO_6$ and demonstrated its robust performance and stability in acidic OER and HER environments. As summarized from the DigCat platform, $RbSbWO_6$ stands out as one of the most effective bifunctional MO catalysts for acidic water splitting compared with other reported stoichiometric non-noble MO catalysts without significant engineering or modification. This demonstrates the effectiveness of our comprehensive strategy.

References

[1] **X. Jia**, Z. Zhou, F. Liu, T. Wang, Y. Wang, D. Zhang, H. Liu, Y. Wang, S. Ye, K. Amezawa*, L. Wei*, and H. Li*, Journal of the American Chemical Society, 2025, 147, 226

Development of First-principles Berry Phase Calculation codes for Application to Large Systems

Naoya YAMAGUCHI
Nanomaterials Research Institute (NanoMaRi), Kanazawa University
Kakuma-machi, Kanazawa, Ishikawa 920-1192

This year, we focused particularly on refining computational methods and applying them to complex systems, conducting calculations based on first-principles electronic structure calculations.

First, we further advanced the computational methods and code development for intrinsic anomalous Hall conductivity (AHC), and improved algorithms to overcome computational difficulties arising in complex material systems containing defects, impurities, layered materials, and artificial superlattices. In such systems, numerous degenerate points may appear due to the folding of the electronic band structure, requiring high-density k-point sampling and increasing computational costs. In this study, we further developed the minor determinant method based on the local Berry phase (LBP) method [1] developed in the previous year, implementing an algorithm capable of efficiently evaluating AHC while suppressing numerical instability. This year, we additionally implemented a tetrahedron method and confirmed that it suppresses numerical oscillations in AHC associated with changes in chemical potential. This has enabled stable and high-precision calculations of chemical potential-dependent AHC. Furthermore, by adding a checkpoint function to the computational code for the LBP method, we enabled the resumption of calculations even if they were interrupted midway, thereby making it possible to handle long-duration computations exceeding one day.

In addition, we advanced the development of a method that combines the LBP method with the hybrid Wannier function method to analyze the contribution of each AHC layer (layer anomalous Hall conductivity) [2]. We performed computational studies applying this method to magnetic topological insulators and magnetic metal thin films, and released the computational code as `layerAHC` [3].

Furthermore, we developed the giant molecule band unfolding (GMBU) procedure as a method for analyzing electronic states in non-periodic nanostructures [4]. In this procedure, in a finite-size giant molecular model, we first calculate the eigenvalues and eigenvectors for the molecular orbitals. We then introduce relative position vectors of atoms in place of lattice parameters in periodic systems and evaluate spectral weights by assigning effective wave number parameters, thereby enabling the depiction of band-like structures corresponding to band structures even in non-periodic or finite systems. We applied this procedure to various nanoflakes, confirming that it can reproduce clear band-like structures even in finite-size systems. We have released the computational code for this procedure as `GMBU.jl` [5]. As described above, we have continued to develop and release computational methods for electron transport based on the Berry phase and for analyzing electronic states in non-periodic systems. Furthermore, by utilizing computational resources, we have achieved the analysis of electronic states and Berry phase-related physical properties in complex material systems.

References

[1] H. Sawahata, N. Yamaguchi, S. Minami, F. Ishii, Phys. Rev. B **107**, 024404 (2023).

[2] Y. Morishima, F. Ishii, N. Yamaguchi, arXiv:2506.01160.

[3] https://isspns-gitlab.issp.u-tokyo.ac.jp/n-yamaguchi/layerAHC.

[4] N. Yamaguchi, S. Yunitasari, W. Amalia, C.-C. Lee, T. Ozaki, F. Ishii, Nano Lett. **25**, 17725 (2025).

[5] https://isspns-gitlab.issp.u-tokyo.ac.jp/n-yamaguchi/GMBU.jl; https://doi.org/10.5281/zenodo.17815785.

A novel framework for predicting non-van der Waals two-dimensional materials

Shota ONO
Muroran Institute of Technology, Muroran, Hokkaido 050-8585, Japan

Many two-dimensional (2D) materials are categorized as van der Waals (vdW) type-systems, in which the parent 3D crystals have layered structures. However, there also exists non-vdW 2D materials whose 3D counterparts exhibit no geometrical anisotropy. To date, no physically transparent descriptors for predicting non-vdW 2D materials have been proposed.

In this project, we developed a framework for identifying non-vdW 2D materials [1]. This is achieved by calculating the thickness dependence of total energy of thin films truncated from a specific surface. Non-vdW materials in the monolayer limit exhibit a downward deviation from the law of finite-thickness excess energy (FTEE) inverse to the number of layers:

$$\Delta E \propto N^{-1}, \tag{1}$$

where ΔE is the total energy of N layered thin film relative to the bulk energy. The total energies of thin films in single-component systems were calculated using Quantum Espresso (QE). The thin film geometries derived from bulk surfaces were constructed using Atomic Simulation Environment (ASE).

Figure 1(a) shows a breakdown of N^{-1} law below $N \leq 2$ for IV and V group systems. Noble metals including Au also exhibit a deviation from the N^{-1} law, as shown in Fig. 1(b). Such deviations indicate that these systems prefer 2D structures in the monolayer limit and can thus be regarded as 2D materials. This is consistent with experimental realization of non-vdW 2D materials such as silicene (Si), germanene (Ge), and goldene (Au). Figure 1(c) lists $p = d\ln\Delta E/d\ln N$ at $N = 1$ for single-component systems in the periodic table. Elements having small negative values of p can adopt 2D structures. This may be useful for comparisons with future experiments.

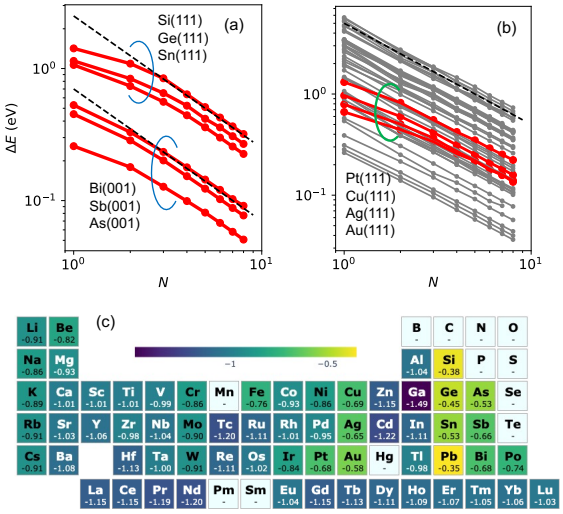

Figure 1: ΔE versus N for (a) IV and V group and (b) metallic elements. The dashed line indicates $\Delta E \propto N^{-1}$. (c) $p = d\ln\Delta E/d\ln N$ at $N = 1$ for elements in the periodic table. p at $N = 2$ is shown for Pb. Data reproduced from Ref. [1].

References

[1] S. Ono: Phys. Rev. B **112**, 075403 (2025).

Anomalous electron-phonon coupling in Cu-Ni alloys

Shota ONO
Muroran Institute of Technology, Muroran, Hokkaido 050-8585, Japan

Ultrafast relaxation following excitation by a femtosecond laser pulse enables the investigation of electron-phonon (e-ph) coupling in metals. The ultrafast luminescence dynamics have been studied in various elements [1]. The decay rate of luminescence has been successfully described by a modified two-temperature model (TTM), in which the e-ph coupling parameters are determined using first-principles calculations. In this project, we extend this framework to the luminescence of Cu-Ni solid solutions, and demonstrate an anomalous dependence of the e-ph coupling strength on Ni concentration [2].

According to the modified TTM, the decay rate Γ of non-equilibrium electrons in metals is proportional to the e-ph coupling constant $\lambda\langle\omega^2\rangle$. This is expressed as

$$\Gamma = \frac{3\hbar\lambda\langle\omega^2\rangle}{2\pi k_{\mathrm{B}} T_0}, \qquad (1)$$

where $\hbar$ is the Planck constant, k_{B} is the Boltzmann constant, and T_0 is the phonon temperature. We calculated $\lambda\langle\omega^2\rangle$ for $\mathrm{Cu}_{1-x}\mathrm{Ni}_x$ alloys using Quantum Espresso. We assumed a $2\times2\times2$ supercell containing eight atoms, and tuned the Ni concentration x.

Figure 1(a) shows the time-evolution of luminescence intensity of $\mathrm{Cu}_{1-x}\mathrm{Ni}_x$ for various x. The luminescence intensity decreases by an order of magnitude within a few picoseconds. As shown in Fig. 1(b), the decay rate Γ exhibits an anomalous dependence on Ni composition, i.e., it decreased first by adding Ni up to $x = 0.17$ and then started to increase with x. This behavior is well reproduced by the theoretical values of Γ given in Eq. (1). The agreement between experiment and theory indicates that the e-ph coupling strength in $\mathrm{Cu}_{1-x}\mathrm{Ni}_x$ alloys is a nonlinear function of x. A possible origin for this nonlinear behavior is a reduction in the magnitude of the matrix elements and/or a decrease in the available phase space for e-ph scattering in dilute alloys.

We further performed systematic calculations of $\lambda\langle\omega^2\rangle$ for X_7Y_1 alloys with X = Cu, Ag, Au and Y = Ni, Pd, Pt, Cu, Ag, Au. We confirmed that a small inclusion of group 10 elements gives rise to a decrease in $\lambda\langle\omega^2\rangle$. This suggests that alloying can enhance the luminescence lifetime.

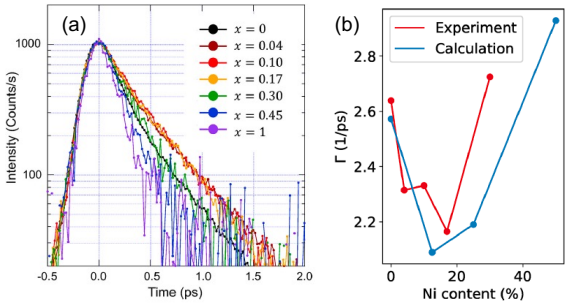

Figure 1: (a) Luminescence decay at 0.6 eV for alloys with various x. Each curve is normalized to 1000 at maxima. (b) The decay rate Γ as a function of Ni content. Data reproduced from Ref. [2].

References

[1] T. Suemoto, S. Ono et al.: Phys. Rev. B **111**, 035150 (2025).

[2] T. Suemoto, H. Morino, S. Ono et al.: Phys. Rev. B **112**, 035138 (2025).

Influence of Laser Excitation on Non-thermal Melting in α-Quartz

Mizuho ONO, Atsuki KOMIYA

Institute of Fluid Science,

Tohoku University, Katahira, Aoba-ku, Sendai, Miyagi 980-8577

When an ultrashort laser pulse is directed at a material, its electrons can become strongly excited, leading to unique properties. Among the resulting phenomena, non-thermal melting, in which the crystal lattice of a solid rapidly collapses, is particularly effective for precision machining [1]. The objective of this work is to clarify the influence of excited electronic states on non-thermal melting through numerical simulations using time-dependent density functional theory (TDDFT). α-quartz was selected as the target material.

Figure 1(a) and 1(b) show the occupied states after laser irradiation at photon energies of 1.55 eV and 3.10 eV, respectively. The results confirm that there is virtually no difference between the two cases in terms of the excited electrons. This is because tunnel ionization dominates, largely eliminating the photon energy dependence. Figure 1(c) displays the occupied electron states and the projected density of states (PDOS) at an electron temperature of 2.5 eV, calculated using finite-temperature DFT. This result shows that electrons near the Fermi level are excited to the conduction band. In the finite-temperature calculations, the conduction band minimum (CBM) is occupied according to the Fermi–Dirac distribution; however, under laser excitation, it is evident that electrons are not present near the CBM but are instead excited to higher energy levels. These differences imply that the interatomic bonding strength after excitation varies depending on the process, suggesting that the atomic behavior during non-thermal melting will also differ.

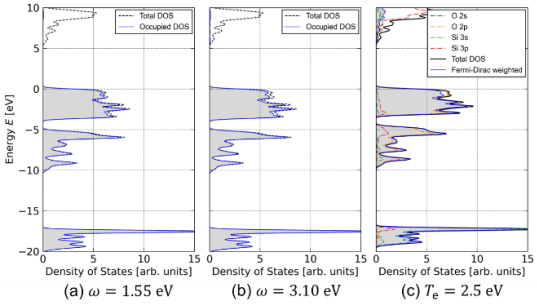

Fig. 1: (a, b) Comparison of the initial DOS and projection of electron orbitals onto the ground state after laser irradiation at $I = 1.00 \times 10^{14}$ W/cm^2 for (a) 1.55 eV and (b) 3.10 eV. (c) PDOS of the ground state overlaid with the occupied states derived from the Fermi–Dirac distribution.

References

[1] M. Boero, A. Oshiyama, P. Luigi Silvestrelli, and K. Murakami, Physica B: Condensed Matter **376-377**, 945 (2006).

First-Principles Study of Optoelectronic Properties of Organic Molecular Aggregates

Takatoshi Fujita
Institute for Quantum Life Science, National Institutes for Quantum Science and Technology
Anagawa, Inage-ku, Chiba 263-8555

We have developed large-scale excited-state methods based on the GW/Bethe-Salpeter equation (GW/BSE) in combination with the fragment molecular orbital (FMO) framework. In parallel, we have established a multi-scale simulation scheme based on quantum dynamics methods using model excited-state Hamiltonians derived from the FMO-GW/BSE. This scheme allows for first-principles simulations of exciton dynamics in realistic molecular aggregates .

As an application of our multi-scale approach [1], we have elucidated the role of charge-transfer (CT) state manifold in the exciton dissociation processes in donor/acceptor (D/A) blends. Understanding the relationship between the driving energy and the charge photogeneration in D/A blends is crucial to improving the power conversion efficiency of organic solar cells. Here, we investigate the exciton dissociation dynamics in P3HT/PCBM blends by employing the FMO-GW/BSE, ensemble-averaged wave packet dynamics, and the Marcus-Levich-Jortner rate formalism. Analysis of the rate constants suggests that direct exciton dissociation into low-energy CT states is inefficient, occurring on timescales longer than ∼1 ns, whereas dissociation into higher-energy CT states can proceed on the ∼1 ps timescale. The thermally-corrected wave packet dynamics simulations for the amorphous structure show that the initial exciton dissociation to high-energy CT state takes place at ∼100 fs after photoexcitation, followed by the thermal relaxation toward low-lying CT. These results demonstrate that higher-energy CT states, often overlooked in conventional models, play a significant role in facilitating exciton dissociation.

As another application [2], we have studied the relationship between the crystal polymorphs and excited states of dipolar azobenzene molecules bearing electron-donating and -accepting units. To gain microscopic insight into the relationship, we have performed FMO-GW/BSE calculations on molecular clusters consisting of 54 dipolar azobenzene molecules extracted from two polymorphs. Our calculations suggest that the low-lying excited states consist of a mixture of intramolecular transitions ($n \rightarrow \pi^*$ and $\pi \rightarrow \pi^*$) and intermolecular CT transitions between the n or π orbital of one molecule to π^* orbital of another. Differences in the degree of mixing among these excitation characters result in distinct spectral features in the two polymorphs.

References

[1] T. Fujita, M. Nozaki, Phys. Chem. Chem. Phys. **38**, 20765 (2025).

[2] M. Yamauchi, E. Machida, M. Nozaki, T. Fujita, H. Sotome, K. Yamamoto, Y. Mizuhata, N. Aratani, H. Yamada, S. Masuo, Adv. Opt. Mater. **14**, e03396 (2026).

Phase transformation and electric state of high entropy alloys

Yoko Yamabe-Mitarai

Frontier Science Graduate School,

The University of Tokyo, Kashiwa-no-ha, Kashiwa, Chiba 277-8561

High-entropy alloys (HEAs) have been attracting attention as new-generation structural and functional materials since this new paradigm was proposed in 2004 [1]. Most HEAs have a single face-centered-cubic (fcc), body-centered-cubic (bcc) structure, or their mixtures. Not many examples of HEAs with the hexagonal-close-packed (hcp) structure have been studied. We are applying to find HEAs with hcp structure experimentally and a few alloys were found to have an hcp structure [2].

Among the hcp-HEAs, CoReRu alloys are of particular interest. By combining Cr, Fe, and V, and by making multiple additions of these elements, the hcp region becomes stable over a wide temperature range between 600 and 1600 ˚C [3]. The equiaxed single-phase hcp phase was observed after heat treatment. The strength of these alloys was around 200 MPa at 1000 ˚C [4].

To investigate whether strong multi-elemental interaction or short-range order formation occurs, Mean Square Atomic Displacement, MSAD and an electron charge of density, Bader Charge, was calculated using DFT [5]. A supercell model with 128 atoms was used to indicate the solid solution phase. Special Quasirandom Structure was used to simulate random atomic positions. The internal coordinate was optimized using Quantum Espresso (QE). The electron charge density was calculated on the optimized coordinates. It is found that atomic displacement of Re and Ru was larger than those of other elements indicating in large lattice distortion by Re and Re. Cr, Fe, and V did not show a specific effect for MSAD and their effect was changed by the combination of elements. The distance between two neighbor atoms calculated from MSAD indicates longer distance of Re-Re, Re-Ru, Ru-Ru compared with the ideal distance indicates large lattice distortion. The strong solid-solution strengthening caused by these three bonds. The Barder charge also indicates the strong bonding between Re-Re, Re-Ru, and Ru-Ru.

References

[1] B. Cantor et. al., A. J. B. Vincent, Mater. Sci. Eng. A, **375-377**, 213 (2004).

[2] Y. Yamabe-Mitarai et. al., JALCOM, **911**, 164849 (2022)

[3] M.C Gao, B. Zhang, et al., Metall. Mater. Trans. A, V47, (2015), p3322-3332.

[4] S. J, Liang, Ph D Thesis, Spt. (2024)

[5] Y. Sakai, Master’s Thesis, Mar. (2026).

Ab initio DFT study of lattice defect electronic structures for emergent polar skyrmions

Takahiro SHIMADA and Susumu MINAMI

Graduate School of Engineering, Kyoto University,

Kyoto daigaku-Katsura, Nishikyo-ku, Kyoto 616-8540

This study proposes a novel strategy to generate atomic-scale ferroelectricity and ultrahigh-density polar skyrmions in a paraelectric perovskite oxide by means of twist grain boundary and/or moiré engineering [1]. Using ISSP supercomputer system B and first-principles density functional theory calculations with the VASP code, we demonstrate that twisting two monolayers of centrosymmetric $SrTiO_3$ induces robust ferroelectric polarization and stabilizes a lattice of polar skyrmions with characteristic sizes on the order of one nanometer. This result overcomes the long-standing critical thickness limitation for ferroelectricity and polarity, which typically suppresses ferroelectric order in ultrathin oxide films.

The twisted $SrTiO_3$ boundaries form moiré superlattices or twist grain boundary in which strong interlayer coupling leads to substantial lattice reconstruction and ion displacement. These structural distortions break local inversion symmetry, giving rise to sizable electric polarization comparable to that of conventional ferroelectrics such as $PbTiO_3$, despite $SrTiO_3$ being intrinsically non-ferroelectric. The polarization vectors curl in the plane and exhibit a continuous reversal in the out-of-plane component from the center to the moiré unit cell. Topological analysis, based on interpolated polarization fields, confirms that these polarization textures correspond to genuine polar skyrmions with a topological charge of approximately ±1.

Notably, polar skyrmions emerge in twist boundaries as thin as a single unit cell and persist across a range of large twist angles. For twist angles of 36.87° and 22.62°, the resulting skyrmion diameters are approximately 0.87 nm and 1.40 nm, respectively, yielding array densities up to $\sim 1.3 \times 10^{18}$ m^{-2}. These values represent the highest polar skyrmion densities reported to date, surpassing those achieved in conventional ferroelectric superlattices and heterostructures by more than an order of magnitude. The absence of a critical thickness and the extreme miniaturization are attributed to the nonlocal strain fields and charge redistribution inherent to moiré superlattices, rather than to geometric confinement alone.

Beyond ferroic topology, the study reveals that twisting engineering also profoundly alters

the electronic structure of $SrTiO_3$. Ultrathin twisted boundaries exhibit remarkably flat valence bands, with bandwidths below 5 meV over a wide range of twist angles, and as small as 0.24 meV at specific angles. Such ultraflat bands, narrower than those in twisted bilayer graphene, suggest strong electronic localization and potential for correlated electronic phenomena.

Overall, this work establishes defect-moiré engineering of perovskite oxides as a powerful platform for creating atomic-scale polar topologies and ferroelectricity in otherwise non-ferroelectric materials. The demonstrated combination of ultrathin ferroelectricity, ultrahigh skyrmion density, and emergent electronic flat bands opens new opportunities for fundamental studies and for the development of ultrahigh-density skyrmion-based memory and nanoelectronic devices.

References

[1] T. Xu, Q. Tao, J. Pang, J. Zhang, S. Li, R. He, J. Wang, T. Shimada, Research. **8**, 0621 (2025).

Density-functional studies on light-element effects in permanent magnets and on metal surfaces

Insung SEO

Graduate School of Natural Science and Technology,

Shimane University, Matsue, Shimane 690-8504

In this project, we conducted first-principles density-functional-theory (DFT) calculations on two subjects, both centered on the role of light elements (B, C, N, O, F): (i) the crystal-field parameters of light-element-doped permanent-magnet compounds $NdFe_{12}X$ under lattice strain, and (ii) the 1s core-level binding energies of light-element atoms on (111) metal substrates. Both studies were carried out on the ISSP system B, ohtaka, using the VASP and OpenMX codes.

Strain response of crystal-field parameters in $NdFe_{12}X$. The $ThMn_{12}$-type RFe_{12} (R = Nd, Sm) compound is a candidate for next-generation permanent magnets, and small light-element doping is widely investigated for stabilizing the structure and tuning the magnetocrystalline anisotropy. Our preliminary calculations on $NdFe_{12}X$ (X = B, C, N, O, F) revealed that the Stevens crystal-field parameter $A_2^0\langle r^2\rangle$, which dominates the single-ion anisotropy of Nd^{3+}, varies significantly and discontinuously across different light elements. To clarify the microscopic origin of this discontinuous variation, in this project we extended the calculations to include lattice strain along the *a*- and *c*-axes from −10% to +10% in 1% increments. Structural relaxation was performed with VASP under the GGA-PBE functional, treating the Nd 4*f* electrons with an open-core pseudopotential, and the crystal-field parameters were extracted from OpenMX electronic-structure calculations through a crystal-field analysis.

For undoped $NdFe_{12}$, $A_2^0\langle r^2\rangle$ remained nearly constant under both *a*- and *c*-axis strain within ±5%, whereas every $NdFe_{12}X$ showed a pronounced and largely monotonic response (Fig. 1). In $NdFe_{12}N$, for example, $A_2^0\langle r^2\rangle$ varies by more than 1300 K across the strain range, with the *a*- and *c*-axis strains giving nearly opposite-sign responses. $NdFe_{12}C$ exhibits a sign change of $A_2^0\langle r^2\rangle$ under sufficiently large *c*-axis compression, suggesting a potential easy-axis switching driven by epitaxial strain. These results indicate that the strain response of the crystal-field environment at the Nd site is qualitatively governed by the chemical bonding of the doped light element.

Core-level binding energies on metal surfaces. In parallel, we evaluated the 1s binding energies of B, C, and N atoms at on-

surface and subsurface sites of Al(111), Cu(111), and Ir(111) substrates using OpenMX with the exact-Coulomb-cutoff method [1]. The (4×4) slab models consisted of four metal layers with a vacuum spacing larger than 15 Å, and seven candidate sites (fcc-/hcp-hollow, ontop, bridge, and three subsurface sites) were considered for each species and substrate.

For B on Ir(111), the hcp-hollow site was found to be the most stable adsorption configuration, and its B 1s binding energy is calculated to be 189.30 eV, which is higher than that reported for the borophene B 1s peak. This identifies a plausible defect origin for the higher-binding-energy shoulder observed in experimental XPS spectra of borophene grown on Ir(111). The site- and substrate-dependent binding-energy table compiled in this study should aid the interpretation of XPS spectra of two-dimensional materials grown on metal surfaces. Part of these results was presented at the 72nd JSAP Spring Meeting (2026) [2].

Outlook. For both studies, further analyses such as internal-coordinate relaxation under strain and an extension to $SmFe_{12}X$ for the magnet study, and an extension to further substrate–adsorbate combinations for the surface XPS study, are envisioned as future work. Manuscripts based on the present results are currently in preparation.

References

[1] T. Ozaki and C.-C. Lee, Phys. Rev. Lett. **118**, 026401 (2017).

[2] I. Seo and H. Kageshima, 72nd JSAP Spring Meeting, 17a-PA3-5 (2026).

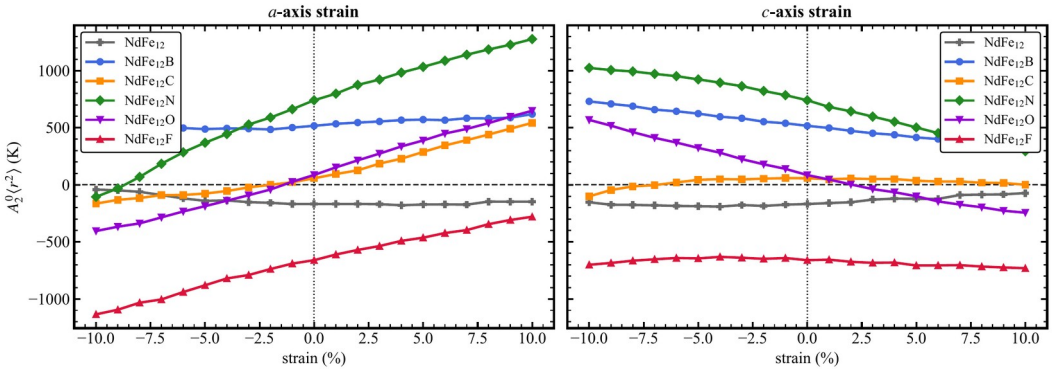

Fig. 1: Crystal-field parameter $A_2^0\langle r^2\rangle$ of $NdFe_{12}X$ (X = none, B, C, N, O, F) under uniaxial lattice strain along the *a*-axis (left) and *c*-axis (right).

Stable Structure of Cu cluster around Fe vacancy

Kazuhito Ohsawa

Institute for Applied Mechanics, Kyushu University,

Kasuga-koen 6-1, Kasuga, Fukuoka 816-8580

Introduction

Iron (Fe) and steel are important structural materials in fusion and fission reactors. Trace amount of cupper (Cu) is included in steel as impurity and precipitates in the irradiation circumstance. Cu clusters cause embrittlement of the steel because they inhibit dislocation motion. Besides, large amount of vacancy type lattice defects are nucleated in the irradiation circumstance by knock-on damage. In the present study, interaction between a Fe vacancy and an impurity Cu in Fe lattice are investigated. Besides, stable structures of Cu clusters nucleated around the Fe vacancy. We expect that vacancy type lattice defects will promote the precipitation of Cu and growth of the Cu cluster.

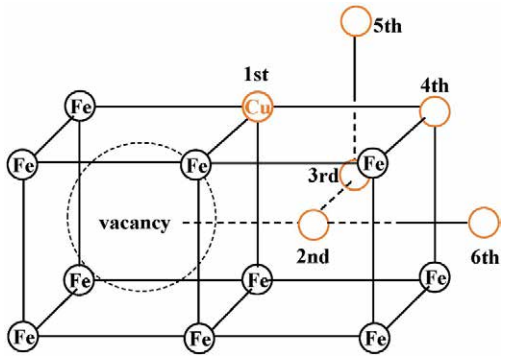

Fig. 1: Schematic view of Fe vacancy and nearest neighbor sites.

Simulation method

First-principle calculations based on density functional theory are performed by Vienna ab-initio simulation package (VASP) with generalized gradient approximation (GGA) and projector augmented wave method (PAW). We used supercell composed of 250 lattice points (5x5x5 bcc lattice) including a vacancy. In the present simulations, Fe atoms are supposed to be ferromagnetic elements.

Binding energy E_b between a Fe vacancy and an impurity Cu is defined, as follows.

$$E_b = E[\mathrm{Fe}_{m-1}\mathrm{V}] + E[\mathrm{Fe}_{m-1}\mathrm{Cu}] - E[\mathrm{Fe}_{m-2}\mathrm{VCu}(k)] - E[\mathrm{Fe}_m], \quad (1)$$

where E is cohesive energy of supercell. For example, supercell $\mathrm{Fe}_{m-1}\mathrm{V}$ is composed of m-1 iron atoms (Fe), one vacancy (V), where m=250. Impurity Cu located at k-th nearest neighbor site from the vacancy is expressed by Cu(k), as shown in Fig. 1.

The most stable structures of Cu clusters around a Fe vacancy are selected among many types of Cu cluster, which is steady work. But first and second nearest neighbor sites would be favorable for Cu atoms. So, the stable structures are able to predict beforehand, to some extent.

Results and discussion

We estimated binding energies of impurity Cu to vacancy in Fe lattice, according to equation (1). As shown in Fig. 2, first and second nearest neighbor sites from the vacancy are energetically favorable for Cu. Therefore, attractive interaction supposed to act between Cu and Fe vacancy, which is good agreement with the fact that Cu does not dissolve in Fe at all. In particular, the first nearest neighbor is the most stable site for Cu. Therefore, we expected that multiple Cu atoms will preferentially occupy the first nearest neighbor sites from Fe vacancy. However, the prediction is not necessarily correct.

Fig. 3 shows the most stable structures of Cu clusters around Fe vacancy. There are 8 first nearest neighbor sites around the Fe vacancy. However, Cu atoms occupy first and second nearest neighbor sites, as shown in Fig. 3 (b)-(e). For example, Fig. 3 (b) exhibits the most stable structure of two Cu atoms. One is at the first nearest neighbor site and the other is at second nearest neighbor site. At the moment, we can not think of a reason why that would happen. But that would be a subject for future research.

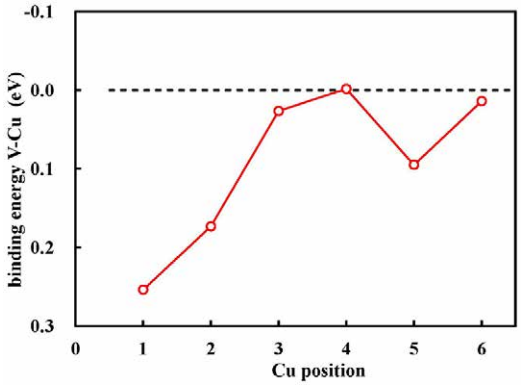

Fig. 2: Binding energy of Cu to Fe vacancy.

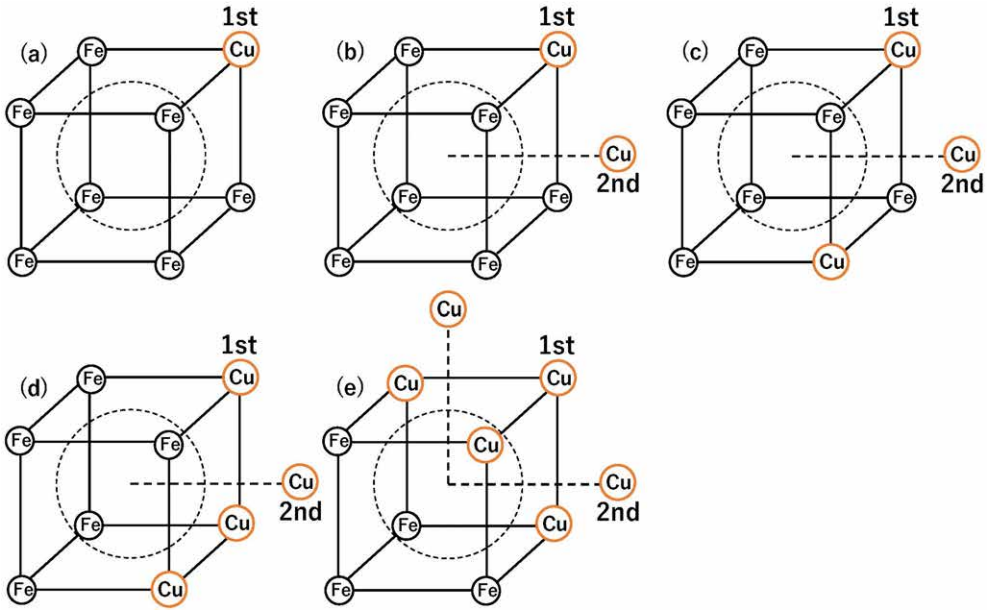

Fig. 3: Schematic view of most stable structures of Cu clusters around Fe vacancy.

First-principles design of magnetic tunnel junctions with an antiferromagnet Mn_3Sn

Katsuhiro Tanaka[1,2] and Yuta Toga[1,3]
[1]*Department of Physics, University of Tokyo, Bunkyo-ku, Tokyo 113-0033, Japan*
[2]*Department of Materials Design and Engineering, University of Toyama, Toyama-shi, Toyama 930-8555, Japan*
[3]*JSR-UTokyo Collaboration Hub, CURIE, JSR Corporation, Minato-ku, Tokyo 105-8640, Japan*

The tunnel magnetoresistance (TMR) effect is one of the prototypical spintronic phenomena, which has been applied to the electric readout. Conventionally, the TMR effect has been discussed in ferromagnetic tunnel junctions since ferromagnets have a net spin polarization and thus give rise to the spin-polarized tunneling current. However, recent studies have revealed that antiferromagnets (AFMs) can also produce a finite spin-polarized tunneling current when the magnetic order of the AFM breaks the macroscopic time-reversal symmetry [1–3], which is owing to the spin splitting in momentum space. This spin-polarized current in such spin-splitting AFMs leads to the realization of a finite TMR effect with antiferromagnets, the TMR ratio of which can be as large as that of ferromagnets.

In this study, we examine the TMR effect from first principles, using the noncollinear antiferromagnet Mn_3Sn as the electrode [4]. Mn_3Sn exhibits an inverse 120° magnetic structure at room temperature, where a finite spin polarization appears in momentum space. For Mn_3Sn, the experimental observation of the TMR effect has been reported as well as theoretical proposals [5–7]. Here, we adopt MgO, one of the representative barrier materials used in the magnetic tunnel junctions (MTJs), as the barrier layer, and investigate the $Mn_3Sn(01\bar{1}0)/MgO(110)/Mn_3Sn$ tunnel junction.

We calculate the TMR effect with the scattering theory formalism [8–11]. We separate the MTJ into the two lead regions and the scattering region in between. The lead and the scattering regions are Mn_3Sn and $Mn_3Sn/MgO/Mn_3Sn$, respectively. When constructing the scattering region, we optimize the interfacial distance between Mn_3Sn and MgO allowing for several percent of the lattice mismatch. After performing the electronic structure calculations for each region, we combine the lead and scattering regions to construct the MTJ, and calculate the transmission. We also calculate the distribution of the spin polarization on the Fermi surface of the bulk Mn_3Sn and the complex band structure of the bulk MgO. The simulations are performed using the Quantum ESPRESSO [12, 13] and Wannier90 [14] packages.

As a result, we obtain a finite TMR effect in the $Mn_3Sn/MgO/Mn_3Sn$ MTJ. The momentum-dependent transmission in the MTJ combined with the spin-split Fermi surfaces of Mn_3Sn and the complex energy bands of MgO reveals that the TMR effect appears due to the spin polarization of Mn_3Sn in the momentum space and the screening effect of MgO. The obtained TMR ratio reaches as high

as $\sim 1000\%$ with a thick barrier, which will be comparable to that in the ferromagnetic MTJs. Our MTJ employs a widely used barrier MgO, and therefore our results will serve as a realistic baseline for the development of the MTJs based on Mn_3Sn.

References

[1] J. Železný *et al.*, Phys. Rev. Lett. **119**, 187204 (2017).

[2] D.-F. Shao *et al.*, Nat. Commun. **12**, 1 (2021).

[3] L. Šmejkal *et al.*, Phys. Rev. X **12**, 011028 (2022).

[4] K. Tanaka, Y. Toga, S. Minami, S. Nakatsuji, T. Nomoto, T. Koretsune, and R. Arita, Phys. Rev. Mater. **10**, 044405 (2026).

[5] X. Chen, T. Higo, K. Tanaka, *et al.*, Nature **613**, 490 (2023).

[6] J. Dong *et al.*, Phys. Rev. Lett. **128**, 197201 (2022).

[7] C.-T. Chou *et al.*, Nat.Commun. **15**, 7840 (2024).

[8] H. Joon Choi and J. Ihm, Phys. Rev. B **59**, 2267 (1999).

[9] A. Smogunov *et al.*, Phys. Rev. B **70**, 045417 (2004).

[10] A. D. Corso and A. M. Conte, Phys. Rev. B **71**, 115106 (2005).

[11] A. Dal Corso *et al.*, Phys. Rev. B **74**, 045429 (2006).

[12] P. Giannozzi *et al.*, J. Phys.: Condens. Matter **21**, 395502 (2009).

[13] P. Giannozzi *et al.*, J. Phys.: Condens. Matter **29**, 465901 (2017).

[14] G. Pizzi *et al.*, J. Phys.: Condens. Matter **32**, 165902 (2020).

Efficient implementation of spin-cluster expansion for general spin models

Tomonori TANAKA
Department of Materials Science and Engineering, Institute of Science Tokyo, Yokohama 226-8501

Evaluating finite-temperature magnetism and spin textures directly from microscopic electronic-structure calculations remains an important challenge in computational materials science. We adopt the spin-cluster expansion [1], which provides a systematic framework for constructing general spin models from first-principles calculations. Within this framework, we determine the model parameters using torque-based regression instead of conventional energy fitting. Because torques encode the local gradient structure of the energy surface, a fixed number of spin configurations carries more information and yields accurate parameters with fewer data—a clear advantage for large systems and models with many interaction channels.

To validate the proposed method, we applied it to B20-type chiral magnetic materials, $Mn_{1-x}Fe_xGe$ and $Fe_{1-y}Co_yGe$. In these compounds, the lack of inversion symmetry in the crystal structure gives rise to the Dzyaloshinskii–Moriya interaction (DMI), which stabilizes twisted spin textures and leads to helical spin structures. Since the quantitative evaluation of the DMI is itself an important challenge in first-principles studies of magnetism, we first assessed the validity and efficiency of the proposed method through its ability to evaluate this interaction accurately.

Figure 1 shows the DMI parameter for first-nearest-neighbor Fe–Fe pairs in FeGe as a function of the number of sampled DFT calculations. Compared with the conventional energy-fitting approach, the torque-fitting method exhibits much faster convergence of the interaction parameters with respect to the number of data points, demonstrating a clear advantage in data efficiency. Moreover, the final values of the obtained interaction parameters were found to be in good agreement with those reported in previous studies, confirming the quantitative reliability of the present approach.

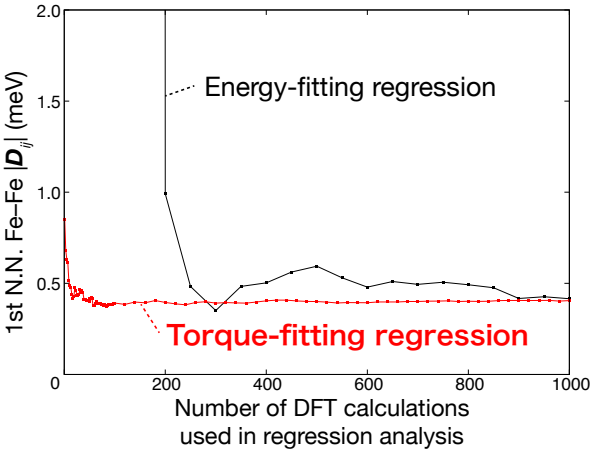

Figure 1: Convergence of the magnitude of the Dzyaloshinskii–Moriya interaction parameter $\boldsymbol{D}_{ij}$ at the first-nearest-neighbor Fe–Fe pairs in FeGe as a function of the number of sampled DFT calculations.

Figure 2 shows the DMI constant D and the helical spin period λ, obtained by mapping the derived spin model onto a micromagnetic model. The divergence of the helical spin period near the composition where $D = 0$,

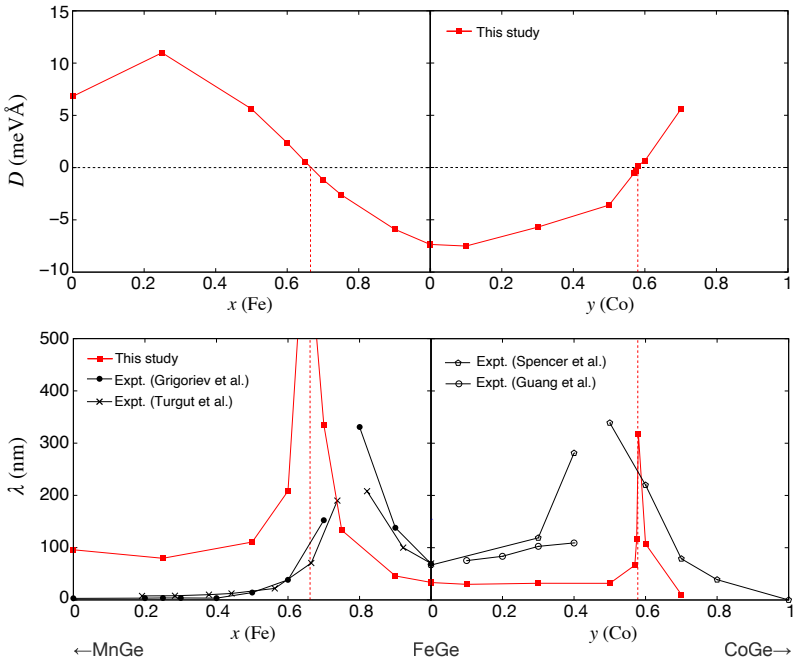

Figure 2: Composition dependence of the micromagnetic D parameter (upper panel) and the helical spin period λ (lower panel) for $Mn_{1-x}Fe_xGe$ and $Fe_{1-y}Co_yGe$. Experimental results are also shown for comparison [4, 5, 6, 7].

which has also been observed experimentally, was successfully reproduced. This result indicates that the present method can correctly capture the composition at which the helical period diverges, and thus that the constructed spin model has sufficient accuracy to describe the magnetic textures of real materials.

These results demonstrate that the spin-cluster expansion combined with torque-based fitting remains accurate when magnetic interactions are anisotropic and mutually competing, while substantially improving efficiency relative to conventional energy fitting. The formulation is anchored in a general multispin Hamiltonian rather than in any specific chemical family, so the same workflow applies broadly across magnetic materials. Wider use of this route should provide a unified first-principles basis for evaluating finite-temperature magnetic behavior over extended temperature windows from a single spin model.

These results have been released on arXiv [2]. In addition, the developed program has been made publicly available on GitHub as the `Magesty.jl` package [3].

References

[1] R. Drautz and M. Fähnle, *Phys. Rev. B* **69**, 104404 (2004).

[2] T. Tanaka and Y. Gohda, arXiv:2512.04458.

[3] https://github.com/Tomonori-Tanaka/Magesty.jl.

[4] S. V. Grigoriev et al., *Phys. Rev. Lett.* **110**, 207201 (2013).

[5] E. Turgut et al., *Phys. Rev. Mater.* **2**, 074404 (2018).

[6] C. S. Spencer et al., *Phys. Rev. B* **97**, 214406 (2018).

[7] Y. Guang et al., *JPhys Mater.* **7**, 025009 (2024).

TDDFT Simulation of Subcycle Reciprocal-Space Electron-Density Dynamics Driven by Intense Laser Fields

Yasushi SHINOHARA[1,2]

[1]*Photon Science Center,*

The University of Tokyo, Hongo, Bunkyo-ku, Tokyo 113-8656

[2]*Basic Research Laboratories,*

NTT Inc. 3-1 Morinosato Wakamiya, Atsugi, Kanagawa 243-0198.

We investigated the behavior of extended materials exposed to strong optical fields by means of time-dependent density functional theory (TDDFT) [1]. When the applied field reaches a magnitude comparable to the internal electric field of the material, highly nonlinear phenomena emerge that are beyond the scope of perturbative approaches. Describing such dynamics therefore requires direct real-time propagation of the time-dependent Kohn–Sham equation. The SALMON-TDDFT code [2] enables real-time simulations of crystalline solids, molecules, and atomic systems based on the Kohn–Sham framework. In the present work, the calculations were carried out using system B at SCC-ISSP.

We carried out TDDFT calculations to investigate subcycle reciprocal-space electron-density images in monolayer hexagonal boron nitride (hBN) and graphene driven by an intense electric field. Real-space electron densities were subsequently obtained through spatial Fourier transformation of the reciprocal-space data. The external field was linearly polarized, with a pulse duration of 14 fs in terms of full width at half maximum (FWHM), a photon energy of 0.4 eV, and a peak intensity of 1 TW/cm^2.

The reciprocal component of the time-dependent density is described by the complex-value amplitudes. Our analysis reveals that the phase (amplitude) time-evolution mainly determines the real-space evolution for monolayer hBN (graphene).

References

[1] Erich Runge and E. K. U. Gross, Phys. Rev. Lett. 52, 997 (1984).

[2] https://salmon-tddft.jp/, M. Noda, S.A. Sato, et al., Computer Physics Communications. 235, 356 (2019).

Ab initio electronic structure analysis for $Ca_5Ir_3O_{12}$

Kazuma NAKAMURA
Quantum Physics Section, Kyushu Institute of Technology
1-1 Sensui-cho, Tobata, Kitakyushu, Fukuoka, 804-8550

Materials with strong spin-orbit interaction (SOI) and their properties are actively studied. In the transition metal oxides, in addition to SOI, crystal field, electronic correlation, Hunds coupling, and frustration are relevant and affect low-energy physics. In the present study, we present *ab initio* calculations for 5*d* transition metal oxide $Ca_5Ir_3O_{12}$.

In $Ca_5Ir_3O_{12}$, there are two phase transitions; the first one is at 107 K, the second one is at 7.8 K [1,2]. Recently, it was clarified that the 107-K transition is the transition to the superlattice structure of $3a \times 3a \times 3c$ [3]. Space group was identified as R_3 with X-ray diffraction analysis [3]. The mechanism is discussed in terms of the order of the electric toroidal moments [3], and the moment configuration in the $3a \times 3a \times 3c$ lattice is proposed. The low-temperature phase transition at 7.8 K is not known apart from the entropy release [1,2].

This report focuses on the origin of the insulating properties of $Ca_5Ir_3O_{12}$. This material is insulating even above 800 K. Although several mechanisms have been proposed, a clear microscopic understanding is still lacking. We show that the insulating behavior of Ca5Ir3O12 originates from a threefold periodic spin structure along the c axis, where the spins rotate in the plane defined by the c axis and the magnetic easy axis. This noncollinear spin structure opens a band gap of approximately 0.2 eV, in good agreement with experiment. We further examine the experimentally observed R_3 structure and find that it can be naturally understood as being based on this threefold periodicity along the c axis. At the

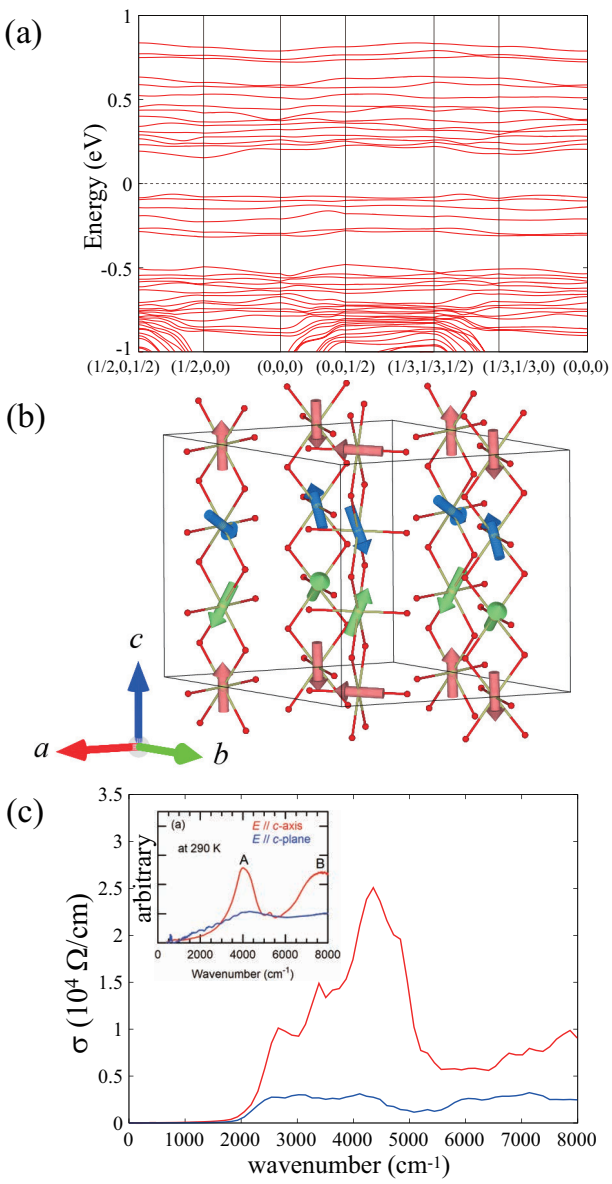

Figure 1: (a) Band structure for the $a \times a \times 3c$ hexagonal supercell, and (b) the corresponding spin configuration. (c) Optical conductivity, where the red and blue curves represent the spectra for $E \parallel c$ and $E \perp c$, respectively. The inset shows the experimental spectrum.

same time, the R_3 structure locally stabilizes a 120-degree spin configuration within the basal plane. As a consequence, local chiral degrees of freedom may emerge, associated with fluctuations of this in-plane 120-degree Neel-like structure.

We performed *ab initio* noncollinear spin density functional calculations using QUANTUM ESPRESSO in which the wave functions were expanded on a plane-wave basis. We employed norm-conserving pseudopotentials, and the generalized-gradient approximation for the exchange-correlation energy. The cutoff energies for the wave function and charge density are 100 Ry and 400 Ry, respectively. The optical spectrum is calculated by using RESPACK, where the energy cutoff for the polarization function was set to 10 Ry, and the total number of bands considered in the polarization calculation was determined to cover unoccupied states up to 10-15 eV above E_F.

Figure 1(a) shows the calculated band structure for the $a \times a \times 3c$ hexagonal supercell, which incorporates the threefold periodicity along the c axis. The system exhibits an insulating band structure with a band gap of approximately 0.2 eV. Panel (b) illustrates the corresponding spin configuration, where spins rotate along the c axis. Panel (c) shows the calculated optical conductivity, together with the experimental spectrum shown in the inset.

Figure 2(a) shows the calculated band structure for the R_3 structure with a rhombohedral lattice. We again obtain an insulating state with a band gap of approximately 0.2 eV. Panel (b) illustrates the corresponding spin configuration. The structure is shown in a $3a \times 3a \times 3c$ hexagonal supercell. We observe a locally stabilized 120-degree Neel-type spin configuration (red vectors) embedded within the antiferromagnetic background. Panel (c) shows the calculated optical conductivity. The agreement with the experimental spectrum is reasonable. This suggests that multiple noncollinear spin configurations can give rise to a similar insulating state.

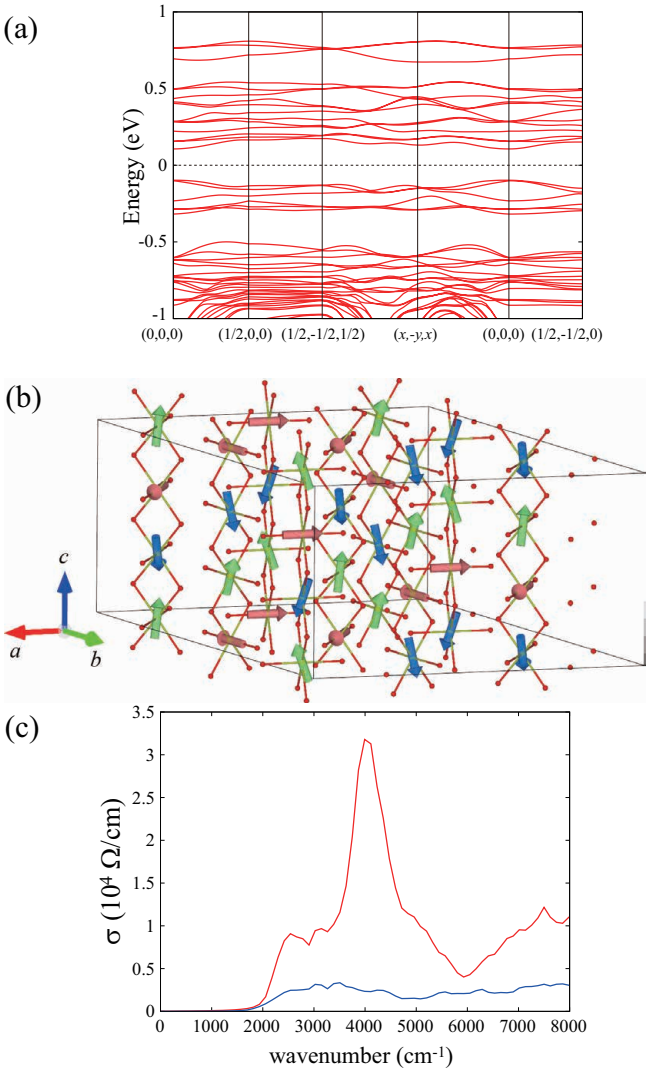

Figure 2: Computational results for the R_3 structure: (a) calculated band structure, (b) corresponding spin configuration, and (c) calculated optical conductivity.

[1] M. Wakeshima, N. Taira, Y. Hinatsu, Y. Ishii, Solid State Commun. **125**, 311 (2003).

[2] K. Matsuhira, K. Nakamura, Y. Yasukuni, Y. Yoshimoto, D. Hirai, Z. Hiroi, J. Phys. Soc. Jpn. **87**, 013703 (2018).

[3] H. Hanate, T. Hasegawa, S. Hayami, S. Tsutsui, S. Kawano, K. Matsuhira, J. Phys. Soc. Jpn. **90**, 063702 (2021).

Ab initio study on static and dynamic properties of light metal alloys

Akihide KOURA

Technical division, Kumamoto University, Kumamoto 860-8555

We have studied static and dynamic properties of light metal alloys, Mg-Zn-Y alloys based on *ab initio* molecular dynamics (AIMD) simulations and MD simulations using machine learning interatomic potentials (MLIPs). In this project, we focused on the concentration of $Mg_{0.8}Zn_{0.08}Y_{0.11}$ alloy to clarify the static structure and dynamic properties. We employed QXMD code for AIMD and MD simulations [1]. We also used the Aenet package to train MLIPs [2].

To develop the robustness of MD simulations using MLIP, we constructed many MLIPs by F4cpu class. Obtained MLIPs were used to make MD simulation robust by the potential averaging method [3]. However, too many MLIPs increase computation time, and the presence of poorly potentials can lead to MD failure. Therefore, it is necessary to carefully select the best MLIPs. In this project, we used four selected MLIPs. Although the calculations were performed without failure, there is room for improvement in the surrounding structure of Zn.

On the other hand, to investigate the concentration dependence of physical properties, we also performed AIMD for liquid $Mg_{0.85}Zn_{0.06}Y_{0.09}$ alloy. As a result of the test run, although average Mulliken charges of Mg and Zn do not depend on the concentration, that of Y at $Mg_{0.85}Zn_{0.06}Y_{0.09}$ alloy is Q = 0.25 in spite of Q = 0.3 at $Mg_{0.8}Zn_{0.08}Y_{0.11}$ alloy. While, the average charge of Zn is approximately $Q = -0.2$. This fact suggests that the Coulombic interaction of Zn and Y atoms contributes the Zn-Y cluster formation ability.

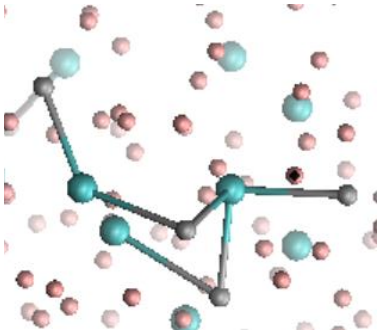

Fig. 1. Fragment of the Zn-Y cluster in liquid $Mg_{0.8}Zn_{0.08}Y_{0.11}$ alloy. Pink, grey, and blue balls correspond to Mg, Zn, and Y atoms, respectively.

References

[1] F. Shimojo, *et al.*, SoftwareX **10**, 100307 (2019).

[2] N. Artrith and A. Urban, Comput. Mater. Sci. **114**, 135 (2016).

[3] D. Wakabayashi, *et al.*, J. Phys. Soc. Jpn. **92**, 074002 (2023).

Machine learning potential for tungsten with defects and hydrogen atoms

Daiji KATO[1], Yuki NOGUCHI[2]

[1]*National Institute for Fusion Science, 322-6 Oroshi-cho, Toki-city, Gifu*

[2]*IGSES, Kyushu University, 6-1 Kasugakoen, Kasuga-city, Fukuoka*

In this project, we performed atomistic simulations to investigate hydrogen–defect interactions in tungsten using system B of the supercomputer facility at ISSP. The primary objective of this study is to develop a novel Machine learning potential to reduce the discrepancy between conventional molecular dynamics simulations based on empirical interatomic potentials and first-principles calculations.

First-principles calculations based on density functional theory (DFT) were carried out using the Vienna ab initio Simulation Package (VASP) [1]. We employed the Perdew–Burke–Ernzerhof (PBE) generalized gradient approximation (GGA) exchange-correlation functional with a plane-wave cutoff energy of 400 eV. To efficiently utilize computational resources, parallel computations were performed using MPI. Each calculation typically used 384 cores, combining k-point parallelization (KPAR = 4) and band parallelization (NCORE = 32). These settings enabled efficient scaling for large supercell calculations containing up to 432 atoms.

To overcome the high computational cost of DFT calculations, a machine learning interatomic potential (MLP) was constructed based on DFT datasets. The MLP was developed using an on-the-fly learning method [2] with the Smooth Overlap of Atomic Positions (SOAP) descriptor and Bayesian linear regression. The training data were generated via high-throughput DFT calculations on the supercomputer, in which a large number of atomic configurations, energies, and forces were computed in parallel. This data generation step required substantial computational resources and was efficiently handled by distributing independent calculations across multiple nodes.

The constructed MLP was applied to structural exploration and cohesive energy calculations. Compared to

first-principles calculations for the same atomic structures, the computational speed was improved by approximately five orders of magnitude. This significant acceleration enabled efficient evaluation of many structures by performing multiple calculations simultaneously, thereby greatly enhancing computational efficiency. Several optimization and tuning techniques were implemented to maximize computational efficiency.

The main results obtained in this study are shown in Fig. 1. It is well known that vacancies in tungsten have positive binding energies for hydrogen atoms, indicating their trapping capability. Figure 1 compares the binding energies of hydrogen atoms to a mono-vacancy in tungsten as a function of the number of hydrogen atoms. For cases with seven or more hydrogen atoms, the results obtained using empirical interatomic potentials exhibit significant uncertainty and deviate from the DFT results. In contrast, the machine learning interatomic potential developed in this study successfully reproduces the DFT results for up to nine hydrogen atoms, thereby improving the reliability and reducing the uncertainty of the predictions [3].

References

[1] G. Kresse and J. Hafner, PRB **47**, 558–561(1993).

[2] R. Jinnouchi et al., PRL 122, 22570 (2019).

[3] Y. Noguchi, and D. Kato, “Machine-learning force fields for hydrogen and vacancy complex in tungsten” Poster presented at: 20th International Conference on Plasma-Facing Materials and Components for Fusion Application (PFMC-20); May 20, 2025; Ljubljana, Slovenia.

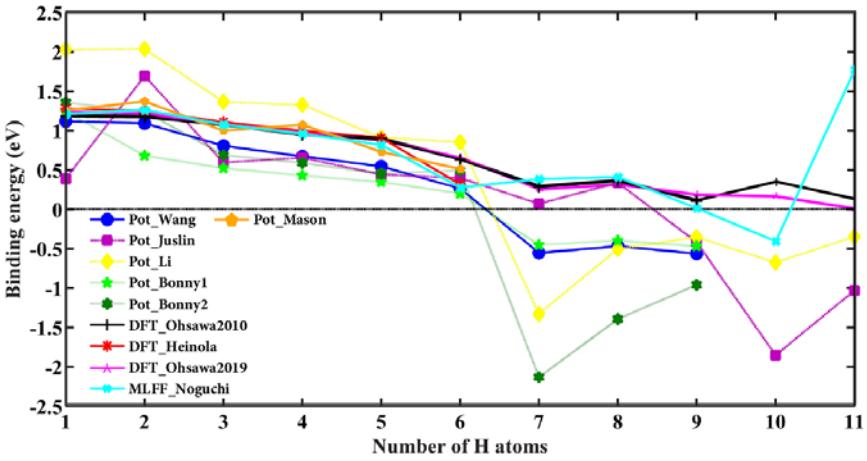

Fig. 1: Binding energy of hydrogen atoms at a mono-vacancy in tungsten. The light blue line (MLFF_Noguchi) is obtained using MLP.

Theoretical study on electronic devices using nitrogen-doped carbon nanotubes

Yoshitaka FUJIMOTO
School of Engineering, Kyushu University, Fukuoka 819-0395

The performance of digital electronic devices has continuously improved through the scaling down of silicon (Si)-based field-effect transistors (FETs) in accordance with Moore's law. However, this downsizing is reaching its physical limits, resulting in the degradation of the device performance. To further enhance the performance of the FETs, novel device structures and new materials with high carrier mobilities for use in the high-speed transport channels have been explored. Among these materials, carbon nanotubes (CNTs) are promising candidates to replace the Si channels due to quasi-one-dimensional structure and high carrier mobility.

The CNTs have been reported to often show p-type conduction property under ambient conditions due to the existence of adsorbates such as oxygen although they originally possess intrinsic semiconducting property. The substitutional doping with nitrogen atoms is expected to be one of the most effective ways to realize the n-type doping property of CNTs. However, the electronic properties of N-doped CNTs and N-doped graphene show p-type doping property under high-temperature growth or high dopant-density conditions of N-doped systems [1].

In this article, we study the electronic transport of the pyridine-type N-doped CNTs and its adsorption effect of an NH_3 molecule based on the first-principles electronic transport theory. We calculate the adsorption energy of NH_3 molecules on the pyridine-type N-doped CNTs. Our calculations suggest that the adsorption of NH_3 molecules induces n-type transport in the system.

We firstly examine the adsorption energy E_a for the adsorption of the NH_3 molecule on the pyridine-type N-doped (10,0) CNTs. Here, the adsorption energy E_a is defined as $E_a = E_{\rm tot} - E_{\rm CNT} - E_{\rm mol}$, where $E_{\rm tot}$, $E_{\rm CNT}$, and $E_{\rm mol}$ are the total energies of the pyridine-type N-doped (10,0) CNTs with and without the adsorption of the NH_3 molecule and the isolated NH_3 molecule, respectively. The adsorption for the NH_3 on the pyridine-type (10,0) CNTs is found to be energetically favorable with $|E_a| = 1.28$ eV for the LDA calculation.

We next examine the electronic transport properties of the pyridine-type N-doped CNTs. The pristine (10,0) CNT shows a semiconducting property with its energy gap of about 0.7 eV. When the pyridine-type N defects are introduced to the nanotubes, they give rise to acceptor-like states near the VBM, rendering the N-doped CNT a p-type semiconductor [2]. We further examine the NH_3 adsorption effects on the electronic transport of the N-doped CNTs. The adsorption of NH_3 molecules can change the electronic transport properties of the pyridine-type N-doped (10,0) CNTs. It is found that the Fermi energy moves towards the CBM from the VBM, and the NH_3 adsorption gives rise to the n-type conduction.

In summary, we have investigated the adsorption effects of NH_3 molecules on the energetics and the electronic transport of pyridine-type N-doped (10,0) CNTs. It is found that the adsorption of the NH_3 molecule on the pyridine-type defects becomes energetically favorable. Our results clarify that the carrier transport (p-type or n-type) is tunable by adsorption of NH_3 molecules on the pyridine-type N-doped CNTs.

References

[1] Y. Fujimoto, Micromachine **15**, 1172 (2024).

[2] Y. Fujimoto, Chem. Phys. **601**, 112933 (2026).

GPU-accelerated QSGW calculations: Application for modulated martensite phases of Ni_2MnGa

Masao OBATA

Institute of Science and Engineering, Kanazawa University, Kanazawa, Ishikawa 920-1192

The quasiparticle self-consistent *GW* (QSGW) method [1] is a powerful first-principles approach that surpasses the G_0W_0 approximation by incorporating off-diagonal elements of the self-energy Σ self-consistently. However, the key steps, evaluation of the screened Coulomb interaction W and the Σ, scale as the fourth power of system size and the square of the number of k-points, restricting QSGW applications to relatively small unit cells. We addressed this limitation by implementing GPU acceleration in the QSGW code ecalj (available on GitHub) using OpenACC and GPU-accelerated math libraries, enabling calculations with 20 or more atoms per unit cell to be practically feasible [2].

Ni_2MnGa exhibits magnetic field-induced strain in its martensite phases, where nanoscale twin boundary modulation plays a central role. Experiments identify modulated martensite structures designated 10M (20 atoms/cell) and 14M (28 atoms/cell) depending on composition and temperature. Standard GGA calculations predict the 10M phase to be metastable, contrary to experimental observations [3], highlighting the importance of beyond-DFT methods. Our previous QSGW studies on the austenite phase suggested that electronic instabilities drive the formation of modulated structures. We extended the QSGW analysis to the 10M and 14M phases, enabled by the GPU acceleration. We find that the minority-spin density of states of Ni near the Fermi level exhibits a characteristic valley structure, with the Fermi level positioned at its minimum in the modulated phases. This suggests that the modulated structures are electronically stabilized by band-energy lowering, a feature absent in GGA calculations, providing a microscopic rationale for GGA's failure to reproduce the stability of the 10M phase.

References

[1] M. van Schilfgaarde et al., Phys. Rev. Lett., 96, 226402 (2006). [2] M. Obata et al., Comp. Mat. Sci, 260, 114190 (2025). [3] M. Zelený et al., Mater. Des. 209, 109917 (2021).

Calculation of adsorption energy of fluorinated molecules on chromate conversion coating layer using DFT+U method

Yuji OHKUBO, Kota YAMAGUCHI, and Kouji INAGAKI
Graduate School of Engineering, The University of Osaka,
2-1 Yamadaoka, Suita, Osaka 565-0871

To realize 6G, which will surpass the performance of current communications systems such as 4G and 5G, high-frequency printed circuit boards capable of high-speed communication with lower dielectric loss than ever before are required. PTFE has significantly lower values of the relative dielectric constant and dielectric loss tangent. Using it as a substrate material enables decreased dielectric loss and increased communication speeds. The substrate material, Cu foil, readily undergoes natural oxidation even in air. Since the formation of this natural oxide layer degrades conductivity and uniformity, industrial applications require corrosion prevention treatment for Cu foil. Among these methods, chrome conversion coating forms an extremely thin layer with high corrosion-resistance properties, making it a suitable treatment for Cu foil used in printed circuit boards. In this study, we calculated the adsorption energies and activation energies for reactions between a chromate conversion coating layer (Cr_2O_3) and fluorinated molecules using DFT calculations, and investigated the functional groups that contribute to improved adhesion.

The calculations were performed using the STATE (Simulation tool for atom technology) code based on density functional theory (DFT) with plane-wave basis and ultra-soft pseudopotentials. In this study, we used the DFT+U method. The generalized gradient approximation exchange-correlation functional based on Perdew-Burke-Ernzerhof (PBE) was used. The wave function and the charge density of cutoff energies were 36 Ry and 400 Ry, respectively. The k-point mesh was 6 × 6 × 2 when calculating bulk Cr_2O_3.

The adsorption energy (E_{ads}) per molecule was calculated using the following equation (1).

$$E_{ads} = (E_{surf} + E_{mol}) - E_{mol/surf} \quad (1)$$

where E_{surf} is the energy of the naked surface slab; E_{mol} is the energy of the isolated fluorinated molecules; $E_{mol/surf}$ is the total energy of the adsorbate–substrate system.

Transition state energies (E_a) were calculated using the CI-NEB method to determine the activation energies of various adsorption reactions. The activation energies (E_{act}) were calculated using the following equation (2).

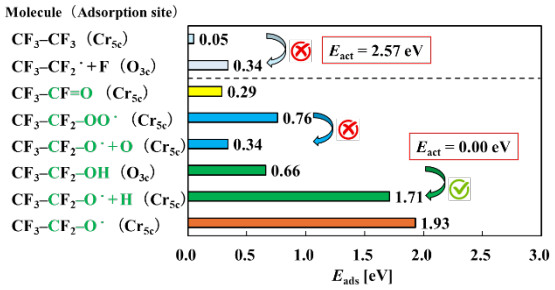

Figure 1 E_{ads} of fluorine-based molecules on the Cr_2O_3 $(10\bar{1}2)$ surface.

$$E_{act} = E_a - E_{ini} \quad (2)$$

Figure 1 shows the calculated adsorption energies of fluorine-based molecules on the Cr_2O_3 $(10\bar{1}2)$ surface. The + in the molecule indicates that atoms from the functional group dissociated and adsorbed separately. CF_3–CF_3 did not adsorb at any site, exhibiting adsorption energies below 0.1 eV. Next, we investigated a system in which F atom is extracted by a surface Cr_{5c} site, undergoing defluorination, and the C atom adsorbs onto a surface O_{3c} site. The E_{act} for this process is extremely high at 2.57 eV, making adsorption onto the Cr_2O_3 surface difficult. On the other hand, fluorinated molecules with oxygen-containing functional groups exhibited higher adsorption energies than CF_3–CF_3, potentially contributing to improved adhesion. Specifically, CF_3–CF_2–OH showed the highest adsorption energy of 1.71 eV after the H atom dissociated during the calculation to form a Cr–O–C bond. The adsorption energy of CF_3–CF_2–O・, lacking the H atom, was exceptionally high

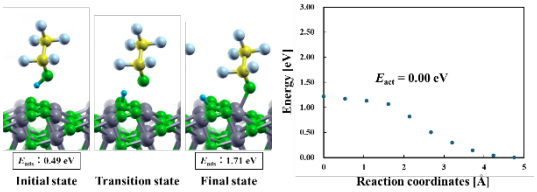

Figure 2 NEB calculation results and model diagram for CF_3–CF_2–OH

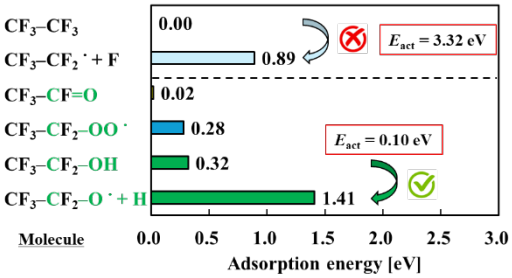

Figure 3 E_{ads} of fluorine-based molecules on the Cr_2O_3 $(10\bar{1}2)$_OH surface.

at 1.93 eV, confirming the strong Cr–O bond. **Figure 2** shows the NEB calculation results and a schematic diagram for the system where H atoms dissociate and adsorb. From **Figure 2**, we found that the E_{act} required for H atom dissociation is 0.00 eV, and the reaction proceeds readily. Therefore, CF_3–CF_2–OH, which has high adsorption energy and sufficiently low E_{act} for the reaction, is considered to be highly effective in contributing to improved adhesion. **Figure 3** shows the calculation results for the surface with OH groups introduced onto the Cr_2O_3 $(10\bar{1}2)$ surface. It was found that even on surfaces with OH groups, CF_3–CF_2–OH contributed most significantly to improving adhesion.

Establishment of guidelines for controlling open-shell nature of molecules by solids

Kohei TADA

Department of Materials Engineering Science, Graduate School of Engineering Science, The University of Osaka, Toyonaka, Osaka 560-8531, Japan

When covalent bonds weaken, the electrons shared in the molecule begin to localise to the atoms, acquiring the properties of unpaired electrons. Such unpaired electrons, originating from covalent bonds, are correlated and cause interesting molecular functions. The unpaired electrons are called open-shell electrons, and molecules possessing the unpaired electrons are called open-shell molecules. The degree of open-shell electrons in molecule, open-shell nature, is utilised in molecular design. However, guidelines for controlling the open-shell nature by solids have yet to be established.

In this project, I analysed the effects of solids on open-shell nature using a proprietary developed method (AP-DFT/plane-wave) [1,2], with the aim of elucidating material functions and designing novel composite materials. I conducted research on catalytic, magnetic, and battery materials, and submitted eight papers (of which five have been accepted) [3–10]. The calculations were performed using Systems B (ohtaka) and C (kugui), and the programme for DFT, VASP, was used. The published papers and concept are summarised in Figure 1. This report provides an overview of (1) surface open-shell nature in Ni_3C catalysts [4], (2) a theoretical proposal for the control of magnetism via solid-molecule interactions [6], and (3) open-shell bands in organic cathodes for batteries [7].

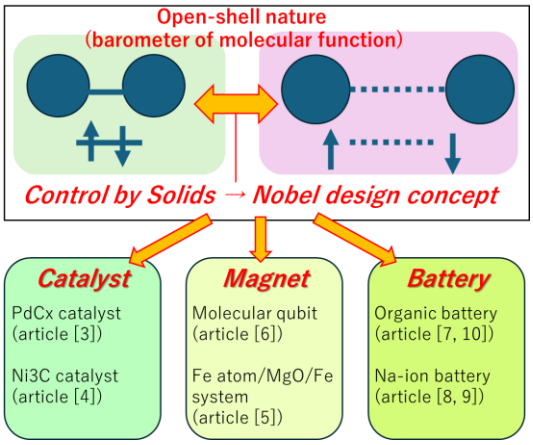

Fig. 1: Concept and Outcome of this study.

In recent years, metal carbides have attracted attention for their unique catalytic activities. However, understanding of their electronic states is insufficient. This study revealed that the surface-exposed carbon atoms in Ni_3C possess intrinsic unpaired electron properties [2]. This is attributed to the covalent nature of the Ni–C, and it will be a factor of different surface reactivity from the metallic or ionic bonds found in metals and oxides.

By controlling the spin of unpaired electrons, open-shell molecules will be applied to high-density memory devices and molecular qubits. Although the integration of the functional molecules into devices requires their incorporation with solids, delocalisation of the unpaired electrons—the source of these functionalities— to the solids has been caused. To propose a solution, I conducted a detailed analysis of the interaction between complexes with radical ligands and metal surfaces, and two approaches were suggested: control of unpaired electron transfer via coverage control, and screening via the insertion of graphene layers [6], which would be verified by experimental study in the future.

Reducing the weight of batteries expands their potential applications. Organic cathodes are attracting attention for the weight reduction. However, redox processes in organic materials often include states with unpaired electrons, which are generally highly reactive. In this study, I investigated a highly durable organic cathode material (trioxotriangulene: TOT) and confirmed the formation of a radical band. To evaluate the stability of this radical band, we quantified the overlap of wave functions between different spins using a developed method. The results demonstrated that the overlap of wave functions in TOT crystals increases with expansion. This implies that intermolecular interactions increase with expansion, suggesting that the radical band will exhibit high robustness against crystal structure changes associated with the insertion of charge carriers such as Li and Na [7].

References

[1] K. Tada, H. Ozaki, K. Fujimaru, Y. Kitagawa, T. Kawakami, and M. Okumura, Phys. Chem. Chem. Phys. **23**, 25024 (2021).

[2] K. Tada, R. Sugimori, R. Kishi, and Y. Kitagawa, Chem. Commun. **61**, 11758.

[3] S. Yamaguchi, M. Sarmiento-Diaz, T. Kawakami, K. Tada, T. Mitsudome, and T. Mizugaki, ACS Appl. Nano Mater. **8**, 13886 (2025)

[4] K. Tada, K. Matsuyama, S. Yamaguchi, R. Kishi, T. Mizugaki, and Y. Kitagawa, Phys. Chem. Chem. Phys. **28**, 1118 (2026)

[5] T.K. Yamada, N.K.M. Nazriq, and K. Tada, Appl. Surf. Sci. Adv. **33**, 100965 (2026)

[6] R. Hirota, K. Tada, K. Ikenaga, K. Katoh, R. Kishi, and Y. Kitagawa, J. Phys. Chem. C, *under review*

[7] Y. Kitano, K. Tada, R. Hirota, T. Kawakami, R. Kishi, and Y. Kitagawa, Bull. Chem. Soc. Jpn. **99**, uoag036 (2026)

[8] R. Kataoka, A. Machida, K. Tada, N. Taguchi, and N. Takeichi, Electrochim. Acta **549**, 148038 (2026)

[9] R. Kataoka, Y. Kitano, K. Tada, Y. Kitagawa, and N. Takeichi, J. Alloy Comp., *under review*

[10] Y. Kitano, K. Tada, T. Kawakami, R. Kishi, and Y. Kitagawa, J. Phys. Chem. C, *under review*

DFT Study of Interfacial Reactions in Plasma-assisted Polishing

Jiayuan Dong and Rongyan Sun

Research Center for Precision Engineering,

The University of Osaka, 2-1 Yamadaoka, Suita, Osaka, 565-0871

Plasma-assisted polishing (PAP) is an advanced technique developed for ultra-precision processing of diamond materials. However, the underlying mechanisms, particularly the interfacial tribochemical reactions, remain unclear at the atomic scale. Therefore, this project employs density functional theory (DFT) calculations to investigate the interfacial chemical processes and clarify the mechanism of material removal in PAP. All calculations were performed using the Quantum ESPRESSO package.

In this study, silicon and diamond surfaces, as well as their friction interface, were constructed to simulate the PAP process. First, the oxidation of the Si(100) surface under oxygen plasma was investigated. The formation of Si–O bonds, replacing Si–Si bonds, indicates a strengthening of the polishing plate due to the higher bond energy of Si–O. Subsequently, the silicon–diamond interface was constructed, as shown in Fig. 1(a), and further oxidized interface, as shown in Fig. 1(b). At the initial interface, Si–C bonds are formed to connect the two surfaces; however, their bond energy is lower than both the C–C back bonds in diamond and the Si–O bonds in the plate,

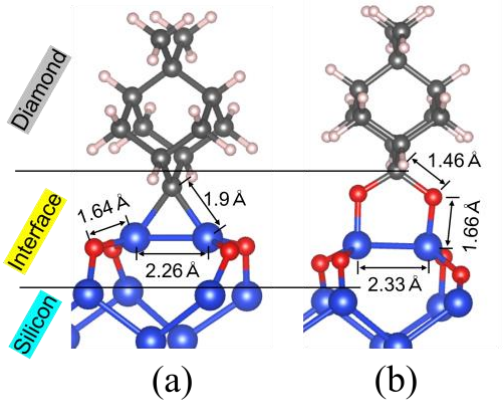

Fig. 1 Frictional interface models. (a) Interface between oxidized Si and diamond surfaces. (b) further oxidized configuration based on (a).

making them insufficient to induce material removal. In contrast, with further oxidation, active oxygen atoms weaken the diamond back bonds and form strong bridging bonds (Si–O–C) across the interface, enabling the breaking of C–C bonds during sliding.

These findings provide theoretical insight into the tribochemical mechanisms governing PAP [1].

References

[1] J. Dong et al., *J. Mater. Process. Technol.*, **348**, 119187 (2026).

Machine Learning-based DFT Calculation of Lignin Adsorption and Oxidative Activity on Co/CeO_2 (111) and Ni/CeO_2 (111)

TEPPEI NUNOURA and ZHIHE ZHAO

Graduate School of Frontier Sciences,

The University of Tokyo, 5-1-5 Kashiwanoha, Kashiwa, Chiba 277-8581

To explore the adsorption behavior of lignin on transition metal cluster-loaded CeO_2 (111) surfaces, we integrated machine learning to the stable adsorption configurations. The machine learning workflow integrates the Atomic Simulation Environment (ASE) with the VASP and the Optuna optimization framework to explore and identify thermodynamically stable adsorption configurations of molecules on solid surfaces. Starting from predefined surface and adsorbate structures, the program systematically varies molecular orientations (Euler angles φ, θ, ψ) and in-plane translation and vertical height (x, y, z) parameters. The adsorption energy is computed as

$$E_{ads} = E_{slab+molecule} - E_{slab} - E_{molecule}$$

Bayesian optimization implemented in Optuna is employed to efficiently sample the high-dimensional configuration space and minimize E_{ads} .

We first identified the thermodynamically stable (111) surface of CeO_2 and modeled Ni and Co cluster loading on this surface. Using a machine learning-assisted workflow, we generated and screened over 500 different lignin adsorption configurations, enabling high-throughput identification of the most stable structures. Among the 500 adsorption configurations, p-Hydroxyphenyl showed the highest adsorption capacity on the Ni/CeO_2 (111) surface than Syringol and Guaiacyl units, and Syringol showed highest adsorption capacity on the Co/CeO_2 (111) surface than p-Hydroxyphenyl and Guaiacyl.

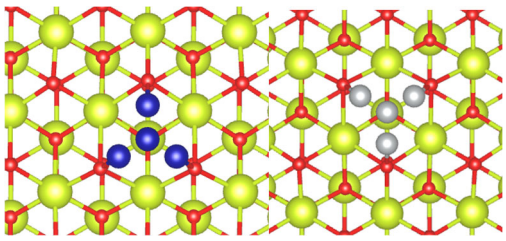

Fig.1 Co/CeO_2 (111) and Ni/CeO_2(111) surfaces.

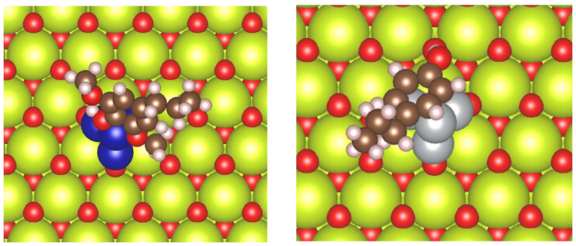

Fig.2 p-Hydroxyphenyl unit adsorbed on Co/CeO_2 (111) and Syringol unit adsorbed on Ni/CeO_2(111) surfaces.

References

[1] Xie, Jin.; et al. *ACS Catal.* **2023**, *13* (14), 9577–958

Surface electronic structure of double perovskite

Kazume NISHIDATE
Graduate School of Science and Engineering, Iwate University
4-3-5 Ueda, Morioka, Iwate, 020-8551

Double-perovskite oxides can be expressed in a general formula $A_2BB'O_6$ and have attracted much attention due to their intriguing physical and chemical properties originating from the mixed valencies of small cations at the B and B' sites. The material is also a potential candidate for the photo-catalysis sensible to the visible light. The energy bandgap separating the valence band and conduction band of semiconductors plays a crucial role in the design of visible-light-driven photocatalysts. It is desirable that the valence and conduction band edges are optimized to effectively facilitate photocatalytic oxidation and reduction processes. Here, the magnitude of the energy bandgap is controlled by the B-site substitution of Sb at Bi ion site.

Higher photocatalytic activities are probably achieved by reducing the rapid recombination of electrons and holes, leading to the photo-excited charge separation, before the progress of the redox reaction at the surface. This fact is related to the presence of multivalent B-site cations. This year, we focused on the double-perovskite oxide $Ba_2Ce(Bi_{1-x},Sb_x)O_6$ We examined the energy band structures and total density of states near the Fermi levels for monoclinic Ba_2CeBiO_6 and cubic Ba_2CeSbO_6 using the density functional theory calculations as implemented in the Quantum ESPRESSO. We applied the Heyd–Scuseria–Ernzerhof hybrid functional (HSE06) formalism for the exchange–correlation in the calculations. Pseudopotentials of the **pslibrary** were used for the relaxation calculations, while in the HSE06 hybrid functional calculations, the norm-conserving pseudopotentials of the **PseudoDojo** were used to accelerate the convergence. We confirmed this transferability by checking the valence band energies at various k-points.

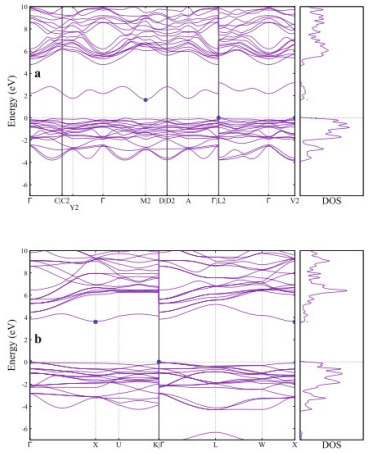

Figure 1: Energy band structures and total density of states near the Fermi levels for **a** monoclinic Ba_2CeBiO_6 and **b** cubic Ba_2CeSbO_6.

We revealed that the band structures, crystalline sizes, and multivalent B-site cations play a significant role in the observed photocatalytic improvements [1].

References

[1] H. Sakou, K. Hata, M. Matsukawa, M. Arakida, K. Nishidate, S. Aisawa, K. Akiba, and D.C. Roy: J Mater Sci: Mater Electron **36**, 1800 (2025)

Density Functional Theory Calculations of CO_2 Adsorption and the Reduction Pathway to CH_4 on Fe (1 1 1) Surface

Masahito Sasaki, Tomoki Oyumi, and Yasuo Izumi

Graduate School of Science

Chiba University, Yayoi 1-33, Inage-ku, Chiba, Japan 263-8522

Photocatalytic CO_2 reduction has attracted considerable attention as a promising approach for establishing a C-neutral cycle to achieve a sustainable society. However, its practical implementation remains challenging because of the high cost of photocatalytic materials and reactor systems. Among the first-row transition metals, Fe is the most abundant and cost-effective element, making it an attractive candidate for CO_2 reduction photocatalysts.

Previously, we demonstrated that Fe–ZrO_2 photocatalysts can reduce CO_2 not only to CO but also to methane, ethane, and propane [1]. It has been suggested that CO_2-derived species activated on the ZrO_2 surface migrate to metallic Fe^0 sites, where sequential hydrogenation proceeds. Furthermore, the product selectivity strongly depended on the irradiated light intensity: CO formation proceeded steadily < 472 mW cm^{-2}, whereas steady CH_4 formation was observed at irradiation intensities > 472 mW cm^{-2}.

Despite these findings, the origin of the initial catalyst deactivation and the mechanism responsible for the change in product selectivity with irradiation intensity have not yet been sufficiently understood on the atomic level. In particular, the detailed nature of CO_2-derived species adsorbed and the reduction pathway on the metallic Fe^0 surface remain unclear.

In this study, a slab model of the Fe (1 1 1) surface was constructed to investigate the adsorption behavior of CO_2 and the reaction pathway from CO_2 to CH_4 by density functional theory calculations using the Vienna Ab Initio Simulation Package code version 6.4.2 with the generalized gradient approximation in the revised Perdew–Burke–Ernzerhof functional. The reaction pathway was calculated based on the climbing-image nudged elastic band (CI-NEB) method to evaluate the activation energy (E_{act}) barriers of the elementary reaction steps. The memories and processors of supercomputer system at ISSP were indispensable for CI-NEB calculations.

The calculation results showed that the CO_2 molecule adsorbed on the Fe surface in an M-shaped configuration with the adsorption energy = −0.92 eV (Scheme 1b), oxidizing partially the surface Fe atoms by the O atoms of CO_2. This result was consistent with the experimental Fe K-edge shift toward higher energy under CO_2, H_2, and the UV–visible light irradiation. Furthermore, the CO_2 adsorbed on the Fe surface was consistent with the appearance of vibrational peaks in FTIR [1].

The analysis of the reaction pathway from the adsorbed CO_2 to CH_4 revealed relatively large E_{act} values for the three steps: 1.24 eV for CO_2 → OCOH (Scheme 1b and c), 1.26 eV for CO → HCO (e and f), and 1.32 eV for CH_3 → CH_4 (j and k). These steps were comparable energy barriers.

Scheme 1. (A) Proposed reaction pathway for the reduction of CO_2 to CH_4 on the Fe (1 1 1) surface and (B) the corresponding free-energy changes of the reaction.

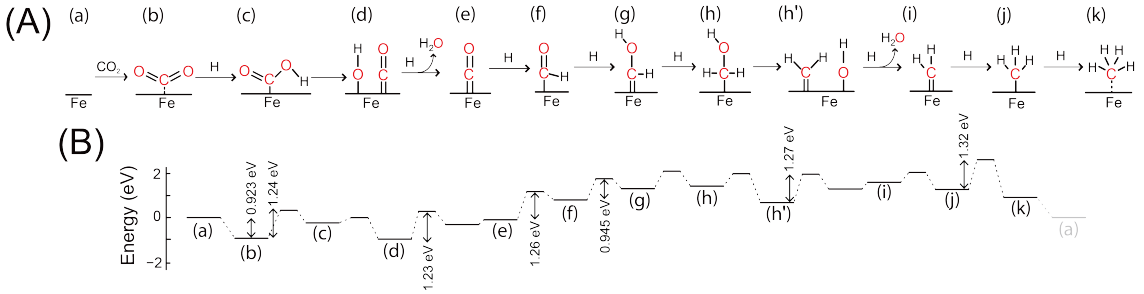

These results suggested that the intermediate CO, CH_2, and especially CH_3 species competed with H species on Fe^0 surface during the photocatalytic reduction reactions of CO_2. More importantly, this study focused on the catalytic behavior over the Fe (1 1 1) surface assuming sufficient irradiated UV–visible light intensity [2]. In fact, in the preliminary DFT calculation results indicated facilitated reaction pathway to CH_4 than that depicted in Scheme 1 if the three electron reduced relatively unstable COH species from CO_2 transferred from ZrO_2 surface to Fe^0 nanoparticles [3]. The calculations of the step of CO and/or COH from ZrO_2 surface to Fe^0 is underway, and soon reported.

References

[1] T. Oyumi, I. Abe, M. Sasaki, and Y. Izumi, *Chem. Commun.* **61**, 8671–8674 (2025).
[2] M. Sasaki, T. Oyumi, K. Hara, H. Zhang, and Y. Izumi, *J. Am. Chem. Soc.* **148**, 13570–13580 (2026).
[3] K. Hara, M. Nozaki, R. Hirayama, R. Ishii, K. Niki, and Y. Izumi, *J. Phys. Chem. C* **127**, 1776–1788 (2023).

Theoretical exploration of goniopolar high-performance thermoelectric materials

Hidetomo USUI

Department of Engineering Science,

The University of Electro-Communications, Chofugaoka, Chofu, Tokyo 182-8585

Goniopolar materials, in which p-type and n-type transport characteristics appear along different crystallographic directions, are promising for transverse thermoelectric applications [1]. In this work, we theoretically explored goniopolar thermoelectric materials by performing first-principles calculations for approximately 150 compounds selected from the Materials Project [2]. The electronic structures were calculated using the VASP [3] and WIEN2k [4] packages, and the Seebeck coefficients were evaluated using BoltzTraP2 [5] within Boltzmann transport theory.

We found several candidate materials showing large directional dependence of the Seebeck coefficient. Among them, $BaPdS_2$ is a representative example. This compound has a quasi-one-dimensional crystal structure, as shown in Fig. 1. This crystal structure gives rise to different Fermi-surface topologies between the valence and conduction bands. This difference leads to a large anisotropy of the Seebeck coefficient and produces goniopolar thermoelectric behavior.

Our results show that first-principles screening combined with Boltzmann transport calculations is an effective approach for discovering goniopolar thermoelectric materials. The present study also suggests that quasi-one-dimensional crystal structures and orbital-dependent band dispersions are important design principles for realizing large anisotropic thermoelectric responses.

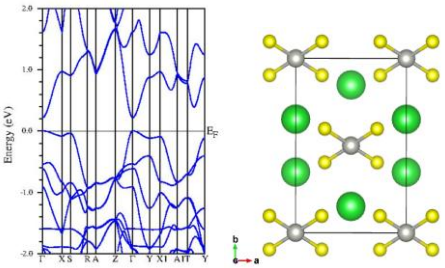

Fig. 1: Electronic and crystal structure of $BaPdS_2$.

References

[1] Y. Tang *et al.*, J. Electron. Mater. **44**, 2095 (2015).

[2] A. Jain *et al.*, APL Mater. **1**, 011002 (2013).

[3] G. Kresse and J. Furthmüller, Comput. Mater. Sci. **6**, 15–50 (1996); G. Kresse and J. Furthmüller, Phys. Rev. B **54**, 11169 (1996).

[4] P. Blaha *et al.*, J. Chem. Phys. 152, 074101 (2020).

[5] G. K. H. Madsen *et al.*, Comput. Phys. Commun. **231**, 140 (2018).

First principles calculation for electron chirality

Shintaro HOSHINO

Department of Physics,

Chiba University, Yayoicho 1-33, Inage-ku, Chiba-shi, Chiba, 263-8522

Recently, chiral materials have attracted significant attention due to characteristic phenomena such as chiral-induced spin selectivity (CISS) and circular dichroism. Quantifying chirality and investigating its relationship with these phenomena are expected to deepen our understanding of their unique properties. This study aims to quantify the chirality of electrons governing material properties, thereby establishing a chirality measure applicable to arbitrary materials.

One candidate for the measure is electron chirality in relativistic quantum theory, which is described by a four-component Dirac spinor at each point in spacetime [1,2]. In condensed matter physics, it is more convenient to use a non-relativistic expression described by the two-component spinor [2-4].

We have studied electron chirality in crystal systems using first-principles calculations and discussed the relationship with the circular dichroism spectrum [5]. Our previous studies have been limited to analyses of semiconductors with simple crystal structures, such as Te. Here, we extended the analysis to other crystal systems. We performed the density functional calculations using Quantum ESPRESSO [6]. After the calculation, we evaluate the electron chirality at each point in space from the obtained Bloch wave function. In this process, we use DiracBilinears.jl, which is a Julia package for computing the electron chirality and other physical quantities in relativistic quantum theory [7].

We employed MPI parallelization in the Quantum ESPRESSO calculations. This enabled efficient computation of the electronic structure, which allowed us to extend our analysis to more complex crystal systems. Furthermore, in the process of calculating electron chirality from the Bloch functions, we also use MPI parallelization over the k-points to achieve additional efficiency improvements.

We apply the present method complex and large-scale material systems. We have computed the electron chirality in organic materials by appropriately employing parallel computations. In addition, to extend our method to the magnetic materials, we examined the computational performance for evaluating Dirac bilinears that characterize the time-reversal symmetry breaking, and confirmed that they can be computed efficiently.

References

[1] J. J. Sakurai, “Advanced quantum mechanics”, Addison-Wesley, (1967).

[2] S. Hoshino, M.-T. Suzuki, and H. Ikeda, Phys. Rev. Lett. **130**, 256801 (2023).

[3] M. Fukuda, K. Soga, M. Senami, A. Tachibana, Int. J. Quantum Chem. **116**, 920 (2016).

[4] S. Hoshino, T. Miki, M.-T. Suzuki, and H. Ikeda, Phys. Rev. B **113**, 115113 (2026).

[5] T. Miki, H. Ikeda, M.-T. Suzuki, and S. Hoshino, Phys. Rev. Lett. **134**, 226401 (2025).

[6] Paolo Giannozzi *et al.*, J. Phys.: Condens. Matter **21**, 395502 (2009).

[7] T. Miki, H.-Y. Chen, T. Koretsune, and Y. Nomura, Comput. Phys. Commun. **317**, 109857 (2025).

Reductive decomposition of fluoroethylene carbonate at electrolyte/electrode interfaces in lithium–sulfur batteries

Yasuhiro UMEBAYASHI

Graduate School of Science and Technology,

Niigata University, 8050 Ikarashi, 2-no-cho, Nishi-ku, Niigata, 950-2181

Fluoroethylene carbonate (FEC) has been widely used as an additive in lithium-ion batteries. More recently, its use as a primary solvent has been reported to suppress polysulfide (PS) dissolution by forming a stable cathode–electrolyte interphase (CEI) on the cathode in lithium–sulfur (Li–S) batteries [1]. However, the detailed mechanisms of CEI formation and PS suppression remain insufficiently understood. In this study, we elucidate the formation of the CEI at the Li metal anode and sulfur cathode, with a focus on the reductive decomposition of solvents and anions.

In the electrolyte/Li anode interface model, a Li (001) slab was constructed by expanding the lattice to a 4 × 4 supercell in the surface plane. The slab initially consisted of four layers with a vacuum region of 15 Å along the c-axis, where each layer contained 16 Li atoms (64 atoms in total). The bottom layer was removed, and the remaining three layers (48 Li atoms) were used as the Li electrode and kept fixed during the simulation. The electrolyte was composed of LiFSA (FSA: $(FSO_2)_2N^-$) and FEC with a molar ratio of 1:12. A cubic simulation cell with a lattice parameter of 11.607 Å ($\alpha = \beta = \gamma = 90°$) was employed.

For the electrolyte/S_8/conductive additive three-phase interface model, a graphene slab was employed as the conductive additive. The slab was constructed by expanding the graphene unit cell to a 3 × 3 supercell in the surface plane, with lattice parameters a = b = 7.392 Å and c = 25.067 Å. The initial four-layer slab was reduced to three layers by removing the bottom layer, and the remaining three layers (54 C atoms in total) were kept fixed during the simulation. The electrolyte composition was set to S_8 : Li : FSA : FEC = 1 : 3 : 12 : 1. The total numbers of atoms and electrons in this model were 358 and 1322, respectively. The initial interface structure was generated by combining the electrode and electrolyte cells. First-principles molecular dynamics simulations were carried out using OpenMX (ver. 3.9.9). The electronic structure was described within the framework of the generalized gradient approximation using the Perdew–Burke–Ernzerhof (GGA-PBE) functional. The basis sets employed were Li8.0-s3p2, N6.0-s2p2d1, S7.0-s2p2d1, O6.0-s2p2d1, F6.0-s2p2d1, C6.0-s2p2d1, and H6.0-s2p1. At the electrolyte/Li interface, FEC solvated to Li^+ was found to undergo reductive decomposition at ~ 1.1 ps, yielding Li_2O and LiF on the Li surface

and CO_2 in the electrolyte. The produced CO_2 may further react to form nonvolatile compounds. No additional reactions were observed even when the simulation was extended beyond 20 ps. During a 23 ps simulation of the electrolyte/S_8/conductive additive three-phase interface, CO_2 formation and FEC dimerization leading to oligomeric species (–HC–O–COO–COO–CH_2CH–) were observed. Sulfur species were also found to decompose into S_5 and S_3 fragments. The LUMO of $Li(FEC)_4$ is significantly lower in energy than that of isolated FEC. The CEI formation is likely facilitated by the presence of chemical species with low-lying LUMO levels that can efficiently accept electrons from polysulfides in the vicinity of the cathode.

References

[1] Y. Torii *et al.*, *J. Phys. Chem. C*, **127**, 15069 (2023)

First-principles studies of magnetic tunnel junctions with noncollinear antiferromagnets

ALPIN N. TATAN

Department of Physics, The University of Tokyo, 7-3-1 Hongo, Bunkyo-ku, Tokyo, 113-0033

Tunneling magnetoresistance (TMR) ratio is an important metric for magnetic tunnel junctions (MTJ). MTJs are commonly made with ferromagnets (FM, e.g. Fe-based compounds) that sandwich an insulating barrier (e.g. MgO). Recently, MTJs made with noncollinear antiferromagnets (AFM) such as Mn_3Sn have been proposed **[1]**. So far, the measured TMR for Mn_3Sn MTJs with MgO barrier is still low (~ few %). This research is thus aimed at exploring new AFM MTJ designs that may achieve a high TMR ratio.

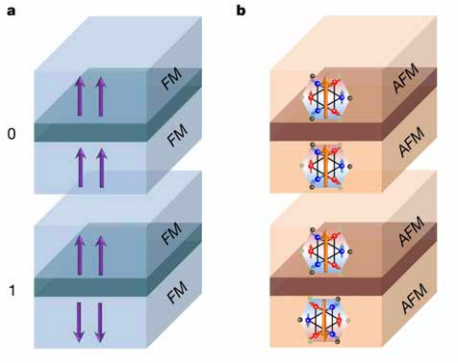

Fig. 1: Illustration of (a) FM- and (b) Mn_3Sn-based AFM MTJs, Figure adapted from **[1]**, which is under Creative Commons Attribution 4.0 International (CC BY 4.0) license.

The open-source first-principles calculation package Quantum Espresso **[2-3]** is used to calculate the electronic structure properties of MTJ models. In particular, the transmission coefficients from solving the quantum scattering problem are connected to the conductance and the TMR, via Landauer-Büttiker formula **[4-5]**:

$$G_{P/AP} = (e^2/h)\sum_{\boldsymbol{k}_\perp} T_{P/AP}\ (\boldsymbol{k}_\perp)$$

$$\mathrm{TMR} = (G_P - G_{AP})/G_{AP}$$

In these first 6 months (Oct 2025~), we screened material databases for barrier candidates and performed interface optimizations by a series of total energy calculations. We then performed TMR calculation on several configurations and obtained mixed results which still require further studies. We believe our preliminary results have promise, and we are collecting more data in the 2026 fiscal year to improve this research comprehensively towards publications.

References

[1] X. Chen et al. Nature **613**, 490 (2023).

[2] P. Giannozzi, et al. J. Phys. Condens. Matter **21**, 395502 (2009); **29**, 465901 (2017)

[3] A. Smogunov, A. Dal Corso, and E. Tosatti. Phys. Rev. B **70**, 045417 (2004)

[4] R. Landauer. IBM J. Res. Dev. **32**, 306 (1988)

[5] M. Büttiker. IBM J. Res. Dev. **32** 317 (1988)

Band tuning of ZnO with varied impurity

Ken-ichi SHUDO

Dep't of Phys, Yokohama National University,

Tokiwadai 79-5, Hodogaya-ku Yokohama, Kanagawa 240-8501

We obtained ultra-violet photoemission spectra (UPS) of nano-particles of ZnO crystals. In the fabrication processes, the purity was varied as the Mg oxide are mixed into the matrix material, and impurity-derived shift of work functions was observed. To elucidates the origin of the shift, we calculated the electronic states for several structures of large-scale crystalline systems (primitive to 5x5x5 unitcell), using a package, the Vienna *Ab initio* Simulation Package (VASP) chiefly.

The band-gap was estimated by means of several methods (LDA, GGA, and +U correction. However, the dependence to the impurity concentration did not reproduce the experimental results, nor apparent tendency to the experimental systematic dose was found. As to size effect, the deeper level electron, chiefly originated from oxygen, was strongly affected by the surface ad-molecules (possible contamination from air) or amorphous peroxide structures.

Thus, the impurity effect is further studied from the view point of calculation methods and re-examination of possible structures. The calculational results suggests requirements for further experimental measurements, in that the surface state in terms of oxidation number should be examined by means of, for example, core shift measurements with X-ray photoemission spectroscopy (XPS) and/or surface local structure using scanning tunneling microscope (STM).

Novel quantum phases in organic Mott insulators based on first-principles calculations

Ryuta IWAZAKI
Department of Physics, Tohoku University
Sendai 980-8578

In a class of materials known as Mott insulators, where electrons are localized at each site due to strong Coulomb repulsion, spin and orbital degrees of freedom become active. As a consequence, Mott insulators provide a platform for rich physical phenomena such as excitonic insulators, in which electrons and holes form bound states called excitons and undergo Bose–Einstein condensation, as well as spin-liquid states [1]. In order to quantitatively elucidate the origin of such phenomena in Mott insulators, analyses based on first-principles calculations are required.

In this study, we aim to explore novel quantum phases using effective models constructed from first-principles calculations for a novel organic Mott insulator λ-(BEST)$_2$GaCl$_4$ (BEST is an abbreviation for the molecule bis(ethylenediseleno)tetrathiafulvalene).
This material exhibits an antiferromagnetic transition at 22 K under ambient pressure. Compared to λ-(BEDT-TTF)$_2$GaCl$_4$, in which the transition temperature is 13 K, the higher magnetic transition temperature suggests that it is located on the negative-pressure side of the temperature–pressure phase diagram, and is considered to be a more strongly correlated system [2]. Furthermore, under applied pressure, it exhibits successive antiferromagnetic–paramagnetic–antiferromagnetic transitions, and the paramagnetic phase realized at intermediate pressure has been suggested to be a spin-liquid state originating from frustration between the magnetic structures of the two antiferromagnetic phases.

We performed density functional theory (DFT) calculations using `Quantum ESPRESSO` [3] for both ambient-pressure and pressurized crystal structures, and constructed a tight-binding model using `Wannier90` [4]. By examining the transfer integrals, we found that the degree of frustration in the triangular-lattice component changes with pressure. Furthermore, based on the constructed Wannier functions, we evaluated Coulomb interactions using `RESPACK` [5]. As a result, we found that the direct integrals differ between molecules. The interface `wan2respack` [6] was used to connect `Wannier90` and `RESPACK`. As a future perspective, we plan to analyze the constructed extended Hubbard model using our developed theoretical framework for localized multi-orbital electron systems [7].

References

[1] As a review, D.I. Khomskii, ECS J. Solid State Sci. Thecnol. **11**, 054004 (2022).

[2] A. Ito *et al.*, Phys. Rev. B **106**, 045164 (2022); N. Yasumura *et al.*, Phys. Rev. B **106**, 245103 (2022).

[3] P. Giannozzi *et al.*, J. Phys.: Condens. Matter **21**, 395502 (2009).

[4] G. Pizzi *et al.*, J. Phys.: Condens. Matter **32**, 165902 (2020).

[5] K. Nakamura *et al.*, Comp. Phys. Commun. **261**, 107781 (2021).

[6] K. Kurita *et al.*, Comp. Phys. Communn. **292**, 107781 (2021).

[7] R.I. and S. Hoshino, Phys. Rev. B **103**, 235145 (2021); R.I. *et al.*, Phys. Rev. B **108**, L241108 (2023); R.I. *et al.*, in preparation.

Decomposition of fluoroethylene carbonate at the electrolyte/Li_2S interface in lithium-sulfur batteries

Jihae HAN

Graduate School of Science and Technology,

Niigata University, 8050 Ikarashi, 2-no-cho, Nishi-ku, Niigata, 950-2181

Dissolution of polysulfides (PS) into the electrolyte during discharge in lithium-sulfur (Li-S) batteries leads to self-discharge and consequently reduces cycle life. The use of fluoroethylene carbonate (FEC) as a primary solvent has been reported to reduce polysulfide (PS) solubility by forming a stable cathode–electrolyte interphase (CEI) on the cathode. [1] However, the formation mechanisms of the cathode–electrolyte interphase (CEI) and the suppression of polysulfide (PS) dissolution in Li-S batteries remain unclear. We have studied to clarify the early-stage formation of the CEI at the electrolyte/cathode active material interface via the reductive decomposition of solvents and anions.

In the electrolyte/Li_2S interface model, Li_2S (fcc, Fm–3m) was constructed as an S-Li-S-terminated slab expanded to a 3 × 3 supercell in the (001) plane, with a vacuum layer of 20 Å along the c-axis. The slab, consisting of 27 Li_2S units, was used to represent the Li_2S active material. The electrolyte was composed of LiFSA (FSA: $(FSO_2)_2N^-$) and FEC with a molar ratio of 1:12. The simulation cell parameters were set to a = b = 12.137 Å and $\alpha = \beta = 90°$, $\gamma = 60°$. The total number of atoms and electrons in the model were 358 and 1322, respectively. The initial structure was constructed by interfacing the two cells. First-principles molecular dynamics simulations were performed using OpenMX ver. 3.9.9. The GGA-PBE functional was used and the basis sets are assigned as follows: Li8.0-s3p2, N6.0-s2p2d1, S7.0-s2p2d1, O6.0-s2p2d1, F6.0-s2p2d1, C6.0-s2p2d1, and H6.0-s2p1.

At the electrolyte/Li_2S interface, FEC solvated to Li^+ was found to undergo ring opening at 0.4-0.5 ps, forming LiF, CH_2CHO, and $LiCO_2$ on the Li_2S surface. No further reactions were observed even when the simulation was extended to 25 ps. The CH_2CHO species is regarded as an intermediate and may subsequently decompose to yield CO_2 and CH_3CH_2OH as final products. This reaction is attributed to the lowering of the LUMO of FEC upon solvation with Li^+, which promotes reductive decomposition. The three-phase interface is crucial for CEI formation, a new electrode model will be developed for further study.

References

[1] Y. Torii *et al.*, *J. Phys. Chem. C*, **127**, 15069 (2023)

Parametric dielectric response and electronic structure analysis of several rare-earth monoxides

Takayuki MAKINO
Research Center for Development of Far-infrared Region, University of Fukui
Bunkyo, Fukui, Fukui 910-8557

1 The Metastable Nature of Rare-Earth Monoxide

Rare-earth sesquioxides are stable wide-gap insulators ($E_g \approx 5.6$ eV), whereas rare-earth monoxides (ReO) form only as metastable phases with an unstable +2 valence. PLD-grown ReO films show a dark brown color, clearly distinct from transparent sesquioxides.

A key difficulty is identifying the origin of low-energy absorption. Earlier work suggested a narrow 0.2 eV gap from linear extrapolation, but this interpretation is limited [1]. Distinguishing a true semiconductor gap from a Drude tail requires a more rigorous multilayer optical model and statistical inference.

The studied heterostructure consists of CaF_2(001), a 180 nm ReO film, a 30 nm sesquioxide reference, and a 10 nm AlO_x cap. Determining the ground state hinges on whether the response is dominated by interband transitions or a semi-metallic Drude contribution.

2 Bayesian Derivation of Dielectric Functions

A three-layer optical model (Substrate / ReO / Effective Layer) with the Denton Fresnel formulation was used to convert R and T into ε_1 and ε_2. To avoid model bias, ε_2 was expanded using 3rd-order B-splines with 40 knots across 0.05–6.5 eV [2], ensuring smoothness and Kramers–Kronig consistency. ε_1 was obtained via KK transformation with a high-energy constant term [3].

Parameter estimation employed STAN's HMC-NUTS algorithm, jointly optimizing film thickness, high-frequency dielectric constant, and spline weights. Computations were performed on a Ryzen 7950X workstation in our lab.

3 Statistical Validation of Free-Electron Response

To identify the physical origin of the optical response, we compared a Drude–Lorentz model (free + bound electrons) with a Lorentz-only model. Model selection used PSIS-LOO cross-validation to estimate ELPD. Calculations were performed on the same Ryzen 7950X system.

Model	ELPD	ΔELPD
Drude-Lorentz	12780.0	—
Lorentz	12734.2	-45.8

The sizable ΔELPD = 45.8 strongly favors the Drude–Lorentz model, indicating a plasma frequency below the measurement window and supporting a semi-metallic ground state.

4 Correlated Electronic Structure Calculations

To validate this interpretation, DFT calculations (Quantum ESPRESSO v7.2) were per-

formed on a Ryzen 7950X system and the ISSP supercomputer. SCF and band calculations used PBE-GGA and PAW potentials. The rock-salt structure was optimized, and a doubled cell with AFM ordering was used to mimic paramagnetic behavior.

Because standard DFT over-delocalizes d-electrons, DFT+U was applied. Linear-response calculations yielded $U = 1.36$ eV for cation-4d and 7.77 eV for anion-2p. Even with U, the band structure retains a semi-metallic overlap, consistent with the Drude–Lorentz optical preference. 4d and 5d monoxides show semi-metallic or metallic ground states, and unlike 3d monoxides, a Hubbard U alone cannot open an insulating gap due to weaker electron localization.

5 Conclusion

Bayesian optical modeling combined with correlated DFT+U calculations establishes ReO as a semi-metallic material. Although earlier absorption extrapolations suggested a narrow-gap insulator, LOOCV strongly supports a Drude contribution, and DFT+U confirms a finite density of states at the Fermi level. This integrated approach resolves the long-standing ambiguity surrounding the electronic ground state of metastable ReO.

References

[1] K. Kaminaga, R. Sei, K. Hayashi, N. Happo, H. Tajiri, D. Oka, T. Fukumura, and T. Hasegawa: Appl. Phys. Lett. **108**, 122102 (2016).

[2] D. Likhachev: Thin Solid Films **636**, 519 (2017).

[3] T. Kurachi, T. Yamaguchi, E. Kobayashi, T. Soma, A. Ohtomo, and T. Makino: Physica B **621**, 413259 (2021).

Theoretical Study on Electronic Properties in New Nanoscale Surfaces and Interfaces

Katsuyoshi KOBAYASHI
Department of Physics, Ochanomizu University
2-1-1 Otsuka, Bunkyo-ku, Tokyo 112-8610

In 2025 we theoretically studied the electronic structure of spiral silicene. In 2024 we had already studied the electronic structure and transmission properties of spiral graphene. The difference between silicene and graphene is the presence or absence of buckling in the atomic structure. The electronic structure is expected to be complex due to the mixing of π and σ states in spiral silicene.

We considered a simple structure for spiral silicene shown in Fig 1. First we calculated

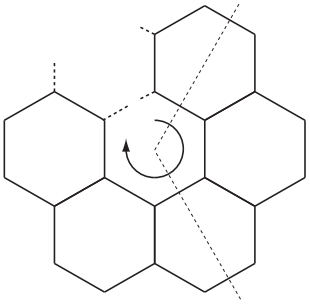

Figure 1: Atomic structure of a spiral silicene. The area enclosed by the thin dotted line is the unit cell of the spiral structure.

the electronic states of a two-dimensional silicene by the density-functional method. The electronic states of a free-standing silicene was calculated. Quantum Espresso was used. Maximally localized Wannier functions were constructed to calculate the electronic states of the spiral silicine. Wannier90 was used. The unit cell of the spiral structure considering the AB sublattice in the bucked structure is shown in Fig 1. The rotational periodic boundary condition was imposed. The calculations took into account that the σ orbitals change direction with a 120° rotation.

Figure 2 shows a band structure calculated as a function of the Bloch phase of the rotational periodic structure. While some bands in the spiral silicene have a shape similar to the π-bands of the spiral graphene, it has been found that the spiral silicene has a complex band structure that is quite different from that of the spiral graphene.

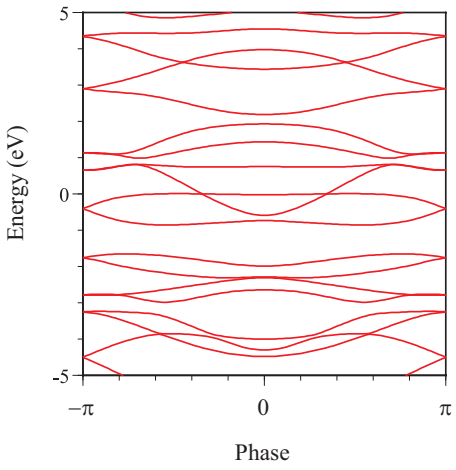

Figure 2: Band structure of a spiral silicene. The origin of energy is the Fermi energy.

Density Functional Tight Binding Calculations of Fullerene Adsorbed on a Tungsten Surface

Hirotaka KITOH-NISHIOKA
Department of Energy and Materials, Faculty of Science and Engineering, Kindai University
3-4-1 Kowakae, Higashiosaka City, Osaka 577-8502

The peculiar field-emission microscope (FEM) images, such as clover-shaped forms, are obtained for the fullerene (C_{60}) adsorbed tungsten (W) nanotip, which is subjected to the strong electric field.[1, 2] Ab initio electronic structure calculations of the C_{60}/W system under strong electric fields are essential to elucidate the mechanisms of the phenomena. However, two primary challenges are remain: (1) the huge computational cost associated with the large system size, and (2) the technical difficulty on performing electonic structure calculations under strong electric-field conditions. This study evaluates the application of the Density Functional-Based Tight-Binding (DFTB) method, which offers computational speeds more than 1,000 times faster than conventional Density Functional Theory (DFT). To focus on the challenge (1) above, all calculations were conducted under zero-electric-field conditions.

A five-layer W slab model with a single adsorbed C_{60} molecule was constructed in a unit cell. For the DFTB calculations, the Slater-Koster parameters for W–W and W–C interactions were adopted from the periodic table-based parameters (PTBP). Dispersion interactions were accounted for using Grimme's DFT-D3(BJ) correction, and all DFTB simulations were performed using the DFTB+ software package. For comparison, reference DFT calculations were performed using the vdW-DF2-B86R functional with the Quantum ESPRESSO package in addition to the calculations using the machine learning potentials with Matlantis.

Figure 1 shows the resultant adsorption energies of C_{60} on the W(100) bridge site as a function of the distance from the surface. The equilibrium distances and adsorption energies at the minima show excellent agreement between the DFTB and DFT methods.

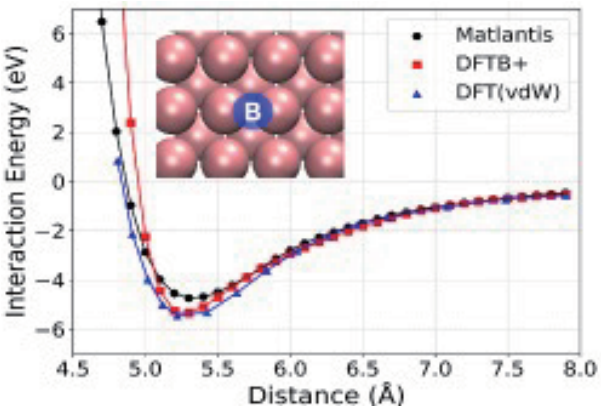

Figure 1: Adsorption Energy Curves for C_{60} on W(100) Bridge Sites, Calculated using DFTB, DFT, and Matlantis(Machine Learning Potential).

References

[1] H. Yanagisawa, M. Bohn, H. Kitoh-Nishioka, F. Goschin, and M. F. Kling: Phys. Rev. Lett. **130**, 106204 (2023).

[2] H. Yanagisawa: Appl. Phys. Lett. **126**, 010501 (2025).

Search and realization of novel electronic properties of surfaces and interfaces and of nanostructures

Takeshi INAOKA
Department of Physics and Earth Sciences, Faculty of Science, University of the Ryukyus, 1 Senbaru, Nishihara, Okinawa 903-0213

We have been performing first principles calculations of the electronic structure of x-form phthalocyanine (x-Pc) crystals [1]. The Pc molecule is a planar π-conjugated macrocyclic molecule which can incorporate an atom of various species at its center position and many kinds of side chains around its molecular plane. The x-Pc crystal is formed by a square-lattice arrangement of molecular chains. In each chain, molecules are stacked with double period and with molecule planes normal to the stacking direction. We can expect effective orbital overlapping between neighboring face-to-face molecule planes. We employed the program package VASP [2-5] mainly on system B.

(I)Pressure-induced metallization of iodine chains in x-LiPcI crystal

The x-LiPcI crystal with Li atoms at molecular centers have iodine (I) atomic chains in open channels between Pc molecule chains. In the stable structure, the I atoms form pentamers as I_5^- in each chain, and this atomic chain is not metallic.

Last year, we reported that, when uniaxial compressive strain is applied to x-SiPcI crystal, trimeric I chains transform into equally spaced metallic atomic chains. In the stable state, the bond length of each trimer is 3.00 Å, and the distance between neighboring trimers is 3.55 Å. With increasing compression in the stacking direction, although the trimer bond length remains unchanged, the intertrimer distance decreases, until it becomes equal to the trimer bond length.

In the case of x-LiPcI, since Pc chains have two-fold periodicity and I atoms are pentamers in each chain, we need to consider a structure with ten-fold periodicity in the stacking direction, in order to track changes in the electronic structure with increasing compression. However, since this primitive unit cell is too large for computational purposes, we calculate that final state in which compressive strain results in equally spaced I atomic chains with the bond length 3.00 Å.

Using the van der Waals density functional theory, we have calculated the electronic structure of the x-LiPcI crystal compressed in the stacking direction to the c-axis lattice constant c_0=6.00 Å (double period). Figure 1 shows the band dispersion on the Γ-Z line in the Brillouin zone. We can identify that rapidly falling band which crosses the Fermi level E_F and which is folded at the Z point because of double period in the stacking direction. Figure 2 exhibits the electron density distribution of the state b193 circled red and that of the state b153 squared red in Fig. 1. As shown clearly in Fig. 2, this

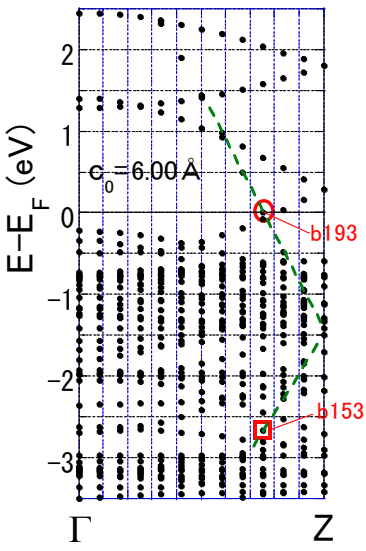

Fig. 1 Band dispersion on the Γ-Z line of x-LiPcI crystal strained compressively in the stacking direction.

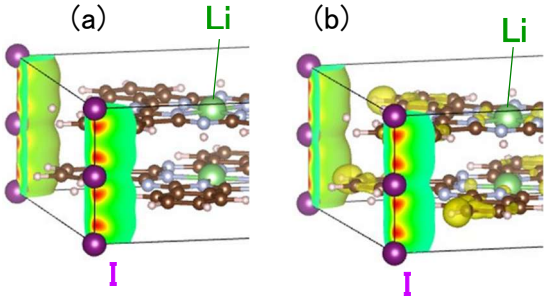

Fig. 2 Electron density distribution of (a) the state b193 circled red and (b) the state b153 squared red in Fig.1.

metallic band is formed by p_z orbital overlapping between adjacent I atoms.

From the gradient of the band energy and the wavenumber at the E_F–crossing point, we can estimate the effective mass ratio and the one–dimensional electron density of the I–derived conduction band to be m^*/m_0=0.09 and n_{1D}=0.83×10^7/cm, respectively. From the strain dependence of the total energy, we found that the uniaxial compressive stress of 1.5 GPa is required to achieve the above compressive strain.

By applying uniaxial compression in the stacking direction, we can transform nonmetallic pentameric I atomic chains into equally spaced metallic ones with high electrical conductivity.

(II) Electronic structure and magnetic properties of x–FePc(CN)$_8$ crystal

In the x–FePc(CN)$_8$ crystal, eight cyano groups are arranged around each molecule plane, and an iron (Fe) atom occupies the center of the molecule plane. We have performed collinear GGA+U calculations and analyzed the electronic structure and magnetic properties of the x–FePc(CN)$_8$ crystal.

Convergent solutions can be obtained in each case of the ferromagnetic (FE) and antiferromagnetic (AF) Fe chains.

Figure 3 (a) displays the total electron density distribution (isosurfaces) of the lower molecule in the unit cell for FE Fe chains. We can observe bonding between the N and H atoms of laterally adjacent molecules, as indicated by red circles. This bonding does not depend on the magnetic state of the Fe atomic chains. From the perspective of avoiding Coulomb repulsion, a stacking angle of 45° is advantageous. However, the staggering angle shifts to 40° to form the N–H bonding.

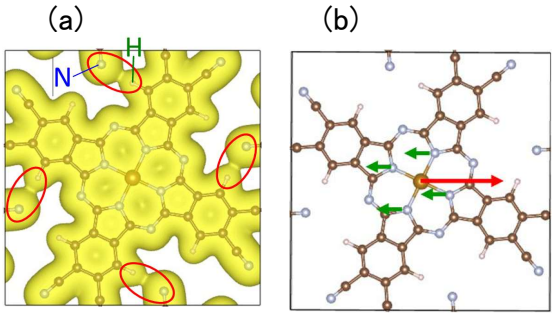

Fig. 3 (a) Total electron density distribution (isosurfaces) of the lower molecule of x–FePc(CN)$_8$ crystal. (b) Magnetic moments of an Fe atom (red) and of its surrounding Ni atoms (green).

Whether the Fe atomic chains are FE or AF, each Fe atom weakly spin–polarizes its surrounding atoms, particularly its nearest N atoms in an AF manner. Figure 3 (b) shows the magnetic moments of an Fe atom and of its surrounding N atoms for the FE Fe chains. The magnetic moment of the Fe atom (red arrow) is 2.1 μ_B (μ_B: Bohr magneton), which is close to the bulk Fe value 2.2 μ_B. The magnetic moments of the N atoms (green arrows) is about 0.035 μ_B, which is two orders of magnitude smaller than that of the Fe atom.

The energy difference between the FE and AF Fe chains is really small, and when using the GGA+U method, we often encounter semistable solutions. After evaluating these magnetic states carefully and accurately, we will conduct a comparative analysis with the comprehensive experimental results [6].

References

[1] T. Inaoka, AIP Advances **14**, 085016 (2024).
[2] G. Kresse and J. Hafner: Phys. Rev. B **47**, 558–561 (1993).
[3] G. Kresse and J. Furthmüller: Comput. Mat. Sci. **6**, 15–50 (1996).
[4] P. E. Blöchl: Phys. Rev. B **50**, 17953 (1994).
[5] J. Klimeš, D. R. Bowler, and A. Michaelides: Phys. Rev. B **83**, 195131 (2011).
[6] M. Isobe et al., ACS Omega **8**, 27264 (2023).

Regional Chemical Potential Analysis for Dimerized Diamond (001) Surface

Masahiro FUKUDA

Institute for Solid State Physics,

The University of Tokyo, Kashiwa-no-ha, Kashiwa, Chiba 277-8581

In this study, we propose the RCP (Regional Chemical Potential) analysis method and demonstrate that it can predict adsorption sites for C dimers and Si atoms on the diamond (001) surface [1]. The RCP on the material surface can be used to evaluate the electron-donating ability of the surface when it tends to form a chemical bond with a probe tip. It can also be used for discussion of where and to what extent atoms or molecules can be selectively adsorbed on the material surface. Specifically, by color-plotting the RCP values within a selected energy range on the zero isosurface of the kinetic energy density of the system, one can visualize regions where covalent bonding is likely to occur, namely sites where atoms or molecules are likely to adsorb.

RCP analysis can be performed by applying post-processing to the density matrix obtained from first-principles electronic structure calculations. As a post-processing code for DFT code, OpenMX [2], we developed a highly parallelized local physical quantity calculation code, FLPQ [3] along with FLPQViewer [4] for visualizing the local RCP.

This analysis enabled visualization of favorable adsorption sites for individual C dimers on the clean diamond (001) surface and allowed prediction of the surface growth process. The results were found to be consistent with AFM experimental observations [5, 6]. We have also applied this approach to the adsorption process of Si atoms on the diamond (001) surface and are exploring the prediction of novel materials ahead of experimental realization.

References

[1] M. Fukuda, M. Senami, Y. Sugimoto, and T. Ozaki, J. Chem. Phys. **164**, 084123 (2026).

[2] T. Ozaki *et al.*, OpenMX package, http://www.openmx-square.org/.

[3] M. Fukuda, FLPQ package, https://github.com/mfukudaQED/FLPQ.

[4] M. Fukuda, FLPQViewer, https://github.com/mfukudaQED/FLPQViewer.

[5] R. Zhang, Y. Yasui, M. Fukuda, T. Ozaki, M. Ogura, T. Makino, D. Takeuchi, and Y. Sugimoto, Nano Letters **25**, 1101 (2025).

[6] R. Zhang, Y. Yasui, M. Fukuda, M. Ogura, T. Makino, D. Takeuchi, T. Ozaki, and Y. Sugimoto, Phys. Rev. Res. **7**, 023036 (2025).

Reexamination of the electron renormalization in conventional superconducting theory

Ryosuke AKASHI
Department of Applied Physics and Physico-Informatics, Keio University
Hiyoshi, Yokohama, Kanagawa 223-0061

The accuracy to theoretically estimate the superconducting transition temperature (T_c) has recently been improved thanks to the development of first-principles electronic and phononic structure calculations. In particular, T_cs of many conventional phonon-mediated superconductors are nowadays calculable from first principles with enough practical accuracy, which are thanks to the development of superconducting density functional theory [1, 2] and Eliashberg theory [3]. There, the screened Coulomb interaction is treated as independent of frequency. The extension to inlude its frequency dependence may enable to treat more significant Coulomb effects but it requires substantially increased computational cost. Practical algorithms are desired.

In this study, we have developed a program to calculate the superconducting properties on the basis of the Eliashberg theory with the frequency dependent screened Coulomb interaction and applied it to a uniform electron gas model with the Einstein-type phonon mode. By linearizing the Eliashberg equations [4] with respect to the anomalous component of the electron self energy, we obtain two set of equations that may be solved sequentially. First one is for the normal state self energy:

$$\Sigma(\mathbf{k}, i\omega_j) = -T\sum_{j'}\sum_{\mathbf{k}'} G(\mathbf{k}', i\omega_{j'})W(\mathbf{k}-\mathbf{k}', i(\omega_j - \omega'_j)) \quad (1)$$

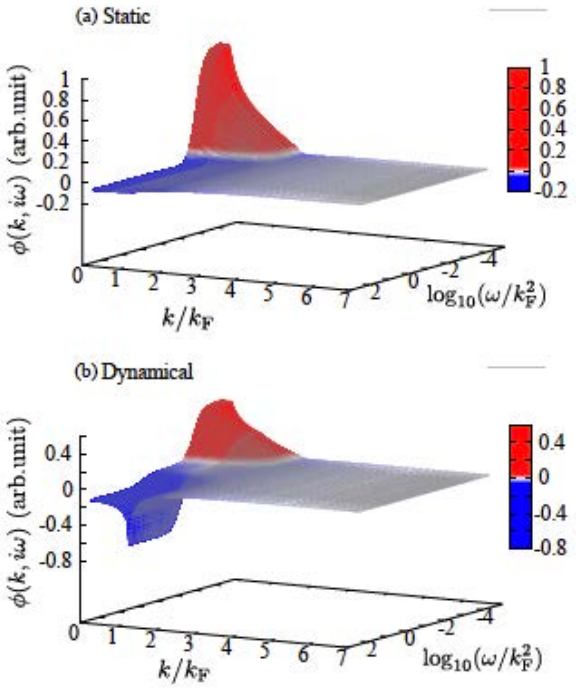

Figure 1: Normalized gap functions at T_c as the eigensolution to Eq. 3. Panels (a) and (b) show the results with the frequency-independent and dependent screened Coulomb interaction, respectively. Taken from Ref. [5].

$$\frac{1}{G(\mathbf{k}, i\omega_j)} = \frac{1}{G_0(\mathbf{k}, i\omega_j)} - \Sigma(\mathbf{k}, i\omega_j). \quad (2)$$

The second one is for the anomalous self-energy component

$$\phi(\mathbf{k}, i\omega_j) = -T\sum_{i'j'} \frac{\phi(\mathbf{k}, i\omega_{j'})W(\mathbf{k}-\mathbf{k}', i(\omega_j-\omega_{j'}))}{\bar{\Theta}(\mathbf{k}, i\omega_j)}, \quad (3)$$

$$\bar{\Theta}(\mathbf{k}, i\omega_j) = \left[\omega_{j'} Z(\mathbf{k}, i\omega_{j'})\right]^2 + \left[\xi(\mathbf{k}) + \chi(\mathbf{k}, i\omega_{j'})\right]^2 . \quad (4)$$

The latter has a nontrivial solution only at the transition temperature. Note that Z and χ in Eq. (3) through $\bar{\Theta}$ are the normal state values related to Σ in Eq. (1) by

$$i\omega_j Z(\mathbf{k}, i\omega_j) = \frac{1}{2}\left[\Sigma(\mathbf{k}, i\omega_j) - \Sigma(\mathbf{k}, -i\omega_j)\right], \quad (5)$$

$$\chi(\mathbf{k}, i\omega_j) = \frac{1}{2}\left[\Sigma(\mathbf{k}, i\omega_j) + \Sigma(\mathbf{k}, -i\omega_j)\right], \quad (6)$$

$W(\mathbf{q}, i\nu)$ is the total interaction between the electrons, that in this case is composed of the Einstein phonon-mediated attraction and the screened Coulomb interaction with the random phase approximation. This model is characterized by four parameters: Wigner-Seitz radius r_s, Debye wavenumber k_D, Einstein frequency ω_E and electron-phonon coupling strength λ: see Ref. [5] for details. We have developed an efficient algorithm to solve those sets using the intermediate representation [6] and continuous Euler transformation [7].

We show in Fig. 1 the calculated gap functions at T_cs with the static and frequency dependent screened Coulomb interactions, respectively. For both cases, the sign changes from low energy ($k \sim k_\mathrm{F}; \omega \sim 0$) to high energy, which indicate the retardation effect. For the dynamical case, we observe a dip at $k \simeq k_\mathrm{F}$ in the intermediate frequency $\omega \gtrsim k_\mathrm{F}^2$. The impact of the dip structure on the resulting T_c is significant, especially in the large r_s regime. We made thorough calculations on the impact for varying model parameters, which should be useful as a reference for the limiting behavior of the first-principles Eliashberg calculations [5].

Also, we have studied the electronic structure of a pressure-induced high-T_c superconductor H_3S [8]. Despite it is formed by compressing the molecular solid phase of H_2S, we have recently found its remarkable uniform-electron like feature of the band structure [9]. To get a deeper insight into this, we calculated the momentum resolved spectral function

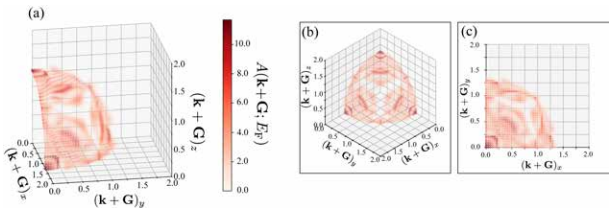

Figure 2: Plane-wave resolved spectral function for the electronic states of H_3S at the Fermi level. Panels (a)–(c) show different views. Taken from Ref. [10].

around the Fermi level

$$A(\mathbf{k}+\mathbf{G}; E_\mathrm{F}) = \sum_n |c_{n\mathbf{k}}(\mathbf{k}+\mathbf{G})|^2 \delta(E_\mathrm{F} - \varepsilon_{n\mathbf{k}}), \quad (7)$$

where $c_{n\mathbf{k}}(\mathbf{k}+\mathbf{G})$ denotes the plane-wave expansion coefficient of the Kohn-Sham eigenstate and $\varepsilon_{n\mathbf{k}}$ is the Kohn-Sham eigenvalue. As clearly shown in Fig. 2, the resulting intensity is concentrated around a spherical region, which indicate that the electronic states around the Fermi level is indeed formed by the uniform-electron-like states. Upon this result we have successfully formulated the nearly uniform electron model for the global band structure with very few parameters [10].

Parts of the model and first principles calculations were executed on System B (Ohtaka). The latter calculations were performed using Quantum Espresso [11] with norm conserving pseudopotentials from Pseudo dojo [12]. See the related publications Refs. [5, 10] for details.

References

[1] M. Lüders *et al.*: Phys. Rev. B **72**, 024545 (2005).

[2] M. A. L. Marques *et al.*: Phys. Rev. B **72**, 024546 (2005).

[3] A. Sanna *et al.*: J. Phys. Soc. Jpn. **87** 041012 (2018).

[4] E. R. Margine and F. Giustino: Phys. Rev. B **87** 024505 (2013).

[5] R. Akashi and H. Shinaoka: Phys. Rev. B **113**, 014507 (2026).

[6] H. Shinaoka, J. Otsuki, M. Ohzeki, and K. Yoshimi: Phys. Rev. B **96**, 035147 (2017).

[7] T. Ooura: J. Comput. Appl. Math. **130**, 259 (2001).

[8] A. P. Drozdov, M. I. Eremets, I. A. Troyan, V. Ksenofontov, and S. I. Shylin: Nature **525**, 73 (2015).

[9] R. Akashi: Phys. Rev. Research **6**, 033012 (2024).

[10] R. Akashi: Ann. Phys. **538**, e00003 (2026).

[11] P. Giannozzi *et al.*: J. Phys. Condens. Matter **29**, 465901 (2017).

[12] G. Pizzi *et al.*: J. Phys. Condens. Matter **32**, 165902 (2020).

Development of a Surface Structure Exploration Program and Supporting Infrastructure

Materials DX Research Center, National Institute of Advanced Industrial Science and Technology (AIST), 1-1-1 Umezono, Tsukuba, Ibaraki 305-8560, Japan

Fumiaki Kuroda

First-principles structure prediction is an important approach for discovering functional materials. By evaluating candidate atomic structures using quantum mechanical calculations, it can identify stable structures without relying only on experimental trial and error. This is especially useful for surfaces, where atomic arrangements strongly affect catalytic activity, electronic properties, and magnetic behavior.

However, surface structure searches are still difficult because many existing methods assume fixed in-plane periodicity and fixed composition. In realistic surface systems, the most stable structure may have a different supercell shape, adsorbate coverage, reconstruction pattern, or alloying composition from those assumed in advance. Therefore, fixing these degrees of freedom can miss important low-energy surface structures.

In this work, we develop a global search framework that treats both two-dimensional superlattice periodicity and stoichiometry as variable degrees of freedom [1]. The method can directly compare surface structures with different supercell shapes and compositions in a unified search. It combines an evolutionary algorithm with surface-specific variation operators and symmetry-enriched initialization, allowing efficient generation of diverse surface candidates.

To reduce computational cost, the framework also uses Bayesian optimization with atomic cluster expansion descriptors. These descriptors represent atomic environments in a form suitable for machine-learning prediction. Bayesian optimization then selects promising structures for further first-principles evaluation, reducing the number of expensive calculations required during the search.

The method is applied to oxygen-induced surface structures on FCC Pt(111) and diamond Ge(100). In both cases, stable structures consistent with experimental observations are obtained. The same framework is also applied to Sn alloying on FCC Au(111), where the predicted alloying motifs agree with reported surface-structure trends.

These results show that the proposed framework can efficiently explore complex surface-structure spaces with variable periodicity and composition. It provides a general route for studying functional materials in heterogeneous catalysis, electronics, and spintronics, where structural and compositional degrees of freedom are strongly coupled.

[1] paper under review.

DFT calculations of the electronic states of guest adsorbates trapped in porous metal-organic thin films

Noriyuki Tsukahara
National Institute of Technology, Gunma College
Maebashi, Gunma 371-0845

I have studied porous two-dimensional metal-organic network (2D-MON) on Cu(111) with guest molecules in the pores of the 2D-MON. The 2D-MON used in this study consists of 1,3,5-tris(pyridyl)benzene (TPyB) molecules and Cu atoms on Cu(111).

DFT calculations were performed using VASP. The slab consists of three layers of Cu(111) substrate, the 2D-MON, and a vacuum layer (about 4 nm thickness), and 405 atoms are included in the slab. In addition, various guest molecules are contained in the pore of the 2D-MON. 2x2x1 k-point sampling was used to perform structural and electronic relaxation, and the adsorption structures and the adsorption energies were calculated.

1. Formation of specific HCOOH oligomer by the 2D-MON

HCOOH molecules aggregate on the Cu(111) surface via hydrogen bonds, forming one-dimensional chain structures. A model was constructed based on the STM results, and structural relaxation was performed on the model. In the pore, a tetramer chain is formed, and its ends are stabilized by electrostatic interactions with the 2D-MON [1].

2. Modulation of adsorption structures of guest 1,3,5-triphenylbenzen (TPhB) and 1,3,5-tris(bromophenyl)benzene (TBB) molecules by the host-guest interaction.

To clarify how the adsorption state of guest molecules in pores is modulated by host-guest interactions, DFT calculations were performed for the host 2D-MON with guest TPhB and TBB molecules. The distance between the TPhB molecule and the Cu substrate is approximately 0.06 Å smaller due to host-guest interactions compared to the TPhB molecule on Cu(111) without the 2D-MON. For guest TBB molecules, the terminal Br interacts attractively with the 2D-MON, causing them to separate from the substrate slightly.

References

[1] N. Tsukahara and J. Yoshinobu, *Small* **21**, e05213 (2025).

Two-dimensional Ag stripe formation on the Ni(110) surface

Tsuneo FUKUDA

Department of Physics and Electronics, Graduate School of Engineering, Osaka Metropolitan University, 1-1 Gakuen-cho, Naka-ku, Sakai, Osaka, 599-8531

The synthesis of materials with novel functionalities is a central goal of materials science. In particular, two-dimensional (2D) metal alloys provide unique opportunities for catalytic and electronic applications that surpass those of their bulk counterparts.

As a model system for such metal-on-metal architectures, we investigate a monolayer of Ag on the Ni(110) surface [1]. Experimentally, Ag deposition on Ni(110) yields a well-defined 2D stripe structure (Fig. 1). Despite its high stability, the mechanism responsible for the formation and stabilization of this Ag stripe phase remains unclear.

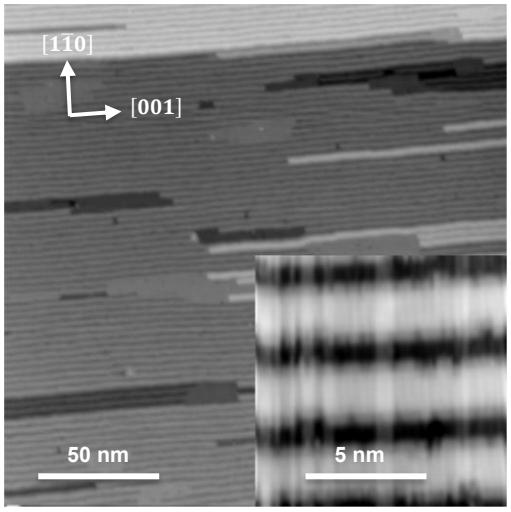

Fig. 1: Typical STM image of Ag-deposited Ni(110) surface showing Ag stripe structure. Inset: Magnified image of the Ag-stripe.

The Ag stripe is composed of one-dimensional (1D) Ag clusters aligned along the [1$\bar{1}$0] direction, which extend in the [001] direction to form a stripe. Our calculations indicate that 1D Ag clusters containing more than seven atoms are unstable, primarily due to the significant lattice mismatch between the Ni substrate and Ag adatoms [2]. This conclusion is based on formation energy comparisons between an n-atom cluster and an (n−1)-atom cluster with an additional Ag atom adsorbed at a neighboring stable site one unit-cell away.

However, such static analyses do not account for kinetic effects, particularly energy barriers associated with atomic motion. To elucidate the dynamics underlying this self-limiting nanocluster formation, we employ the nudged elastic band (NEB) method.

All calculations were performed using VASP with the PBE exchange–correlation functional. To evaluate the stability of 1D Ag clusters, a 12×1 slab model was constructed by extending the Ni(110) surface unit cell along the [1$\bar{1}$0] direction. The slab consists of seven atomic layers and includes vacuum regions of 0.88 nm on both sides, yielding a total of 84 Ni atoms. To allow lattice relaxation along the [001]

Table 1: Calculation Parameters

Parameters	Values
Slab geometry	12×1 or 6×2 units
k- points	4×32 or 8×16
Cutoff energy	384.1 eV
Fermi Energy Smearing	Methfessel–Paxton method σ = 0.12 eV
Vacuum regions	0.88 nm each side
Convergence Condition	Atom position: 0.1 eV/nm Electron energy: <1 μeV
Number of images	Image = 4 (three intermediate states)
Number of cores for each image	256

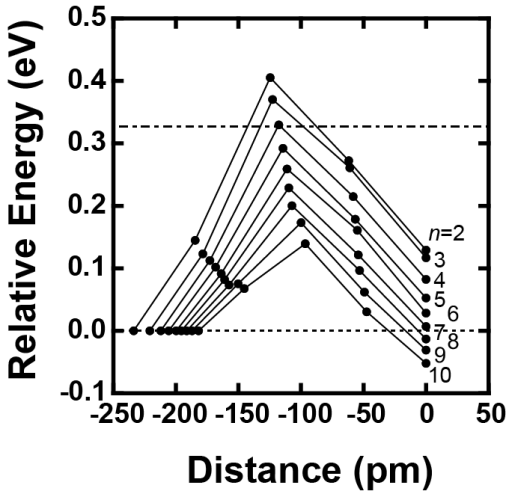

Fig. 2: Potential barrier for the detachment of peripheral Ag atom in the *n*-atom cluster. Number of initial Ag atom (*n*) is indicated nearby each line. Diffusion barrier of single adatom is represented by a dash-dot line.

direction, a 6×2 surface unit cell was also used. Other computational parameters are provided in Table 1.

Transition states for the attachment and detachment of edge Ag atoms were determined using the NEB method. The calculations employed three intermediate states (four images), with convergence criteria identical to those used for adsorption energy calculations.

The results are presented in Fig. 2, where the final state—with the Ag atom at the two-fold hollow site—is taken as a reference position, and the energy barriers are plotted as a function of atomic displacement. For small clusters (n = 2–3), the diffusion barriers are significantly higher than that of a single Ag atom, reflecting the cooperative motion of multiple adatoms. In contrast, for larger clusters (n > 5), the barriers become lower than that of an isolated Ag atom. This reduction arises because edge Ag atoms are subject to lattice mismatch and exhibit weaker adsorption, facilitating their detachment from the cluster.

Thus, edge atoms readily detach (effectively "evaporate") from the 1D clusters, leading to intrinsically self-limiting growth of the Ag stripes. Our results elucidate the origin of stripe formation and the emergence of non-wetting regions between stripes, providing insight into the mechanisms governing this novel nanostructure.

References

[1] A. Mizuhara, T. Fukuda, and K. Umezawa, Surf. Sci. **761**, 122807 (2025).

[2] A. Mizuhara, DaeGwi Kim, and T. Fukuda, e-J. Surf. Sci. Nanotechnol. **24**, 13 (2026).

Structure of Ce-Ti-O honeycomb ultrathin films on Pt(111)

Li Xu and Junji YUHARA

School of Engineering, Nagoya University,

Furo-cho, Chikusa-ku, Nagoya, Aichi 464-8603

Recently, it has been reported that Ba-Ti-O honeycomb structures can be transformed into oxide quasicrystals and approximant structures via Stone-Wales transformations upon oxygen addition [1]. Our group has successfully fabricated Ce-Ti-O ultrathin films on Pt(111) surfaces, featuring both honeycomb and oxide quasicrystal-related structures (Fig. 1) [2]. To gain a deeper understanding of the relationship between honeycomb and quasicrystal structures, it is essential to elucidate the nature of the honeycomb structure itself. The purpose of this study is to characterize the structure of Ce-Ti-O ultrathin films using first-principles calculations.

When 0.5 ML Ce and 2 ML Ti were deposited onto a Pt(111) surface and subjected to annealing in an oxygen atmosphere, followed by vacuum annealing, a Ce-Ti-O-(3×3) honeycomb superstructure was observed (Fig. 1). In the scanning tunneling microscopy (STM) image, the unit cell marked in green corresponds to a (√3 × √3)R30° superstructure; based on the arrangement of bright spots and faint linear features, we interpret this as a honeycomb structure. X-ray photoelectron spectroscopy and resonant photoelectron spectroscopy revealed that Ce corresponds to Ce^{3+}, while Ti corresponds to both Ti^{3+} and Ti^{2+}.

The honeycomb superstructure was modeled based on a Ti_2O_3 honeycomb structure, with Ce atoms decorating the hollow sites of the honeycomb network. Structural optimization was performed using density functional theory with VASP (Fig. 2). The density functional calculations were performed with VASP 5.4.4. The optimized model reveals that the Ti atoms are distributed at different heights. Furthermore, the oxygen atoms in the honeycomb lattice occupied by Ce are found to be positioned closer to the center of the Ce atoms [3].

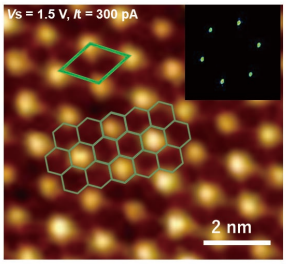

Fig. 1: STM image of the (√3×√3)R30° honeycomb structure

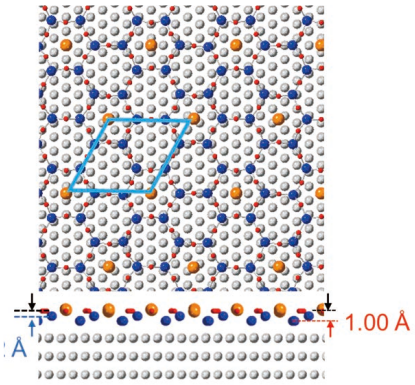

Fig. 2: Computational model of the (√3×√3)R30° honeycomb structure

References

[1] S. Schenk *et al*. Nature Comm. 13, 7542 (2022).

[2] X. Li *et al*., Phys. Chem. Chem. Phys. 25, 26065 (2023).

[3] X. Li *et al*., J. Phys. Chem. C 128, 47, 20238 (2024).

First-principles study of point defects in perovskite photocatalyst $PbTiO_3$

Kazutaka NISHIGUCHI
Graduate School of System Informatics, Kobe University
Rokkodai-Cho, Nada-Ku, Kobe 657-8501

Efficient dopants for perovskite photocatalyst $PbTiO_3$

Perovskite oxide $PbTiO_3$ (PTO) is not only a photocatalyst for overall water splitting but also a ferroelectric material. [1] As in other photocatalysts such as STO:Al, photocatalytic activity is expected to be enhanced through defect control using appropriate dopants. We investigated the electronic structure of doped PTO using first-principles calculations based on density functional theory (DFT). A $3 \times 3 \times 3$ supercell of the primitive PTO cell was used to describe point defects, including oxygen vacancies and substitutional dopants. The DFT calculations were performed within the PBE+U functional using the projector augmented-wave (PAW) method, as implemented in VASP. [2] The Hubbard U parameter was set to 4.75 eV for the Ti-3d orbitals, which reproduces the relative positions of the defect levels with respect to the valence and conduction bands. We also focus on oxygen vacancies V_O and divalent cation D substitution at the nearest Ti site. We consider divalent cations D^{2+} with ionic radii similar to that of Ti^{4+} to introduce hole carriers: D = Mg, Ni, and Zn. Because of the tetragonal crystal structure, the oxygen sites around Ti are distinguished as apical and in-plane oxygens, O_{ap} and O_{in}.

Figure 1 shows the PDOS of PTO:V_{Oap} and PTO:Mg. The presence of V_{Oap} introduces a defect level composed mainly of Ti 3d states below the conduction band. In contrast, Mg substitution at the nearest Ti site (Mg_{Ti}) removes this defect level and restores the band gap. The same trend is observed for V_{Oin}, which is not shown here. Therefore, divalent cation substitution is expected to enhance the photocatalytic activity, similarly to the case of STO. The effects of other divalent cation substitutions, as well as the formation energies of these dopants, will be investigated in future work.

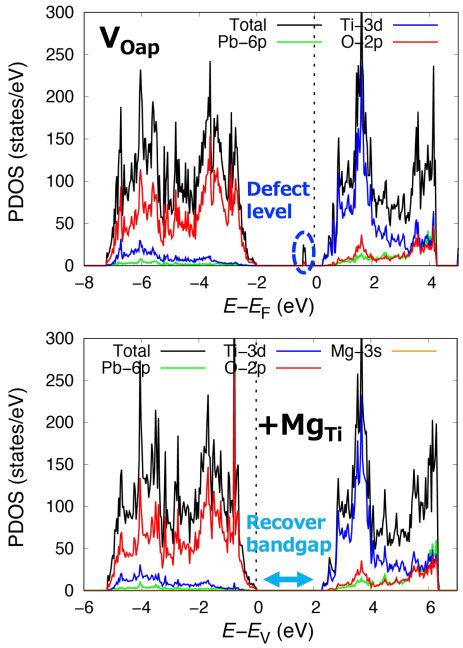

Figure 1: PDOS for PTO:V_{Oap} and PTO:Mg.

Calculation conditions

We have performed hybrid (MPI+OpenMP) parallel computing using, where the parallelization over bands and k-points is used by VASP version 6.4.2.

References

[1] G. Wan *et. al.*: J. Am. Chem. Soc. 2022, 144, 20342–20350.

[2] G. Kresse *et. al.*: Phys. Rev. B **47**, 558 (1993); Phys. Rev. B **49**, 14251 (1994); Computational Materials Science **6** (1996) 15–50; Phys. Rev. B **54**, 11169 (1996).

Development of On-the-fly Machine Learning Potentials in High-Accuracy Phonon Calculations

Takuya NARUSE
Department of Materials Science and Engineering, Kyoto University, Kyoto 606-8501, Japan

Lattice anharmonicity plays an essential role in describing finite-temperature vibrational properties of solids. In particular, temperature-dependent phonon frequencies and finite-temperature thermodynamic properties such as Helmholtz free energy, entropy, specific heat, thermal expansion, and phase stability cannot be fully captured within the conventional harmonic approximation. The stochastic self-consistent harmonic approximation (SSCHA) [1] is a powerful approach for incorporating anharmonic effects at the mean-field level by optimizing an effective harmonic Hamiltonian. However, SSCHA calculations require repeated evaluations of energies and atomic forces for a large number of displaced supercell configurations. Direct application of density functional theory (DFT) to all ensemble structures is therefore computationally prohibitive, especially when wide ranges of temperatures and volumes must be explored.

In this work, we accelerated SSCHA calculations using polynomial machine learning potentials (PolyMLPs) [2] for efficient evaluation of energies and atomic forces. We applied this approach to 33 nonmagnetic elemental metals over wide ranges of temperature and volume to systematically evaluate temperature- and volume-dependent vibrational frequencies and thermodynamic properties. The ISSP supercomputer resources were used primarily for generating DFT reference datasets required for the on-the-fly construction of PolyMLPs and carrying out the SSCHA calculations for these elemental metals.

The PolyMLPs used in this study were constructed through an on-the-fly procedure tailored to SSCHA calculations. For each elemental metal, an initial model was trained from DFT energies and forces of randomly displaced and strained supercells. The model was then used to sample SSCHA ensemble structures at representative temperatures and volumes. When these configurations were not sufficiently described, selected structures were evaluated by DFT and added to the training set. This cycle of SSCHA sampling, DFT data generation, and model retraining was repeated until stable energy and atomic force predictions were obtained, enabling the construction of robust PolyMLPs for 33 non-magnetic elemental metals.

In an SSCHA calculation at a specified temperature and volume, (1) the procedure begins with generating 5,000 configurations based on the density matrix derived from the effective force constants. (2) Next, the energies and atomic forces of these configurations are evaluated using polynomial MLPs. (3) Then, the effective force constants are updated by performing linear regression on the obtained set of displacements and atomic forces. These steps (1)–(3) are repeated starting from the harmonic force constants until the effective force constants converge to a consistent set.

The above SSCHA calculation was performed for 15 volumes with isotropic compression or expansion from the equilibrium volume at 0 K, with temperature increased in 50 K increments. The resulting Helmholtz free energies were fitted to an equation of state to determine the equilibrium volume at each temperature. Subsequently, SSCHA calculations were repeated for the equilibrium volume at each temperature to obtain temperature-dependent frequencies and thermodynamic properties including thermal-expansion effects.

Figure 1 shows the phonon dispersion curves for the body-centered cubic (bcc) phase of Ti. While the dispersion curve obtained from the conventional harmonic approximation exhibits imaginary frequencies, the SSCHA results at 1300 K show no such instabilities and are in good agreement with experimental data. Figure 2 shows the temperature dependence of entropy for both the hexagonal close-packed (hcp) and bcc phases of Ti. The calculated entropies are consistent with experimental values across the

entire temperature range. Similarly, for the other 32 elemental metals, both the calculated phonon dispersion curves and entropies showed good agreement with experiments.

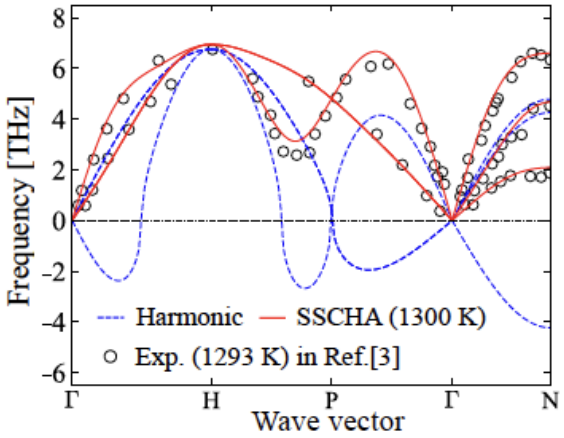

Fig. 1. Phonon dispersion curves from harmonic approximation (dashed line) and SSCHA at 1300 K (solid line) of bcc-Ti. The open symbols are experimental data at 1293 K adapted from Ref. 3.

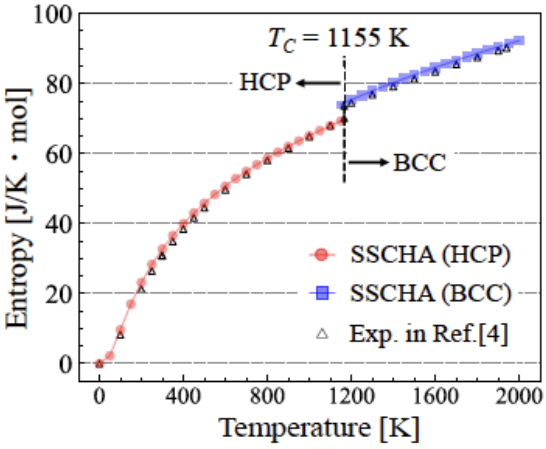

Fig. 2. Entropy as a function of temperature for hcp-Ti (circles) and bcc-Ti (squares). The triangle symbols are experimental values taken from Ref. 4.

Acknowledgment

The computation in this work has been done using the facilities of the Supercomputer Center, the Institute for Solid State Physics, the University of Tokyo (ISSPkyodo-SC-2025-Ba-0028).

References

[1] L. Monacelli, et al., J. Phys.: Condens. Matter 33, 363001 (2021).

[2] A. Seko, J. Appl. Phys. 133, 011101 (2023).

[3] W. Petry, et al., Phys. Rev. B Condens. Matter 43, 10933 (1991).

[4] M. W. Chase, NIST-JANAF Thermochemical Tables (American Institute of Physics, New York, 1998).

Electronic Structure of Rhenium

Takahiro Maehira
Faculty of Science, University of the Ryukyus, Nishihara, Okinawa 903-0213

Rhenium (Re) is a group-VII transition metal with a half-filled d band (electronic configuration $6s^2 5d^5$). The systematics of cohesive energies, bulk moduli, and equilibrium atomic volume for transition metals as the d bands are filled is well understood [1, 2]. The half-filled d band metals are characterized by high cohesive energy, low atomic volume and low compressibility. The early high-pressure work of Bridgman[3] indicated that rhenium is the least compressible of all metals. Re crystallizes in the hexagonal-close-packed (hcp) structure and retains this structure up to its melting temperature of 3180 °C

The compound Re has two phases: a low temperature phase is hexagonal Re. We studied simple cubic Re with a space group of $P6_3mmc$ which contains one molecule in the unit cell. The lattice parameter a and c are 0.2491, 0.402 Å, respectively. The calculation for the energy band structures was carried out by using the OpenMX code(`http://www.openmx-square.org/`). First, we discuss the calculated results for Re as shown in Figure 1, in which we depict the energy band structure along the symmetry axes in the Brillouin zone, which is shown in Figure 1, in the energy region from -10.0 to 10.0 eV. The Fermi level $E_{\rm F}$ is at 0.0 eV. for Re and indicated by dashed lines in Figure 1.

With respect to the energy band structure near $E_{\rm F}$, we emphasize that there is always hybridization between the Re $5d$ and Re $5p$ states in Re. The total number of holes is equal to that of electrons, which represents that Re is a compensated metal. Since the lowest six bands are fully occupied, as shown in Figure 1, the next five bands are partially occupied, while higher bands are empty. This compound is compensated metal because of having two chemical units in the unit cell. We move to discuss the Fermi surface of Re. five bands cross the $E_{\rm F}$, therefore Re has five Fermi surfaces in Figure 2. The color on the Fermi surface illustrates the distribution of the Fermi velocity components. Fermi surfaces for Re centered at the Γ points, respectively. The 10th band has one Cylindrical column-like electron sheet centered at the Γ point. Red-shift indicate the increase of the admixture of Fermi velocity components. The Fermi surfaces were calculated with FermiSurfer [4].

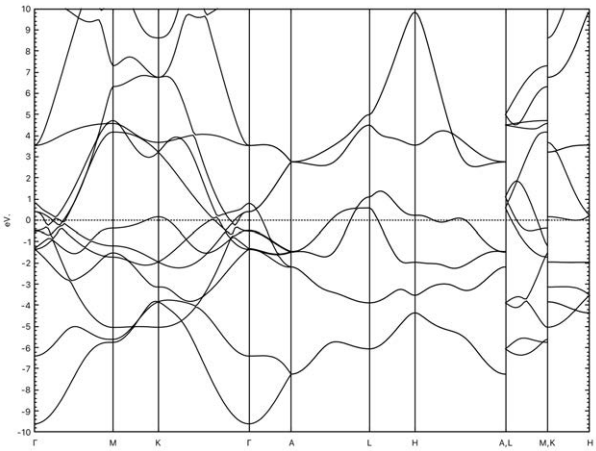

Figure 1: The energy band structure for Re, the symmetry points and axis for the hexagonal structure. $E_{\rm F}$ indicates the position of the Fermi level.

The calculated total density of states (DOS) for Re is shown in Figure 3, in the energy region from -10.0 to 10.0 eV. The total density of states for Re is shown by the solid black line

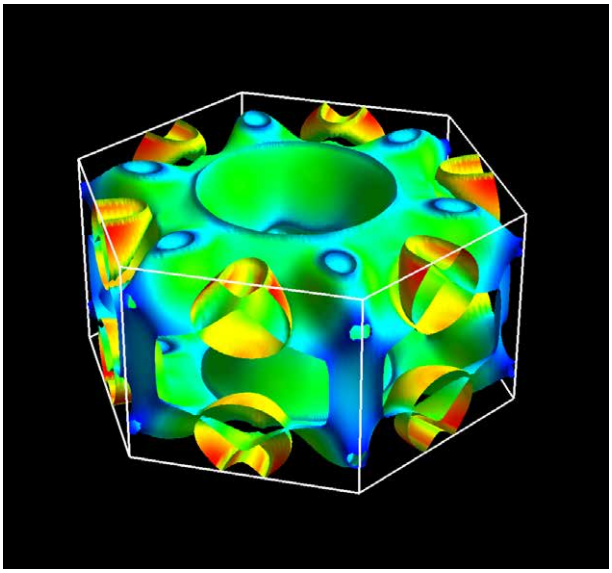

Figure 2: The Fermi surface for Re centered at Γ point. Colors indicate the Fermi velocity components on the Fermi surface.

and the s, p, d and f states are shown by the solid color lines, respectively. This figure tells us that the DOS of the d states is higher than that of the f states at the Fermi level.

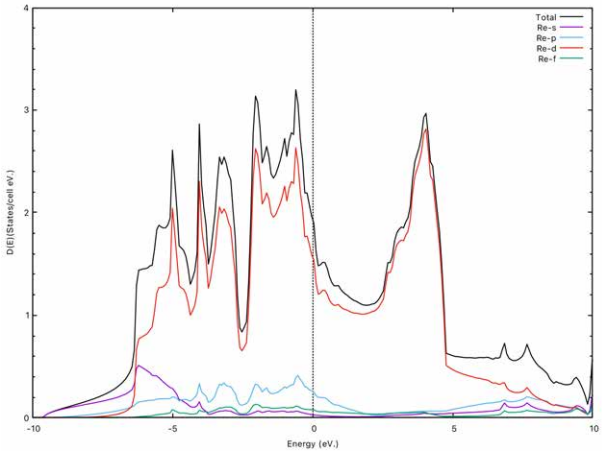

Figure 3: The density of states for Re. E_{F} indicates the position of the Fermi level shown by the dashed line.

References

[1] V. L. Moruzzi, A. R. Williams, and J. F. Janak: Phys. Rev. B 15, 2854 (1977).

[2] C. D. Gelatt, H. Ehrenreich, and R. E. Watson: Phys. Rev. B 15, 1613 (1977).

[3] P. W. Bridgman: Proc. Am. Acad. Arts Sci. 84, 111 (1955).

[4] M. Kawamura: Comp. Phys. Commun 239, 197 (2019).

Analyses of semiconductor surface processes by machine-learning based potentials

Kouji INAGAKI

Graduate School of Engineering, Osaka University

Yamadaoka 2-1, Suita, Osaka 565-087

The mechanochemical processing, a type of ultra-precision surface-flattening and -smoothening technique, utilizes the synergistic effects of mechanical interactions and chemical reactions. The atomic level mechanism, however, remains unclear and its proper understanding is essential for efficient development of the method.

The purpose of this study is to establish and apply a machine learning potential (MLP) based molecular dynamics method to analyze the mechanism. In contrast to previous studies that used MLP trained on structures close to stable (or meta-stable) atomic configurations to explorer new materials with metastable structures, this study aims to realize accurate MLP in the structures near formation and breaking of interatomic bonds to simulate processing phenomena with high accuracy. Nowadays, pretrained potential has widely applied to molecular dynamics. However, because these MLPs incorporate many elements and the total amount of training data is limited, their accuracy is not particularly high, especially for structures in which bond formation occurs. To obtain an accurate MLP, it is necessary to train the model individually by users using a dataset that contains many structures where bond formation occurs, within the range of elements of interest.

Using the diffusion process of hydrogen adsorbed on a Si(001) surface as an example, we implemented an iterative MLP improvement process consisting of training data preparation, MLP generation, MD simulations, and the collection of additional training data. This iterative process enabled the execution of MD simulations. We are currently evaluating the energy barriers associated with the diffusion process. Next, to apply this to mechanochemical processes, we began creating an MLP in Nequip targeting the processes of contact and detachment between two SiO_2 surfaces in water. Furthermore, since SiO_2 in water involves a wide variety of structures, we anticipate that the required training data will be vast; therefore, we have also begun exploring the use of MACE, which can suppress fragmentation even with a small amount of data.

References

[1] K. Inagaki, The 72th JSAP Spring Meeting 2025 14p-K507-9.

Computational study on nanoscale surface/interface structural design based on functional materials

Masaaki MISAWA
Department of Intelligent Mechanical Engineering, Fukuoka Institute of Technology
3-30-1 Wajiro-higashi, Higashi-ku, Fukuoka 811-0295

In this study, we have performed density functional theory (DFT) calculations to investigate structural and electronic properties of (1) in-plane heterostructure of Janus transition metal dichalcogenides (Janus-TMDs), (2) Al (111)/B_4C (001) interfaces, and (3) adsorbed bisphenol-A (BPA) molecule on Al surfaces. All calculations are conducted using the VASP code [1].

Janus-TMDs, which feature different chalcogen atoms on their top and bottom faces, generate an out-of-plane dipole moment due to their structural asymmetry [2]. Based on this property, the new physical phenomena not found in conventional TMDs have been theoretically predicted. This study focuses on the in-plane heterostructure of Janus WSeS/WSeTe, which features a domain wall where the direction of the dipole moment changes. We have performed DFT calculations on the WSeS/WSeTe monolayer and have revealed that it possesses an indirect transition band structure. While the valence states show a mixture of features from both WSeS and WSeTe, the conduction states are primarily derived from WSeTe.

Among lightweight metal-based nanocomposites, Al/B_4C composites have been reported to exhibit excellent mechanical and thermal properties, making them a promising material for advanced structural applications [3]. To clarify the relationship between the Al/B_4C interface structure and its thermal stability, we have performed DFT calculations for the Al (111)/B4C (001) interface with the Al-C stack and the Al-B stack structure, in which C and B atoms are positioned directly below Al atoms, respectively. It is revealed that the Al-B stack model has a greater number of shorter Al-C and Al-B bonds than the Al-B stack model at their interface. On the other hand, the work of adhesion of the Al-C stack model is higher than that of the Al-B stack model, indicating that the Al-C stack model has a more stable Al/B_4C interface.

It has been theoretically and experimentally reported that the adhesion strength of epoxy resins to Al is significantly lower than that to Cu or Fe [4]. To investigate the adsorption properties of epoxy-resin on Al surfaces at atomistic scale, we have performed DFT calculations of the adsorbed BPA molecule, which is a fundamental constituent of epoxy resins, on Al(111), (100), and (110) surfaces. The results showed that a chemical Al-O bond was only formed on the (110) surface, and the vdW interaction plays a dominant role on the other surfaces.

References

[1] G. Kresse and D. Joubert, *Phys. Rev.* **59**, 1758 (1999).
[2] J. Zhang *et al.*, *ACS Nano* **11**, 8192 (2017).
[3] J. Zhou *et al.*, *Nucl. Mater.* **603**, 155465 (2025).
[4] M. Yamazaki *et al.*, *J. Solid Mech. Mater. Eng.* **5**, 54 (2011).

First-principles study of layer-dependent Anomalous Hall Effect in heterostructures

Hana Pratiwi KADARISMAN

Nanomaterials Research Institute (NanoMaRi), Kanazawa University

Kakuma machi, Kanazawa, Ishikawa 920-1192

Anomalous Hall Effect is a Hall effect that occurs in certain magnetic materials where a transverse voltage appears even without an external magnetic field (or with a much smaller role from the external field than in the ordinary Hall effect). The anomalous Hall effect (AHE) arises from two primary mechanisms, namely intrinsic and extrinsic contributions. The intrinsic mechanism originates from the electronic band structure, where spin–orbit coupling (SOC)-induced interband mixing leads to a nonzero Berry curvature.

We performed first-principles calculations of layer-dependent AHE in heterostructures using a local Berry-curvature method on a two-dimensional Brillouin-zone mesh, combined with hybrid Wannier functions localized along a single direction. The electronic structure was investigated through density functional theory (DFT) calculations implemented in the OpenMX code. The results reveal the characteristic features of the anomalous Hall conductivity decomposed by layers, indicating significant contributions from specific layers compared to the other layers [1]. The computational investigation of Fe thin films, Cr thin films, and their combination demands substantial computational resources. For these purposes, we utilized the ISSP Tokyo.

References

[1] H. P. Kadarisman, Y. Morishima, N. Yamaguchi, and F. Ishii: in preparation.

First-principles research on the Catalytic Properties of Quasi-One-Dimensional Boron Chains of CuB/Cu(111)

Takeru Nakashima[1], Yuki Tsujikawa[2], Takahiro Kondo[3], Takanori Koitaya[4], Iwao Matsuda[5], Yasunobu Ando[1]

[1]*Institute of Integrated Research, Institute of Science Tokyo, Yokohama, Kanagawa, 226-8501*

[2]*Department of Chemistry, Keio University, Yokohama, Kanagawa, 223-8522*

[3]*Institute of Pure and Applied Sciences, University of Tsukuba, Tsukuba, Ibaraki, 305-8573*

[4]*Department of Chemistry, Graduate School of Science, Kyoto University, Sakyo-Ku, Kyoto, 606-8502*

[5]*The Institute for Solid State Physics, The University of Tokyo, Kashiwa, Chiba, 277-8581*

We investigated the catalytic properties of the recently reported CuB/Cu(111) surface [1-3], which features unique quasi-one-dimensional boron (B) chains as shown in Fig.1. Using first-principles calculation code based on density functional theory (DFT), we analyzed the adsorption of key intermediates in CO_2 hydrogenation—specifically, hydrogen (H), oxygen (O), and formate (HCOO)—on this surface.

Our calculations revealed that the B chains act as active sites for each step of CO_2 hydrogenation due to significant charge transfer from the Cu atoms to the B atoms. We also identified the stable adsorption configurations of intermediates. Furthermore, we found that H atoms preferentially migrate along these B chains through a three-center two-electron (3c-2e) bonding mechanism at the transition state (see Figs.2 and 3). These findings suggest that the CuB/Cu(111) surface holds great potential as a tunable catalyst for CO_2 conversion.

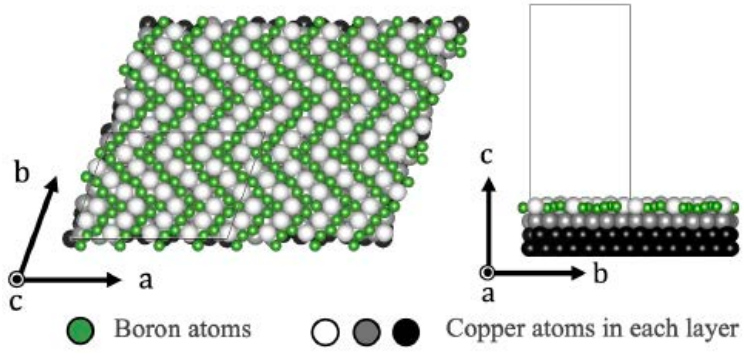

Fig. 1: Slab model of CuB/Cu(111). Spheres, with green and a grayscale gradient from white to black, denote B and Cu atoms, respectively. The reference-slab model has a vacuum layer of 20 Å or more. The system was constructed with monoclinic cell parameters of a=30.0, b=21.8, c=15.9 Å, and α=70.28 degree (a is unique axis). This structure was reported by experimentally by Yue(2021).

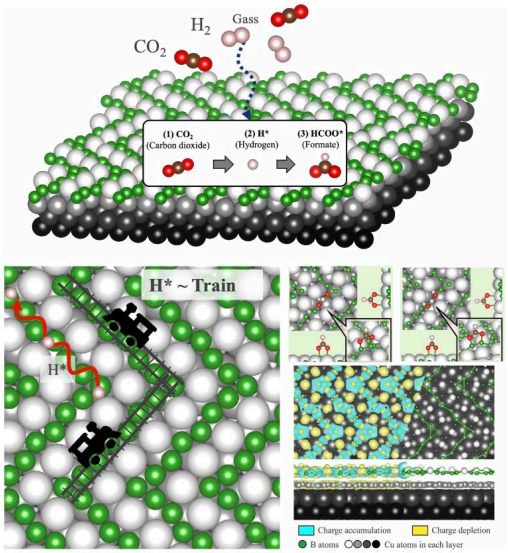

Fig. 2: The concept figure of this research. We focused on the elementary steps relevant to CO_2 hydrogenation—hydrogen, oxygen, and formate adsorption on this surface—by using first-principles calculations (OpenMX), mainly.

The computational resources of the ISSP supercomputer were primarily utilized for large-scale DFT calculations. We employed the OpenMX (Open source package for Materials eXplorer) code (v.3.9) [4], which is based on DFT with norm-conserving pseudopotentials and a local basis of pseudoatomic orbitals (PAOs). The simulations include the structure optimization and charge transfer, and analysis on the nudged elastic band (NEB) calculations from chine-learning potential method (Matlantis)

To manage the high computational cost ociated with these tasks, we utilized the I/OpenMP hybrid parallelization scheme. high-performance computing environment vided by the ISSP enabled us to perform se extensive simulations with high efficiency scalability.

ferences

T. Nakashima, Y. Tsujikawa, T. Kondo *et al.*, J. Phys. Chem. C **130**, 5411 (2026).

[2] Y. Tsujikawa, M. Horio, Z. Zhang *et al.*, Phys. Rev. B **106**, 205406 (2022).

[3] C. Yue, X-J Weng, G. Gao *et al.*, Fundam. Res. **1**, 482 (2021).

[4] T. Ozaki and H. Kino, Phys. Rev. B **72**, 045121 (2005).

[5] S. Takamoto, C. Shinagawa, D. Motoki *et al.*, Nat. Commun. **13**, 2991 (2022).

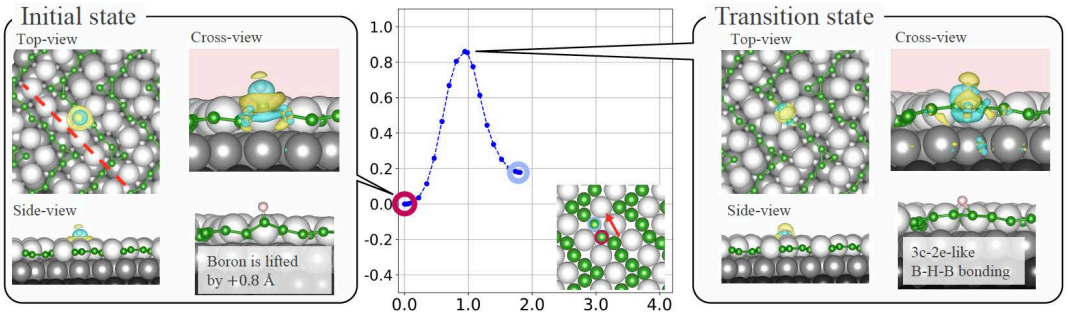

Fig. 3: The charge transfer calculations via OpenMX (transition states are simulated by the Matlantis). We found that H atoms preferentially migrate along these B chains through a three-center two-electron (3c-2e) bonding mechanism at the transition state.

Preliminary Screening of Interfacial Charge Control in Ni/CeO_2 Catalysts for Dry Reforming

Takaya FUJISAKI

Faculty of Materials for Energy, Shimane University,
Matsue, Shimane 690-8504, Japan

Background and objective

Dry reforming of methane (DRM; $CH_4 + CO_2 \rightarrow 2CO + 2H_2$) is an important reaction for the efficient utilization of biogas in solid oxide fuel cells. Biogas typically contains both CH_4 and CO_2, and the direct conversion of these molecules into syngas is therefore attractive for improving the overall efficiency of biomass-derived energy systems. However, DRM proceeds through several elementary reaction steps at the catalyst surface, including CH_4 adsorption and dissociation, CO_2 adsorption and dissociation, oxygen transfer, and the formation and desorption of CO and H_2. The reaction efficiency is strongly affected by the local atomic and electronic structures of the metal–oxide interface. Identifying an appropriate catalyst-design strategy therefore requires an atomistic understanding of how the supported metal cluster, oxide surface, and interfacial charge distribution influence the activation barriers of the elementary reactions.

In our previous DFT and experimental study [1], methane dissociation on $Ni_4/CeO_2(111)$ was investigated using two supported-cluster configurations: a Ni_4-above-Ce configuration and a Ni_4-above-O configuration. Although the exposed Ni atoms directly interacting with methane were similar in the two models, the atomic species located below the supported Ni_4 cluster differed. This difference altered the charge transfer between the CeO_2 support and the Ni cluster. Bader charge analysis showed that the Ni_4 cluster was more positively charged in the Ni_4-above-O configuration (+1.03|e|) than in the Ni_4-above-Ce configuration (+0.78|e|). Correspondingly, the DFT-derived apparent activation barrier for methane dissociation decreased from 0.83 to 0.80 eV. The calculated value was also reasonably consistent with the experimentally estimated activation energy of 0.69 eV obtained using a flower-like Ni-supported CeO_2 catalyst. These results indicated that the reactivity of supported Ni nanoparticles cannot be explained solely by their geometric structures. Instead, the electronic state of the interfacial Ni atoms, which is influenced by the underlying oxide support, is also an important factor in controlling the reaction barrier.

On the basis of this finding, we proposed interfacial charge control as a catalyst-design concept for further improving DRM activity. In particular, substitution of an oxygen atom by a more electronegative fluorine atom near the Ni/CeO_2 interface was examined as a chemically simple approach for modifying the local electronic environment of the supported Ni cluster. During FY2025, we constructed several fluorine-substituted $Ni_4/CeO_2(111)$ interface models and performed structural optimization calculations for the initial and final states of the elementary reactions. We also carried out preliminary screening of CO_2 dissociation pathways because CO_2 activation is another important elementary step in DRM and may become a limiting factor when the methane dissociation barrier is reduced. These calculations were intended to clarify whether fluorine substitution can systematically stabilize favorable reaction states and lower the activation barrier through interfacial electronic modulation. Although a clear low-barrier configuration has not yet been identified, the calculations revealed that the reaction energetics are sensitive to the fluorine-substitution site, the CO_2 adsorption geometry, and the position of the dissociated oxygen atom. The results provide a basis for refining the reaction models and selecting representative pathways for more detailed climbing-image nudged elastic band calculations.

Computational approach

Geometry optimizations and trial climbing-image nudged elastic band (CI-NEB) calculations were conducted with VASP. The computational workflow followed the previous $Ni_4/CeO_2(111)$ model and used PBE-D3 with a GGA+U treatment for Ce 4f states (U = 7 eV). Selected F-substituted interface models were calculated using SCC-ISSP resources, including System B (ohtaka). For each candidate, the initial state (IS) and dissociated final state (FS) were optimized before selected pairs were promoted to more expensive NEB calculations. Because dopant sites, endpoint geometries, and NEB images can be evaluated independently, job-level parallelism was used to screen multiple structures efficiently.

This hierarchical workflow was adopted to avoid spending large computational resources on poorly constructed paths. It is particularly important for supported nanoclusters, where a small change in local geometry can alter the optimized endpoint and the resulting reaction energy.

To examine the effect of fluorine substitution on the local electronic environment of the Ni/CeO_2 interface, an oxygen atom near the supported Ni cluster was replaced by a fluorine atom. Figure 1 shows a representative initial-state structure constructed for the calculation of CH_4 dissociation on the F-substituted $Ni/CeO_2(111)$ interface. A CH_4 molecule was placed near the supported Ni cluster, where the elementary dissociation reaction is expected to occur, and the atomic positions were subsequently optimized by DFT calculations. The fluorine atom was introduced in the vicinity of the Ni cluster to investigate whether local substitution at the oxide surface modifies the interfacial electronic structure and the reaction energetics.

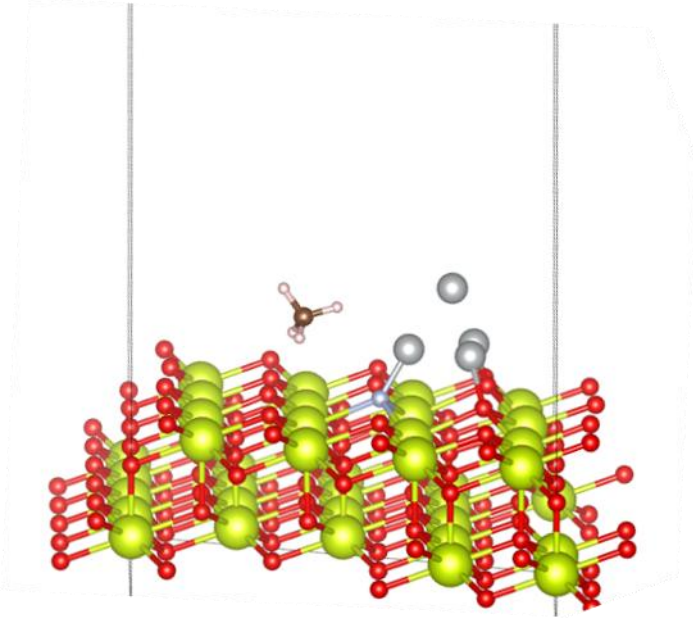

Fig. 1. Representative initial-state structure for CH_4 dissociation on a Ni cluster supported on an F-substituted $CeO_2(111)$ surface. A fluorine atom was introduced near the Ni/CeO_2 interface to modify the local electronic environment of the supported Ni cluster. Gray, pale-colored, red, yellow, brown, and white spheres represent Ni, F, O, Ce, C, and H atoms, respectively.

F-substituted interface models

As a first step, F atoms were placed near the supported Ni_4 cluster and several optimized endpoint structures were compared. The calculated endpoint reaction energies for CH_4 dissociation, ΔEFS-IS, were +0.72, +0.70, +0.21, and -0.19 eV for four representative configurations (Fig. 2). The wide variation demonstrates that the result is sensitive to the dopant position and local geometry. The negative value for Model 4 means that the optimized FS is thermodynamically lower than its IS; however, it does not by itself demonstrate a smaller kinetic barrier.

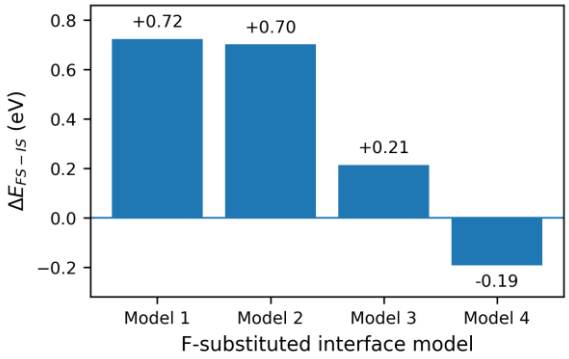

Fig. 2: Endpoint reaction-energy screening for CH_4 dissociation on four F-substituted $Ni_4/CeO_2(111)$ interface models. The values are ΔEFS-IS and should not be interpreted as activation barriers.

Preliminary screening of CO_2 dissociation

Several CO_2 adsorption and dissociation structures were optimized, and a trial NEB pathway was evaluated. A representative profile exhibited a maximum relative energy of approximately 2.60 eV (Fig. 3). This high value is a diagnostic result rather than a final activation barrier: adsorption sites, dissociated-oxygen positions, and IS-FS interpolation require further refinement.

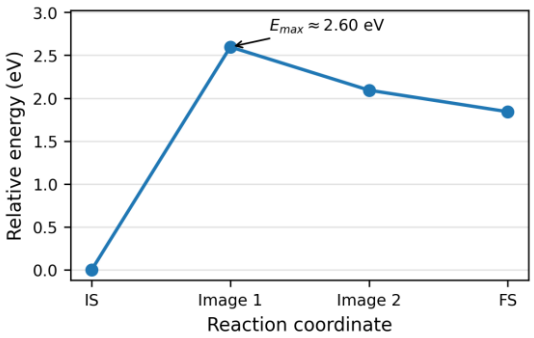

Fig. 3: Representative preliminary CI-NEB profile for CO_2 dissociation on $Ni_4/CeO_2(111)$. The pathway requires further optimization.

Interpretation of the FY2025 calculations

Although a robust low-barrier composition has not yet been identified, the FY2025 calculations yielded a clear intermediate outcome. Simple placement of F close to the Ni cluster does not automatically lower the methane-dissociation barrier. The endpoint results instead show that the interfacial electronic state must be considered together with the detailed local structure. Likewise, the preliminary CO_2 pathway shows that chemically reasonable initial and final structures must be constructed before comparing activation barriers.

Progress relative to the proposed project

The original project aimed to screen $Ce_{1-x}Zr_xO_2$ supports and heteroatom-modified Ni clusters for CO_2 dissociation. The calculations remained at the workflow-establishment stage because both F substitution and CO_2 dissociation exhibited strong configuration sensitivity. This finding changes the order of the screening steps: direct large-scale NEB calculations should be avoided until endpoint structures have been validated. The FY2025 study therefore refined the computational protocol needed for reliable large-scale exploration.

Use of ISSP supercomputer resources

The SCC-ISSP systems were used for multiple VASP geometry optimizations and trial NEB calculations. The resource-intensive component was not a single large job but the parallel evaluation of multiple candidate structures and reaction images. Candidate dopant sites and endpoint pairs were first compared using independent jobs. Only selected pairs were promoted to CI-NEB calculations. This job-level parallel strategy improved throughput and reduced the risk of expending resources on unphysical pathways.

Refined next-stage workflow

The subsequent screening will proceed in four steps (Fig. 4): (i) generate several local configurations for each support and dopant composition, (ii) optimize IS and FS endpoint structures, (iii) retain only physically reasonable endpoint pairs, and (iv) perform CI-NEB calculations followed by Bader-charge and bonding analyses for promising transition states. The refined workflow will be applied to $Ce_{1-x}Zr_xO_2$ supports and heteroatom-modified Ni clusters while retaining multiple local arrangements for each composition.

Summary

During FY2025, SCC-ISSP resources were used to examine interfacial electronic-state control in Ni/CeO_2 catalysts for DRM. Endpoint screening of F-substituted interfaces revealed strong site dependence, and preliminary CO_2-dissociation calculations clarified the need for careful reaction-path optimization. These results provide a practical basis for subsequent systematic exploration of lower-barrier catalyst structures.

References

[1] T. Fujisaki et al., Phys. Chem. Chem. Phys., DOI: 10.1039/d4cp01324g (2024).
[2] H. Jia et al., Curr. Appl. Phys. 43, 9-14 (2022).

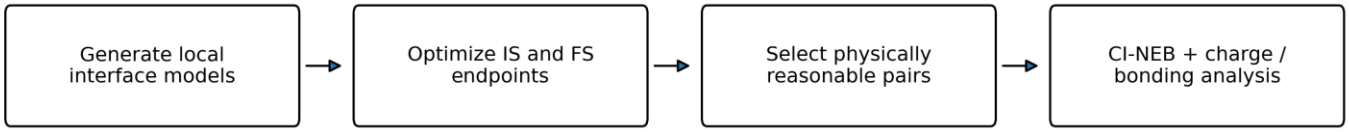

Fig. 4: Refined screening workflow established through the FY2025 SCC-ISSP calculations. Expensive CI-NEB calculations are restricted to physically reasonable endpoint pairs.